Study of the role of two dimensional nanosheets as fillers in Sol-Gel anticorrosion coatings deposited on metal surface

Yu Shi

N°d'ordre NNT : 2021LYSEI004

THESE de DOCTORAT **DE L'UNIVERSITE DE LYON**
opérée au sein de
INSA de Lyon

École Doctorale 34
L'École Doctorale Matériaux

Spécialité/ Génie de matériaux:

Soutenue publiquement le 11/02/2021, par :
Yu SHI

Study of the role of two dimensional nanosheets as fillers in Sol-Gel anticorrosion coatings deposited on metal surface

Devant le jury composé de :

Nom, prénom	grade/qualité	établissement/entreprise	
OLIVIER, Marjorie	Professeur	Université de Mons	Rapporteure
PRORIOL-SERRE, Ingrid	Professeur	Université de Lille	Rapporteure
TOURY, Bérangère	MdC-HDR	Université Lyon 1	Examinatrice
GIGANDET, Marie-Pierre	MdC	Univ Bourgogne Franche-Comté	Examinatrice
BENAYOUN, Stéphane	Professeur	Ecole Centrale de Lyon	Examinateur
NORMAND, Bernard	Professeur	INSA de Lyon	Directeur de thèse
YUAN, Sheng	MdC	INSA de Lyon	Invité

Département FEDORA – INSA Lyon - Ecoles Doctorales – Quinquennal 2016-2020

SIGLE	ECOLE DOCTORALE	NOM ET COORDONNEES DU RESPONSABLE
CHIMIE	**CHIMIE DE LYON** http://www.edchimie-lyon.fr Sec. : Renée EL MELHEM Bât. Blaise PASCAL, 3e étage secretariat@edchimie-lyon.fr INSA : R. GOURDON	**M. Stéphane DANIELE** Institut de recherches sur la catalyse et l'environnement de Lyon IRCELYON-UMR 5256 Équipe CDFA 2 Avenue Albert EINSTEIN 69 626 Villeurbanne CEDEX directeur@edchimie-lyon.fr
E.E.A.	**ÉLECTRONIQUE, ÉLECTROTECHNIQUE, AUTOMATIQUE** http://edeea.ec-lyon.fr Sec. : M.C. HAVGOUDOUKIAN ecole-doctorale.eea@ec-lyon.fr	**M. Gérard SCORLETTI** École Centrale de Lyon 36 Avenue Guy DE COLLONGUE 69 134 Écully Tél : 04.72.18.60.97 Fax 04.78.43.37.17 gerard.scorletti@ec-lyon.fr
E2M2	**ÉVOLUTION, ÉCOSYSTÈME, MICROBIOLOGIE, MODÉLISATION** http://e2m2.universite-lyon.fr Sec. : Sylvie ROBERJOT Bât. Atrium, UCB Lyon 1 Tél : 04.72.44.83.62 INSA : H. CHARLES secretariat.e2m2@univ-lyon1.fr	**M. Philippe NORMAND** UMR 5557 Lab. d'Ecologie Microbienne Université Claude Bernard Lyon 1 Bâtiment Mendel 43, boulevard du 11 Novembre 1918 69 622 Villeurbanne CEDEX philippe.normand@univ-lyon1.fr
EDISS	**INTERDISCIPLINAIRE SCIENCES-SANTÉ** http://www.ediss-lyon.fr Sec. : Sylvie ROBERJOT Bât. Atrium, UCB Lyon 1 Tél : 04.72.44.83.62 INSA : M. LAGARDE secretariat.ediss@univ-lyon1.fr	**Mme Sylvie RICARD-BLUM** Institut de Chimie et Biochimie Moléculaires et Supramoléculaires (ICBMS) - UMR 5246 CNRS - Université Lyon 1 Bâtiment Curien - 3ème étage Nord 43 Boulevard du 11 novembre 1918 69622 Villeurbanne Cedex Tel : +33(0)4 72 44 82 32 sylvie.ricard-blum@univ-lyon1.fr
INFOMATHS	**INFORMATIQUE ET MATHÉMATIQUES** http://edinfomaths.universite-lyon.fr Sec. : Renée EL MELHEM Bât. Blaise PASCAL, 3e étage Tél : 04.72.43.80.46 infomaths@univ-lyon1.fr	**M. Hamamache KHEDDOUCI** Bât. Nautibus 43, Boulevard du 11 novembre 1918 69 622 Villeurbanne Cedex France Tel : 04.72.44.83.69 hamamache.kheddouci@univ-lyon1.fr
Matériaux	**MATÉRIAUX DE LYON** http://ed34.universite-lyon.fr Sec. : Stéphanie CAUVIN Tél : 04.72.43.71.70 Bât. Direction ed.materiaux@insa-lyon.fr	**M. Jean-Yves BUFFIÈRE** INSA de Lyon MATEIS - Bât. Saint-Exupéry 7 Avenue Jean CAPELLE 69 621 Villeurbanne CEDEX Tél : 04.72.43.71.70 Fax : 04.72.43.85.28 jean-yves.buffiere@insa-lyon.fr
MEGA	**MÉCANIQUE, ÉNERGÉTIQUE, GÉNIE CIVIL, ACOUSTIQUE** http://edmega.universite-lyon.fr Sec. : Stéphanie CAUVIN Tél : 04.72.43.71.70 Bât. Direction mega@insa-lyon.fr	**M. Jocelyn BONJOUR** INSA de Lyon Laboratoire CETHIL Bâtiment Sadi-Carnot 9, rue de la Physique 69 621 Villeurbanne CEDEX jocelyn.bonjour@insa-lyon.fr
ScSo	**ScSo*** http://ed483.univ-lyon2.fr Sec. : Véronique GUICHARD INSA : J.Y. TOUSSAINT Tél : 04.78.69.72.76 veronique.cervantes@univ-lyon2.fr	**M. Christian MONTES** Université Lyon 2 86 Rue Pasteur 69 365 Lyon CEDEX 07 christian.montes@univ-lyon2.fr

*ScSo : Histoire, Géographie, Aménagement, Urbanisme, Archéologie, Science politique, Sociologie, Anthropologie

Study of the role of two dimensional nanosheets as fillers in Sol-Gel anticorrosion coatings deposited on metal surface

Abstract

Sol-Gel coating has got attention for the replacement of hazardeous Chromate Conversion Coatings for being environmental friendly, having a mild synthesis condition as well as a controllable microstructure of the product. To overcome the shortcomings of the porous nature, fillers have been introduced to enhance the barrier effect of the coating. Two dimensional (2D) nanosheets have been studied as fillers due to their impermeability in atomic layer. To understand the role of 2D nanofillers in the enhancement of barrier effect to Sol-Gel coating, the electrochemical techniques have been performed. The role of 2D materials were probed with the interpretation of Electrochemical Impedance Spectroscopy (EIS) with 2D nanosheets charged Sol-Gel/metal systems with different reactivities to corrosion. The hexagonal Boron Nitride, electrochemically expanded Graphite and Molybdenum Disulfide derived nanosheets were exfoliated in pure solvants as fillers. For possible applications, the coated systems were immersed in NaCl 30g/L solution.

Key Words: Corrosion, Sol-Gel, 2D materials, EIS

L'étude de rôle des matériaux bidimensionnelles chargés dans les revêtements Sol-Gel déposé sur les métaux

Résumé

Les revêtements Sol-Gel ont attiré attentions en tant qu'un candidature pour remplacer le traitement d'Alodine grace à son nature respectueux de l'environnement, condition d'élaboration douce et microstructure controllable. Pour ressoudre les risques potentiels conduit par ses nature poroux, les charges sont souvent appliqués, dont les matériaux bidimensionnelle (2D matériaux) ont été étudié pour ses impermeabilité à l'échelle nanométriquee. A l'objet de comprendre les rôles des 2D matériaux sur le renforcement d'effet barrière des revêtements Sol-Gel, caractérisation electrochimique sont appliqué. Les rôles des 2D matériaux sont analysé par les interpretations de la Spectroscopie d'Impédance d'Electrochimique (SIE) en chargant dans les systemes Sol-Gel/métaux avec des reactivités différents à la corrosion. Les feuilles nanométrique dérivé par nitride de bore hexagonale, graphite expandé par moyen electrochimique et disulfure de Molybdene sont exfolié dans les solvants pures. Pour application future possible, tous les échantillons couvertus sont immersés dans le milieu NaCl 30g/L.

Mots-Clés: Corrosion, Sol-Gel, 2D matériaux, SIE

Acknowledgement

This thesis may never be realized without the help of the people who had supported me from the begining to the very end.

I firstly give my thanks to my parents, to my grandparents and to my dear relatives and friends in China.

I give my sincere thanks to China Scholarship Council to give me financial support. I also give my thanks to to **Professor Bernard Normand** for the support to the thesis scientifically, adminstratively and financially with professionalism, patience and generosity. I also thanks him for being my mentor, guiding and supporting me to be fully trained as a *Ph.*D with all his knowledge, experience, and ressources.

I give my special thanks to **Dr. Sheng Yuan** for the whole time supporting me, as my first mentor, a teacher, a friend who gave me all the introduction, guides and cooperation to the scientific world, especially during the difficult times that we have confronted together.

I give my thanks to **Dr. Kurt Hermange**, for his cooperation and guide in my thesis, and also for being my dearest friend.

I give my thanks to **Dr. Dwaipayan Mallick**, as one best friend of mine. All this memories and experience we've shared in France and throughout the world between us are appreciated and will be carefully protected.

I give my thanks **Dr. Hela bin Mensour**, for her being my dearest friend, for her support, for her understanding and for every moment we've shared.

I give my thanks to **Mrs. Ying Huo**, **Mr. Zhiheng Zhang**, and **Dr. Elizavieta Lapuskana** for being my dearest friend and for all the experience that we have shared in these years.

I give my thanks to **Dr. Quentin Lemarie**, **Mr.Philippe Martinet**, **Mrs. Imen Ferjani** for the friendship as well as the sharings and supportings.

I give my thanks to **Dr. Benoit Ter-Ovanessian**, **Dr. Sabrina Marcelin** for their scientific support , helps and hard works during my thesis.

I give my thanks to **Professor Marion Frégonèse**, **Dr.José Bolivar** for guiding me with patience and consideration.

I give my thanks to all the crews in CorrIS group, especially for **Mrs. Yasmina Salhi**, and for the crews in the Laboratory of MATEIS, for the support and cooperation.

I give my special thanks to **Mr.Long LIANG** for supporting me thoughout the whole time, and sharing so much experience and precious moments that I may never forget in my life.

Thank you

Yu SHI

Contents

General Introduction

The economic cost caused by metal corrosion is equivalent to around 3% of the global GDP every year, which requires the intensive effort of the industry domain for researching, developing, and applying anti-corrosion solutions.[1] For the most widely used metallic structural materials such as steels and aluminum-based alloys, the chromium conversion coatings (CCC) were considered as an efficient solution. However, the toxic nature of Chromium hexavalent Cr (VI) makes CCC hazardous to the environment and the human health.[2] According to the policy of "**R**egistration, **E**valuation and **A**uthorization of **CH**emicals" (REACH) launched by European Union (EU), Cr (VI) containing chemical compounds or components have been strictly restricted in EU territory.[3] The replacement of CCC pushes researchers for the exploration of new materials or different surface treatments. The later one has been investigated to replace CCC according to the applying of materials, surface reactivity, mechanical property, life duration, and of course, the environment to which the final product is exposed.[4,5]

The Sol-Gel process has attracted abundant attention since its first applications from middle of twentieth century.[6] Its mild synthesis conditions, easy to obtain versatile composition, high purity of gel, and the ability of synthesizing thin-films allow it to be an interesting technique for various application environments.[7] The interest of sol-gel coating is two-fold in the industry: 1) as a primer layer to ensure good adhesion property between the top-layer and substrate;[8] 2) as a barrier to prevent the penetration of the corrosive reactants to the underlying metal surface. However, its barrier property depends closely on its density that often requires a high curing temperature. Otherwise, a film derived xerogel is obtained, which is a three-dimensional network of inorganic skeleton surrounded by small compounds and solvent molecules. This structure is mesoporous or micro-porous and enables the connection of the metal to the application environment.[9]

Inorganic-Organic Hybrid (IOH) Sol-Gel coatings combine the properties of organic and inorganic parts allowing to reduce porosity. They can, nevertheless, lead to delamination problems and inferior mechanical properties.[10] The addition of nano-fillers is another solution for the improvement of the barrier effect in Sol-Gel coatings. The fillers have different functionalities as inhibitors[11] or as sacrificial particles like Zn for cathodic protection.[12,13]

The two-dimensional materials (2D materials) posses excellent to small species, such as water, oxygn molecules and ions.[14] This impermeability is of interest for anti-corrosion applications.[15] Being deposited directly on substrates[16] or charged as filler into coatings[17], the hexagonal boron nitride (h-BN), due to its inertness and thermal stability, has been studied for corrosion protection applications.[18,19] Other 2D materials also showed the potential to be applied as anti-corrosion fillers to improve the barrier effect of Sol-Gel in order to allow it to replace the CCC surface treatment.[20,21]

This work has been dedicated to understanding h-BN nanosheet's influence in zirconium-based Sol-Gel coating and to find a promising approach for the anticorrosion protection on various metals.

The nanofillers were exfoliated from raw h-BN by either classic liquid-phase exfoliation. The role of the hexagonal boron nitride nanosheet morphology and concentration in different Sol-Gel matrix, the effect of various 2D materials on enhancing the barrier properties, has been discussed. The anticorrosion property of 2D nanofiller charged coatings have been analyzed using electrochemical methods. This dissertation is divided into five chapters as below:

Chapter I resumes the corrosion mechanism and the Sol-Gel process. The corrosion phenomena and the methodology of corrosion protection are described in detail. For the Sol-Gel, the key parameters on the physico-chemical properties and microstructure of the coatings are summerized. The selection of 2D materials are also explained in this chapter.

Chapter II presents the materials, the sol-gel parameters used for different coating systems, and the 2D materials exfoliation methods. The physico-chemical and structural characterization tools are detailed in the appendix part. The electrochemical analysis, including polarization and electrochemical impedance spectroscopy (EIS), are also described.

Chapter III characterized the three coating systems for different purposes.

In the first part, the h-BN nanosheet filled Zr-based single-component coatings were deposited on the 316L stainless steel surface. The existence of the passive film on stainless steel ensures good coating adhesion after "piranha" solution treatment and reduces the degradation velocity of the metal. Therefore, the deterioration of the coating system was directly correlated to the under-deposit corrosion reaction, which highlights the barrier effect of the nanofillers. In this context, the sol-gel coatings filled with different h-BN nanosheets with different concentrations of nanofillers were prepared.

In the second place, we attempted to transfer the nanocomposite coatings onto a more reactive aluminum alloy. It has been proved that the single-component matrix cannot provide sufficient protection. Moreover, the lack of coating adhesion on aluminum alloy favored the lateral propagation of the oxidation product and the coating delamination. The multi-component sol-gel matrix based on zirconium and silicon oxide was thus used to replace the single-component one to improve the impermeability of coatings.

Until now, we had two ways to optimize the coating's barrier effect with a view to increase its lifetime. The first way consists of the adhesion enhancement, which is generally limited by the coating/ substrate materials coupling and the synthesis conditions. The other way to improve the coating's intrinsic resistance has been selected. For this purpose, the organic-inorganic hybrid coating doped with Octadecyltriethoxysilane (ODTES, -C18 alkyl group) were deposited onto carbon steel.

Chapter IV presents the electrochemical characterizations and the interpretation of the coatings developed in the third chapter. The performance against localized corrosion on 316L and against general corrosion on aluminum and carbon steel are evaluated.

Finally the results of this study and the perspectives for further investigations were given in **General Conclusion and Perspectives**.

[1] Schmitt, G. Global Needs for Knowledge Dissemination, Research, and Development in Materials Deterioration and Corrosion Control. 44.
[2] Durán, A.; Castro, Y.; Conde, A.; de Damborenea, J. J. Sol–Gel Protective Coatings for Metals. In Handbook of Sol-Gel Science and Technology; Klein, L., Aparicio, M., Jitianu, A., Eds.; Springer International Publishing: Cham, 2016; pp 1–65.
[3] Catoire, S. Les substances concernées par l'annexe XIV du règlement 1907/2006. 192.
[4] Twite, R. L.; Bierwagen, G. P. Review of Alternatives to Chromate for Corrosion Protection of Aluminum Aerospace Alloys. Progress in Organic Coatings 1998, 33 (2), 91–100.
[5] Li, Y.; Zhang, Y.; Jungwirth, S.; Seely, N.; Fang, Y.; Shi, X. Corrosion Inhibitors for Metals in Maintenance Equipment: Introduction and Recent Developments. Corrosion Reviews 2014, 32 (5–6).
[6] Dislich, H.; Hinz, P. History and Principles of the Sol-Gel Process, and Some New Multicomponent Oxide Coatings. Journal of Non-Crystalline Solids 1982, 48 (1), 11–16.
[7] Wang, D.; Bierwagen, Gordon. P. Sol–Gel Coatings on Metals for Corrosion Protection. Progress in Organic Coatings 2009, 64 (4), 327–338.
[8] L. Zheludkevich, M.; Miranda Salvado, I.; S. Ferreira, M. G. Sol–Gel Coatings for Corrosion Protection of Metals. Journal of Materials Chemistry 2005, 15 (48), 5099–5111.
[9] Atik, M.; de Lima Neto, P.; Avaca, L. A.; Aegerter, M. A. Sol-Gel Thin Films for Corrosion Protection. Ceramics International 1995, 21 (6), 403–406.
[10] Figueira, R. B.; Silva, C. J. R.; Pereira, E. V. Organic–Inorganic Hybrid Sol–Gel Coatings for Metal Corrosion Protection: A Review of Recent Progress. J Coat Technol Res 2015, 12 (1), 1–35.
[11] Altamirano-Juárez, D. C.; Carrera-Figueiras, C.; Garnica-Romo, M. G.; Mendoza-López, M. L.; Ortuño-López, M. B.; Pérez-Ramos, M. E.; Ramos-Mendoza, A.; Rivera-Rodríguez, C.; Tototzintle-Huitle, H.; Valenzuela-Jáuregi, J. J.; et al. Effects of Metals on the Structure of Heat-Treated Sol-Gel SiO2 Glasses. Journal of Physics and Chemistry of Solids 2001, 62 (11), 1911–1917.
[12] Dennis, R. V.; Patil, V.; Andrews, J. L.; Aldinger, J. P.; Yadav, G. D.; Banerjee, S. Hybrid Nanostructured Coatings for Corrosion Protection of Base Metals: A Sustainability Perspective. Mater. Res. Express 2015, 2 (3), 032001. https://doi.org/10.1088/2053-1591/2/3/032001.
[13] Yu, Q.; Ma, X.; Wang, M.; Yu, C.; Bai, T. Influence of Embedded Particles on Microstructure, Corrosion Resistance and Thermal Conductivity of CuO/SiO2 and NiO/SiO2 Nanocomposite Coatings. Applied Surface Science 2008, 254 (16), 5089–5094.
[14] Hu, S.; Lozada-Hidalgo, M.; Wang, F. C.; Mishchenko, A.; Schedin, F.; Nair, R. R.; Hill, E. W.; Boukhvalov, D. W.; Katsnelson, M. I.; Dryfe, R. a. W.; et al. Proton Transport through One-Atom-Thick Crystals. Nature 2014, 516 (7530), 227–230.
[15] Snapp, P.; Kim, J. M.; Cho, C.; Leem, J.; Haque, M. F.; Nam, S. Interaction of 2D Materials with Liquids: Wettability, Electrochemical Properties, Friction, and Emerging Directions. NPG Asia Materials 2020, 12 (1), 1–16. https://doi.org/10.1038/s41427-020-0203-1.
[16] Andrieux, A.; Dorval, N.; Fossard, F.; Schué, L.; Lavenus, P.; Loiseau, A. CVD Synthesis and Characterization of Hexagonal Boron Nitride Thin Films. 4.
[17] Husain, E.; Narayanan, T. N.; Taha-Tijerina, J. J.; Vinod, S.; Vajtai, R.; Ajayan, P. M. Marine Corrosion Protective Coatings of Hexagonal Boron Nitride Thin Films on Stainless Steel. ACS Appl. Mater. Interfaces 2013, 5 (10), 4129–4135.
[18] Wu, Y.; Yu, J.; Zhao, W.; Wang, C.; Wu, B.; Lu, G. Investigating the Anti-Corrosion Behaviors of the Waterborne Epoxy Composite Coatings with Barrier and Inhibition Roles on Mild Steel. Progress in Organic Coatings 2019, 133, 8–18. .
[19] Qin, Z.; Zeng, Y.; Hua, Q.; Xu, Q.; Shen, X.; Min, Y. Synergistic Effect of Hydroxylated Boron Nitride and Silane on Corrosion Resistance of Aluminum Alloy 5052. Journal of the Taiwan Institute of Chemical Engineers 2019, 100, 285–294.
[20] Zhao, X.; Zhang, B.; Jin, Z.; Chen, C.; Zhu, Q.; Hou, B. Epoxy Coating Modified by 2D MoS2/SDBS: Fabrication, Anticorrosion Behaviour and Inhibition Mechanism. RSC Adv. 2016, 6 (100), 97512–97522.
[21] Pourhashem, S.; Vaezi, M. R.; Rashidi, A.; Bagherzadeh, M. R. Distinctive Roles of Silane Coupling Agents on the Corrosion Inhibition Performance of Graphene Oxide in Epoxy Coatings. Progress in Organic Coatings 2017, 111, 47–56.

Chapter I. Bibliography

I.1 Introduction

In this chapter, the corrosion mechanisms are introduced according to the types of corrosion : general corrosion, localized corrosion. The commonly used anti-corrosion methods are presented, including conversion coatings, corrosion inhibitors, sacrificial coatings, noble metal coatings, and non-metal inert coatings.

The Sol-Gel has been studied as a promising way for coating synthesis due to its mild synthesis conditions and ecofriendly properties. The hydrolysis/condensation reaction and the classification of Sol-Gel coatings are introduced. Inorganic/Organic Hybrid (IOH) Sol-Gel coatings are considered as an important category that has attracted much attention in recent years. It could increase coating thickness and flexibility compared to pure inorganic coatings by mixing organic group functionalized silane to the metal-alkoxide precursors.

The 2D materials have different physical, chemical, and mechanical properties. The selection of the hexagonal Boron nanosheet as fillers in this work is due to their inertness and impermeability.

I.2 Corrosion of metallic materials

Metals are applied in industry as structural materials. According to their different physical and mechanical properties, metallic materials such as steels, aluminum alloys, magnesium alloys, copper and copper alloys, etc., have been widely applied in different industry domains.[1] However, the common problem for metallic materials is their sensibility to oxidation and corrosion. A «NACE» report in 2016 revealed that the global cost of corrosion per year is estimated to be $2.5 trillion US dollars, which is 3.4% of the Global Domestic Production (GDP) in 2013 and could be reduced by 15 – 35% with available controlling process.[2] (**N**ational **A**ssociation of **C**orrosion **E**ngineering (NACE))

No perfect solution exists. In order to prolong the lifetime and manage the material failure, the efficient anticorrosion strategy is eagerly demanded and to be optimized. To this end, the understanding of the mechanism of the corrosion process is mandatory.

I.2.1 Mechanism of metal corrosion

The mechanism of the corrosion is related to the electrochemical phenomenon taking place on the surface of metal.[3] Reactions are driven by the difference of potential of local heterogeneities. The part with a higher potential is called cathode, while the part with a lower potential is called anode. In metals, the electrons are moving freely inside the bulk materials. As shown in Fig. I.2 - 1. The Reduction-oxidation reaction (Redox) is noted below:

Oxidation reaction: $M \rightarrow M^{n+} + ne^-$ ***React. 1***

For the Reduction reaction, according to different aeration and pH condition, the reactions can be shown as below:

Aerated acidic condition: $O_2 + 4H^+ + 4e^- \rightarrow 2H_2O$ ***React. 2***

Deaerated acidic condition: $2H^+ + 2e^- \rightarrow H_2$ ***React. 3***

Aerated neutral or alkaline condition: $O_2 + 2H_2O + 4e^- \rightarrow 4OH^-$ ***React. 4***

Fig. I.2 - 1a illustrates the different steps of the corrosion reaction, in which the oxidation & dissolution of bulk material, reduction, conducted circuit are denoted from 1 to 3. Corrosion protection can be realized by either preventing these three main processes or by increasing the relative potential of the protected electrode with a sacrificial metal, as shown from No.4 in Fig. I.2 - 1b.[4] The corrosion modes are presented in the next part.

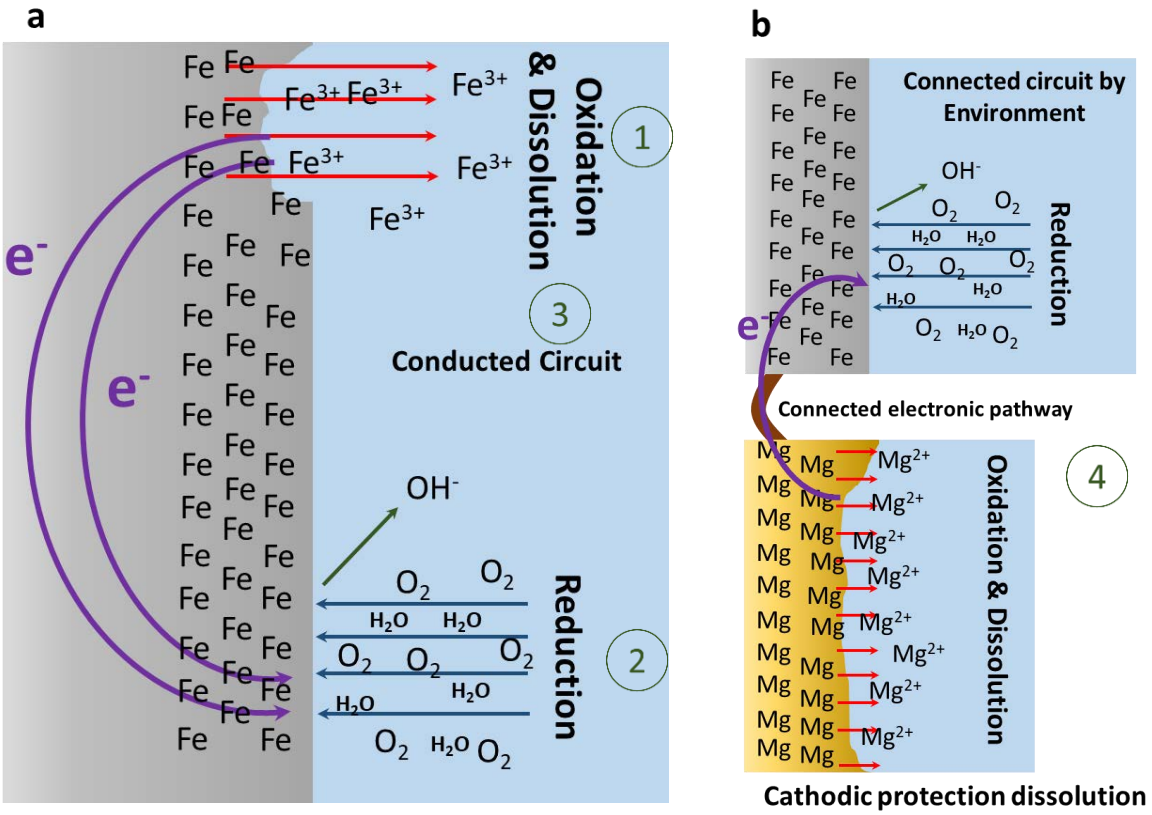

Fig. I.2 - 1 Schemes of a) mechanism of corrosion and b) mechanism of cathodic protection

I.2.2 Corrosion modes

The corrosion modes can be classified into three main categories: the generalized corrosion, the localized corrosion, and the mechanically assisted corrosion.[5]

Generalized corrosion

Uniform corrosion: Uniform corrosion is also called General corrosion. It is the corrosion that happens homogeneously over the whole material surface in contact with the corrosive media.[6] General corrosion causes the mass loss of materials that can be estimated by the corrosion current density according to Faraday's law.[7] Fig. I.2 - 2 shows the mechanism of general corrosion. On the bulk material, the anodes and cathodes are alternatively distributed, which depends on the metallurgical properties of the metals.

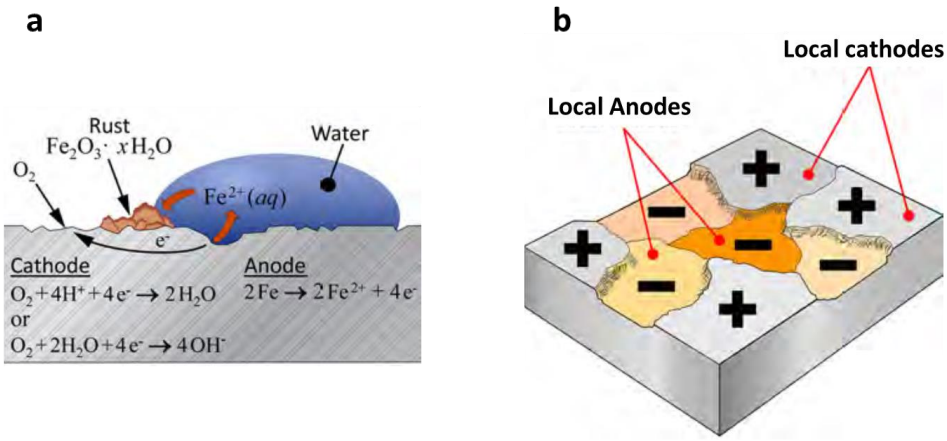

Fig. I.2 - 2 Scheme of mechanism of general corrosion from a) side view b) top view[8]

Passivation: Passivation is a phenomenon that promotes the initiation and growth of a natural dense thin film on the surface of the metal due to the oxidation of the metal atoms. [9] An alloy of non passive metal could also behave passive behavior with the passif film introduced by the passsif alloy element like Cr, etc.[10] Taking stainless steel as an example, by introducing alloy elements which can form passive film such as chromium into iron-based steels, a thin layer of chromium oxide is generated on the metal surface. By electrochemical dynamic polarization curve, the passivation phenomenon of the passive metal typically presents a curve, as shown in Fig. I.2 - 3.

The polarization curve of passive metal could be separated into different regions. [5]

Region I: Cathodic zone, in which the applied potential is lower than the corrosion potential of the working electrode. In Region I, there is no corrosion, reduction phenomenon are privileged.

> ***E_{corr}:*** The corrosion potential separate the Region I and Region II, where current density equals to 0 $mA.cm^{-2}$. At this potential $i_{anode} = - i_{cathode}$.

Region II: Active zone. It is composed of 2 different parts:

Between E_{corr} and E_{crit}: When the potential is inferior to the potential E_{crit}, the overall current density increases to prepare the metal surface for the initiation of the passive film growth.

> ***E_{crit}:*** The critical potential is located at the point where the current density starts to decrease.

In the second part, the current density decreases since the passive film is initiated and grows.

Region III: Passive zone, this region corresponds to the potential field for the maintenance of passive film. The current density corresponds to I_{pass}, which is generated from maintaining the passive film by migration phenomenon.

Region IV: Transpassive zone, where the current increases again and keeps increasing. The applying potential is much higher than the corrosion potential of oxide compounds in the passive film, which promotes the dissolution of material.

Region V: The reigion characterizes the oxidation of water. The oxygen evolution takes place.

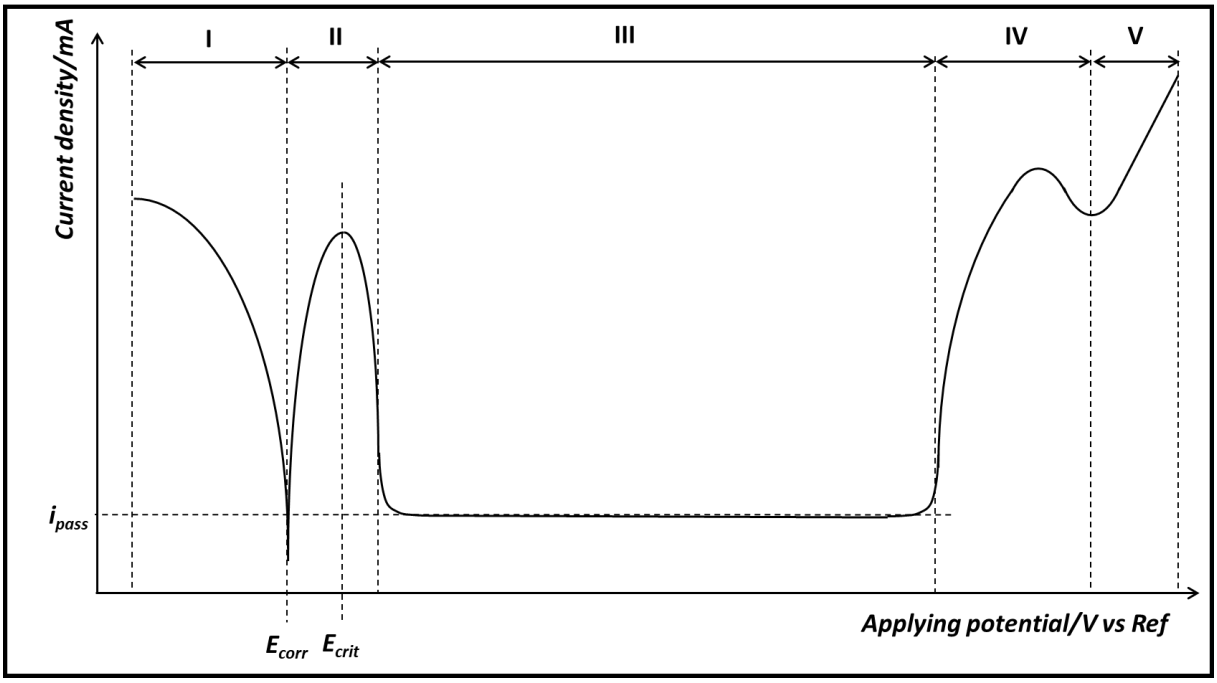

Fig. I.2 - 3 Typical Electrochemical Dynamic Polarization curve of a passive material [11]

Localized Corrosion

Localized corrosion is defined according to the heterogeneity of the reaction. Localized corrosion does not happen on the whole material, but a localized part of the metal surface instead.[12] Once the corrosion is inhomogenous, it is a localized corrosion. Thus, the localized corrosion could be, as for a non-passive metal, an under-coating corrosion, or, as for a passive metal, a pitting corrosion.

Galvanic corrosion: We discuss here specifically the galvanic corrosion on the metal surface, not including cathodic protection.

Different metals have different corrosion potential. When two metallic materials are getting in touched, which is called a galvanic couple, the anode metal will be corroded, while cathode metal will act as the conducting pathway for electrons. [13] Admittedly, the galvanic corrosion activity depends on the corrosion potential difference between the galvanic couple. However, the kinetic features of galvanic corrosion are also influenced by each specific couple and also by the corrosion product. [13] For example, the potential difference between zinc and steel is not the highest. However, the corrosion rate measured from this galvanic couple is much higher than the galvanic couple composed by zinc and other alloys. [14] The standard potential of some metal elements in water solution is shown in Fig. I.2 - 4. Moreover, the corrosion potential of a galvanic couple will be influenced also by the characteristic of the solution.

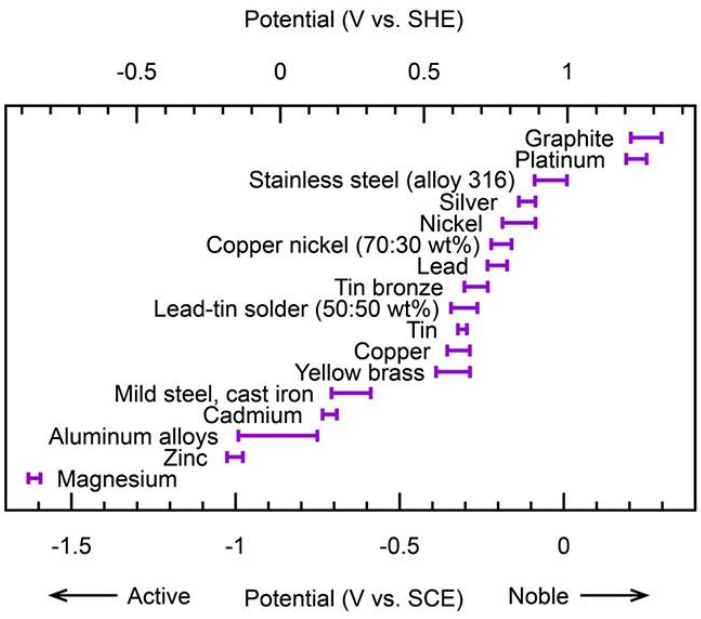

Fig. I.2 - 4 Distribution of potential in aqueous media of frequently used metals or alloys in industry[13]

Pitting corrosion: Pitting corrosion happens on the passive metals. It is a localized corrosion that is initiated in the surface area of the micro-scale.[15] The passive films have different microstructures on different metals or produced by different surface treatments. The passive films isolate the corrosive media from penetrating through the substrate. However, once the passive film exhibits a defect, a break by friction or collision, or with the presence of chloride ions, the exposed metal surface will act as an anode. All passivated part acts as a large cathode.[4] Pitting corrosion is a very localized phenomenon that propagates deeply into the bulk material.

The mechanism of the chloride ions assisted pitting corrosion is briefly presented in Fig. I.2 - 5a. The passive film of stainless steel consists of a thin and dense chromium oxide layer. Therefore, the corrosive species can not directly reach the metal surface. According to the literature, the chloride ions slowly penetrate into the passive film and cause the breakdown of the film, see Fig. I.2 - 5b.[15] The exposed surface will thus initiate the pitting, as shown in Fig. I.2 - 5c.

The pitting corrosion propagates rapidly by an autocatalytic phenomenon.[15]

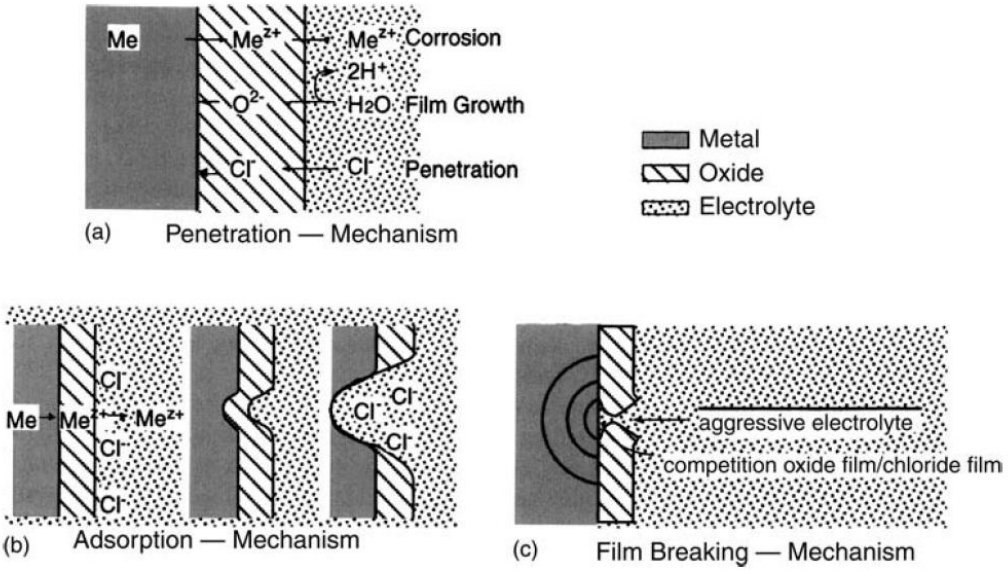

Fig. I.2 - 5 Mechanism of break down of passive film by the presence of Cl^- and introduced pitting corrosion[31]

Crevice corrosion: Crevice corrosion is the corrosion where the corrosive electrolyte are accessible to the substrate in a confined space, which always happen under coating or around junctions. [31] Lacking oxygen at the confined space will provoke an evolution of pH, which could promote corrosion. This mechanism differs from the pitting corrosion in the initiation step while the propagation step of both phenomena are the same.

Selective corrosion: The selective corrosion is also called dealloying or selective leaching. [16] One classical example is the dezincification of brass containing Cu 70%-Zn 30%, from which the oxidation of Zn element is preferred.[17] The selective corrosion causes a decrease in the mechanical property of the alloy.

Nevertheless, dealloying could be used as a method to create nano-porous structure due to the selective elimination of participants in a solid solution material. [16] As shown in Fig. I.2 - 6, by applying dealloying and re-dealloying process, the Zn phase are all removed from the Copper alloy matrix, which leaves a highly porous microstructure.

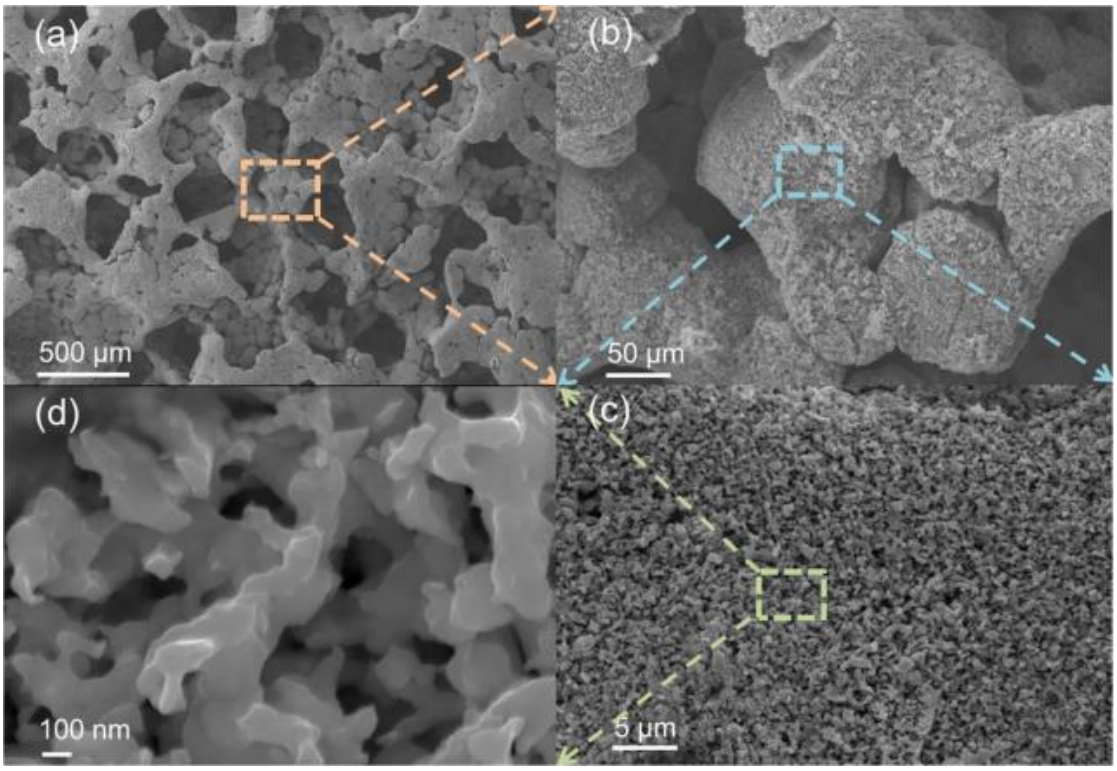

Fig. I.2 - 6 SEM images of porous structure synthesized by dealloying-redealloying method done by Zhu et al with different magnifications a) 40 b) 300 c) 3000 d) 30,000[16]

Intergranular corrosion: The intergranular corrosion happens when the crystallized materials has a difference in corrosion potential between the inner part of the grain and the grain boundary. With stainless steel for example, as shown in Fig. I.2 - 7, the chromium carbide precipitation in the middle of the grain boundary causes a rich Cr region. [18] Meanwhile, this precipitation leaves the chromium depletion region as a region with very low content of Cr, since all the chromium are diffused into the chromium carbide precipitation region. Thus, the grain contains higher content of Cr than the Chromium depletion region, which creates a galvanic couple between the Chromium depletion region and the grain. As anode, Chromium depletion region will firstly be corroded, and the propagation of corrosion will preferentially be in the direction of the grain boundary. [19]

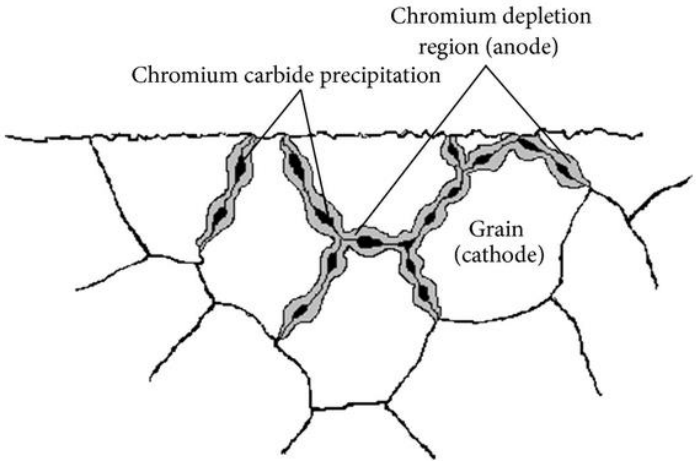

Fig. I.2 - 7 Mechanism of intergranular corrosion[18]

Mechanically Assisted Corrosion

As mentioned above, once the passive film is broken due to a mechanical reason, the localized corrosion will be initiated and propagated. This corrosion is called mechanically assisted corrosion. [14]

Stress corrosion cracking: Stress corrosion cracking (SCC) is caused by the synergy effect of the pitting corrosion or other localized corrosion and the stress distribution at the corroded site. As the scheme of pitting corrosion shown in Fig. I.2 - 8, once there is a pitting or crevice corrosion, the stress field around the opened site may further break the repassivated area and promote the corrosion to propagate. The stress corrosion cracking can behave intergranular corrosion or transgranular corrosion, which is depending on the microstructure of the materials. [20]

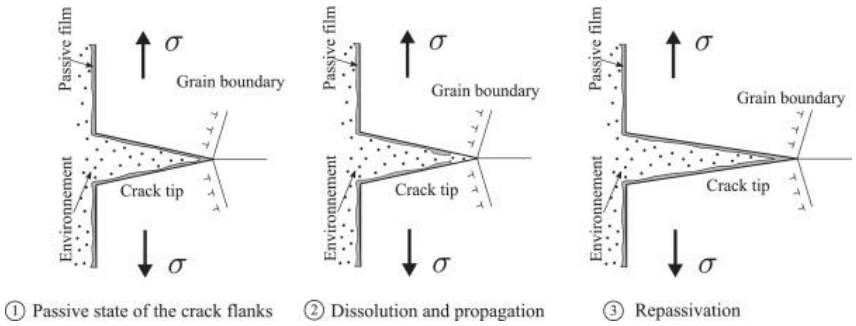

Fig. I.2 - 8 Scheme of mechanism of pitting corrosion[20]

Corrosion fatigue: Corrosion fatigue is the corrosion assisted fatigue phenomenon. All materials have fatigue limits, and the existence of corrosion like SCC or pitting will decrease the fatigue life-time of a material.

Erosion / abrasion / Cavitation corrosion: The direct mechanical erosion caused by flowing liquid, solid particles abrasion, cavitation from air bubbles could be assumed as erosion/abrasion/cavitation corrosion. These procedures include the loss of passive film by dissolution or by mechanical removal and pH changes due to geometrical modification of the solid/liquid interface. It causes the acceleration of corrosion as well as the initiation of new corrosion.[21]

Tribocorrosion: Tribocorrosion is the phenomenon when a wear takes place between the metallic surface and the applying interface. [22] It is a complex phenomenon which includes several corrosion types mentioned above: corrosion fatigue, abrasion, erosion, cavitation etc. The corrosive environment, the possible particles size, nature of coating and metal substrate, the fatigue cycle characteristics as well as the stress distribution all influence the tribocorrosion.[23]

Hydrogen Embrittlement: The embrittlement is caused by the presence of hydrogen, which decreases the toughness or ductility of metal. The presence of hydrogen atoms will react and produce hydrogen and increase the internal pressure of the material. The tendency of a material to allow the penetration of hydrogen or to trap the hydrogen atoms by its inner defect may influence the severity of embrittlement of the material.

I.2.3 Anticorrosion methods

As shown in Fig. I.2 - 1, the anticorrosion mechanism consists of the prevention of one or several reactions 1, 2, 3 as shown in Fig. I.2 - 1a. Otherwise, the connection with an extra anode can also protect the metals which becomes cathode, see Fig. I.2 - 1b. Four main anticorrosion methods are presented here.[3]

Passivation alloying or surface modification

Though carbon steel is of good mechanical properties, it behaves very low anticorrosion property. The introduction of passive film on alloying surfaces is an effective method. The elements like chromium, nickel, and cobalt, are introduced into alloys for this reason.[24,25] Stainless steel was thus developed and can be classified as martensite stainless steel, austenite stainless steel, and duplex stainless steel according to the different alloy compositions and heat treatment.[14] However, the pitting corrosion resistance plays an essential role in the use of stainless steel in chloride ions containing environment. Thus, the protection against Cl^- contamination for stainless is eagerly demanded by the industry.[1]

However, the change of composition for existing material may cause a consequently increase in the cost in the industry domain.[26] Thus, the "local" surface modification is a more cost-worthy method. The most efficient surface modification for stainless steel is chromium conversion coatings (CCC). However, Cr(VI) is hazardous for the environment and human. Its utilization has been forbidden according to the « REACH » rule launched by the European Union.[27] The alternative surface modification methods have been developed, such as the carburizing[28], the nitriding[29], the laser surface treatment[30], the nano-crystal surface modification[31], etc. The improvement of corrosion resistance of the modified materials have been proved in the litterature.

The effect of surface modification varies according to the composition after surface treatment. Taking nitriding as an example, Lavigne et al. reported that the passive film in stainless steel bearing a high nitrogen content shows a better crystallization rate but a lower corrosion resistance comparing to the low content containing sample.[29]

The trivalent chromium conversion coating was firstly proposed by Matzdorf et al. and patented by the US Navy in the year 2000.[32] It has been developed for the adjustment of different pH conditions one year later by Sheasby et al.[33] The Cr(III) compound shows lower toxicity compared with the Cr(VI) species.[34] Rare earth elements, especially Lanthanide elements, shows potential in anticorrosion applications. The cerium-based conversion coatings have been developed on Aluminum alloys[35], 316L[36], etc. These coatings showed a good anticorrosion effect due to its inhibition property of cerium.[37] Transition metal oxyanions based conversion coatings like MnO_4^{2-}, MoO_4^{2-}, V^{5+}/V^{4+} oxides behave similar properties to CCC and have much lower toxicity.[38] For instance, the zirconium-based[39] and Zirconium/Titanium-based conversion coatings have been deposited on aluminum alloys by modifying the adhesion property with the addition of hexafluorometallate complexes (with H_2ZrF_6, H_2TiF_6 for example). These coatings showed improvement of corrosion resistance in 3.5wt% NaCl solution.[11]

Corrosion inhibitors

Corrosion inhibitor is a kind of chemical compound that can directly limit the corrosion reaction by different mechanisms. It stops the metal dissolution by producing a complex compound or a precipitation on the metal surface to inhibit the electrochemical reaction between the corrosive media and the metal surface. The inhibitors can be either directly added into the liquid environment or charged into protective coatings. Many families of inhibitors have been explored and applied for different conditions in terms of pH, saline, and other working conditions. [40]

Inhibitors are mainly classified as:

- the inorganic complexes composed by Mo, Mn, Co, Ni, etc., which shows less toxicity than Cr(VI) based inhibitors;[41,42,43]
- the organic molecules like benzotriazole and its derivatives, amino acid etc.;[44]
- The "green inhibitors" are natural products such as Vernonia Amydalina for steels, as well as the extract of Hisbiscus subdariffa for Aluminum and Zinc etc.[45] Another "green inhibitor" branch is the rare earth elements including cerium and other lanthanide elements due to its low toxicity. [46]

The inhibition mechanisms are different according to the nature of the inhibitor and the substrate. For example, cerium salt precipitates and recovers the substrate connective area. It is one of the most used inorganic inhibitors and has been applied to different substrates like copper, steels, aluminum alloys, etc.[46] The inhibitors based on cerium derivatives were directly introduced into solution with the form of cerium salts (e.g. $CeCl_3$) or charged into cerium rich coatings.[46] The organic inhibitors, on the contrary, will react with the substrate and finally compose a chemical compound to block the corroded area.[3] Benzotriazole was applied on aluminum alloys and copper applications.[3,47] It has been charged into Titania nano-containers for the protection of Al7075 in 3.5wt% NaCl solution.[19] However, both inorganic and organic inhibitors showed toxicities to the human body.[48,49]

Cathodic protection or sacrificial coating

As shown in Fig. I.2 - 1b, if the protected metal is connected to another metal with a lower potential, it will be protected by cathodic protection.[50] The cathodic protection is considered as an efficient and secure way to protect pipelines or other underground components and has already been widely applied in industry.

By different deposition technologies such as spray coating [51], hot painting [52], and electrodeposition[53], the anode metal could be deposited on the metal surface or charged into other coatings. Zn, Sn/Mn, Zn/Ni coatings can be deposited on steels and showed satisfied anticorrosion properties.[53,54] Fig. I.2 - 9 illustrates the scheme of how the Zinc-rich primers works and the self-healing mechanism of the zinc-rich primer coatings. Zinc particles are released to the damaged zone on the metal surface. As zinc is priorly corroded, the corrosion product will mask the connective zone.[55]

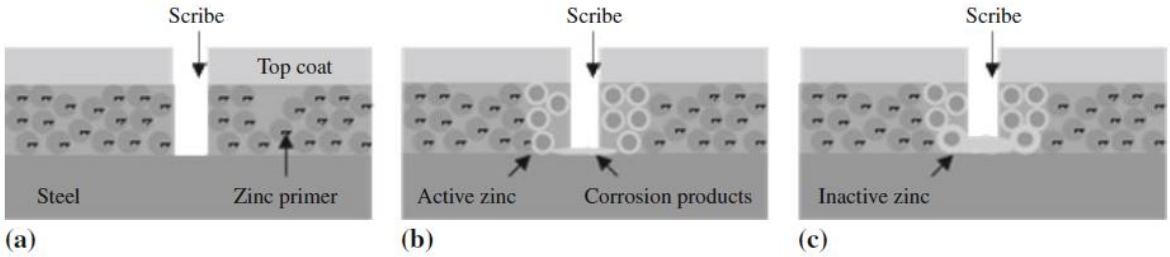

Fig. I.2 - 9 Mechanism of Zn particles charged sacrificial coating[55]

Noble metal coating or non-metallic barrier coating

Different from other methods, the barrier coatings simply use the barrier effect to totally reduce the contact between the metal surface and corrosive media. This method works on the whole 1st, 2nd and 3rd parts of the corrosion. Barrier coatings do not have any interaction with the electrolyte. Nevertheless, if the corrosive media penetrates through the porosity or defects to the protected metal, the later behaves as anode and be corroded even more rapidly.

Non-metallic barrier coatings have different categories. The Zn-silicate coating allows over critical concentration pigment volume. Zn-silicate and Zn-epoxy are applied as primers, but the cracks may occur if the thickness is too high.[55]

Organic coatings are applied as top layers for many applications. Epoxy/resin[56], thermoplastic polymer[57], thermoset polymer[58], conducting polymers[59] were developed for corrosion protection. However, the main shortcoming for organic coatings is related to the low adhesion and delamination during service.[60] Taking Epoxy coating as an example, different fillers such as silica particles[61], nanotubes[62], etc., were introduced to improve its mechanical and barrier properties.

Sol-Gel is a suitable way to elaborate inorganic and organic-inorganic hybrid coating. It is of the mild synthesis conditions (low temperature), the easy to control composition and the microstructure. [63] The low toxicity makes it one of the promising candidates for the replacement of CCC.[3]

The inorganic silicon-based Sol-Gel coatings have already been applied as a several first layers on the substrate to introduce suitable adhesion property for primer coatings onside.[63] Nevertheless, the porous nature of Sol-Gel coating allows the penetration of the corrosive media and limits the applications. [3]

Hybrid coatings with different organic ratios have drawn attention, which allows overpassing the shortcoming of both inorganic and organic coatings.[64]

In order to overcome the porous nature of Sol-Gel and take advantage of its non-toxic nature, the 2D nano-fillers will be charged into the Sol-Gel coatings in this work. Further exploration with hybrid coatings are done to deeply discover the role of 2D fillers inside the hybrid and inorganic coatings. Thus, from next part, the Sol-Gel process and both the inorganic and hybrid coatings will be detailed.

I.3 Sol-gel process

Sol-Gel is a chemical process that allows the production of solid materials from precursors through a sequence of hydrolysis reactions and condensation reactions.[65] Sol-Gel process has mild synthesis conditions, such as low temperature, low toxicity allowing the various applications, as shown in Fig. I.3 - 1.[3] By using silicon-based precursors and/or transition metal (Zr, Ti, Al, Ce...) alkoxide based precursors, glasses and solid ceramic materials can be obtained after a curing treatment. [66] Moreover, the addition of different chelating additives like chelating agent, acidic or basic catalyst, amino-containing functional group and so on, is a common method to modify the microstructure and the properties of the final product.[67]

Sol-gel technique has been applied for monoliths synthesis thanks to its high mass transfer efficiency. [68] Sol-gel can potentially replace the solid-phase microextraction for fibers fabrication.[69] Sol-gel can also be used for fuel cell membrane elaboration with well-controlled porosity. [70] The derived solid spheres, with different shapes such as hollowed spheres, mesoporous spheres, hierarchically multiporous spheres and hierarchically porous spheres, have been applied in the biological domain for the drug delivery and the catalysts introducing to a target system.[71]

Sol-gel derived coatings have been proved efficient against wear, oxidation, and corrosion on the metal surfaces thanks to the high hardness, the chemical stability, the suitable adhesion property, the thermal toughness, and its low thermal conductivity. [72]

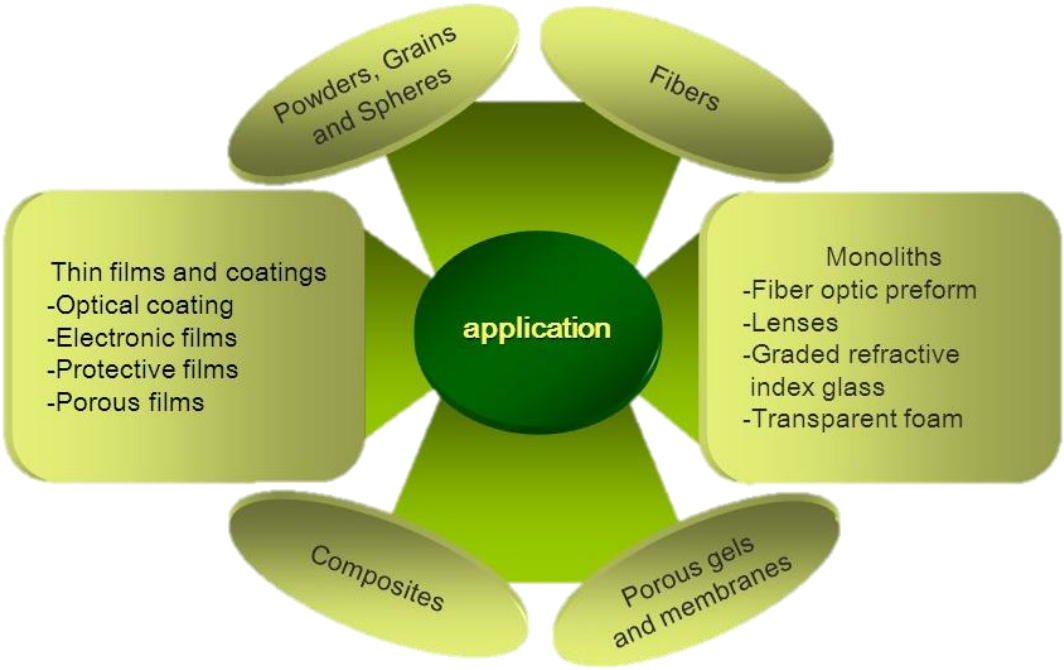

Fig. I.3 - 1 The applications of Sol-Gel process [73]

The Sol-Gel anticorrosion coating is a promising solution for the tremendous demands in replacing hazardous Cr(VI) containing coatings since the beginning of the new century.[74] Wang et al. have reviewed the recent researches on Sol-Gel coatings for the anticorrosion application. [66] Among all the choices, the Si-based precursors have been the mostly explored

for the last decades. The principal shortcoming of these coatings is their limited barrier effect due to the avoidable defects and pores in the matrix.[3] The electrolyte and the corrosive species penetrate through these weak parts of the coating. In order to overcome this issue, the fillers like ZrO_2, Al_2O_3, TiO_2 were incorporated in sol-gel coating that showed improved corrosion resistance on 316L, carbon steels, aluminum alloys substrates.[75,76,77,78]

Besides, instead of pure inorganic or organic matrix, the use of organic inorganic hybrid (OIH) material allows the combination of the properties from different precursors and prevents defect formation.[79,80] As reviewed by Figueira et al., researchers have proposed the methods for the improvement of anticorrosion properties for aluminum alloys, copper alloys and magnesium alloys. [81]

The principle reaction and the reaction parameters will be discussed in the next section.

I.3.1 Sol-Gel reactions

This study will be limited to the alkoxide method in which the "Sol" represents the colloidal solution containing the undissolved particles of nanometric size (1- 100 nm). Along the evolution, the so-obtained "Gel" is a three-dimensional (3D) diphasic system that has a solid network mixed with a liquid phase and small molecules.[82]

Sol-Gel process consists of two main reaction steps, one is the hydrolysis reaction, and the other one is the condensation reaction. Their reaction are shown as below:[83]

The hydrolysis reactions:

$M(OR)_4 + H_2O \rightarrow M(OR)_3OH + ROH$ ***React.5***

$M(OR)_3OH + H_2O \rightarrow M(OR)_2(OH)_2 + ROH$ ***React.6***

$M(OR)_2(OH)_2 + H_2O \rightarrow MOR(OH)_3 + ROH$ ***React.7***

$MOR(OH)_3 + H_2O \rightarrow M(OH)_4 + ROH$ ***React.8***

The condensation reactions:

$(OR)_3MOR + HOM(OR)_3 \rightarrow (OR)_3M\text{-}O\text{-}M(OR)_3 + HOR$ ***React.9***

$(OR)_3MOH + HOM(OR)_3 \rightarrow (OR)_3M\text{-}O\text{-}M(OR)_3 + H_2O$ ***React.10***

where M represents the center atoms like Si or a transition metal atom, R represents the alcoholic organic group. The scheme of the Sol-Gel process can be shown as Fig. I.3 - 2. The hydrolysis reaction consists of the replacement of the alcohol group in a precursor molecule by a hydroxide group.

On the other hand, the condensation has two different kinds of reaction: 1) alcoholic and 2) non-alcoholic, as shown above. The condensation process connects two precursor molecules to each other and forms a 3D skeleton.

The hydrolysis and condensation are two competing processes that should be carefully controlled to obtain expected microstructure and properties. Indeed, the hydrolysis and

condensation reaction velocity can be manipulated by different parameters.[83]

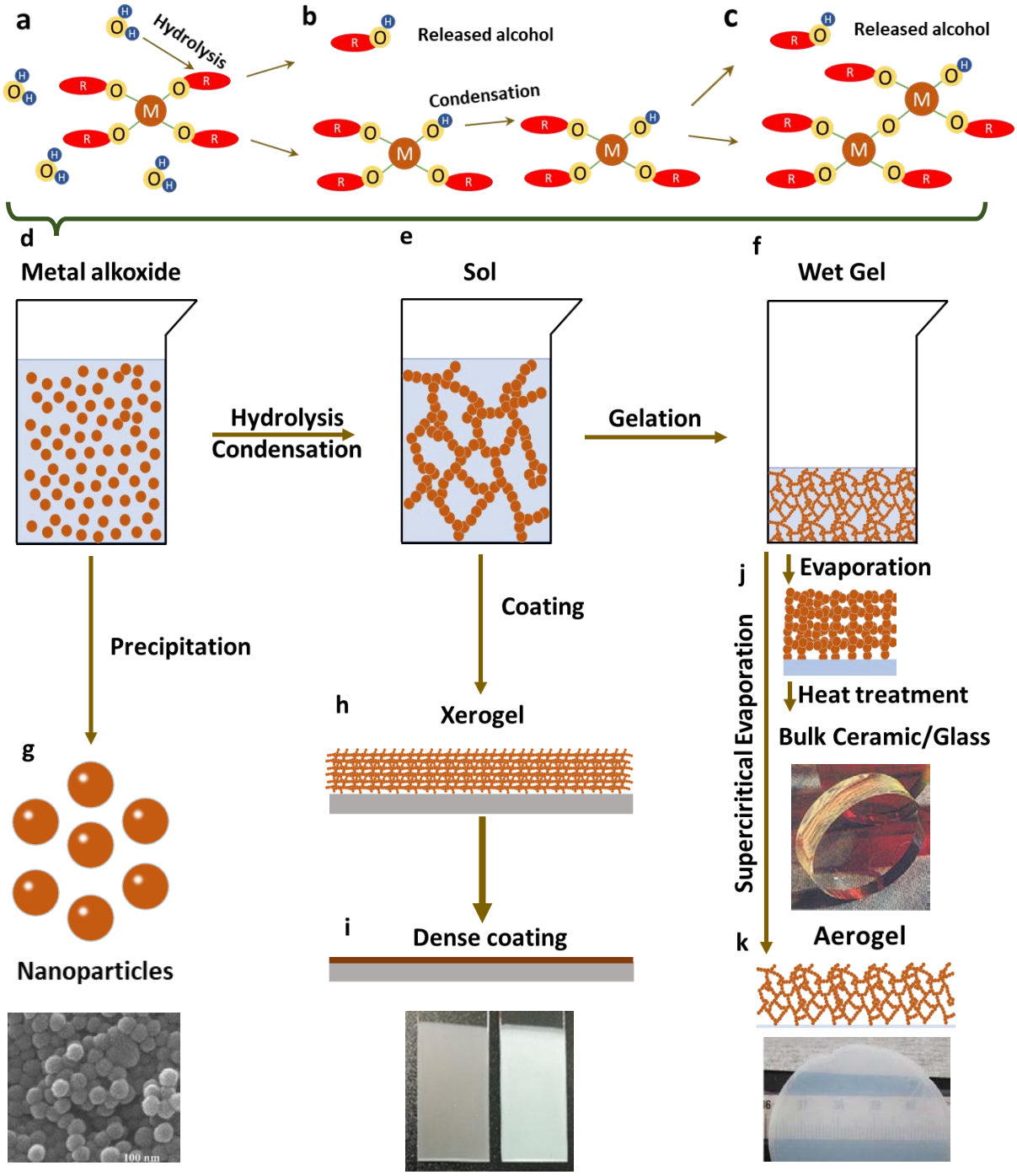

Fig. I.3 - 2 Scheme of a) – c) Sol-Gel reaction as well as d) – k) solidification procedure for applications

Fig. I.3 - 2d to k shows the scheme of solidification and shaping process of Sol-Gel technique. The metal alkoxide solution can be directly used to form nanoparticles on SiO_2, TiO_2, ZrO_2, etc.[84] The Sol-Gel coating can be directly synthesized by nanoparticles by spraying or brushing.[85] The Sol can be deposited on metal surface by dip-coating, spin-coating, electrodeposition and other methods to forge Xerogel film.[86] A heat treatment of the xerogel film is classically required to remove the residual liquid phase (the solvent) accompanied with a densification and a significant amount of shrinkage.[68] Finally, a relatively dense solid coating

is obtained. Moreover, by supercritical evaporation like CO_2 assisted evaporation, the aerogel can be prepared.[87]

I.3.2 The main parameters of Sol-Gel process

The main parameters to control Sol-Gel process are the precursor nature, the solvent, the pH of Sol, the addition of chelating agent, the aging time and aging temperature, the evaporation, the cure temperature, and the deposition method, etc. The well control of these parameters allows to tune the composition, microstructure as well as the associated physico-chemical properties of the Sol-Gel product.

The Precursor

Sol-Gel precursors are mostly Si or transition metal-based alkoxide. Treated at high temperature (> 400°C), pure inorganic material can be obtained. On the contrary, the precursors can be chemically modified with organic groups, for which the curing temperature is usually limited (< 200°C).[72] Otherwise, the organic compound will decompose. This part will mainly discuss the properties of the inorganic precursor, while the role of organic containing precursors will be discussed in the latter part.

The precursors play a primordial role in the microstructure and the final properties of the Sol-Gel coatings. The order of reactivity of different precursors is given by:

$Si(OR)_4 <<< Sn(OR)_4 < Ti(OR)_4 < Zr(OR)_4 < Ce(OR)_4$, according to the center atom.[72]

The reactivity of the precursor based on the same transition metal is also influenced by the organic groups. For example, zirconium acetate hydroxyl(ZAH), zirconium propoxide (ZPO), zirconium n-butoxide(ZBO), zirconium tetra-butoxide (ZTB), the molecules are presented in Fig. I.3 – 3. The coordination number of ZAH, ZPO, ZBO and ZTB molecules is 4, meaning four available sites for another molecule to connect. The interaction is generally ensured by forming a Zr-O-Zr covalent bonding. The presence of acetate groups reduces the reactivity of these sites, which makes the ZAH stabler than the other three precursors. Comparing ZPO and ZBO, the length of Zr-O bonding (varying in Å level) decides the reactivity of hydrolysis and condensation of each precursor. As a consequence, ZPO is more active than ZBO. [88] Thus, there is a difference in the reactivity between different Zr based precursors : ZAH <<< ZPO < ZBO. This difference can be observed on other precursor pairs, ZTB and ZBO for example.

As reviewed, the silica coatings have been reported to be efficient in the protection of metals against oxidation and corrosion in acidic conditions.[66] Vasconcelos has reported SiO_2 sol-gel coating deposited on 304L stainless steel showing enhanced corrosion resistance in 1 N H_2SO_4 solution and 3.5% NaCl solution.[89] Thim et al. reported the silica thin film showing better corrosion protection over aluminum alloy in 0.5 mol/L NaCl solution.[90] However, the low thermal expansion coefficient causes delamination limiting the application of Si-based precursors for corrosion resistance of metallic components.[91]

The aluminum-based coating has low conductivity, excellent wear resistance. The similar nature to passive film on aluminum alloys make it largely applicated and been studied for improvement of corrosion resistance.[59] The titanium-based precursors are chemically stable

and UV-sensitive. They generally have low conductivity and high thermal resistance. [59] The biological compatibility makes titanium-based material interesting in medical implants for biomedical components. [92] The cerium precursors, which show similar physical and mechanical properties to Ti-based precursors without UV sensibility and with an inhibiting nature to corrosion, are used as inhibitor as well as inert anticorrosion coatings.[81]

The zirconium-based precursors derived zirconia coating shows excellent chemical stability and biological compatibility.[2] Furthermore, the comparable thermal expansion of zirconia can largely reduce the number of defects during heat treatment. Thanks to these advantages, the zirconia coating has been used on steels under high application temperature by plural researchers.[72,93]

Compared with using single-component precursors, the multi-component precursor derived Sol-Gel inorganic coatings allow to combine the properties of each component.[3] Li et al. reported the improvement of durability for solar cells with the deposition of TiO_2-SiO_2 coating and ZrO_2-SiO_2 coating comparing to pure SiO_2 surface.[94] As reported by Mumjitha et al., the TiO_2-SiO_2 coatings showed superior wear resistance, corrosion resistance and cell adhesion with less cytotoxicity than the pure TiO_2 coating.[95] Other researchers have shown that multi-component coatings Al_2O_3-SiO_2, TiO_2-SiO_2, ZrO_2-TiO_2 coatings have improved anticorrosion properties on stainless steels in NaCl solution thanks to the less crack tendency.[63,96,97]

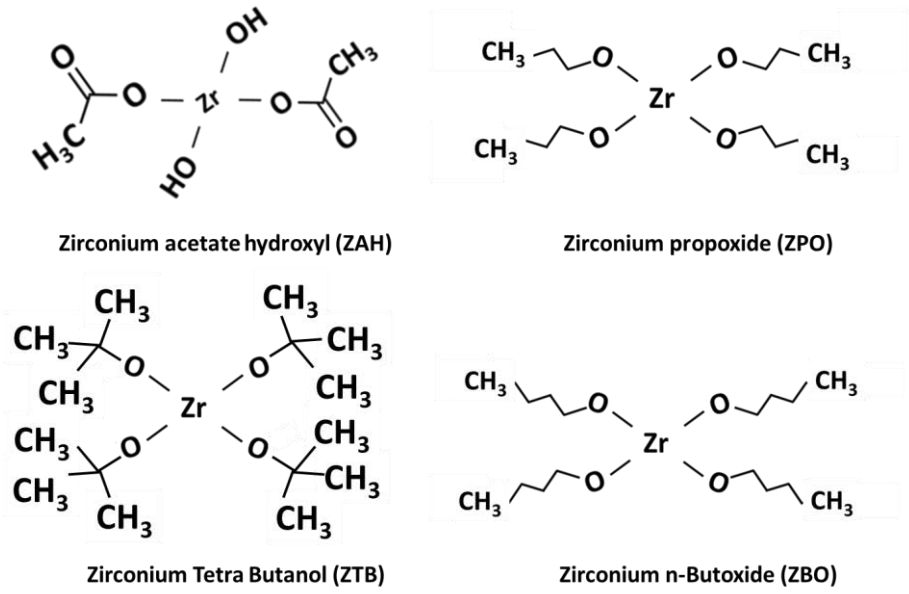

Fig. I.3 - 3 Four different Zirconium based precursors

The solvent

The polarity, caused by the distribution of dipolar moment in a molecule, predominate the intermolecular interactions.[98] The molecules with similar polarity will attract each other while the dissimilar polarity does repulse. The solvents are of different polarities, such as water and ethanol are more polar than solvent like isopropanol, n-butanol etc. [99] The difference in polarity is reported to be able to change the hydrolysis reaction of Sol-Gel colloidal particle

size.[100] Moreover, the water molecule participates in the hydrolysis reaction, which will also influence the final structure of the Sol-Gel coating.

The pH

The pH can catalyze the hydrolysis reaction, which makes the pH-control essential for the preparation of stable Sol. In acidic conditions, the cations are attracted by oxygen atoms that accelerate the hydrolysis reaction releasing -OR groups. In basic conditions, the hydroxide OH^- is attracted by the metal atom inside the metal alkoxide molecule favoring the formation of M-O-M bonds, which makes the condensation reaction privileged.[83] Fig. I.3 - 4a shows the velocity of hydrolysis and condensation reaction in Sol as the functions of the pH value. It is clearly shown that both hydrolysis and condensation reaction has the lowest rate when the pH is close to 7, that is why catalyst (acidic or basic) are frequently used to accelerate the reaction.

As hydrolysis and condensation are influenced by pH, the macromolecules will show different structures. In acidic conditions, the long chains, often called ''spaghetti'' shape, are formed, resulting in a dense structure and more critical internal stress in the solid phase, as shown in Fig. I.3 - 4b. On the contrary, a basic condition leads to the formation of spherical colloid. The so-prepared solid phase is ''piled particles'' that have more pores but less internal stress. The relationship between the colloid size and the pH can be roughly illustrated as Fig. I.3 - 4c.

Of note, the pH of the Sol is also limited by the sensitivity of the metal substrate. The deposition of the coating on metal that is sensitive to an acidic or alkaline environment will cause a weak coating/substrate interface.

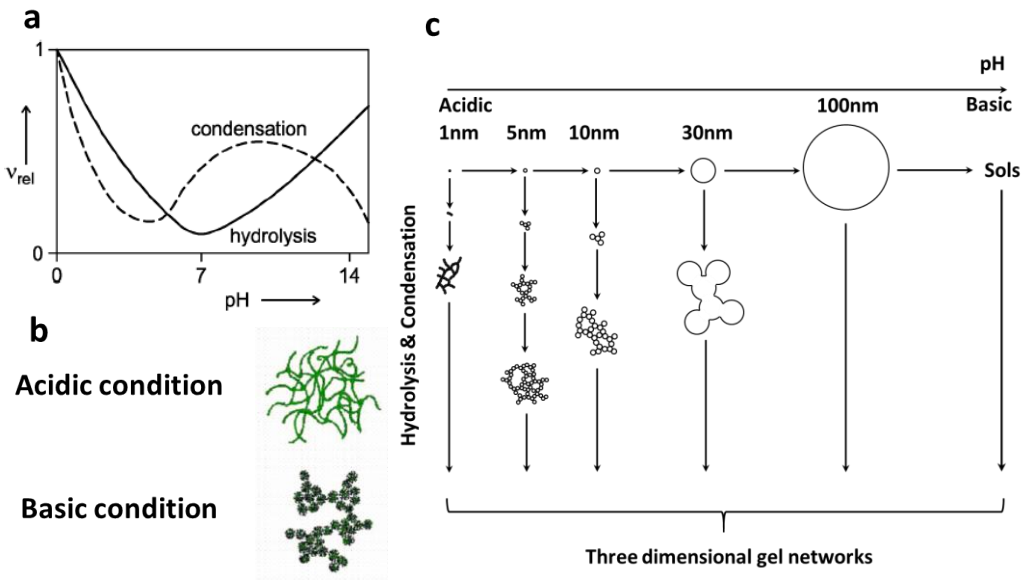

Fig. I.3 - 4 Influence of pH to the microstructure a) the figure of the reaction speed of hydrolysis and condensation influenced by pH b) particles size influence by pH c) the shape of the final product influenced by pH (reform from the work of Pandey et el.) [83,101 102]

The chelating agent

The chelating agents react with the alcoholic site on the precursor molecule and form a chelation complex. As shown in Fig. I.3 - 5, the chelating agent will block the active site of

metal alkoxide precursor. [103] Pappet et al. reported, by studying zirconium alkoxide based Sol-Gel, with appropriate content of chelating added into the solvent, the gelating reaction could be stabilized comparing to the instant gelation with low content of chelating agent.

Too much chelating agents may slow down the hydrolysis and condensation, the formation of colloidal structure could take years, which is also not desired. [104] The concentration of chelating agent influence the reaction rate of hydrolysis and condensation, ended up in a microstructure modified according to the different content of chelating agent.[104] Various molecules can be used as chelating agents such as carboxyl acid, β-diketone, amines, β-ketoester, etc.[105]

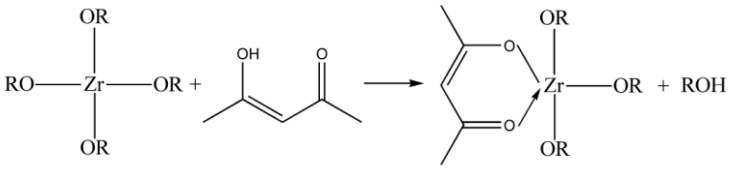

Fig. I.3 - 5 Mechanism of chelating agent blocking precursor active sites for Zr-based precursor and diketone[103]

The aging time and aging temperature

The aging of the Sol-Gel will influence the colloid size as well as the final product microstructure. The aged Sol is able to lead to a more porous structure. Liu et al. have proved that the formation of hydroxyapatite sol-gel coating is highly dependent on the aging time to have sufficient apatite structure.[106] Chou et al. have reported that the aged Sol deposited coating will behave a decreased corrosion resistance comparing to the original Sol deposited coating.[107] Ginter et al. have reported that the aging time will have a crucial influence on microstructure of synthesized zeolite Y particles by SiO_2 and Al_2O_3 Sols. [108] The aging temperature as well as pH condition are also reported to be influencial for the microstructure final product from the same report. Bosc et al. reported that a small change of aging temperature will lead to a great drop of stability for titania Sol.[109]

The evaporation and curing temperature

During the drying in room temperature or curing in oven, the evaporation of the solvent molecule produces pores inside of the coating.[83] The slow evaporation reduces the chance of cracking and big pores, while internal stress is also lower. [110]

The curing time and temperature will both play an important role in the final microstructure of the coating.[111] High temperature post-treatment could be applied in the case that the crystallization of the coating matrix are desired. [112]

Deposition methods

Different deposition methods could be applied to prepare sol-gel coatings such as dip-coating[113], spin-coating[114] and electrophoretic deposition, spray coating, cathodic plasma deposition, Electrodeposition, and etc.[115,116] It has been reported in detail that the most widely applied deposition method are: dip coating and spin coating, respectively.[117,118] The

electrodeposition was lately reviewed to be able to synthesize thick and defect-free coatings.[72]

This work will mainly explain the principle of the dip-coating process. As the figure of dip coating shown in Fig. I.3 - 6, the Sol will wet the dipping coupon surface driven by the microscale capillary force during the withdrawing step. The thickness of the coating will follow Landau-Levich law: [119]

$$h = 2.29\frac{(v_0\eta)^{2/3}}{\sigma^{1/2}\sqrt{\rho g}} \qquad \textit{Eq. I - 1}$$

where h is the thickness of the coating, η is the viscosity of the Sol, v_o is the dragging speed, σ is the surface tension of the Sol, ρ is the density of the Sol, and g is the gravity factor. Thin coating can be obtained after the drying step with the evaporation of the solvent. Since the coating shrinks during the solvent evaporation and the heat treatment, tensile stress may be induced between the substrate and the coating.

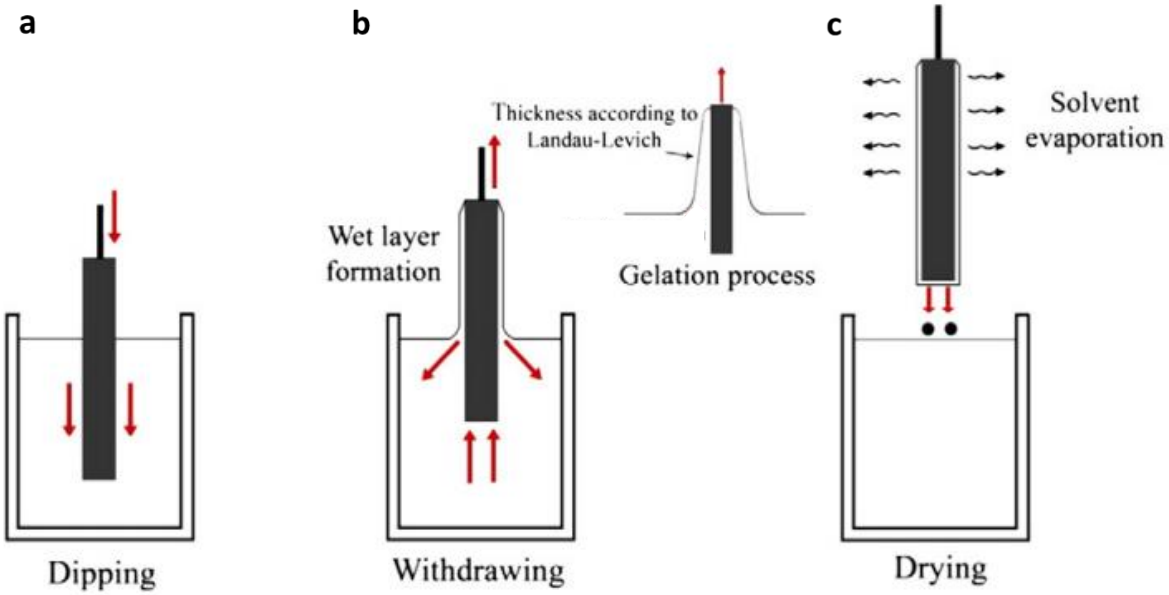

Fig. I.3 - 6 The scheme of a) dip coating b) spin coating and c) electrochemical deposition

I.4 Inorganic/Organic Hybrid Sol-Gel coatings

I.4.1 Definition of hybrid coatings

The barrier effect of inorganic and organic coatings can be shown in Fig. I.4 - 1. As shown from Fig. I.4 - 1a and b, the inorganic coatings have mesopores and macro-porous formed during the evaporation process, as mentioned above. These pores allow the penetration of electrolyte if the coatings are in amorphous phase. A heat treatment is often required to densify the sol-gel film but making the coating prone to cracks at the same time.[66]

As shown from Fig. I.4 - 1d and e, For organic coatings, the barrier effect reduces over time because of the electrolyte penetration in the coating. Once the electrolyte reaches the metal surface, under-paint corrosion takes place that prompts the delamination of the coating.[120] The hybrid coatings, as shown in Fig. I.4 - 1c, allows it to combine the properties of the inorganic and organic parts. In a general way, the addition of inorganic components can improve the coating's mechanical properties while the organic component brings better flexibility.[73.] However, the decomposition of organic compound limits the temperature of heat treatment for hybrid coating. [3]

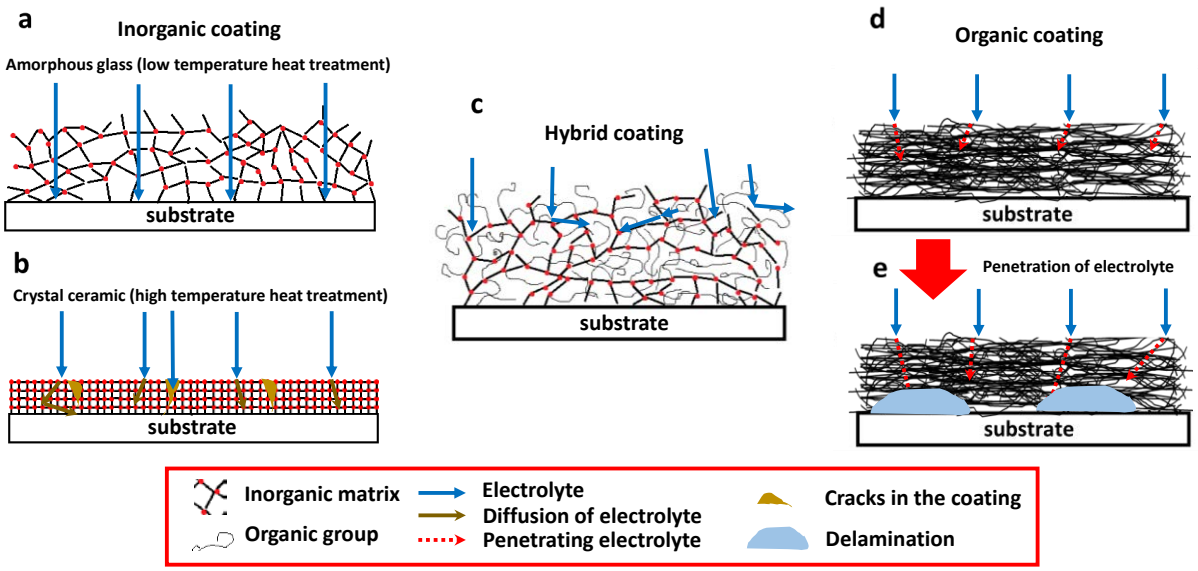

Fig. I.4 - 1 Scheme of the barrier effect of a) and b) inorganic coating, c) hybrid coating and d) and e) organic coating

Generally, hybrid materials can be categorized into two classes. [81] For class I, in the hybrid materials, the organic group and the inorganic groups are connected with weak force (Van der Waals, Hydrogen force), while non chemical bonding forms between each other. In Class II, on the contrary, the chemical bondings are established. Fig. I.4 - 2 shows an example of how the inorganic and the organic part can be connected with the help of organic functionalized silane precursor GPTMS.

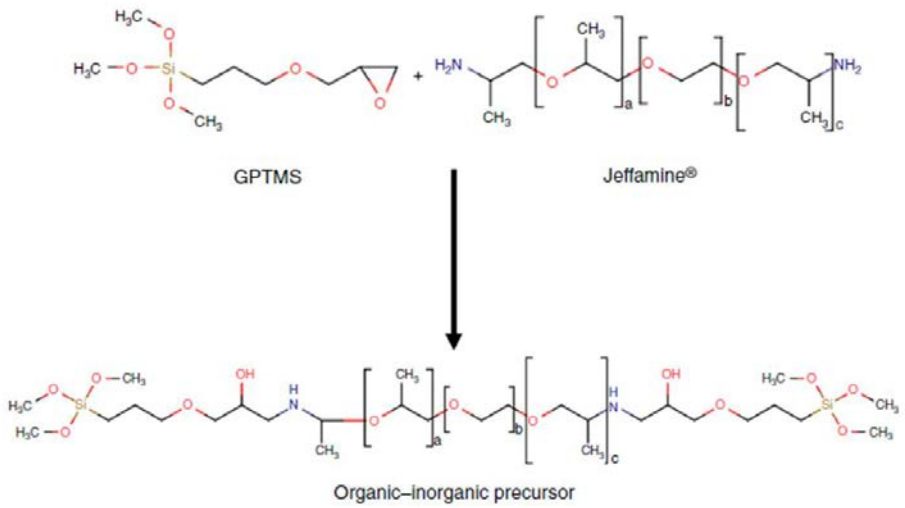

Fig. I.4 - 2 Incorporation of Inorganic and organic compound by the use of GPTMS[81]

The hybrid coating's properties depend on the organic/inorganic ratio. As shown in Fig. I.4 - 3, the left end of the composition axis corresponds to the pure inorganic materials such as glasses or ceramics, while the right end of the axis corresponds to the pure organic materials such as the thermal plastic or epoxy. Different examples of hybrid coatings are noted in the axis of the organic compound percentage in the coating. Indicating the hybrid coatings with more organic participation like Silicone containing epoxy[121] and Polydimethylsiloxane[122]; more inorganic participation such as MTMS or PTMS derived coatings;[81] and coatings with both participation of inorganic and organic parts like SiO-PVP coating[123] as well as Epoxy coating modified with GPTMS.[124]

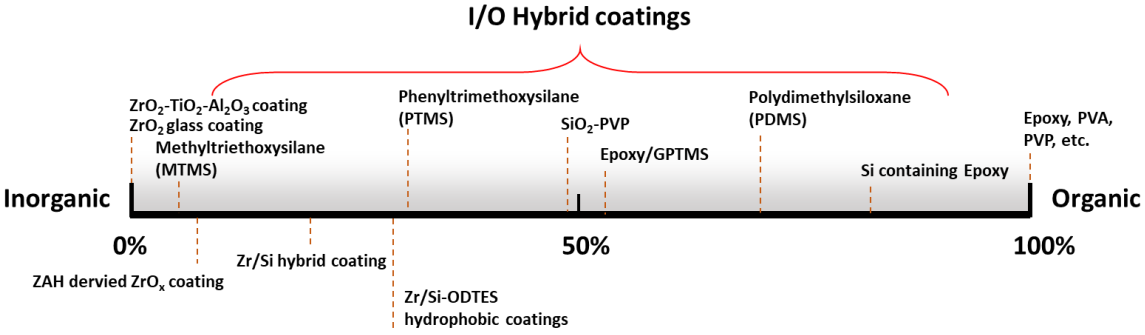

Fig. I.4 - 3 Classification of hybrid coatings with the x-axes showing the ratio of organic compound in the coatings

I.4.2 Organic functionalized silane precursors

The sol-gel coatings are mostly synthesized with organic silane (> 90%). Unlike other precursors, the organic silanes are the silicon precursors with one or plural organic functional groups (alkyl chains…). [81]

The organic silane can be represented commonly as:

$(RO)_x$-Si-R_y' (x+y=4)

where the R' represents a functional group, x represents the number of alcohol groups connected to the central Si atom, y represents the number of organic groups. It has x+y equaling to the coordinate number the central metal atom (x + y = 4 in the case of Si). For example, Phemytrimethoxysilane (PTMS) is derived from Tetraethoxysilane (TEOS) with one Benzene cycle. The Octadecyltriethoxysilane (OTDES) has an alkyl chain (C_{18}). Fig. I.4 - 4 lists the frequently used Si-based precursors.

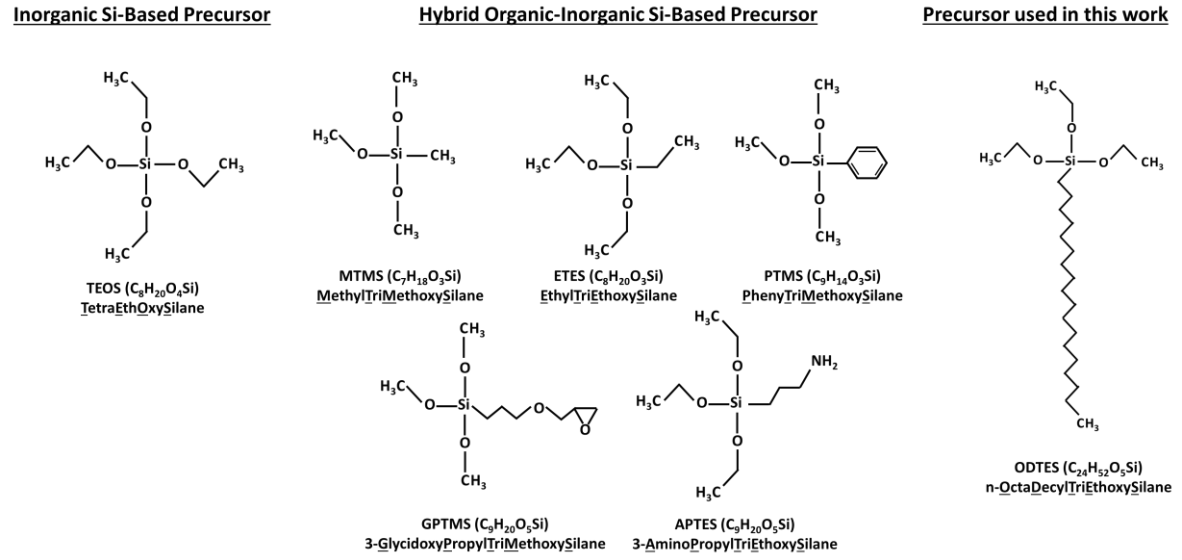

Fig. I.4 - 4 Names and structures of the most frequently used inorganic Si-based precursors; Frequently used hybrid organic-inorganic Si based precursors and the Si-based precursor used in this work

I.5 Sol-Gel coatings for corrosion protection

As discussed in the corrosion part, the Sol-Gel coatings provide mainly the barrier effect to prevent the contact of corrosive species with the underlying metal surface. Several mechanisms can be used to promote the barrier effect:

-Blocking of penetration of electrolyte. [125]

-Prolonging the penetration path of corrosive media. [126]

-Inhibition effect with penetrating corrosive media by fillers inside the coating. [59]

I.5.1 Physical properties influencing Sol-Gel coatings for corrosion protection

Morphology - Thickness

The barrier layer plays a vital role in blocking electrolytes from getting in touch with the substrate Once the coating is saturated by the electrolyte, the coating can prolong the penetration path of corrosive media and reduce the exposed domain on the metal surface to the corrosive media. For crack-free coating, the thicker the coating is, the better barrier effect the coating behaves.

Other than the Landau-Levich showed in ***Eq. I - 1***, the coating thickness can also be influenced by thermal treatment since the coating shrinks during the solvent evaporation. During the

heat treatment, the stress is induced by the different thermal expansion ratio between the metal and the coating, limiting thickness acquired by heat treatment.

Sol-Gel inorganic coating or hybrid coating with a high inorganic ratio is difficult to achieve a high thickness due to the inner stress. Wang et al. have reviewed and reported that a crack-free inorganic Sol-Gel coating is limited to 2 µm, for which 200 nm to 1 µm thickness is frequently observed.[66] In order to increase the coating's thickness, the addition of organic groups is considered as one of the most efficient ways to modify the flexibility of the coating. By introducing organic groups in precursor as GPTMS or PTMS, the coating thickness can reach 10 µm as reviewed by Wang et al.[66] Other authors had reported the preparation of the 50 µm hybrid coating using a multi-layer process.

Fillers in Sol-Gel coatings are also reported to be able to increase the thickness. [158] Castro et al. have synthesized Sol-Gel hybrid coating with TEOS and MTES doped with Si-nanoparticle fillers. [127] The thickness and the life-time of the coating in 0.5M NaCl solution are increased coherently. Hammer et *al.* also reported that the carbon nanotube could increase 500 nm thickness of the siloxane-PMMA based hybrid coating.[128]

In order to increase the thick crack-free coatings, some new methods have been developed. For example, the Layer by Layer deposition (LbL) consists in depositing layers with opposite charge on the substrate in sequence.[129] The so-prepared coatings have also been applied for corrosion protection applications.[130]

Morphology - Porosity

During the evaporation procedure after deposition, the removal of the solvent molecules will leave the pores in the coating. As already been shown in Fig. 2 – 4 in earlier part, the size of the pores will be influenced by the colloidal size in the Sol, the assemblage of colloid, and the shape of the clusters. [83]

In order to modify the porosity, several common methods can be applied, such as:

- from molecule-level, modifying the microstructure by using a catalyst process (acid, basic, UV…), adding chelating agent, or using multiple precursors or organic silanes[131],
- mixing flexible organic component;
- controlling the evaporation velocity, for Xero-gel;[132,133]
- the phase transfer by heat treatment[134] or multi-phase stabilization;[135]
- adding fillers;[136]
- applying the multi-layer deposition to cover the upper layer pores. [137]

Specifically, the organic groups can be added to increase the density of Sol-Gel coating. Subasri et al. have proposed that the methyl group in the TEOS and MTES based Sol-Gel hybrid coating has important porosity.[131] Instead of that, N-alkylamide group containing precursors can control the porosity in the hybrid coatings.[138]

Adhesion

The adhesion property depicts the ability of the coating to connect with the substrate. The adhesion can be strong or weak according to the bonding nature, like a covalent bond or Van

der Waals force, etc. A good adhesion of the coating on the substrate prevents the diffusion of the corrosive reactant laterally between the coating and substrate. Therefore, the delamination of the coating during service is limited, assuring a longer life-time. As shown in Fig. I.5 - 1a, the Sol-Gel coating can form Si-O-Me covalent bonds with the metal surface. Inorganic Sol-Gel coating principally behaves a good adhesion property, while for organic coating the delamination is a main issue for the failure of the deposited system.[72]

Moreover, the addition of organic compounds in the hybrid coating decrease the adhesion property of Sol-Gel, which explains the frequent delamination phenomenon in organic coatings and hybrid coatings with epoxy-based precursors.[139]

To enhance the coating/ substrate adhesion, surface treatment is usually required to metal surface. As shown in Fig. I.5 - 1c, after immersed in phosphate acid, the Mg surface is activated with phosphate acid groups, which opens the opportunity for the silica matrix to establish the covalent bonding between phosphate ions.[140] Piranha solution, Kroll solution, NaOH, Plasma treatment have been proved to be efficient to active the pure titanium surface. [141,142]

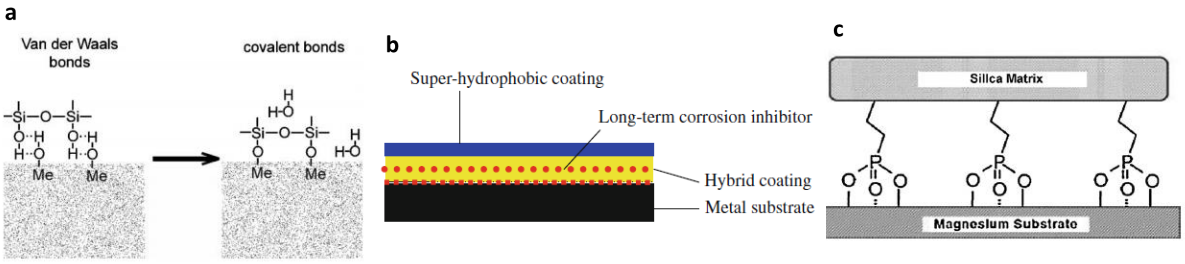

Fig. I.5 - 1 a) The scheme of covalent bond by Sol-Gel coating deposited on metal surface b) The role of Sol-Gel coating in a multi-coating corrosion protection system b) The surface modification by Phosphate acid on Mg surface for better adhesion properties

Hydrophobicity

Hydrophobicity depicts the ability of a surface to repulse water, which is the result of surface tension at the liquid-solid interface. Fig. I.5 - 2a illustrates a solid/ air/ liquid ternary system with the relative surface tensions, where **L** refers to the liquid phase, **G** refers to the gas phase, and **S** refers to the solid phase, respectively. Thus γ_{LG}, γ_{SL}, and γ_{SG} correspond to the surface tension between Liquid-Gas, Solid-Liquid, and Solid-Gas, respectively.

Statistical Contact Angle (SCA) is the most widely applied method to evaluate the hydrophobicity of a surface. Wenzel et al has proposed that a roughness will influence the contact angle while Cassie and Baxter have proposed Cassie's law, indicating that the contact angle can quantify the wettablitliy of the surface.[143] As observed in Fig. I.5 - 2, the θ is the so-called contact angle, which has been used to characterize the surface hydrophobicity. Using pure water drop, when θ is lower than 90°, the surface is hydrophilic, as in Fig. I.5 - 2c. When θ is higher than 90°, the surface is hydrophobic, see Fig. I.5 - 2d. Specifically, when θ is over 150°, the surface is so-called superhydrophobic and allows a strong water-repellency. The superhydrophobic surface usually has small vacancies on the surface, which trapped air bubbles forming a superficial composite, as shown in Fig. I.5 - 2e.

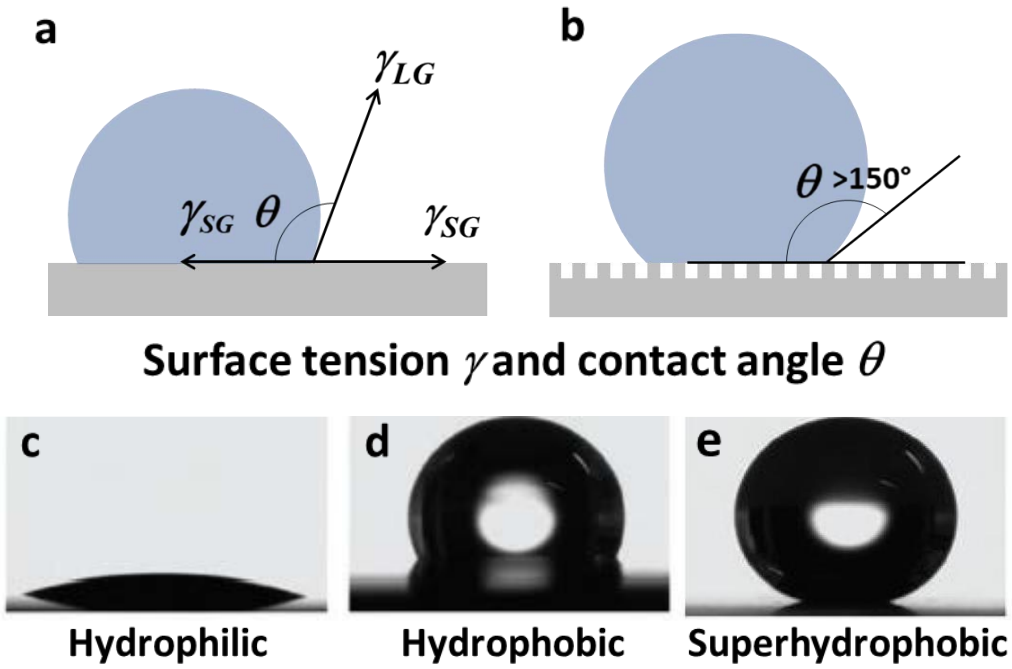

Fig. I.5 - 2 The Scheme of a) surface tension, b) Superhydrophobic coating and the images of contact angle for c) hydrophilic surface, d) hydrophobic surface and e) superhydrophobic surface

Hydrophobic surfaces show a lower penetration rate of the electrolyte due to the lower affinity of water. A highly hydrophobic surface is favored to promote adequate corrosion resistance. However, a long-duration exposure to a humid environment may lead to a severe decrease of the hydrophobicity.[144]

The hydrophobicity for Sol-Gel coatings could be obtained by introducing non-polar organic groups modified silane with methyl groups[145], fluorine groups, long alkyl chain (with precursor like Octyltriethoxysilane (OTES, R_3Si+C8) [146] , Decyltriethoxisilane (DTES, R_3Si+C10) [147] , Octadecyltriethoxysilane (ODTES, R_3Si+C18)[148]). Hydrophobicity can also be introduced by adding fillers such as nano-particles[149], nano clay[150], 2D nanosheets[151], nanotubes[152], etc.

I.5.2 Application of Sol-Gel coatings for corrosion protection

As a new method to replace CCC coatings, Sol-Gel coating has been largely explored in recent decades. For corrosion protection, according to the different requirements for applications and application environments, Sol-Gel coatings should be designed differently.

Inorganic coatings

With the porous nature and low thickness as fact, inorganic Sol-Gel coatings exhibit low corrosion resistance in principle. The xerogel inorganic coatings are treated in different ways: high-temperature heat treatment (over 600 °C, ceramic coatings), medium temperature treated coatings (200°C to 600°C) and low temperature cured coatings.

As reported, high-temperature treatment may cause cracks in the coating.[153] However, as mentioned before, Nouri et al. have proved that Zr-based ceramic coatings could behave adequate corrosion resistance due to similar thermal expansion rate to the substrate. [134]

Coatings treated with medium temperatures are proved to show efficiency in corrosion protection. Atik et al. have reported the influence of different temperatures on corrosion of ZrO_2 deposited 316L immersed in NaCl 30g/L solution.[155] The ZrO_2-based coatings treated over 450°C showed were denser and its EIS curves showed a second time constant at middle frequency relating to porosity of the dense film, other than the charge transfer phenomenon from low frequency.[154]

To overcome the short comings of the inorganic Sol-Gel coating for corrosion protection, multi-precursor are employed to decrease porosity and increase thickness, with relatively low heat treatment temperature. TiO_2-SiO_2 for stainless steel in H_2SO_4 condition[155], SiO_2-CaO-P_2O for stainless steel in Ca enriched SBF condition,[156] SiO_2-ZrO_2 on carbon steel[157] in 3.5% NaCl solution were successfully realized. These different coating systems showed improved corrosion resistance compared with the bare substrate, which is evidenced by a nobler E_{corr} and lower corrosion current density.

Hybrid Sol-Gel coatings

By using organic silane or siloxane, scientists succeeded in synthesizing hybrid Sol-Gel coatings, which overcomes the shortcomings of inorganic sol-gel coatings.

The statistic study of the class II coatings developed between 2001 – 2013 is shown in Fig. I.5 - 3. Hybrid coating has been mainly applied to Aluminium alloys, and steels. The application of hybrid coating on Zn and Zn alloy, Cu and Cu alloy and Mg and Mg alloys are very limited by the surface reactivity of these metals.[81]

For Iron-based alloys, TEOS and GPTMS have been employed for over 70% of researches. [81] TEOS offers a mild synthesis condition and could be used with accompany of other precursor for function groups. Among different hybrid precursors, GPTMS is the most widely applied precursor. GPTMS has a glycidoxy group which can act as a binder enabling the connection between inorganic and organic groups inside the Sol-Gel matrix. Meanwhile, more flexibility and less porosity could be obtained. [81]

For aluminum and its alloys, GPTMS was the most used precursor, which shows 72% among publications of hybrid coating from 2001 – 2013 according to a statistic analysis performed by Figueira et al. [81]

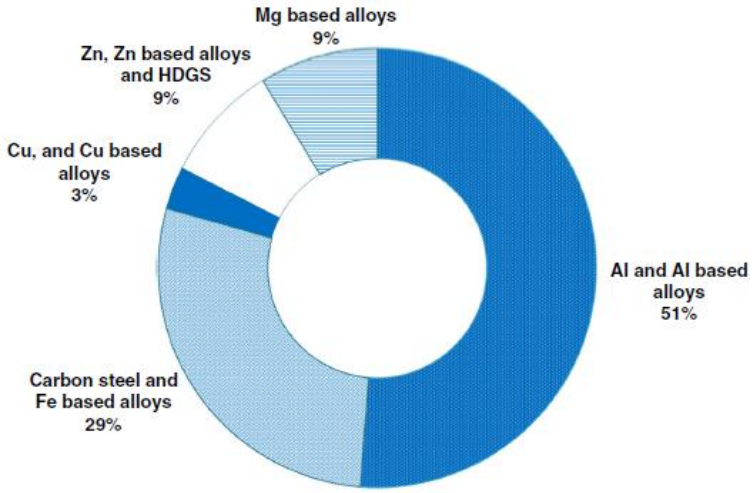

Fig. I.5 - 3 The pie chart of the distribution of the applicated materials of class II coatings[81]

Composite Sol-Gel coatings with additives

In order to improve the production of Sol-Gel coatings, the barrier effect, self-healing effect or sacrificial effect, etc., are introduced into Sol-Gel coatings. As mentioned in the first part of the chapter, metal oxide, lanthanide metals, natural product, nano-container incorporated inhibitors, etc., can be introduced as inhibitors into Sol-Gel matrix. Zinc particles are introduced as sacrifice agents that provide a self-healing effect for the coating.

Allongside the inhibiting fillers, Liu et al. charged inert silica nano-particles into decyltrimethoxysilane (DTMS) coatings and showed improvement of anti-corrosion property and enhancement of the thickness of the coating.[158] Kim et al. have incorporated silica nano-particles with different sizes into TEOS and MTES hybrid coatings on 304 SS. It seems that the sample with 10nm and 50nm particles together gives a suitable anti-corrosion property, while the smaller particle showed a better effect. [159] ZrO_2 and CeO_2 nano-particles were also charged into TEOS and tetraocthylorthosilicate (TEOCS) derived coating on AA2024, among which ZrO_2-CeO_2 coating system revealed the best protection performance.[160]

The barrier effect of Sol-Gel coating can be improved by adding nanofillers that provide prolongation of the penetration path for active reactants. This mechanism is the so-called “zig-zag path” theory proposed by Nielson et al. in the first place.[126] The 2D nanomaterial, like graphene and h-BN nanosheet, exhibit impermeability to molecules as small as helium due to their sp^2 electronic structure.[161] Though not yet applied in hybrid coating, hexagonal boron nitride (h-BN) and Molybdenum disulfide (MoS_2) had been applied in polymer coatings and showed improvement of the anti-corrosion property.[162,163]

I.6 2D materials

Graphene and the compounds with similar layered structures, such as hexagonal Boron Nitride nanosheet (BNNS) and Molybdenum disulfide (MoS_2) nanosheet, are defined as two–dimensional (2D) materials due to their specific atomic-level thickness.[164] Classified with different microstructures, as shown in Fig. I.6 - 1, there are many more categories of 2D materials in recent years.[165] The h-BN is called white graphene due to its similar atomic

layered sp^2 structure and insulating property. Transition Metal Dichalcogenides (TMDS), with MoS_2 as an example, have the closest structure other than h-BN to graphene. The newly explored complex or organic 2D materials have also been studied by researchers like MXenes (transition metal carbide, nitride or carbon nitride such as Ti_2C, Mo_2N, Ti_3CN) and Covalent Organic Frameworks (COFs).[166]

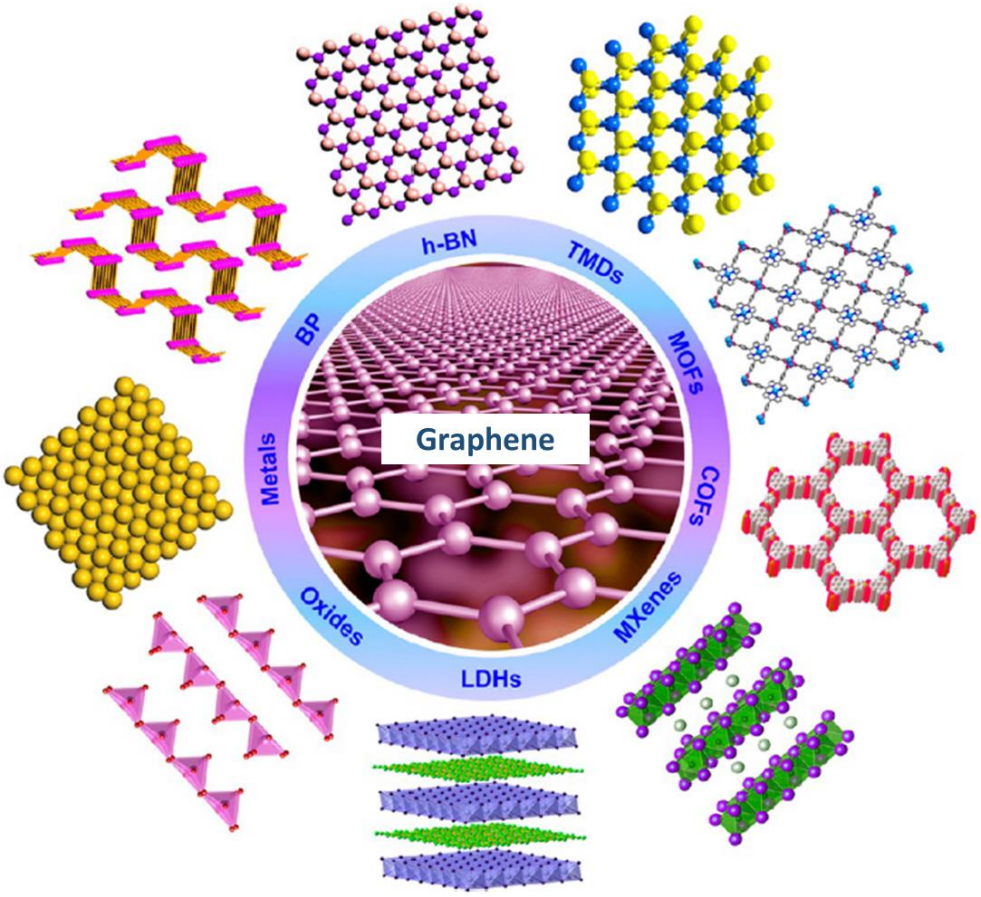

Fig. I.6 - 1 The categories of 2D materials[166]

2D materials have received abundant attention from applications like micro/nano-electronic devices[167] or lubricants[168] by applying their quantum size effect, high surface to volume ratio[169] and weak Van de Waals force between layers. With h-BN as an example, it is a semiconductor (bandgap 5.2eV-5.9eV)[170,171,172], and presents chemical inertness and high stability under high temperature and pressure.[173] Its sp^2 structure allows it to be impermeabe to small molecules as small as hydrogen, making it a promising barrier material for steel protection against corrosion phenomena.[174] Graphene also presented impermeability to oxidation and have been tried to protect Cu and Cu/Ni alloys from oxidation.[175] MoS_2, on the other hand, also proved oxidation resisitivity by its heavy reactivity to oxide and stopping the oxide from penetrating its thin layer.[176]

For anticorrosion applications, h-BN has been widely added into polymer matrix to increase coating's barrier effect by torturing the penetration path of the ions and molecules. Cui et al reported over the influence of h-BN content in an epoxy organic coating, in which an optimized

h-BN content of anticorrosion property has been proposed. [177] Hussain et *al.* have discussed the result about the h-BN charged PVA coatings and proposed a comprehensible role of barrier property of BNNS by EIS analysis.[178] Other researches have been done with BNNS charged in resin[179] , polyimide[180] and PMMA[181] organic coatings. Comparing to graphene,[182] graphene oxide is more applied to epoxy coatings for an improvement of the anticorrosion properties, due to its more functional group on the sheet structure allowing it to integrate better in the coating matrix. [183,184,185] Bing et al. has charged Graphene oxide in ZrO_x/GPTMS coating on AA2024/T3 for improvement of corrosion resistance. [186] MoS_2 has also been charged into composite coating for an improvement of anticorrosion properties. [187,188]

However, few 2D materials had been integrated into inorganic coatings, from which Graphene oxide has been tried in integration with some ceramic coatings for mechanical properties such as reinforcement, adsorption, etc.[189,190]. Facing the demand of improving the barrier effect of inorganic Sol-Gel coating and hybrid coatings, 2D materials shows a promising potential for achieving this aim. Some attempt have been done for charging GO[191], h-BN[192] in hybrid coatings.

I.6.1 Preparation methods

Typically, the 2D materials can be synthsized from Chemical Vapor Deposition method (CVD) or CVD-derived molecule deposition techniques. The “bottom-up” method allows to synthesize mono or few layered large crystal of 2D materials with high purity.[193] Graphene, h-BN, TMDs, Metal oxide all have been synthesized by CVD method.[194]

Otherwise, it is also possible to obtain them through the exfoliation process from the raw materials (bulk crystal) like mechanical cleavage, liquid exfoliation, ion-intercalation assisted exfoliation, chemical vapor deposition method.[166] Other methods have also been developed largely in recent years.

The mechanical cleavage are the original method for the synthesis of 2D materials, as Geim et Novosolov had developed the method to acquire the layered graphene from graphite using scotch on graphite bulk materials.[165]

The ultrasonic-assisted liquid exfoliation allows a larger yield however this method highly depends on the stability between the 2D materials and the solution. Kim et al has studied using pure water to effectuate exfoliation of different 2D materials. [195] Though both the yield and stability are low, the ‘’green’’ way showed capability to enable 2D materials to be exfoliated in water efficiently, and especially at 60 °C. Nicolosi et al has developed ultrasonic assisted liquid exfoliation with different solvent, and the organic solvents proved to be very effective for the improvement of content of 2D materials. [196]

The addition of ionic species allows us to break the Van de Waals force by the ions intercalation between the atomic layers. Moreover, the adsorption of ions stabilize 2D materials in the solvent.[197]

I.6.2 Selection of 2D materials

Generally, the protection effect of 2D materials can be achieved in two ways. At first, the deposition of the film of the 2D materials via CVD or PVD procedure result in a water repellency effect. The reduction of substrate surface energy of the substrate is caused either by chemical functionalization or creating micro/nanoscale roughness forming a superhydrophobic surface. [198] On the other hand, 2D materials have been incorporated into polymer and/or ceramic matrix mitigate passage of oxygen and moisture to the prevented surface.[199] However, graphene is well known as a superconductor that can potentially lead to galvanic corrosion coupling with the underlying metal. Keeping this issue in mind, h-BN nanosheet (BNNS), which have a similar impermeability, could be a better choice as a protective barrier because they are more thermally and chemically stable than graphene and, [200] more importantly, do not cause galvanic corrosion due to their electrical insulation.[201,202,203] Otherwise, the graphene oxide derived by electrochemically expanded graphite as well as MoS_2 have also been interested in the anticorrosion applications.

I.7 Conlusion

In this chapter, the necessity of protection for metals against corrosion has been reviewed. Among various anticorrosion methods, Sol-Gel coating has been proved to be eco-friendly and has mild synthesis conditions for various inorganic or OIH coating. However, the mesoporous or microporous structure nature of Sol-Gel coating needs to be improved to achieve a high barrier effect.

The modified Sol-Gel matrix with organic silane could increase the flexibility as well as the thickness of the coating but in detriment to the adhesion property. The inert fillers act as a barrier that seals the pores and prolongs the penetration pathway, as reported by Nielson et al.[204] Both methods have been proved to be efficient in different application conditions.

Among different nanofillers, the 2D nanosheets show promising properties due to its impermeable structure to small molecules. The microstructure, physical and chemical properties of different 2D materials have been discussed. Notably, the hexagonal Boron Nitride nanosheet has been selected as the fillers due to its low electrical conductivity and excellent impermeability to small molecules and ions.

[1] Michel Colombié. Didier Albert.; Roger Baltus.; Matériaux métalliques propriétés, mise en forme et applications industrielles des métaux etalliages. 2è édition. DUNOD.
[2] G.Koch ; J.Varney. International measures of prevention, application and economics of corrosion technologies study. NACE International Impact. 2016
[3] Durán, A.; Castro, Y.; Conde, A.; de Damborenea, J. J. Sol–Gel Protective Coatings for Metals. In Handbook of Sol-Gel Science and Technology; Klein, L., Aparicio, M., Jitianu, A., Eds.; Springer International Publishing: Cham, 2016; pp 1–65.
[4] Revie, R. W. Uhlig's Corrosion Handbook. 1285.
[5] Normand, B. Corrosion et anticorrosion : Une approche systémique. Corrosion course at INSA de Lyon, France. 2011, 67. http://www.critt-mdts.com/Site_hybriprotech/images/documentations/06-INSA%20lyon.pdf
[6] M.Hélie. Matériaux Métalliques Phénomènes de Corrosion. La Commission Pédagogie du CEFRACOR.
[7] G. Béranger, H. Mazille. Corrosion des métaux et alliages : mécanismes et phénomènes, Lavoisier, France, 2002, p. 202.
[8] Jack, Tinnea.; Albert, Sagues. Corrosion Control Plan for Bridges. 2012, 35.
[9] Olsson, C.-O. A.; Landolt, D. Passive Films on Stainless Steels—Chemistry, Structure and Growth. Electrochimica Acta 2003, 48 (9), 1093–1104.
[10] Kendig, M. W.; Buchheit, R. G. Corrosion Inhibition of Aluminum and Aluminum Alloys by Soluble Chromates, Chromate Coatings, and Chromate-Free Coatings. CORROSION 2003, 59 (5), 379–400.
[11] Normand, B.; Pébère, N.; Richard, C.; Wery, M.; Collectif. Prévention et lutte contre la corrosion : Une approche scientifique et technique; Presses Polytechniques et Universitaires Romandes: Lausanne, 2004.
[12] F, Dabosi.; G, Beranger.; B, Baroux. Corrosion Localisé. Les édition de Physique 1994.
[13] Lyndsie Selwyn. Understanding galvanic corrosion © Government of Canada, Canadian Conservation Institute. CCI 129916-0022.Figure 10.
[14] Revie, R. W. Uhlig's Corrosion Handbook. 1285.
[15] Frankelt, G. S. Pitting Corrosion of Metals. J. Electrochem. Soc. 1998, 145 (6), 13.
[16] Zhu, P.; Wu, Z.; Zhao, Y. Hierarchical Porous Cu with High Surface Area and Fluid Permeability. Scripta Materialia 2019, 172, 119–124.
[17] Al-Kharafi, F. M.; Ateya, B. G.; Allah, R. M. A. Selective Dissolution of Brass in Salt Water. Journal of Applied Electrochemistry 2004, 34 (1), 47–53.
[18] Almubarak, A.; Abuhaimed, W.; Almazrouee, A. Corrosion Behavior of the Stressed Sensitized Austenitic Stainless Steels of High Nitrogen Content in Seawater. International Journal of Electrochemistry 2013.
[19] Shanaghi, A.; Kadkhodaie, M. Investigation of High Concentration of Benzotriazole on Corrosion Behaviour of Titania–Benzotriazole Hybrid Nanostructured Coating Applied on Al 7075 by the Sol–Gel Method. Corrosion Engineering, Science and Technology 2017, 52 (5), 332–342.
[20] Nguyen, T.-T.; Bolivar, J.; Réthoré, J.; Baietto, M.-C.; Fregonese, M. A Phase Field Method for Modeling Stress Corrosion Crack Propagation in a Nickel Base Alloy. International Journal of Solids and Structures 2017, 112, 65–82.
[21] Postlethwaite, J.; Nešić, S. Erosion–Corrosion in Single- and Multiphase Flow. In Uhlig's Corrosion Handbook; John Wiley & Sons, Ltd, 2011; pp 215–227.
[22] Wood, R. J. K. Tribo-Corrosion of Coatings: A Review. J. Phys. D: Appl. Phys. 2007, 40 (18), 5502–5521.
[23] Dalbert, V.; Mary, N.; Normand, B.; Verdu, C.; Saedlou, S. In Situ Determinations of the Wear Surfaces, Volumes and Kinetics of Repassivation: Contribution in the Understanding of the Tribocorrosion Behaviour of a Ferritic Stainless Steel in Various PH. Tribology International 2020, 150, 106374.
[24] Lee, J.-B. Effects of Alloying Elements, Cr, Mo and N on Repassivation Characteristics of Stainless Steels Using the Abrading Electrode Technique. Materials Chemistry and Physics 2006, 99 (2–3), 224–234.
[25] Lyons, M. E. G.; Brandon, M. P. A Comparative Study of the Oxygen Evolution Reaction on Oxidised Nickel, Cobalt and Iron Electrodes in Base. Journal of Electroanalytical Chemistry 2010, 641 (1–2), 119–130.
[26] Schulz, Z.; Sterns, W.; Wachowiak, D.; Whitcraft, P. 4345: Availability and Economics of Using Duplex Stainless Steels. 10.
[27] Catoire, S. Les substances concernées par l'annexe XIV du règlement 1907/2006. 192.
[28] Sun, Y.; Li, X.; Bell, T. Low Temperature Plasma Carburising of Austenitic Stainless Steels for Improved Wear and Corrosion Resistance. Surface Engineering 1999, 15 (1), 49–54.

[29] Lavigne, O.; Alemany-Dumont, C.; Normand, B.; Berger, M. N.; Duhamel, C.; Delichere, P. The Effect of Nitrogen on the Passivation Mechanisms and Electronic Properties of Chromium Oxide Layers. Corrosion Sci. 2011, 53 (6), 2087–2096.
[30] Peyre, P.; Scherpereel, X.; Berthe, L.; Carboni, C.; Fabbro, R.; Béranger, G.; Lemaitre, C. Surface Modifications Induced in 316L Steel by Laser Peening and Shot-Peening. Influence on Pitting Corrosion Resistance. Materials Science and Engineering: A 2000, 280 (2), 294–302.
[31] Kim, K.-T.; Lee, J.-H.; Kim, Y.-S. Effect of Ultrasonic Nano-Crystal Surface Modification (UNSM) on the Passivation Behavior of Aged 316L Stainless Steel. Materials 2017, 10 (7), 713.
[32] Li, L.; Whitman, B. W.; Munson, C. A.; Estrada, R.; Matzdorf, C. A.; Swain, G. M. Structure and Corrosion Performance of a Non-Chromium Process (NCP) Zr/Zn Pretreatment Conversion Coating on Aluminum Alloys. J. Electrochem. Soc. 2016, 163 (13), C718–C728.
[33] P.G. Sheasby and R. Pinner The Surface Treatment and Finishing of Aluminum and Its Alloys, 6th Edition
[34] Li, L.; Whitman, B. W.; Munson, C. A.; Estrada, R.; Matzdorf, C. A.; Swain, G. M. Structure and Corrosion Performance of a Non-Chromium Process (NCP) Zr/Zn Pretreatment Conversion Coating on Aluminum Alloys. J. Electrochem. Soc. 2016, 163 (13), C718–C728.
[35] Qi, J.-T.; Hashimoto, T.; Walton, J. R.; Zhou, X.; Skeldon, P.; Thompson, G. E. Trivalent Chromium Conversion Coating Formation on Aluminium. Surface and Coatings Technology 2015, 280, 317–329.
[36] Lavigne, O.; Alemany-Dumont, C.; Normand, B.; Delichère, P.; Descamps, A. Cerium Insertion in 316L Passive Film: Effect on Conductivity and Corrosion Resistance Performances of Metallic Bipolar Plates for PEM Fuel Cell Application. Surface and Coatings Technology 2010, 205 (7), 1870–1877.
[37] Bethencourt, M.; Botana, F. J.; Cano, M. J.; Marcos, M. High Protective, Environmental Friendly and Short-Time Developed Conversion Coatings for Aluminium Alloys. Applied Surface Science 2002, 189 (1), 162–173.
[38] Becker, M. Chromate-Free Chemical Conversion Coatings for Aluminum Alloys. Corrosion Reviews 2019, 37 (4), 321–342.
[39] Zhou, P.; Liu, Y.; Liu, L.; Yu, B.; Zhang, T.; Wang, F. Critical Role of Pretreatment on the Corrosion Resistance of Zr Conversion Coating on 6061 Aluminum Alloy: The Combined Effect of Surface Topography and Potential Difference between Different Phases. Surface and Coatings Technology 2019, 377, 124904.
[40] Raja, P. B.; Ismail, M.; Ghoreishiamiri, S.; Mirza, J.; Ismail, M. C.; Kakooei, S.; Rahim, A. A. Reviews on Corrosion Inhibitors: A Short View. Chemical Engineering Communications 2016, 203 (9), 1145–1156.
[41] Bailote, L. D.; Ramanauskas, R.; Bartolo-P, P. Mη OXIDE FILM AS CORROSION INHIBITOR OF. 2000, 18 (1), 12
[42] Ilevbare, G. O.; Burstein, G. T. The Inhibition of Pitting Corrosion of Stainless Steels by Chromate and Molybdate Ions. Corrosion Science 2003, 45 (7), 1545–1569.
[43] Leidheiser, H. Cobalt and Nickel Cations as Corrosion Inhibitors for Galvanized Steel. J. Electrochem. Soc. 1981, 128 (2), 242.
[44] Fateh, A.; Aliofkhazraei, M.; Rezvanian, A. R. Review of Corrosive Environments for Copper and Its Corrosion Inhibitors. Arabian Journal of Chemistry 2020, 13 (1), 481–544.
[45] Raja, P. B.; Sethuraman, M. G. Natural Products as Corrosion Inhibitor for Metals in Corrosive Media — A Review. Materials Letters 2008, 62 (1), 113–116.
[46] Bethencourt, M.; Botana, F. J.; Calvino, J. J.; Marcos, M.; RodrÍguez-Chacón, M. A. Lanthanide Compounds as Environmentally-Friendly Corrosion Inhibitors of Aluminium Alloys: A Review. Corrosion Science 1998, 40 (11), 1803–1819.
[47] Finšgar, M.; Milošev, I. Inhibition of Copper Corrosion by 1,2,3-Benzotriazole: A Review. Corrosion Science 2010, 52 (9), 2737–2749.
[48] Mittal, S.; Pandey, A. K. Cerium Oxide Nanoparticles Induced Toxicity in Human Lung Cells: Role of ROS Mediated DNA Damage and Apoptosis https://www.hindawi.com/journals/bmri/2014/891934/ (accessed Feb 8, 2020).
[49] Alotaibi, M. D.; McKinley, A. J.; Patterson, B. M.; Reeder, A. Y. Benzotriazoles in the Aquatic Environment: A Review of Their Occurrence, Toxicity, Degradation and Analysis. Water Air Soil Pollut 2015, 226 (7), 226.
[50] Angst, U. M. A Critical Review of the Science and Engineering of Cathodic Protection of Steel in Soil and Concrete. CORROSION 2019, 75 (12), 1420–1433.
[51] Hassani-Gangaraj, S. M.; Moridi, A.; Guagliano, M. Critical Review of Corrosion Protection by Cold Spray Coatings. Surface Engineering 2015, 31 (11), 803–815.
[52] Edavan, R. P.; Kopinski, R. Corrosion Resistance of Painted Zinc Alloy Coated Steels. Corrosion Science 2009, 51 (10), 2429–2442.
[53] Gavrila, M.; Millet, J. P.; Mazille, H.; Marchandise, D.; Cuntz, J. M. Corrosion Behaviour of Zinc–Nickel Coatings, Electrodeposited on Steel. Surface and Coatings Technology 2000, 123 (2–3), 164–172.

[54] Gong, J. Electrodeposition of Sacrificial TinÁ/Manganese Alloy Coatings. Materials Science and Engineering A 2003, 11.
[55] Sørensen, P. A.; Kiil, S.; Dam-Johansen, K.; Weinell, C. E. Anticorrosive Coatings: A Review. J Coat Technol Res 2009, 6 (2), 135–176.
[56] Montemor, M. F. Functional and Smart Coatings for Corrosion Protection: A Review of Recent Advances. Surface and Coatings Technology 2014, 258, 17–37.
[57] Vaidya, U. K.; Chawla, K. K. Processing of Fibre Reinforced Thermoplastic Composites. International Materials Reviews 2008, 53 (4), 185–218.
[58] Perrin, F. X.; Oueiny, C. Polyaniline Thermoset Blends and Composites. Reactive and Functional Polymers 2017, 114, 86–103.
[59] Twite, R. L.; Bierwagen, G. P. Review of Alternatives to Chromate for Corrosion Protection of Aluminum Aerospace Alloys. Progress in Organic Coatings 1998, 33 (2), 91–100.
[60] Olajire, A. A. Recent Advances on Organic Coating System Technologies for Corrosion Protection of Offshore Metallic Structures. Journal of Molecular Liquids 2018, 269, 572–606.
[61] Wang, H.; Bai, Y.; Liu, S.; Wu, J.; Wong, C. P. Combined Effects of Silica Filler and Its Interface in Epoxy Resin. Acta Materialia 2002, 50 (17), 4369–4377.
[62] Díez-Pascual, A. M.; Gómez-Fatou, M. A.; Ania, F.; Flores, A. Nanoindentation in Polymer Nanocomposites. Progress in Materials Science 2015, 67, 1–94.
[63] L. Zheludkevich, M.; Miranda Salvado, I.; S. Ferreira, M. G. Sol–Gel Coatings for Corrosion Protection of Metals. Journal of Materials Chemistry 2005, 15 (48), 5099–5111.
[64] Amiri, S.; Rahimi, A. Hybrid Nanocomposite Coating by Sol–Gel Method: A Review. Iran Polym J 2016, 25 (6), 559–577.
[65] Liang, J.; Hu, Y.; Wu, Y.; Chen, H. Facile Formation of Superhydrophobic Silica-Based Surface on Aluminum Substrate with Tetraethylorthosilicate and Vinyltriethoxysilane as Co-Precursor and Its Corrosion Resistant Performance in Corrosive NaCl Aqueous Solution. Surface and Coatings Technology 2014, 240, 145–153.
[66] Wang, D.; Bierwagen, Gordon. P. Sol–Gel Coatings on Metals for Corrosion Protection. Progress in Organic Coatings 2009, 64 (4), 327–338.
[67] Figueira, R.; Fontinha, I.; Silva, C.; Pereira, E. Hybrid Sol-Gel Coatings: Smart and Green Materials for Corrosion Mitigation. Coatings 2016, 6 (1), 12.
[68] Siouffi, A.-M. Silica Gel-Based Monoliths Prepared by the Sol–Gel Method: Facts and Figures. Journal of Chromatography A 2003, 1000 (1–2), 801–818.
[69] Kumar, A.; Gaurav; Malik, A. K.; Tewary, D. K.; Singh, B. A Review on Development of Solid Phase Microextraction Fibers by Sol–Gel Methods and Their Applications. Analytica Chimica Acta 2008, 610 (1), 1–14.
[70] Peighambardoust, S. J.; Rowshanzamir, S.; Amjadi, M. Review of the Proton Exchange Membranes for Fuel Cell Applications. International Journal of Hydrogen Energy 2010, 35 (17), 9349–9384.
[71] Du, X.; He, J. Spherical Silica Micro/Nanomaterials with Hierarchical Structures: Synthesis and Applications. Nanoscale 2011, 3 (10), 3984.
[72] L. Zheludkevich, M.; Miranda Salvado, I.; S. Ferreira, M. G. Sol–Gel Coatings for Corrosion Protection of Metals. Journal of Materials Chemistry 2005, 15 (48), 5099–5111.
[73] Sun Ha Lee, Yangkyu Ahn, In Jung, Keunwoo Lee. Origin from the Presentation of Preparation of Spherical Silica-coated Ceria Nanoparticles by Sol-Gel Method.department of nanochemistry & biochemistry konyang university, Korea.
[74] Tallman, D. E.; Spinks, G.; Dominis, A.; Wallace, G. G. Electroactive Conducting Polymers for Corrosion Control: Part 1. General Introduction and a Review of Non-Ferrous Metals. J Solid State Electrochem 2002, 6 (2), 73–84.
75 Balamurugan, A.; Balossier, G.; Kannan, S.; Michel, J.; Faure, J.; Rajeswari, S. Electrochemical and Structural Characterisation of Zirconia Reinforced Hydroxyapatite Bioceramic Sol–Gel Coatings on Surgical Grade 316L SS for Biomedical Applications. Ceramics International 2007, 33 (4), 605–614.
76 Hosseini, S. M. A.; Jafari, A. H.; Jamalizadeh, E. Self-Healing Corrosion Protection by Nanostructure Sol–Gel Impregnated with Propargyl Alcohol. Electrochimica Acta 2009, 54 (28), 7207–7213.
[77] Liu, L.; Hu, J.-M.; Zhang, J.-Q.; Cao, C.-N. Improving the Formation and Protective Properties of Silane Films by the Combined Use of Electrodeposition and Nanoparticles Incorporation. Electrochimica Acta 2006, 52 (2), 538–545.
[78] Boccaccini, A. R.; Schindler, U.; Krüger, H.-G. Ceramic Coatings on Carbon and Metallic Fibres by Electrophoretic Deposition. Materials Letters 2001, 51 (3), 225–230.
[79] Balgude, D.; Sabnis, A. Sol–Gel Derived Hybrid Coatings as an Environment Friendly Surface Treatment for Corrosion Protection of Metals and Their Alloys. J Sol-Gel Sci Technol 2012, 64 (1), 124–134.

[80] Schottner, G. Hybrid Sol−Gel-Derived Polymers: Applications of Multifunctional Materials. Chem. Mater. 2001, 13 (10), 3422–3435.
[81] Figueira, R. B.; Silva, C. J. R.; Pereira, E. V. Organic–Inorganic Hybrid Sol–Gel Coatings for Metal Corrosion Protection: A Review of Recent Progress. J Coat Technol Res 2015, 12 (1), 1–35.
[82] Soler-Illia, G. J. A. A.; Innocenzi, P. Mesoporous Hybrid Thin Films: The Physics and Chemistry Beneath. Chem. Eur. J. 2006, 12 (17), 4478–4494.
[83] F.Collignon. Cahier Technologique Sol-Gel - PDF; CerTech, 2018.
[84] Caruso, R. A.; Antonietti, M. Sol−Gel Nanocoating: An Approach to the Preparation of Structured Materials. Chem. Mater. 2001, 13 (10), 3272–3282.
[85] Shen, G. X.; Chen, Y. C.; Lin, C. J. Corrosion Protection of 316 L Stainless Steel by a TiO2 Nanoparticle Coating Prepared by Sol–Gel Method. Thin Solid Films 2005, 489 (1–2), 130–136.
[86] Brinker, C. J.; Hurd, A. J.; Schunk, P. R.; Frye, G. C.; Ashley, C. S. Review of Sol-Gel Thin Film Formation. Journal of Non-Crystalline Solids 1992, 147–148, 424–436.
[87] Soleimani Dorcheh, A.; Abbasi, M. H. Silica Aerogel; Synthesis, Properties and Characterization. Journal of Materials Processing Technology 2008, 199 (1–3), 10–26.
[88] Peter, D.; Ertel, T. S.; Bertagnolli, H. EXAFS Study of Zirconium Alkoxides as Precursors in the Sol-Gel Process: II. The Influence of the Chemical Modification. J Sol-Gel Sci Technol 1995, 5 (1), 5–14.
[89] Vasconcelos, D. C. L.; Carvalho, J. A. N.; Mantel, M.; Vasconcelos, W. L. Corrosion Resistance of Stainless Steel Coated with Sol–Gel Silica. Journal of Non-Crystalline Solids 2000, 273 (1–3), 135–139.
[90] Thim, G. P.; Oliveira, M. A. S.; Oliveira, E. D. A.; Melo, F. C. L. Sol±gel Silica ®lm Preparation from Aqueous Solutions for Corrosion Protection. 2000, 5.
[91] Mackenzie, J. D.; Bescher, E. P. Physical Properties of Sol-Gel Coatings. 7.
[92] Velten, D.; Biehl, V.; Aubertin, F.; Valeske, B.; Possart, W.; Breme, J. Preparation of TiO2 Layers on Cp-Ti and Ti6Al4V by Thermal and Anodic Oxidation and by Sol-Gel Coating Techniques and Their Characterization. J. Biomed. Mater. Res. 2002, 59 (1), 18–28.
[93] Izumi, K.; Minami, N.; Uchida, Y. Sol-Gel-Derived Coatings on Steel Sheets. KEM 1998, 150, 77–88.
[94] Li, J.; Lu, Y.; Lan, P.; Zhang, X.; Xu, W.; Tan, R.; Song, W.; Choy, K.-L. Design, Preparation, and Durability of TiO2/SiO2 and ZrO2/SiO2 Double-Layer Antireflective Coatings in Crystalline Silicon Solar Modules. Solar Energy 2013, 89, 134–142.
[95] Mumjitha, M.; Raj, V. Fabrication of TiO2–SiO2 Bioceramic Coatings on Ti Alloy and Its Synergetic Effect on Biocompatibility and Corrosion Resistance. Journal of the Mechanical Behavior of Biomedical Materials 2015, 46, 205–221.
[96] Liu, S.; Wang, Y.; Xiu, Z.; Lü, M.; Yu, C. Preparation and Photocatalytic Properties of La-Doped TiO2/ZrTiO4 Heterogeneous Thin Films. Journal of Alloys and Compounds 2006, 425 (1–2), 274–277.
[97] Bu, A.; Wang, J.; Zhang, J.; Bai, J.; Shi, Z.; Liu, Q.; Ji, G. Corrosion Behavior of ZrO2–TiO2 Nanocomposite Thin Films Coating on Stainless Steel through Sol–Gel Method. J Sol-Gel Sci Technol 2017, 81 (3), 633–638.
[98] Mahltig, B.; Audenaert, F.; Böttcher, H. Hydrophobic Silica Sol Coatings on Textiles—the Influence of Solvent and Sol Concentration. J Sol-Gel Sci Technol 2005, 34 (2), 103–109.
[99] hristian Reichardt, Solvents and Solvent Effects in Organic Chemistry, Wiley-VCH Publishers, 3rd ed., 2003.
[100] Malay, O.; Yilgor, I.; Menceloglu, Y. Z. Effects of Solvent on TEOS Hydrolysis Kinetics and Silica Particle Size under Basic Conditions. J Sol-Gel Sci Technol 2013, 67 (2), 351–361.
[101] Pandey, S.; Mishra, S. B. Sol–Gel Derived Organic–Inorganic Hybrid Materials: Synthesis, Characterizations and Applications. J Sol-Gel Sci Technol 2011, 59 (1), 73–94.
[102] Ulrich Schubert. Chemistry and Fundamentals of the Sol–Gel Process.
[103] Yu, M.; Liang, M.; Liu, J.; Li, S.; Xue, B.; Zhao, H. Effect of Chelating Agent Acetylacetone on Corrosion Protection Properties of Silane-Zirconium Sol–Gel Coatings. Applied Surface Science 2016, 363, 229–239.
[104] Papet, P.; Le Bars, N.; Baumard, J. F.; Lecomte, A.; Dauger, A. Transparent Monolithic Zirconia Gels: Effects of Acetylacetone Content on Gelation. J Mater Sci 1989, 24 (11), 3850–3854.
[105] Kurajica, S. A Brief Review on the Use of Chelation Agents in Sol-Gel Synthesis with Emphasis on β-Diketones and β-Ketoesters. Chem. biochem. eng. q. (Online) 2019, 33 (3), 295–301.
[106] Liu, D.-M.; Yang, Q.; Troczynski, T.; Tseng, W. J. Structural Evolution of Sol–Gel-Derived Hydroxyapatite. Biomaterials 2002, 23 (7), 1679–1687.
[107] Chou, T. P.; Chandrasekaran, C.; Limmer, S. J.; Seraji, S.; Wu, Y.; Forbess, M. J.; Nguyen, C.; Cao, G. Z. Organic–Inorganic Hybrid Coatings for Corrosion Protection. Journal of Non-Crystalline Solids 2001, 290 (2–3), 153–162.
[108] Ginter, D. M.; Went, G. T.; Bell, A. T.; Radke, C. J. A Physicochemical Study of the Aging of Colloidal Silica Gels Used in Zeolite Y Synthesis. 9

[109] Bosc, F.; Ayral, A.; Albouy, P.-A.; Guizard, C. A Simple Route for Low-Temperature Synthesis of Mesoporous and Nanocrystalline Anatase Thin Films. Chem. Mater. 2003, 15 (12), 2463–2468.
[110] Sakka, S. Sol–Gel Technology as Representative Processing for Nanomaterials: Case Studies on the Starting Solution. J Sol-Gel Sci Technol 2008, 46 (3), 241–249.
[111] Lampke, Th.; Darwich, S.; Wielage, B.; Steinhäuser, S. Cost-efficient Conversion Coatings for Corrosion Protection Prepared by the Sol-gel Process. Mat.-wiss. u. Werkstofftech. 2008, 39 (7), 460–465.
[112] Nouri, E.; Shahmiri, M.; Rezaie, H. R.; Talayian, F. A Comparative Study of Heat Treatment Temperature Influence on the Thickness of Zirconia Sol–Gel Thin Films by Three Different Techniques: SWE, SEM and AFM. Surface and Coatings Technology 2012, 206 (19–20), 3809–3815.
[113] Mohd Yusoff, M. F.; Abdul Kadir, M. R.; Iqbal, N.; Hassan, M. A.; Hussain, R. Dipcoating of Poly (ε-Caprolactone)/Hydroxyapatite Composite Coating on Ti6Al4V for Enhanced Corrosion Protection. Surface and Coatings Technology 2014, 245, 102–107.
[114] Keyence. Shaping the Future of Automation: Coating & Dispensing Technology.
[115] Liu, L.; Mandler, D. Electrochemical Deposition of Sol-Gel Films. In Handbook of Sol-Gel Science and Technology; Klein, L., Aparicio, M., Jitianu, A., Eds.; Springer International Publishing: Cham, 2018; pp 531–568.
[116] Wu, L.-K.; Wu, J.-J.; Wu, W.-Y.; Cao, F.-H.; Jiang, M.-Y. Sol–Gel-Based Coatings for Oxidation Protection of TiAl Alloys. J Mater Sci 2020, 55 (15), 6330–6351.
[117] Brinker, C. J.; Hurd, A. J.; Schunk, P. R.; Frye, G. C.; Ashley, C. S. Review of Sol-Gel Thin Film Formation. Journal of Non-Crystalline Solids 1992, 147–148, 424–436.
[118] Bornside, D. E.; Macosko, C. W.; Scriven, L. E. Spin Coating: One-dimensional Model. Journal of Applied Physics 1989, 66 (11), 5185–5193.
[119] Landau, L.; Levich, B. Dragging of a Liquid by a Moving Plate. Dynamics of Curved Fronts 1988, 141–153.
[120] Grundmeier, G.; Schmidt, W.; Stratmann, M. Corrosion Protection by Organic Coatings: Electrochemical Mechanism and Novel Methods of Investigation. Electrochimica Acta 2000, 45 (15–16), 2515–2533.
[121] Jin, F.-L.; Li, X.; Park, S.-J. Synthesis and Application of Epoxy Resins: A Review. Journal of Industrial and Engineering Chemistry 2015, 29, 1–11.
[122] Eduok, U.; Faye, O.; Szpunar, J. Recent Developments and Applications of Protective Silicone Coatings: A Review of PDMS Functional Materials. Progress in Organic Coatings 2017, 111, 124–163.
[123] Li, D.; Liu, Z.; Wang, Y.; Shan, Y.; Huang, F. Efficiency Enhancement of Cu(In,Ga)Se2 Solar Cells by Applying SiO2–PEG/PVP Antireflection Coatings. Journal of Materials Science & Technology 2015, 31 (2), 229–234.
[124] Ji, W.-G.; Hu, J.-M.; Zhang, J.-Q.; Cao, C.-N. Reducing the Water Absorption in Epoxy Coatings by Silane Monomer Incorporation. Corrosion Science 2006, 48 (11), 3731–3739.
[125] Figueroa, R.; Nóvoa, X. R.; Pérez, C. Hydrophobic Surface Treatments for Improving the Corrosion Resistance of Anodized AA2024-T3 Alloys. Electrochimica Acta 2019, 303, 56–66.
[126] Nielsen, L. E. Models for the Permeability of Filled Polymer Systems. Journal of Macromolecular Science: Part A - Chemistry 1967, 1 (5), 929–942.
[127] Castro, Y.; Ferrari, B.; Moreno, R.; Durán, A. Coatings Produced by Electrophoretic Deposition from Nano-Particulate Silica Sol–Gel Suspensions. Surface and Coatings Technology 2004, 182 (2–3), 199–203.
[128] Hammer, P.; dos Santos, F. C.; Cerrutti, B. M.; Pulcinelli, S. H.; Santilli, C. V. Carbon Nanotube-Reinforced Siloxane-PMMA Hybrid Coatings with High Corrosion Resistance. Progress in Organic Coatings 2013, 76 (4), 601–608.
[129] Decher, G. Fuzzy Nanoassemblies: Toward Layered Polymeric Multicomposites. Science 1997, 277 (5330), 1232–1237.
[130] Shchukin, D. G.; Zheludkevich, M.; Yasakau, K.; Lamaka, S.; Ferreira, M. G. S.; Möhwald, H. Layer-by-Layer Assembled Nanocontainers for Self-Healing Corrosion Protection. Adv. Mater. 2006, 18 (13), 1672–1678.
[131] Subasri, R.; Jyothirmayi, A.; Reddy, D. S. Effect of Plasma Surface Treatment and Heat Treatment Ambience on Mechanical and Corrosion Protection Properties of Hybrid Sol–Gel Coatings on Aluminum. Surface and Coatings Technology 2010, 205 (3), 806–813.
[132] Brinker, C. J.; Lu, Y.; Sellinger, A.; Fan, H. Evaporation-Induced Self-Assembly: Nanostructures Made Easy. 7.
[133] Grosso, D.; Soler-Illia, G. J. de A. A.; Crepaldi, Eduardo. L.; Cagnol, F.; Sinturel, C.; Bourgeois, A.; Brunet-Bruneau, A.; Amenitsch, H.; Albouy, P. A.; Sanchez, C. Highly Porous TiO 2 Anatase Optical Thin Films with Cubic Mesostructure Stabilized at 700 °C. Chem. Mater. 2003, 15 (24), 4562–4570.
[134] Nouri, E.; Shahmiri, M.; Rezaie, H. R.; Talayian, F. A Comparative Study of Heat Treatment Temperature Influence on the Thickness of Zirconia Sol–Gel Thin Films by Three Different Techniques: SWE, SEM and AFM. Surface and Coatings Technology 2012, 206 (19–20), 3809–3815.

[135] Ryu, H. S.; Lim, T. S.; Ryu, J.; Hong, S.-H. Corrosion Protection Performance of YSZ Coating on AA7075 Aluminum Alloy Prepared by Aerosol Deposition. J. Electrochem. Soc. 2013, 160 (1), C42–C47.
[136] Zheludkevich, M. L.; Serra, R.; Montemor, M. F.; Salvado, I. M. M.; Ferreira, M. G. S. Corrosion Protective Properties of Nanostructured Sol–Gel Hybrid Coatings to AA2024-T3. Surface and Coatings Technology 2006, 200 (9), 3084–3094.
[137] Park, S.-S.; Mackenzie, J. D. Microstructure Effects in Multidipped Tin Oxide Films. Journal of the American Ceramic Society 1995, 78 (10), 2669–2672.
[138] Wen, J.; Wilkes, G. L. Organic/Inorganic Hybrid Network Materials by the Sol−Gel Approach. Chem. Mater. 1996, 8 (8), 1667–1681.
[139] Li, W.; Tian, H.; Hou, B. Corrosion Performance of Epoxy Coatings Modified by Nanoparticulate SiO2. Materials and Corrosion 2012, 63 (1), 44–53.
[140] Hu, R.-G.; Zhang, S.; Bu, J.-F.; Lin, C.-J.; Song, G.-L. Recent Progress in Corrosion Protection of Magnesium Alloys by Organic Coatings. Prog. Org. Coat. 2012, 73 (2–3), 129–141.
[141] Casagrande, R. B.; Kunst, S. R.; Beltrami, L. V. R.; Aguzzoli, C.; Brandalise, R. N.; de Fraga Malfatti, C. Pretreatment Effect of the Pure Titanium Surface on Hybrid Coating Adhesion Based on Tetraethoxysilane and Methyltriethoxysilane. J Coat Technol Res 2018, 15 (5), 1089–1106.
[142] Fu, T.; Wen, C. S.; Lu, J.; Zhou, Y. M.; Ma, S. G.; Dong, B. H.; Liu, B. G. Sol-Gel Derived TiO2 Coating on Plasma Nitrided 316L Stainless Steel. Vacuum 2012, 86 (9), 1402–1407.
[143] Cassie, A. B. D.; Baxter, S. Wettability of Porous Surfaces. Trans. Faraday Soc. 1944, 40 (0), 546–551.
[144] Vazirinasab, E.; Jafari, R.; Momen, G. Application of Superhydrophobic Coatings as a Corrosion Barrier: A Review. Surface and Coatings Technology 2018, 341, 40–56.
[145] Rivero, P.; Maeztu, J.; Berlanga, C.; Miguel, A.; Palacio, J.; Rodriguez, R. Hydrophobic and Corrosion Behavior of Sol-Gel Hybrid Coatings Based on the Combination of TiO2 NPs and Fluorinated Chains for Aluminum Alloys Protection. Metals 2018, 8 (12), 1076.
[146] Jeeva Jothi, K.; Palanivelu, K. Synergistic Effect of Silane Modified Nanocomposites for Active Corrosion Protection. Ceramics International 2013, 39 (7), 7619–7625.
[147] Dalod, A. R. M.; Henriksen, L.; Grande, T.; Einarsrud, M.-A. Functionalized TiO 2 Nanoparticles by Single-Step Hydrothermal Synthesis: The Role of the Silane Coupling Agents. Beilstein J. Nanotechnol. 2017, 8, 304–312.
[148] Qin, L.; Zhao, W.; Hou, H.; Jin, Y.; Zeng, Z.; Wu, X.; Xue, Q. Achieving Excellent Anti-Corrosion and Tribological Performance by Tailoring the Surface Morphology and Chemical Composition of Aluminum Alloys. RSC Adv. 2014, 4 (104), 60307–60315.
[149] Liang, J.; Hu, Y.; Wu, Y.; Chen, H. Facile Formation of Superhydrophobic Silica-Based Surface on Aluminum Substrate with Tetraethylorthosilicate and Vinyltriethoxysilane as Co-Precursor and Its Corrosion Resistant Performance in Corrosive NaCl Aqueous Solution. Surface and Coatings Technology 2014, 240, 145–153.
[150] Seifzadeh, D.; Golmoghani-Ebrahimi, E. Formation of Novel and Crack Free Nanocomposites Based on Sol Gel Process for Corrosion Protection of Copper. Surface and Coatings Technology 2012, 210, 103–112.
[151] Hooda, A.; Goyat, M. S.; Pandey, J. K.; Kumar, A.; Gupta, R. A Review on Fundamentals, Constraints and Fabrication Techniques of Superhydrophobic Coatings. Progress in Organic Coatings 2020, 142, 105557.
[152] Oh, H.-S.; Kim, H. Efficient Synthesis of Pt Nanoparticles Supported on Hydrophobic Graphitized Carbon Nanofibers for Electrocatalysts Using Noncovalent Functionalization. Adv. Funct. Mater. 2011, 21 (20), 3954–3960.
[153] Vallet-Regí, M.; Izquierdo-Barba, I.; Gil, F. J. Localized Corrosion of 316L Stainless Steel with SiO2-CaO Films Obtained by Means of Sol–Gel Treatment. Journal of Biomedical Materials Research Part A 2003, 67A (2), 674–678.
[154] Delimaneto, P.; Avaca, L.; Atik, M.; Aegerter, M.; Rocha, R. Electrochemical Studies of the Corrosion of 316l Stainless-Steel Coated with Sol-Gel Zro2 Films. J. Braz. Chem. Soc. 1995, 6 (1), 33–37.
[155] Atik, M.; De Lima Neto, P.; Aegerter, M. A.; Avaca, L. A. Sol-Gel TiO2-SiO2 Films as Protective Coatings against Corrosion of 316L Stainless Steel in H2SO4 Solutions. J Appl Electrochem 1995, 25 (2), 142–148.
[156] Galliano, P.; De Damborenea, J. J.; Pascual, M. J.; Durán, A. Sol-Gel Coatings on 316L Steel for Clinical Applications. Journal of Sol-Gel Science and Technology 1998, 13 (1), 723–727.
[157] Abdollahi, B.; Afzali, D.; Hassani, Z. Corrosion Inhibition Properties of SiO2-ZrO2 Nanocomposite Coating on Carbon Steel 178. Anti-Corrosion Meth & Material 2017, 65 (1), 66–72.
[158] Liu, L.; Hu, J.-M.; Zhang, J.-Q.; Cao, C.-N. Improving the Formation and Protective Properties of Silane Films by the Combined Use of Electrodeposition and Nanoparticles Incorporation. Electrochimica Acta 2006, 52 (2), 538–545.
[159] Kim, H.; Hwang, T. Corrosion Protection Enhancement Effect by Mixed Silica Nanoparticles of Different Sizes Incorporated in a Sol–Gel Silica Film. J Sol-Gel Sci Technol 2012, 63 (3), 563–568.

[160] Gonzalez, E.; Pavez, J.; Azocar, I.; Zagal, J. H.; Zhou, X.; Melo, F.; Thompson, G. E.; Páez, M. A. A Silanol-Based Nanocomposite Coating for Protection of AA-2024 Aluminium Alloy. Electrochimica Acta 2011, 56 (22), 7586–7595.
[161] Hu, S.; Lozada-Hidalgo, M.; Wang, F. C.; Mishchenko, A.; Schedin, F.; Nair, R. R.; Hill, E. W.; Boukhvalov, D. W.; Katsnelson, M. I.; Dryfe, R. a. W.; et al. Proton Transport through One-Atom-Thick Crystals. Nature 2014, 516 (7530), 227–230.
[162] Husain, E.; Narayanan, T. N.; Taha-Tijerina, J. J.; Vinod, S.; Vajtai, R.; Ajayan, P. M. Marine Corrosion Protective Coatings of Hexagonal Boron Nitride Thin Films on Stainless Steel. ACS Appl. Mater. Interfaces 2013, 5 (10), 4129–4135.
[163] Zhao, X.; Zhang, B.; Jin, Z.; Chen, C.; Zhu, Q.; Hou, B. Epoxy Coating Modified by 2D MoS2/SDBS: Fabrication, Anticorrosion Behaviour and Inhibition Mechanism. RSC Adv. 2016, 6 (100), 97512–97522.
[164] Gupta, A.; Sakthivel, T.; Seal, S. Recent Development in 2D Materials beyond Graphene. Progress in Materials Science 2015, 73, 44–126.
[165] Novoselov, K. S.; Geim, A. K.; Morozov, S. V.; Jiang, D.; Katsnelson, M. I.; Grigorieva, I. V.; Dubonos, S. V.; Firsov, A. A. Two-Dimensional Gas of Massless Dirac Fermions in Graphene. Nature 2005, 438 (7065), 197–200.
[166] Zhang, H. Ultrathin Two-Dimensional Nanomaterials. ACS Nano 2015, 9 (10), 9451–9469.
[167] Radisavljevic, B.; Radenovic, A.; Brivio, J.; Giacometti, V.; Kis, A. Single-Layer MoS2 Transistors. Nature Nanotechnology 2011, 6 (3), 147–150.
[168] Filleter, T.; McChesney, J. L.; Bostwick, A.; Rotenberg, E.; Emtsev, K. V.; Seyller, T.; Horn, K.; Bennewitz, R. Friction and Dissipation in Epitaxial Graphene Films. Phys. Rev. Lett. 2009, 102 (8), 86102.
[169] Xu, M.; Liang, T.; Shi, M.; Chen, H. Graphene-Like Two-Dimensional Materials. Chem. Rev. 2013, 113 (5), 3766–3798.
[170] Kovtyukhova, N. I.; Wang, Y.; Lv, R.; Terrones, M.; Crespi, V. H.; Mallouk, T. E. Reversible Intercalation of Hexagonal Boron Nitride with Bronsted Acids. J. Am. Chem. Soc. 2013, 135 (22), 8372–8381.
[171] Cassabois, G.; Valvin, P.; Gil, B. Hexagonal Boron Nitride Is an Indirect Bandgap Semiconductor. Nature Photonics 2016, 10 (4), nphoton.2015.277.
[172] Wang, J. I.-J.; Yang, Y.; Chen, Y.-A.; Watanabe, K.; Taniguchi, T.; Churchill, H. O. H.; Jarillo-Herrero, P. Electronic Transport of Encapsulated Graphene and WSe2 Devices Fabricated by Pick-up of Prepatterned BNNS. Nano Lett. 2015, 15 (3), 1898–1903.
[173] Zhang, S.; Zhou, J.; Guo, B.; Zhou, H.; Pu, Y.; Chen, J. Friction and Wear Behavior of Laser Cladding Ni/BNNS Self-Lubricating Composite Coating. Materials Science and Engineering: A 2008, 491 (1), 47–54.
[174] Hu, S.; Lozada-Hidalgo, M.; Wang, F. C.; Mishchenko, A.; Schedin, F.; Nair, R. R.; Hill, E. W.; Boukhvalov, D. W.; Katsnelson, M. I.; Dryfe, R. a. W.; et al. Proton Transport through One-Atom-Thick Crystals. Nature 2014, 516 (7530), 227–230.
[175] Chen, S.; Brown, L.; Levendorf, M.; Cai, W.; Ju, S.-Y.; Edgeworth, J.; Li, X.; Magnuson, C. W.; Velamakanni, A.; Piner, R. D.; et al. Oxidation Resistance of Graphene-Coated Cu and Cu/Ni Alloy. ACS Nano 2011, 5 (2), 1321–1327.
[176] Sen, H. S.; Sahin, H.; Peeters, F. M.; Durgun, E. Monolayers of MoS 2 as an Oxidation Protective Nanocoating Material. Journal of Applied Physics 2014, 116 (8), 083508. https://doi.org/10.1063/1.4893790.
[177] Cui, M., Xue, Q., 2017. Anticorrosive performance of waterborne epoxy coatings containing water-dispersible hexagonal boron nitride (BNNS) nanosheets. Appl. Surf. Sci. 397, 77–86.
[178] Husain, E.; Narayanan, T. N.; Taha-Tijerina, J. J.; Vinod, S.; Vajtai, R.; Ajayan, P. M. Marine Corrosion Protective Coatings of Hexagonal Boron Nitride Thin Films on Stainless Steel. ACS Appl. Mater. Interfaces 2013, 5 (10), 4129–4135.
[179] TabkhPaz, Park, S.S., 2017. Development of nanocomposite coatings with improved mechanical, thermal, and corrosion protection properties. Journal of Composite Materials 21998317720001.
[180] Huang, Y.-C., Whang, W.-T., 2014. Anti-corrosion characteristics of polyimide/h-boron nitride composite films with different polymer configurations. Surf. Coat. Technol. 260, 113–117
[181] Coan, T., Machado, R. a. F., 2013. Preparation of PMMA/BNNS composite coatings for metal surface protection. Materials Research 16, 1366–1372.
[182] Chang, K.-C.; Hsu, M.-H.; Lu, H.-I.; Lai, M.-C.; Liu, P.-J.; Hsu, C.-H.; Ji, W.-F.; Chuang, T.-L.; Wei, Y.; Yeh, J.-M.; et al. Room-Temperature Cured Hydrophobic Epoxy/Graphene Composites as Corrosion Inhibitor for Cold-Rolled Steel. Carbon 2014, 66, 144–153.
[183] Ramezanzadeh, B.; Niroumandrad, S.; Ahmadi, A.; Mahdavian, M.; Moghadam, M. H. M. Enhancement of Barrier and Corrosion Protection Performance of an Epoxy Coating through Wet Transfer of Amino Functionalized Graphene Oxide. Corrosion Science 2016, 103, 283–304.

[184] Pourhashem, S.; Vaezi, M. R.; Rashidi, A.; Bagherzadeh, M. R. Exploring Corrosion Protection Properties of Solvent Based Epoxy-Graphene Oxide Nanocomposite Coatings on Mild Steel. Corrosion Science 2017, 115, 78–92.
[185] Yu, Z.; Di, H.; Ma, Y.; Lv, L.; Pan, Y.; Zhang, C.; He, Y. Fabrication of Graphene Oxide–Alumina Hybrids to Reinforce the Anti-Corrosion Performance of Composite Epoxy Coatings. Applied Surface Science 2015, 351, 986–996.
[186] Xue, B.; Yu, M.; Liu, J.; Liu, J.; Li, S.; Xiong, L. Corrosion Protection of AA2024-T3 by Sol-Gel Film Modified with Graphene Oxide. Journal of Alloys and Compounds 2017, 725, 84–95.
[187] Hu, X. G.; Cai, W. J.; Xu, Y. F.; Wan, J. C.; Sun, X. J. Electroless Ni–P–(Nano-MoS 2) Composite Coatings and Their Corrosion Properties. Surface Engineering 2009, 25 (5), 361–366.
[188] Zhao, X.; Zhang, B.; Jin, Z.; Chen, C.; Zhu, Q.; Hou, B. Epoxy Coating Modified by 2D MoS2/SDBS: Fabrication, Anticorrosion Behaviour and Inhibition Mechanism. RSC Adv. 2016, 6 (100), 97512–97522.
[189] Shin, J.-H.; Hong, S.-H. Fabrication and Properties of Reduced Graphene Oxide Reinforced Yttria-Stabilized Zirconia Composite Ceramics. Journal of the European Ceramic Society 2014, 34 (5), 1297–1302.
[190] Li, M.; Yin, X.; Chen, L.; Han, M.; Cheng, L.; Zhang, L. Dielectric and Electromagnetic Wave Absorption Properties of Reduced Graphene Oxide/Barium Aluminosilicate Glass–Ceramic Composites. Ceramics International 2016, 42 (6), 7099–7106.
[191] Ahmadi, A.; Ramezanzadeh, B.; Mahdavian, M. Hybrid Silane Coating Reinforced with Silanized Graphene Oxide Nanosheets with Improved Corrosion Protective Performance. RSC Adv. 2016, 6 (59), 54102–54112.
[192] Karadağ, M.; Karaahmet, O.; Çiçek, B.; Usta, M. İ. Effect of Hexagonal Boron Nitride on the Coefficient of Frictions of Organic-Inorganic Hybrid Polymer Thin Films for Metal Surface Coatings. Journal of Adhesion Science and Technology 2020, 34 (20), 2200–2215.
[193] Kim, K. K.; Lee, H. S.; Lee, Y. H. Synthesis of Hexagonal Boron Nitride Heterostructures for 2D van Der Waals Electronics. Chem. Soc. Rev. 2018, 47 (16), 6342–6369.
[194] Cai, Z.; Liu, B.; Zou, X.; Cheng, H.-M. Chemical Vapor Deposition Growth and Applications of Two-Dimensional Materials and Their Heterostructures. Chem. Rev. 2018, 118 (13), 6091–6133.
[195] Kim, J.; Kwon, S.; Cho, D.-H.; Kang, B.; Kwon, H.; Kim, Y.; Park, S. O.; Jung, G. Y.; Shin, E.; Kim, W.-G.; et al. Direct Exfoliation and Dispersion of Two-Dimensional Materials in Pure Water via Temperature Control. Nature Communications 2015, 6, 8294.
[196] Coleman, J. N.; Lotya, M.; O'Neill, A.; Bergin, S. D.; King, P. J.; Khan, U.; Young, K.; Gaucher, A.; De, S.; Smith, R. J.; et al. Two-Dimensional Nanosheets Produced by Liquid Exfoliation of Layered Materials. Science 2011, 331 (6017), 568–571.
[197] Nicolosi, V.; Chhowalla, M.; Kanatzidis, M. G.; Strano, M. S.; Coleman, J. N. Liquid Exfoliation of Layered Materials. Science 2013, 340 (6139), 1226419. https://doi.org/10.1126/science.1226419.
[198] Pakdel, A.; Zhi, C.; Bando, Y.; Nakayama, T.; Golberg, D. Boron Nitride Nanosheet Coatings with Controllable Water Repellency. ACS Nano 2011, 5 (8), 6507–6515.
[199] Prasai, D.; Tuberquia, J. C.; Harl, R. R.; Jennings, G. K.; Bolotin, K. I. Graphene: Corrosion-Inhibiting Coating. ACS Nano 2012, 6 (2), 1102–1108.
[200] S. Hu, M. Lozada-Hidalgo, F.C. Wang, A. Mishchenko, F. Schendin, R.R. Nair, E.W. Hill, D.W. Boukhvalov, M.I. Katsnelson, R.A.W. Dryfe,
[201] Li, L. H.; Xing, T.; Chen, Y.; Jones, R. Boron Nitride Nanosheets for Metal Protection. Adv. Mater. Interfaces 2014, 1 (8), 1300132
[202] Huang, Y.-C.; Lo, T.-Y.; Chao, C.-G.; Whang, W.-T. Anti-Corrosion Characteristics of Polyimide/h-Boron Nitride Composite Films with Different Polymer Configurations. Surface and Coatings Technology 2014, 260, 113–117.
[203] Yi, M.; Shen, Z.; Zhao, X.; Liang, S.; Liu, L. Boron Nitride Nanosheets as Oxygen-Atom Corrosion Protective Coatings. Applied Physics Letters 2014, 104 (14), 143101.
[204] Nielsen, L. E. Models for the Permeability of Filled Polymer Systems. Journal of Macromolecular Science: Part A - Chemistry 1967, 1 (5), 929–942. https://doi.org/10.1080/10601326708053745.

Chapter II. Materials and Experiments

II.1 Introduction

In this chapter, the raw materials, the preparation of materials, and the experimental procedure are presented.

As discussed in Chapter I, the metals suffer different corrosion phenomena according to their reactivity and surface conditions. Notably, in a highly-concentrated NaCl solution, the stainless steel (316L) exhibits pitting corrosion, while the aluminum alloy (AA2017) and carbon steel (XC10) suffer general corrosion without protective coatings. The Sol-Gel process for three different coating system are detailed, which are respectively:

1) Zirconium oxide single-component coating on 316L
2) Zirconium oxide- Silicon oxide multi-component coating on Aluminium alloy (AA2017)
3) Organic-inorganic hybrid coating on carbon steel (XC90)

The exfoliation methods are also presented. The h-BN, electrochemically expanded graphene, and MoS_2 powders were exfoliated in pure water, n-butanol, or isopropanol. The exfoliation and centrifuge parameters are given, and the names of the associated samples are listed. Finally, the electrochemical characterization techniques employed in this works are reviewed, including the applied three-electrodes electrochemical cell, open circuit potential test, potentiodynamic polarization, Electrochemical Impedance Spectroscopy (EIS) test**.**

II.2 Metal Substrates

In order to study the effect of 2D materials in Sol-Gel coating for barrier property enhancement, a substrate with an adequate surface reactivity is required. The selection of the substrate is based on the stability of the coating/ substrate interface.

II.2.1 Stainless steel

Stainless steel, which contains over a moderate amount of chromium as an alloying element, stands very well the general corrosion.[1] It has a higher tensile strength and better elongation property but lower yield strength than carbon steel.[2] Austenite stainless steels are well explored in industry domains, especially for the steels revealed from American Iron and Steel Institute (AISI): the AISI 316, AISI 304, and AISI 2205. The thin and dense oxide film on the metal surface is called passive film that can stop direct contact of the environment with the underlying metal. This property allows stainless steel to serve for marine field, nuclear plants, high-temperature plants, etc. However, stainless steel is prone to pitting corrosion, which is usually unpredictable and very dangerous for the structures due to the unexpected failure. Chloride ions (Cl^-) promote the pitting corrosion rate.[3]

The stainless steel 316L, which is an Austenite alloy, allows the investigation of the evolution of the Sol-Gel matrix due to its inertness to corrosive environment, which reduces the complexity of the observed system.

Stainless steel 316L is purchased from Goodfellow (the weight percentage: C 0.03%, Cr 18.00%, Ni 10.00%, Mo 3.00%, Mg 2.00%, Si 0.75%, P 0.045%, S 0.03%, N 0.10%). The substrate was cut into 50 x 25 x 3 mm^2 samples and grounded up to 1200 mesh using SiC paper from PRESI.

Before dip coating, samples were rinsed with distilled water, ethanol (96%, Ethanol for analysis, ChimiePlus), and acetone (Acetone for analysis, Chimieplus).

In addition, 316L were immersed in the "Piranha" solution with a ratio of H_2O_2 (35%, Chimie-plus) to H_2SO_4 (96%, Chimie-plus) equals to 1: 2 for 15min. This treatment cleaned the surface up and favored the formation of -OH polar groups, which is necessary for the Sol wettability on the passivation film.

II.2.2 Aluminum alloy

Aluminum and its alloys are interesting for their lightweight in various transportation applications. Pure aluminum exhibits good corrosion resistance due to the existence of a homogeneous Al_2O_3 oxide layer. However, the aluminum alloys inclines to localized corrosion due to the presence of intermetallic compounds.[4] The distinct phase inside the aluminum alloys and the alloying element Mg, Cu, *etc.*, form galvanic couples, which weakens the resistance of the alloy.[5]

Unlike 316L, the passive film of Aluminum alloys is less inert from a chemical and electrochemical point of view. In the same electrochemical system, the evolution of the coated sample is much faster than on 316L, so that the endurance of the coating system can be evaluated.

Aluminum alloy 2017-T4 is purchased from Goodfellow (the weight percentage: Cr 0.05%, Cu 4%, Fe 0.4%, Mg 0.5%, Mn 0.5%, Si 0.4%, Zn 0.2%, compensate by aluminum). The substrate was also cut into 50 x 25 x 3 mm^2 samples and grounded up to 1200 mesh. Samples were rinsed with distilled water, ethanol, and acetone, and no surface pretreatment was performed since Aluminum Alloy behaves good surface reactivity to Sol-Gel coatings.

II.2.3 Carbon steel

Carbon steel is the most frequently applied metallic material in the world.[6] The modifiable property and the low fabrication cost allow the carbon steel to be applied in construction, wire, marine field, and many other industrial domains.[7] However, they are prone to general corrosion even in atmosphere conditions, which increases the difficulty of maintenance and limits the lifetime of the products. [8]

To ensure a satisfying protection performance on carbon steel, the coatings are required to be dense or thick, when it is not dense enough, which presents good adhesion as well as strong barrier properties to limit the connection between the environment and the substrate. Moreover, the synthesis condition must be mild, for which acidic conditions or strong basic conditions should be avoided.

Carbon steel XC90 is purchased from Goodfellow (C 0.80 - 0.93 %, Mn 0.30 - 0.65%, Si 0.15 – 0.35, P 0.03 – 0.035 %, S 0.035 – 0.05 %, compensate by iron).The substrate was similarly cut into 50 x 25 x 3 mm^2 samples and grounded up to 1200 mesh, rinsed with ethanol and acetone before dipping. No pretreatment to the surface was performed since carbon steels are sensitive to the environment.

II.3 Preparation of Sol-Gel procedure

In order to isolate the role of BNNS, it requires the synthesis procedure to be designed attentively. In the following part, the selection of Sol-Gel materials as well as the synthesis procedure will be presented in three different categories: the single-component coating, the multi-component coating, and the organic-inorganic hybrid coating.

II.3.1 ZrO single-component coating on 316L

The first system is dedicated to observing the evolution of Sol-Gel coating on a metal substrate. The effect of the 2D nanofillers are expected to be primitively observed. Thus, a stable coating/ substrate interface is necessary to avoid the delamination. Within this context, the stainless steel 316L is selected as the substrate due to the presence of the stable passive film. The Zirconium Oxide has a similar thermal expansion rate to 316L, allowing the prospective study for future applications in the domain like medical implants, etc. [9]

The inorganic coating was prepared using Zirconium acetate hydroxide (Aldrich Chemistry) (ZrO) as a precursor. The Sol-Gel procedure for ZrO Sol is illustrated in Fig. II.3 - 1. The coatings prepared with this composition will be denoted ZrO in this work. We added 3mg zirconium acetate hydroxide in 50mL ethanol and 2.5 mL acetone. Using acetic acid, the pH of the solution was maintained at 3.2 to obtain low Zetapotential and a stable solution.[10] The ZrO Sol was mixed with pure water with the volume ratio of ZrO : water = 3 : 1 before the dip-coating process. For nanofiller charged samples, the 2D materials were directly exfoliated in water.

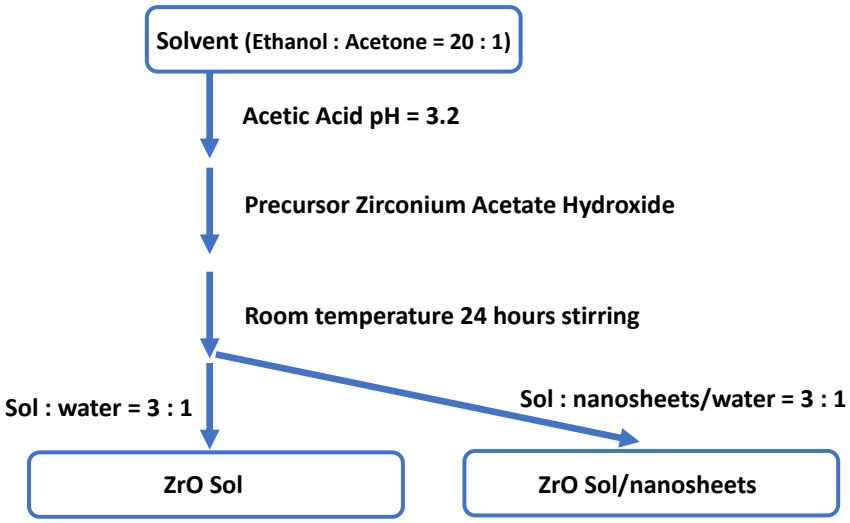

Fig. II.3 - 1 Scheme of preparation procedure for ZrO Sol

II.3.2 ZrO-SiO multi-component coating on Aluminum alloy

To accelerate the electrochemical reaction, we attempted to transfer the coating to a more active metal AA2017, which is more sensitive in NaCl solution than 316L. A multi-component Sol-Gel coating based on ZrO-SiO was used instead of the ZrO single-component coating system to reduce the coating porosity.

Zirconium n-butoxide (ZrBTO, 80% w/w in 1-Butanol, Sigma-Aldrich) was selected as the Zirconium resource. At first, ZrBTO was dissolved into pure isopropanol (2-propanol for

analysis). To reduce the reactivity of ZrBTO, a chelating agent acetylacetone (AcAc, ⩾ 99.5%, Sigma-Aldrich) was introduced immediately and stirred until a homogenous solution was obtained. The chelation reaction between ZrBTO and AcAc is shown in Fig. II.3 - 2. Then (3-glycidyloxypropyl)trimenthoxysilane (GPTMS, ≥98%, Sigma-Aldrich) was added to this mixture at 60°C. We slowly introduced water to initialize the hydrolysis reaction. With Nitric Acid (1 mol/L), the solution pH was tuned to pH = 4. The scheme of preparation procedure for ZrO-SiO Sol is shown in Fig. II.3 - 3.

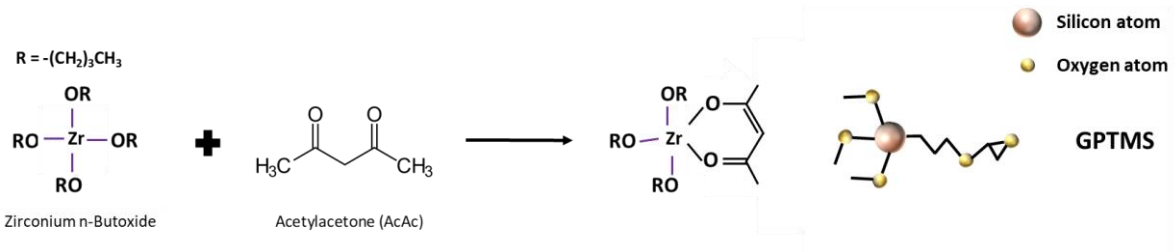

Fig. II.3 - 2 Scheme of the AcAc blocking active sites on Zirconium n-Butoxide and the precursors of ZrO-SiO

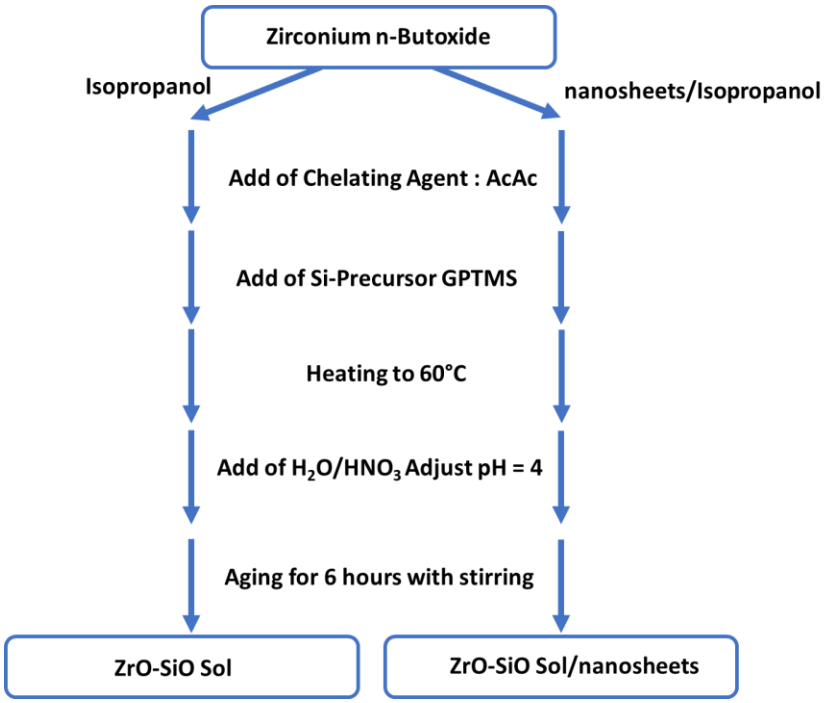

Fig. II.3 - 3 Scheme of preparation procedure for ZrO-SiO Sol

Quantitatively, we fixed the overall concentration of the organometallic precursors (Zr and Si) to 1M and kept the molar ratio to n(*Zr*):n(*Si*) = 1 : 2. The molar ratio of the chelating agent on ZrBTO, n(*AcAc*): n(*ZrBTO*) denoted *R* is fixed at 3 : 1, which is a crucial parameter for solution stability and can influence the coating's microstructure, as schemed in Fig. II.3 - 2. Besides, the hydrolysis ratio n(H_2O): n(M^{z+}) has been fixed to 4 : 1, where *M* substitutes Zr or Si, *z* substitutes the Stoichiometry number of Zr or Si.

II.3.3 Organic-Inorganic hybrid coating on Carbon steel

For the purpose of further increasing the coating barrier effect, we doped alkyl groups (-C18) to modify the coating's polarity. The scheme of preparation procedure for ZrO-SiO/C18 Sol is shown in Fig. II.3 - 4. Unlike the preparation method of ZrO-SiO multicomponent Sol, n-Butanol replaced isopropanol to slow down the reaction velocity, see Chapter I – I.3.3. The molar ratio between n(*Zr*) : n(*Si*) was maintained at 1 : 2, while the molar ratio between GPTMS and ODTES (Octadecyltriethoxysilane, 98%, n-isomer 85% min, Alfa Aesar) was maintained as 1 : 3. The ODTES was added drop by drop to the mixture. The formation of the Micelles was observed at room temperature after the ODTES addition. Heated to 60°C, the Sol became transparent. Therefore, the dip-coating process was also performed at 60°C. The pH of the Sol was maintained with ammonium hydroxide to pH = 9.

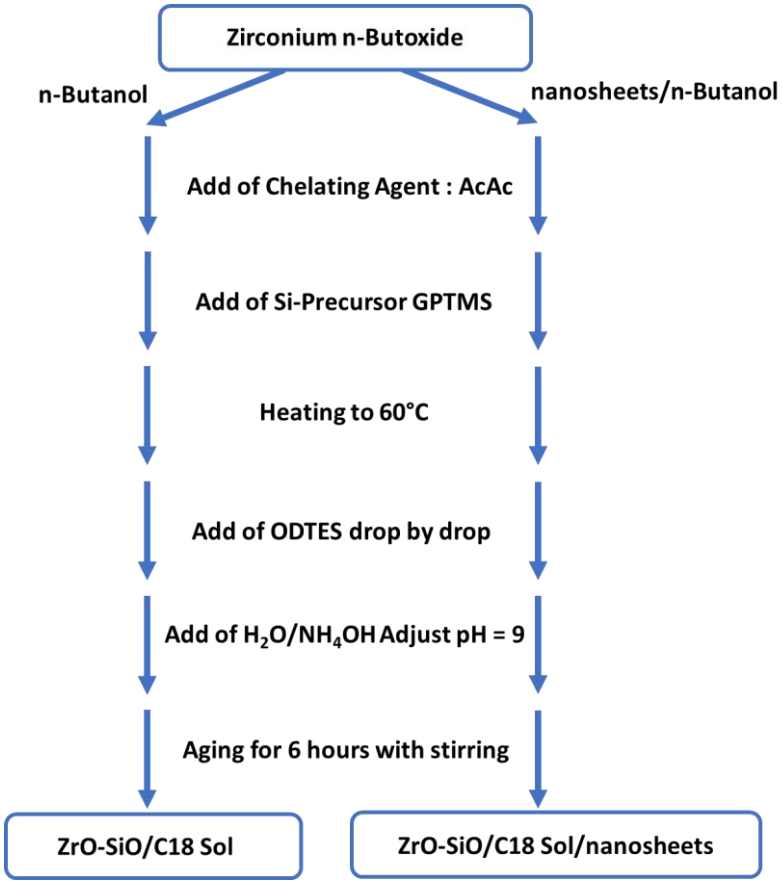

Fig. II.3 - 4 Scheme of preparation procedure for ZrO-SiO/C18 Sol

II.4. Protocols of dip-coating

Fig. II.4 - 1 shows the dipping machine with a homemade heat container connected with a thermostat. The dipping machine is Xdip-SV1 from Apex Instruments. The dipping parameters are listed in Table. 2 - 1.

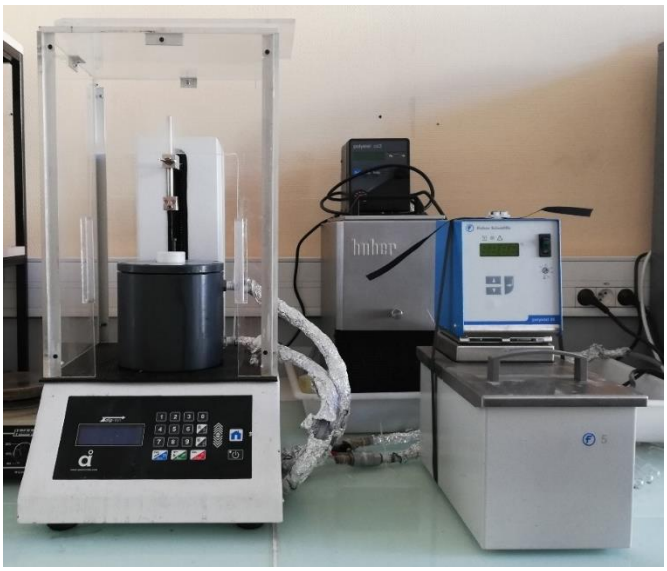

Fig. II.4 - 1 Dip-coating machine connected with heat container and heat generator

Table. 2 - 1 Dipping parameters of the Sol-Gel coatings

Sol	Sub	Dipping temp[1]	Immerse time	Pulling speed	Number of dips	Drying[2] duration/temp	Curing[3] duration/temp
ZrO	SS[4]	RT[5]	10 min	0.5 mm/s	3	10min/RT	24h/120°C
ZrO-SiO	AA[6]	60°C	1 min	30 mm/s	3	10min/150°C	24h/150°C
ZrO-SiO/C18	CS[7]	60°C	1 min	30 mm/s	3	10min/150°C	24h/150°C

[1]Temp: temperature
[2]Drying: the duration between each dipping process.
[3]Curing: the heat treatment for the evolution of the Sol-Gel matrix in oven.
[4]SS: Stainless steel AISI316L
[5]RT: Room temperature
[6]AA: Aluminum Alloy 2017
[7]CS: Carbon Steel XC90

II.5. The exfoliation of 2D materials

In order to adapt to the Sol-Gel synthesis condition, the classic liquid-phase exfoliation method was performed in this work. The solvents are selected according to the Sol-Gel procedure. Fig. II.5 - 1 shows the ultrasonic machine (FB11201, capacity 2.75L, Voltage 115V) with a homemade cooling system.

The raw materials were put in the solvent and directly exfoliated in the ultrasonic bath and then centrifuged with corresponding parameters. Particularly, for graphene, the graphite was preliminerly expended using electrochemical way. The expanded graphite was treated in the ultrasonic bath to obtained the few-layered nanosheet (GENS). The electrochemical method for expanded graphite is introduced in the appendix.

The exfoliation parameter as well as the appellation are listed in Table. 2 - 2.

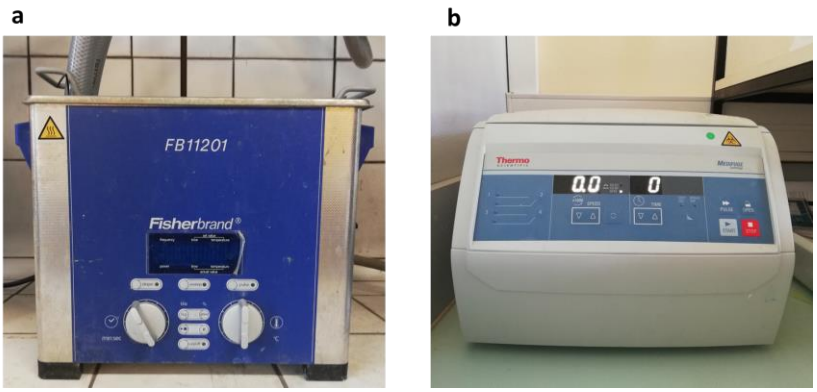

Fig. II.5 - 1 Image of a) Ultrasonic machine for exfoliation b) Centrifuge machine

Table. 2 - 2 All parameters of materials, exfoliation, centrifuge, Sol-Gel substrate and Sample Names

2D materials	Solvant	Exfoliation*[1]	Centrifuge*[2]	Sol-Gel	Substrate	Sample Name
Reference samples				ZrO	316L	ZrO_Ref
				ZrO-SiO	AA2017	ZrO-SiO_Ref
				ZrO-SiO/C18	CS XC 90	ZrO-SiO/C18_Ref
BN-A	water	60	90/1500	ZrO	316L	ZrO_BNA
BN-B	water	60	90/1500	ZrO	316L	ZrO_BNB
BN-C	water	60	90/1500	ZrO	316L	ZrO_BNC
BN-C	water	60	40/2000	ZrO	316L	ZrO_BN60
BN-C	water	60	30/2000	ZrO	316L	ZrO_BN90
BN-C	water	60	20/2000	ZrO	316L	ZrO_BN130
BN-C	water	60	10/2000	ZrO	316L	ZrO_BN170
BN-C	water	60	10/2000	ZrO	AA2017	AA/ZrO_BN
BN-C	Isopropanol	60	10/2000	ZrO-SiO	AA2017	ZrO-SiO_BN
BN-C	*n*-Butanol	60	10/2000	ZrO-SiO/C18	CS XC 90	ZrO-SiO/C18_BN
GE	water	60	10/2000	ZRO	316L	ZrO_GE
GE	*n*-Butanol	60	10/2000	ZrO-SiO/C18	CS XC 90	ZrO-SiO_GE
MoS_2	water	60	10/2000	ZRO	316L	ZrO_MoS_2
MoS_2	*n*-Butanol	60	10/2000	ZrO-SiO/C18	CS XC 90	ZrO-SiO/C18_MoS_2

**1: The exfoliation time with unit of hours*

**2: The Centrifuge time/velocity with unit of min/rad.s^{-1}*

II.6 Electrochemical characterization techniques

The electrochemical techniques allow us to quantitatively explore the relationship between electrode and its behavior under open-circuit conditions or applied potential (like a linearly increased or sinusoidal potential).

The electrochemical cell used for this work is a classical three-electrode system as illustrated in Fig. II.6 - 1. The Working Electrode (WE) is the sample for the electrochemical test. The Reference Electrode (RE) is characterized by its potential *vs.* Standard Hydrogen Electrode (SHE). The RE used in this work is the Saturated Calomel Electrode (SCE) with a standard potential of +0.244 V *vs.* SHE, as indicated in Figure Fig. II.6 - 2. Meanwhile, the auxiliary electrode, often called the counter electrode (CE), connects the working electrode, the Alternating current (AC) or Direct Current (DC) potential source, and the electrolyte to establish a connected electrical circuit. It consists of inert and electronic conductive materials like graphite that we used in this study.

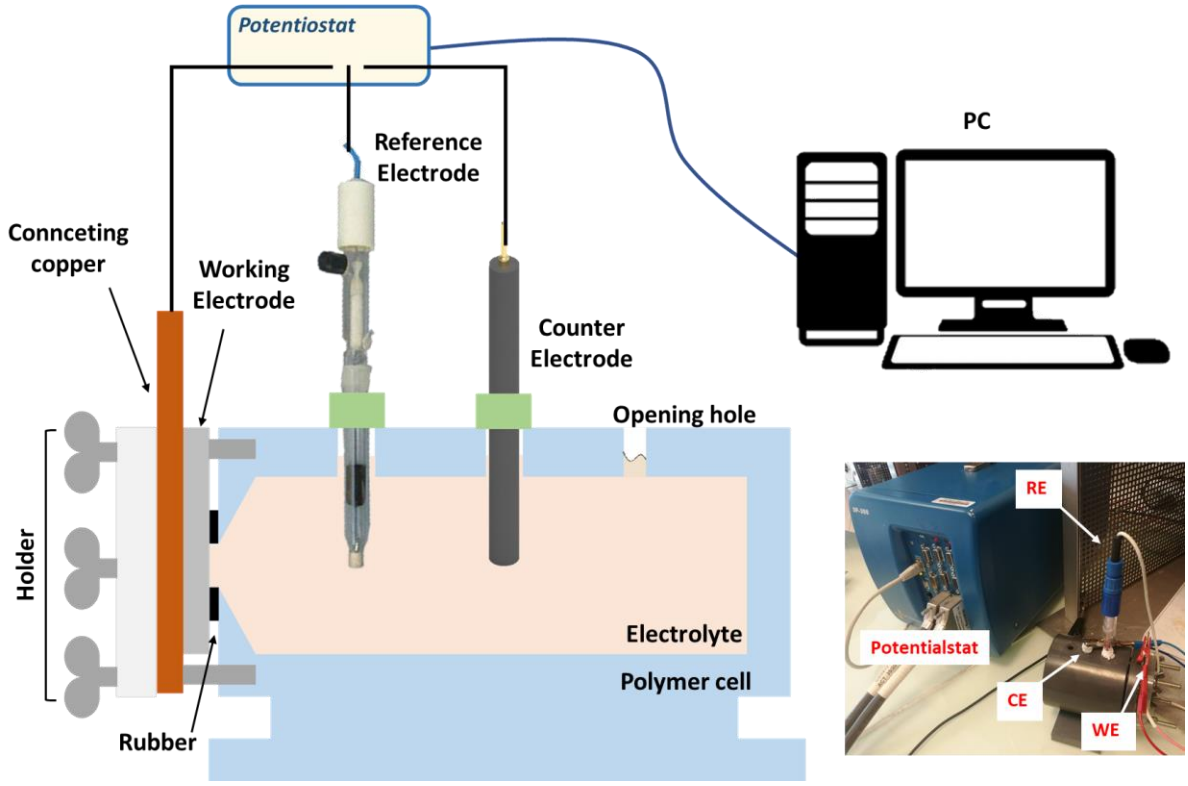

Fig. II.6 - 1 Scheme and image of the electrochemical cell

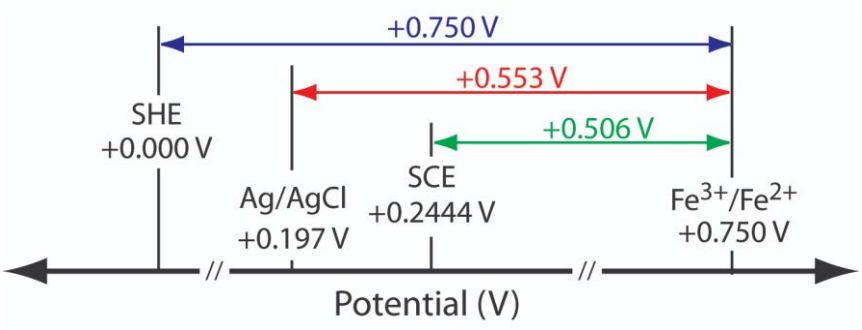

Fig. II.6 - 2 Scheme of potential difference between different reference electrodes[11]

II.6.1 Open circuit potential

The Open Circuit Potential (OCP) is the potential when a metal is immersed in the electrolyte in a natural state. OCP is often used to find the corrosion potential of a system.

II.6.2 Electrochemical Dynamic Polarization

When the immersed metal is submitted to linear potential, reactive steps can soon be observed. At corrosion potential, the anode and the cathode current densities are equal. This current density is called i_{corr} , which is the current observed from both the anode side and the cathode side, which can be calculated by the Bulter-Volmer kinetic law in **Eq. 2 - 1**: [12]

$$i_{total} = i_{corr}[exp\left(\frac{\alpha nF}{RT}\eta\right) - exp\left(\frac{-(1-\alpha)nF}{RT}\eta\right)] \qquad \textit{Eq. 2 - 1}$$

In which the i_{total} is the total current density, α is the transfer coefficient, η is the overpotential between the applied potential and corrosion potential (OCP in most of the case), ***F*** is the faraday constant, ***R*** is the gas constant and ***T*** is the temperature.

Parameters of Polarization

The dynamic polarization was acquired by linear scanning voltammetry (LSV) from Gamry Ref600 potentiostat after 24 hours of immersion in NaCl 30g/mL solution. The scanning potential range was fixed from -50 mV *vs.* OCP until 1000 mV *vs.* SCE, scanning rate 0.167mV/min.

II.6.3 Electrochemical Impedance Spectroscopy

The electrochemical impedance is the impeding phenomenon when an AC current is applied. An electrochemical impedance can be described by a complex number depending on the phase of the sinusoidal signals. The electrochemical impedance is given by:[13]

$$Z(\omega) = \frac{V(\omega)}{i(\omega)} \qquad \textit{Eq. 2 - 2}$$

As a complex number, it could be decomposed into a real part and an imaginary part as shown in:

$$Z(\omega) = Re(\omega) + jIm(\omega) \qquad \textit{Eq. 2 - 3}$$

where *Re* is the magnitude of the real part of impedance, the *Im* is the magnitude of the imaginary part of Impedance and *j* is the imaginary unit. If we plot the *Re* value and *Im* value as x-axis and y-axis respectively, the Nyquist curve is got as shown in Fig. II.6 - 3. From the Nyquist curve, the impedance magnitude of the point(R_0, I_0) is shown as $|Z|$. The slope angle between the imaginary magnitude $|I_0|$ and R_0 is the phase angle, noted φ. As it is shown from Nyquist curve, every point has an impedance value from one specific frequency. If we plot the impedance magnitude $|Z|$ and phase angle φ as a function of the frequency, the Bode curves are obtained as shown in Fig. II.6 - 4 a and b respectively.

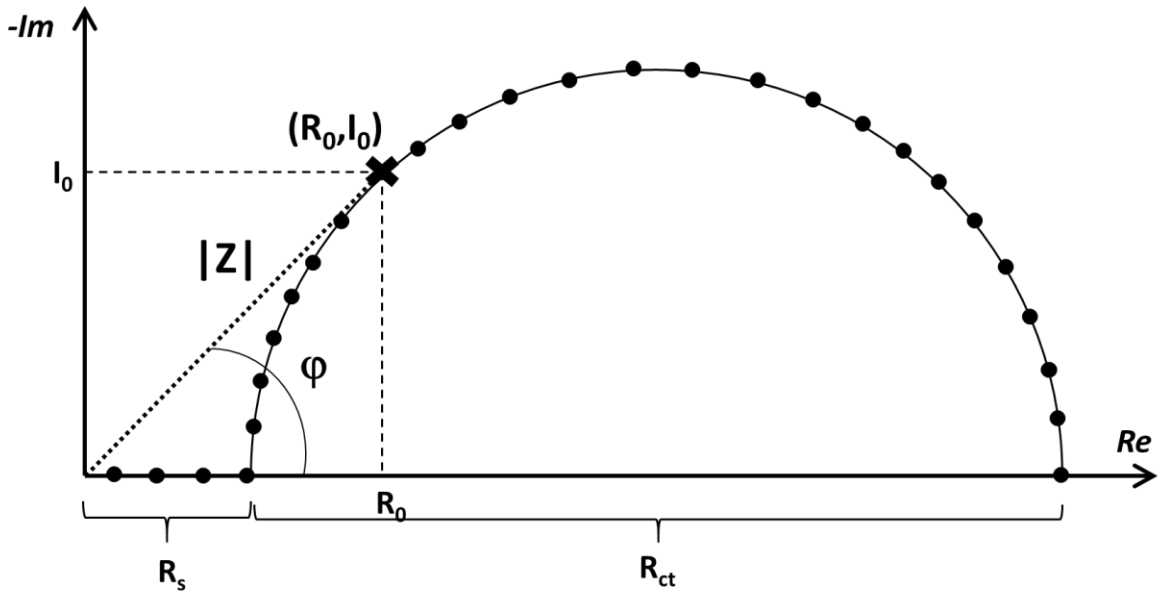

Fig. II.6 - 3 Nyquist curve from Electrochemical Impedance Spectroscopy

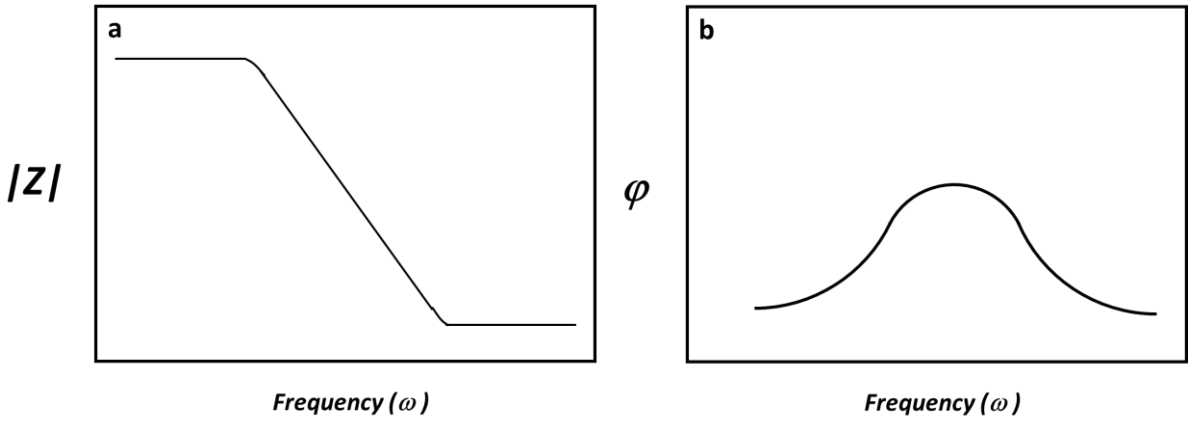

Fig. II.6 - 4 Bode curves a) Magnitude of Impedance b) phase angle

Equivalent circuit and numerical fittings

EIS gives the global impedance response of the electrochemical system. If these responses correspond to the validated physical and chemical phenomenon, the EIS can be fitted by an equivalent electric circuit (EEC) proposed by Randles using numerical tools.[12] Randles assumed that the electrochemical system working electrode is composed of resistors and capacitors. Later reports have proposed Constant Phase Element (CPE) to describe the imperfect capacitors.

Fig. II.6 - 5a shows the simplest Randles model for metals. In this model, the R_s is the resistance from the electrolyte of the immersed system, and R_{ct} is the resistance from the charge transfer reaction on the metal surface. The two resistance parameters are shown in the Nyquist curve in Fig. II.6 - 3. C_{dl} is the double layer resistance at the metal surface caused by the charged transfer procedure. Many reports show that the C_{dl} is not always accurate since the surfaces are not homogeneous. [14] Thus Constant Phase Element (CPE, Q_{dl}) is proposed to introduce a coefficient α associated with the morphological variation and describe the imperfect state of

C_{dl}. The CPE modified model is shown in Fig. II.6 - 5b. When the α value equals 1, it represents a pure capacitive behavior. On the contrary, when the α value equals to 0, it describes a pure resistive behavior.

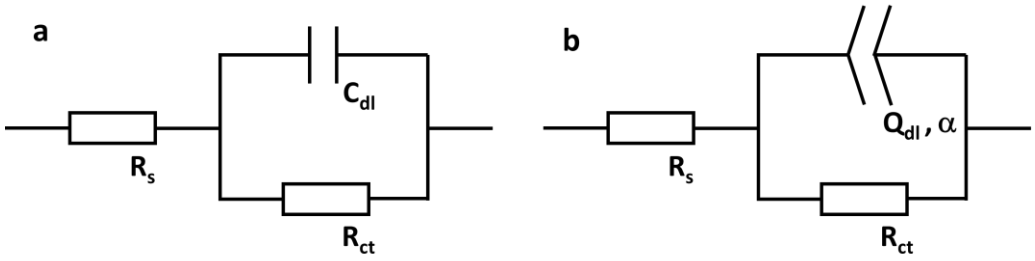

Fig. II.6 - 5 Electrochemical Equivalent Circuit of a) Randles model b) CPE modified Randles model

When coatings are deposited on the metals, supplementary *R/C* or *R/Q* couples should be considered in the EEC. These couples are introduced due to the impedance introduced by the coatings or other surface modifications.[15]

The impedance of the CPE is given by the formula: [16]

$$Z_{CPE} = \frac{1}{Q(j\omega)^{\alpha}} \qquad \textbf{Eq. 2 - 4}$$

The Q value is attributed to the surface current density distribution. The Q value can be evaluated by: [17]

$$Q = |\sin(\frac{\pi}{2} \cdot \alpha) \cdot \frac{(-1)}{Z \cdot \left(2\pi f(t)\right)^{\alpha}}| \qquad \textbf{Eq. 2 - 5}$$

Parameters used for EIS tests

The EIS tests were carried out in this work using Gamry Ref600 potentiostat. The frequency varied from 100 kHz to 3 mHz, while the amplitude of the scanning potential was fixed at 15 mV *vs.* OCP.

[1] H. Bursen, B. Trela, in Winemaking Problems Solved, 2010
[2] Comparison of structural design in stainless steel and carbon steel. British Stainless Steel Association.
[3] Ibrahim, M. A. M.; Abd El Rehim, S. S.; Hamza, M. M. Corrosion Behavior of Some Austenitic Stainless Steels in Chloride Environments. Materials Chemistry and Physics 2009, 115 (1), 80–85.
[4] Davis, J. R. (1999). Corrosion of aluminum and aluminum alloys, Materials Park, OH : ASM International.
[5] Michel Colombié. Didier Albert.; Roger Baltus.; Matériaux métalliques propriétés, mise en forme et applications industrielles des métaux etalliages. 2è édition. DUNOD.
[6] S. Winnik, in Corrosion Under Insulation (CUI) Guidelines, 2008
[7] P. Zarras, J.D. Stenger-Smith, in Handbook of Smart Coatings for Materials Protection, 2014
[8] Faisal Mutahhar, Kenneth P. Roberts, in Trends in Oil and Gas Corrosion Research and Technologies, 2017
[9] Harianawala, H.; Kheur, M.; Kheur, S.; Sethi, T.; Bal, A.; Burhanpurwala, M.; Sayed, F. BIOCOMPATIBILITY OF ZIRCONIA. Journal of Advanced Medical and Dental Sciences Research 2016, 4 (3), 5.
[10] Nouri, E.; Shahmiri, M.; Rezaie, H. R.; Talayian, F. A Comparative Study of Heat Treatment Temperature Influence on the Thickness of Zirconia Sol–Gel Thin Films by Three Different Techniques: SWE, SEM and AFM. Surface and Coatings Technology 2012, 206 (19–20), 3809–3815.
[11] David Harvey. Reference Electrodes. Image and Video Exchange Forum.
[12] Durán, A.; Castro, Y.; Conde, A.; de Damborenea, J. J. Sol–Gel Protective Coatings for Metals. In Handbook of Sol-Gel Science and Technology; Klein, L., Aparicio, M., Jitianu, A., Eds.; Springer International Publishing: Cham, 2016; pp 1–65.
[13] Gamry. Basics of EIS: Electrochemical Research-Impedance. 2017.
[14] Shoar Abouzari, M. R.; Berkemeier, F.; Schmitz, G.; Wilmer, D. On the Physical Interpretation of Constant Phase Elements. Solid State Ionics 2009, 180 (14–16), 922–927.
[15] Mark E. Orazem, Bernard Tribollet. Electrochemical Impedance Spectroscopy. Wiley. 2011
[16] Jorcin, J.-B.; Orazem, M. E.; Pébère, N.; Tribollet, B. CPE Analysis by Local Electrochemical Impedance Spectroscopy. Electrochimica Acta 2006, 51 (8), 1473–1479.
[17] Hirschorn, B.; Orazem, M. E.; Tribollet, B.; Vivier, V.; Frateur, I.; Musiani, M. Determination of Effective Capacitance and Film Thickness from Constant-Phase-Element Parameters. Electrochimica Acta 2010, 55 (21), 6218–6227.

Chapter III. Elaboration of coating and Characterization

III.1 Introduction

As discussed in the above chapter, this work has been separated into three Sol-Gel coated metal systems. Thus, the characterization in this chapter is based on the three coating systems.

For each coated system, the Sol-Gel solution was evaluated with Dynamic Light Scattering Spectroscopy (DLS) to understand the colloidal size as well as the stability within three days. Then, the h-BN exfoliated solution was characterized by TEM to observe the morphology of the nanosheets. The BNNS concentrations for three different raw h-BN were estimated by UV-Visible spectroscopy. Finally, the surface morphology and water contact angle of as-deposited coatings were discussed. Raman spectroscopy and IR spectra were employed to characterize the existence of 2D nanofillers.

III.2 Characterization of raw materials

III.2.1 Characterization of 2D powders

Raw h-BN: The morphology and size distribution of BN-A, BN-B, and BN-C powders and the statistic analysis are shown in Fig. III.2 - 1. It is observed that BN-A has an average lateral size of 4.5 μm. The BN-B shows a size peaked at 1 μm, while BN-C has a size peaked at 7 μm. Lin et al. reported that with controlled exfoliation and centrifuge procedure, the dimension and shape of 2D nanosheets could be tuned.[1] In this work, since the applied exfoliation method was mild in an ultrasonic bath with a one-time centrifuge, the morphology of final exfoliated nanosheets mainly depends on its raw powder morphology. Furthermore, the lateral size of the nanofiller influences the anticorrosion behaviors of sol-gel coatings.[2]

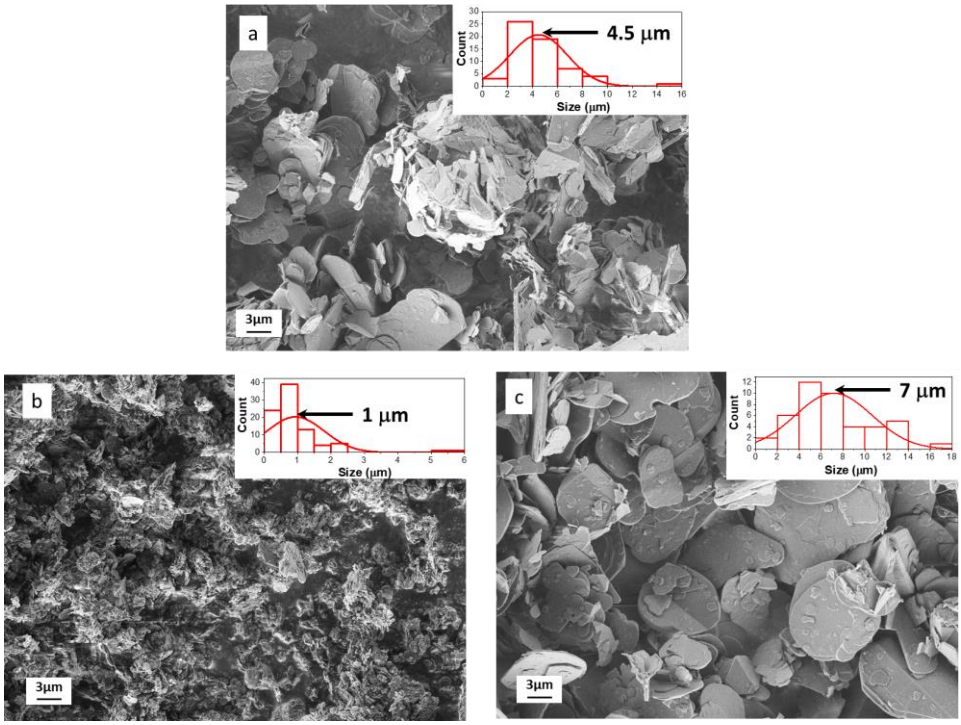

Fig. III.2 - 1 Morphology of raw BN powders of a) BN-A b) BN-B, and c) BN-C

The photo of as-purchased graphite foil and the SEM image of expanded graphite (GE) synthesized with the method proposed by Dhakate et al. are shown in Fig. III.2 - 3a and b,

respectively.[3] After the electrochemical treatment in Na_2SO_4 solution, the expended graphite was obtained, showing cleavage at the crystalline edge due to the ions and gas penetration on the anodic side in the electrochemical cell. The layered structure is clearly shown in Fig. III.2 - 3b. This process is accompanied by a moderate carbon oxidation at the edge and in the atomic plan. The oxygen content of the GE is measured by EDS to be 9 *at*%. Therefore instead of pristine graphene, we have prepared the oxide graphene for the reason that the electrical conductivity is significantly reduced.[4] The so-prepared GE can be easily dispersed in aqueous media with a relatively high concentration than pristine graphene that is insoluble.

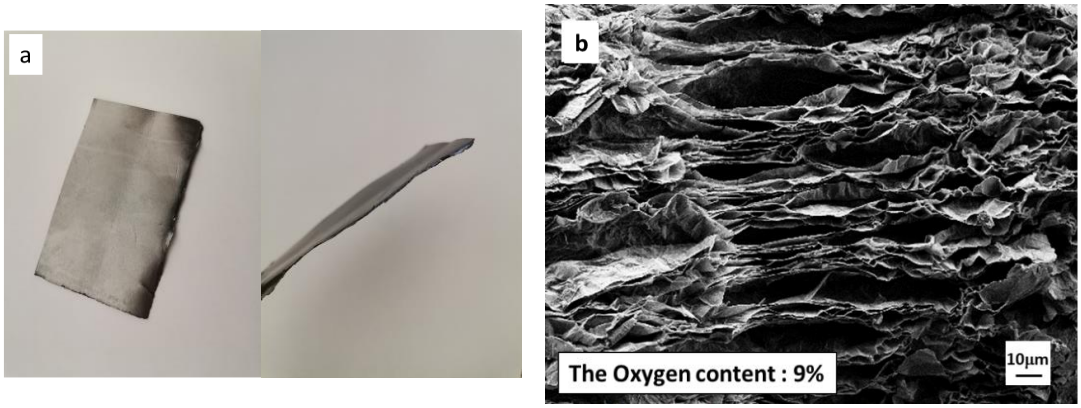

Fig. III.2 - 2 a) The photo of Graphite foil before electrochemical expanding b) and after

The MoS_2 powder employed in this work is shown in Fig. III.2 - 3b. The particle size of MoS_2 is around 1- 2 µm in diameter for the lateral size.

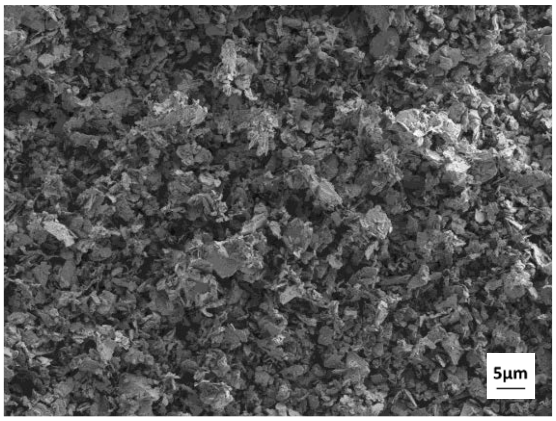

Fig. III.2 - 3 Morphology of MoS_2 by SEM

III.2.2 Characterization of metal substrates

The photos and SEM images of polished substrates are shown in Fig. III.2 - 4. After polishing, the surfaces of all bare substrates show continuous polish traces. The different hardness of the metals leads to rather different roughness.

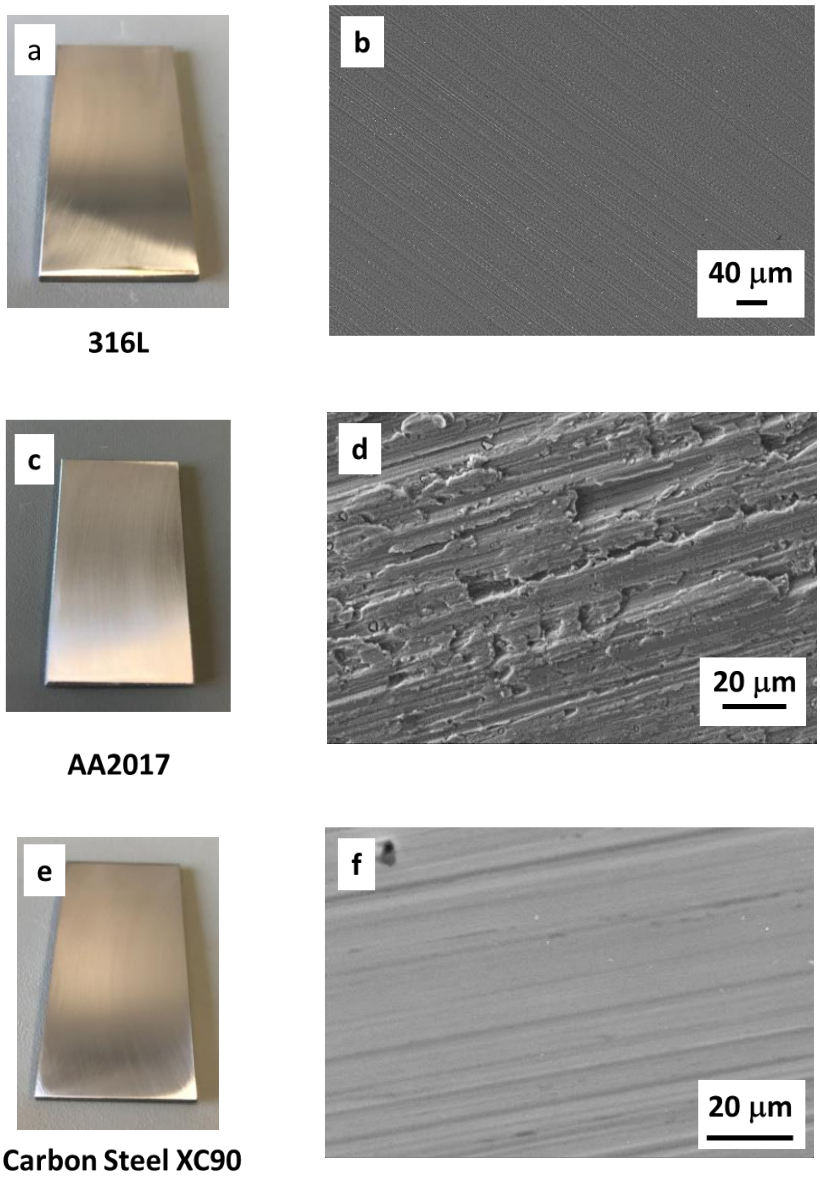

Fig. III.2 - 4 Photos and SEM images of as-polished metal substates of a) and b) 316L, c) and d) AA2017, e) and f) carbon Steel XC90 bare substrates

III.3 Characterization of the Sol-Gel systems

III.3.1 Characterization of BNNS charged ZrO coatings on 316L

Characterization of ZrO single-component Sol-Gel solution

The BNNS was firstly studied and charged into ZrO coatings to probe its behavior in an inert system. The influence on the barrier effect of the Sol-Gel coatings of morphology as well as the concentration of BNNS were studied and discussed in sequence.

The photo of ZrO Sol is shown in Fig. III.3 - 1a. The Sol-Gel solution is transparent with a light white color. The as-exfoliated solution was prepared with a low concentration of BN-A, BN-B, and BN-C, cf. chapter II – II. 5, are shown in Fig. III.3 - 1b, where no apparent sediment can be observed. The colloidal solutions prepared with a high concentration named BNC_Sol60, BNC_Sol90, BNC_Sol130, and BNC_Sol170 are shown in Fig. III.3 - 1c. The BNC_Sol90,

BNC_Sol130, and BNC_Sol170 are not more transparent. Fig. III.3 - 1d showed the solution of ZrO Sol mixed with BNNS/water solution with a ratio of 3 : 1. To disaggregate and to ensure a good homogeneity, a 10 min ultrasonic post-treatment was systematically performed.

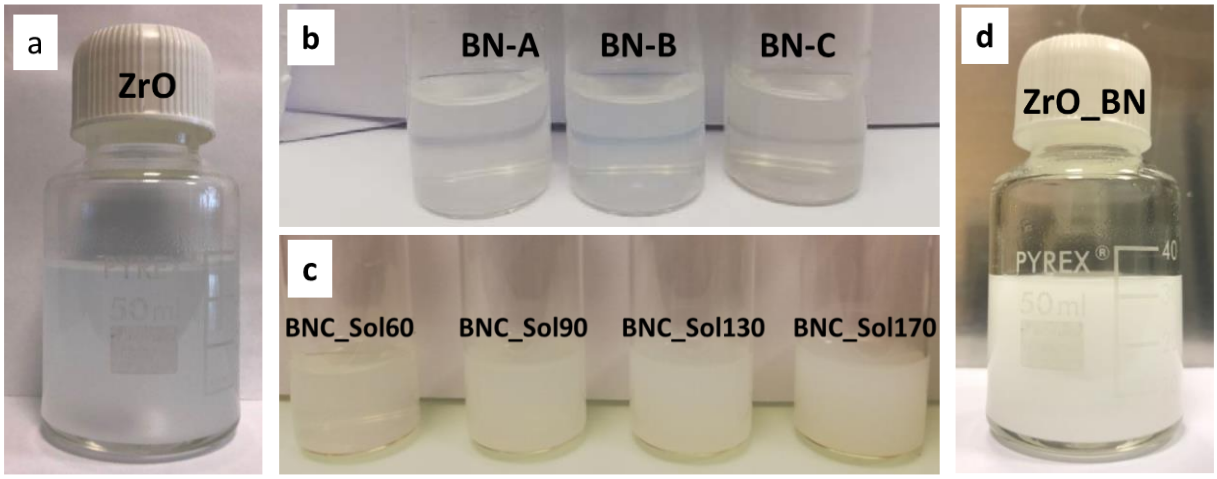

Fig. III.3 - 1 Photo of a) ZrO Sol-Gel solution, b) BN-A, BN-B, and BN-C as exfoliated water solution with low concentration preparation method and c) BNC_Sol60, BNC_Sol90, BNC_Sol130 and BNC_Sol170 as-exfoliated water solution with high concentration preparation method d) the mixed ZrO and BNNS/water solution with ratio 3: 1

The DLS curves obtained with the water injected ZrO sol after stewing for one day, two days, and three days are plotted in Fig. III.3 - 2. It is observed two particle sizes peaked at around 7 nm and 50 nm, respectively. The small one characterized the single colloid size, while the one at 50 nm indicates the agglomeration occurring. The distribution of colloidal size remains stable over three days, and even less agglomeration can be observed at the end. It should be noted that the matrix of zirconium oxide coating will not have a significant influence on the coating anticorrosion behavior. [5]

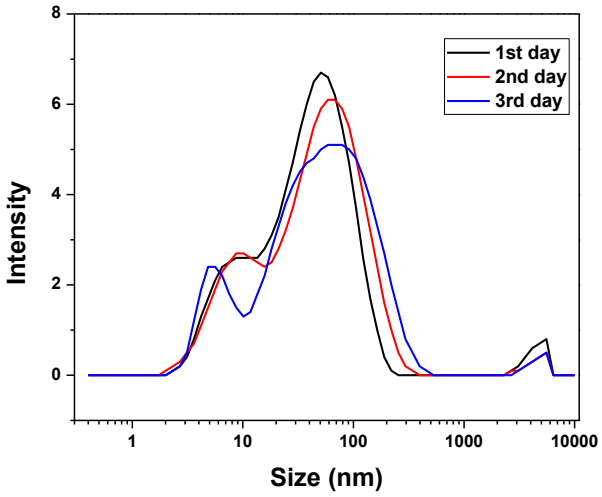

Fig. III.3 - 2 The DLS spectroscopy of three days evolution of ZrO Sol-Gel solution

The zone of cracks shown in Fig. III.3 - 3a to 3c, for ZrO_Ref and ZrO_MoS_2 and ZrO_BN, respectively, depict that the ZrO single-component coating is having a thickness less than 300 nm. Large particles of 2D fillers can be observed.

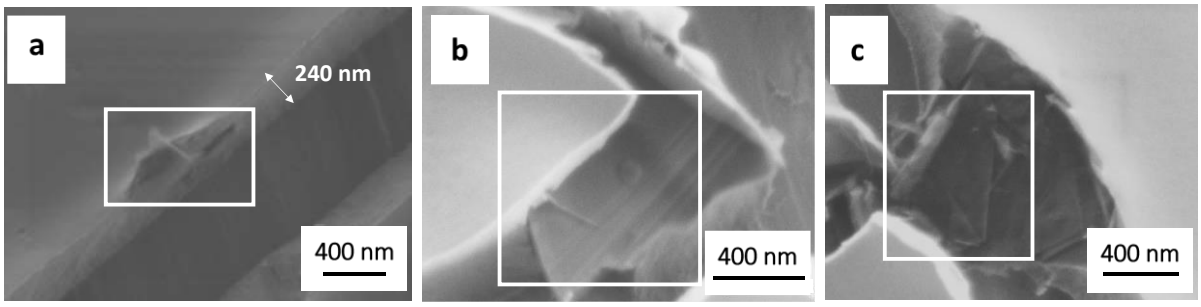

Fig. III.3 - 3 Zone of cracks of a) ZrO single-component coating with BNNS fillers (shown in rectangles)

Characterization of as-exfoliated solution of three different BNNS aqueous solution

The state of h-BN flakes was probed by TEM step-by-step during the exfoliation. Fig. III.3 - 4a shows the TEM images corresponding to a thin single-crystallite of h-BN. The selective area electron diffraction (SAED) pattern exhibits bright hexagonal dots (inset), which are representative of single h-BN crystals. The Moire patterns in Fig. III.3 - 4b indicate misorientation between h-BN layers induced by the exfoliation process around the *c-axis*. In the final colloidal solution, the BNNS has a two-dimensional structure with a thickness of a few atomic layers approaching to that of the graphene, as shown in Fig. III.3 - 4c.

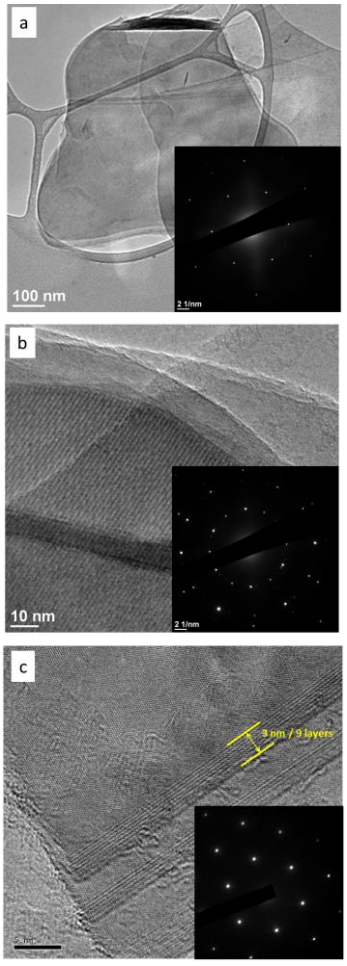

Fig. III.3 - 4 the TEM image for different exfoliation states: a) single crystal, b) misorientation induced by the exfoliation treatment, and c) few-layered BNNS. The inset is the corresponding selected area electron diffraction.

Fig. III.3 - 5 shows the UV-Visible curves of three different BNNSs exfoliated solutions. The band at around 208 - 210 nm is the characteristic peak h-BN for its E_{2g} mode.[6] As mentioned in Chapter II, the extinction coefficient has been calculated by weighting and UV-measurement at 300 nm in order to decrease the influence of diffraction, giving 2924 mg/ml/m. This calculated value is coherent with the value reported by other authors.[7] By applying the Beer-Lambert law, the concentrations of different BNNS were estimated to be 15 µg/mL that is in good agreement with the reported value.[8] Table. 3 - 1 lists the concentrations for BN-A, BN-B, and BN-C without a remarkable difference in concentrations.

However, the Zeta Potential of the colloidal solution of BNNS is different (see Table. 3 - 1). Among them, BN-A shows the lowest value of -30.1 mV, meaning the best stability. Between BN-B and BN-C, the BNNS solution with the bigger size showed a higher stability than the smaller ones.

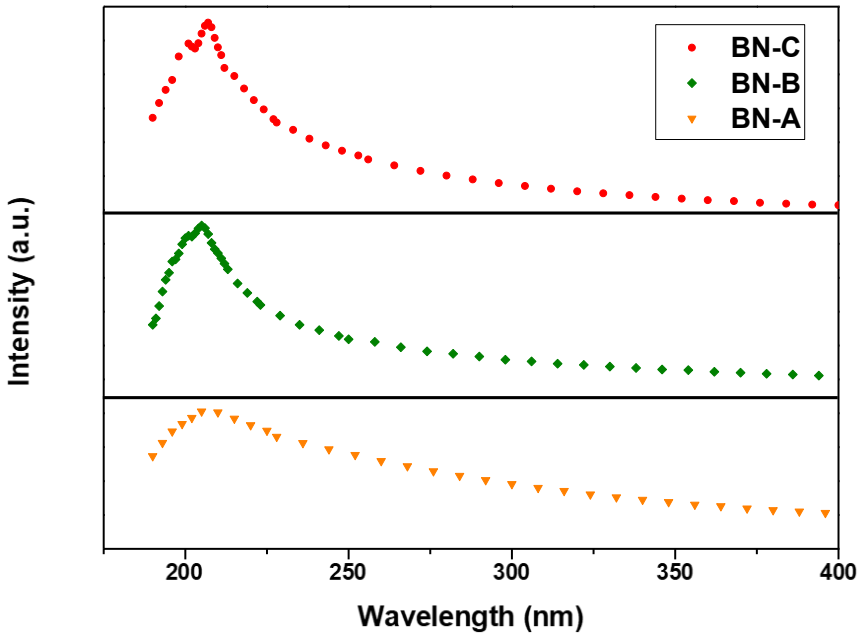

Fig. III.3 - 5 The UV-Vis spectroscopy of BN-A, BN-B, BN-C as-exfoliated solution

Table. 3 - 1 Zeta potential and concentration of as-exfoliated solution from BN-A, BN-B and BN-C

Samples	Zeta Potential (mV)	Concentration (µg/mL)
BN-A	-30.1	15
BN-B	-24.2	15
BN-C	-27.7	15

Characterization of ZrO coatings charged with three different BNNS

The SEM image of surface morphology and photos of contact angle of ZrO_Ref and ZrO_BNA, ZrO_BNB, and ZrO_BNC are shown in Fig. III.3 - 6. The preparation parameters were

introduced in detail in Chapter II. All the coated samples are homogeneous and defect-free. The polish traces on the substrate surface are recovered.

ZrO_Ref shows a static water contact angle of 67°, which means a hydrophile surface due to the content of the polar organic groups in the xerogel coating. It is surprising to observe a significant difference in contact angles among the ZrO_BNA, ZrO_BNB, and ZrO_BNC samples. This result is reproducible, where the difference is most likely due to the different BNNS fillers.

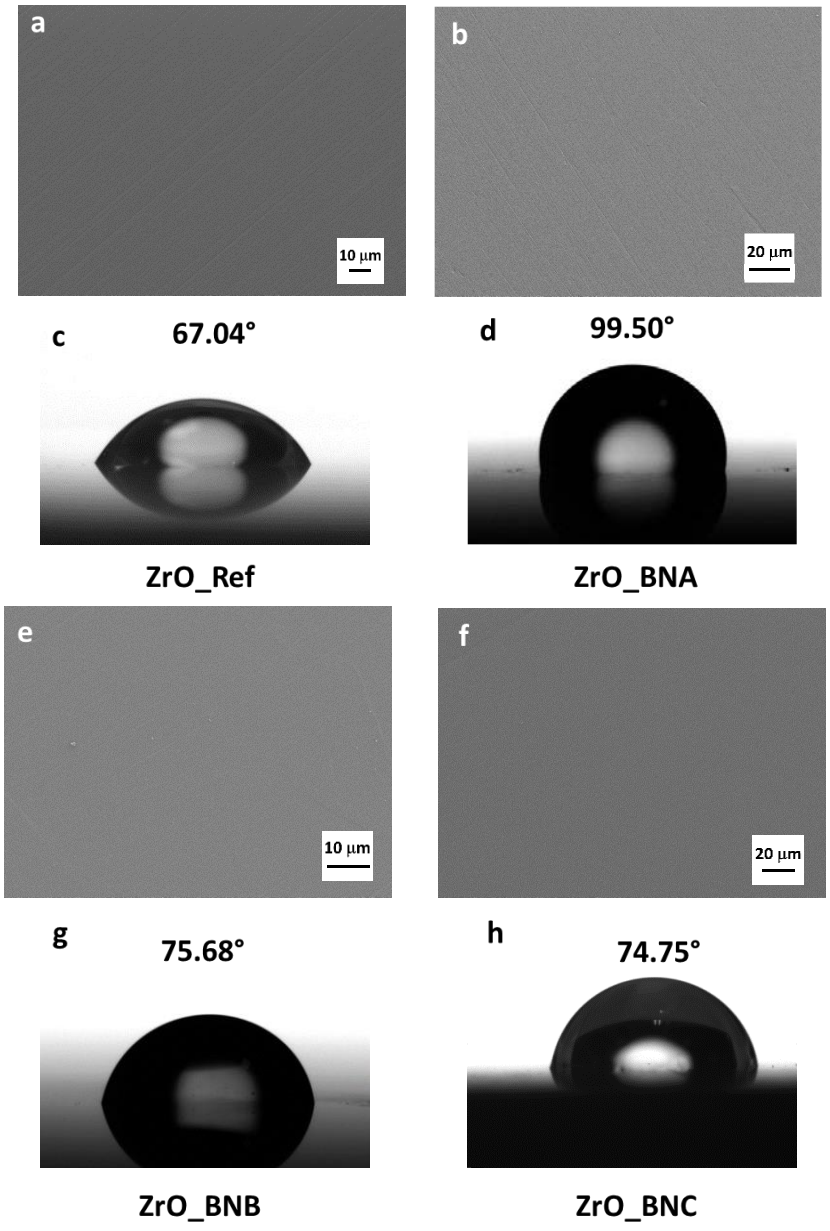

Fig. III.3 - 6 SEM Image and water contact angle of a) and c) ZrO_Ref, b) and d) ZrO_BNA, e) and g) ZrO_BNB and f) and h) ZrO_BNC

The FTIR/ATR is used to verify the composition of the as-deposited BNNS charged ZrO coatings. From the FTIR/ATR curve shown in Fig. III.3 - 7, all three coatings with BNNS filler showed a peak at 1350 cm^{-1}, which is related to shifted B-N stretching. This is not observed on the ZAH_Ref.[9] This phenomenon proves the existence of BNNS inside the charged coatings. We can observe from all the spectra that signals at wavenumber of 1570 cm^{-1} (the spherical mark)

and 1440 cm^{-1} (the triangle mark) are attributed to the acetate (-CO_2 groups) anti-symmetrical and symmetrical stretching vibration.[10,11]

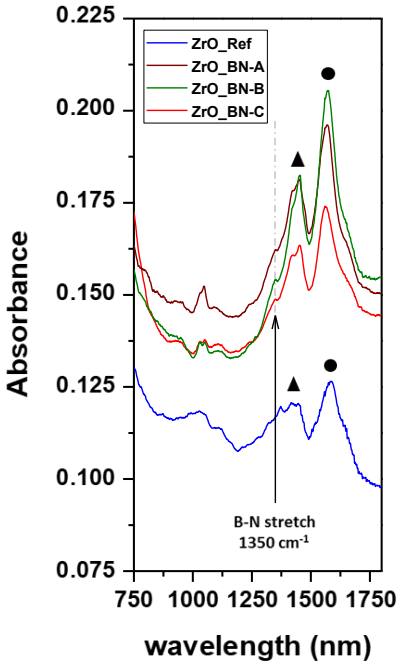

Fig. III.3 - 7 The FTIR/ATR spectroscopy of ZrO deposited coatings with or without three BNNSs fillers

Characterization of as-exfoliated solution of BN-C with different concentration

Fig. III.3 - 8 shows the UV-Vis spectra of BN-C with different centrifuge time of 10 min, 20 min, 30 min, and 40min, which have the concentration measured by weighting and drying in the oven and the zeta potential of the four samples varying from 60 to 170 μg/mL (see Table. 3 - 2). The concentration of the BNNS decreases with the centrifuge time. According to the concentration, the BNNS solutions are named BNC_Sol170, BNC_Sol130, BNC_Sol90, and BNC_Sol60, respectively. The spectra were obtained with the solutions diluted five times to avoid the saturation of the detector.

All four solutions showed similar stability according to the similar zeta potential and can stay stable for only 3 to 4 days before the agglomeration. The re-exfoliation ultrasonic treatment before the synthesis of the coating could help the agglomerated nanosheets to be re-dispersed into the solution.

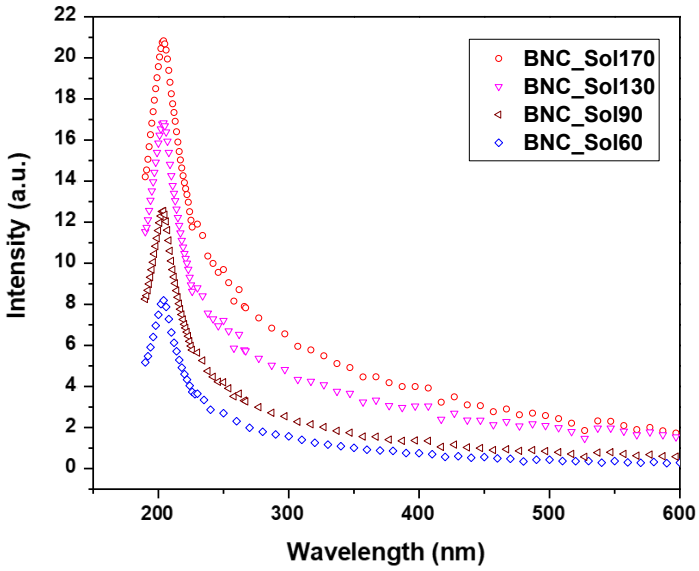

Fig. III.3 - 8 The UV-Vis spectroscopy of BNC_Sol170, BNC_Sol130, BNC_Sol90 and BNC_Sol60 as-exfoliated solution

Table. 3 - 2 Zeta potential and concentration of as-exfoliated solution from BNC_Sol170, BNC_Sol130, BNC_Sol90 and BNC_Sol60

Samples	Zeta Potential (mV)	Concentration (μg/mL)
BNC_Sol170	-23.8	170
BNC_Sol130	-24.8	130
BNC_Sol90	-26.1	90
BNC_Sol60	-27.1	60

Characterization of ZrO coatings charged with BN-C with different concentrations

Fig. III.3 - 9 shows the SEM image and statical contact angle on the ZrO coating charged with BN-C with different concentrations. All coatings show defect-free and homogeneous surfaces, while ZrO_BN170 and ZrO_BN130 have contact angles higher than 90°, indicating a surface hydrophobicity. This hydrophobicity is absent in ZrO_BN90 and ZrO_BN60, while these two coatings showed a slightly higher contact angle than the ZAH_Ref. It is thus understood that the high concentration of BNNS charged ZrO coating shows an increased contact angle until the coating becomes hydrophobic.

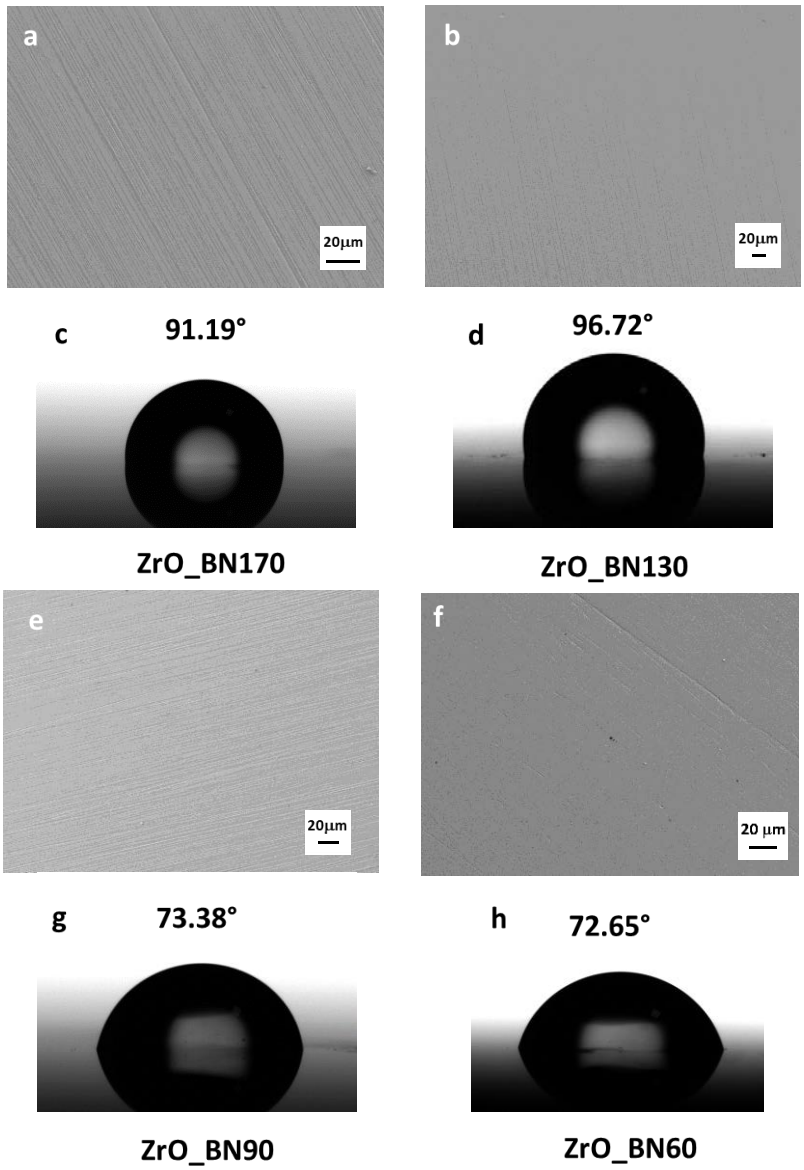

Fig. III.3 - 9 SEM Image and water contact angle of a) and c) ZrO_BN170, b) and d) ZrO_BN130, e) and g) ZrO_BN90 and f) and h) ZrO_BN60

III.3.2 Characterization of BNNS charged ZrO-SiO coatings on AA2017

Characterization of ZrO-SiO multi-component *Sol-Gel solution*

The ZrO-SiO multicomponent coating has been synthesized and deposited on AA2017 to further study the role of BNNS inside the Sol-Gel coatings. Fig. III.3 - 10 shows the image of

solution of Zirconium n-Butoxide and GPTMS. A transparent solution with no sediment inside can be observed. The BNNS exfoliated solution in isopropanol shows white color.

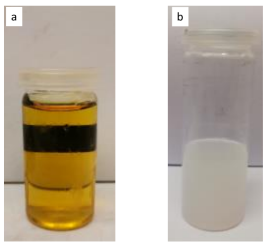

Fig. III.3 - 10 Image of a) As-prepared Sol-Gel solution of ZrO-SiO and b) BNNS solution exfoliated in isopropanol

DLS has been performed for Zirconium n-Butoxide + GPTMS suolution, as shown in Fig. III.3 - 11. The size of the colloid is around 3 nm, and a small amount of agglomeration has an average size of 50 nm – 60 nm. The agglomeration phenomenon is due to the hydrolysis process is favored in an acid solution, leading to a final structure of Sol-Gel solution with longer chains.[12]

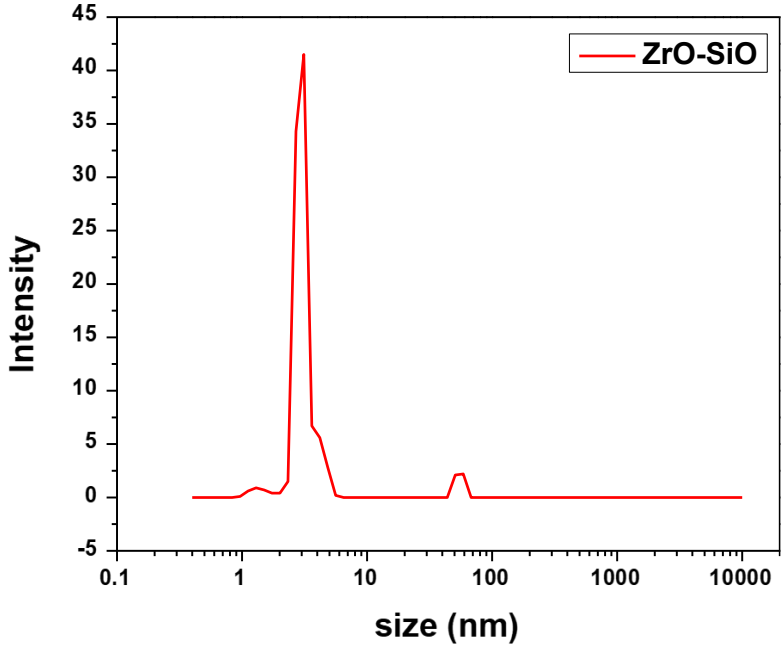

Fig. III.3 - 11 DLS of ZrO-SiO Sol-Gel solution after synthesis

The chemical bonds in ZrO-SiO Sol-Gel coating are characterized with FT-IR spectra shown in Fig. III.3 - 12. The two typical bands at 1591 and 1529cm^{-1} are the characteristic signals of Zr/ AcAc ligand.[13] The bands at 1377 and 1279 cm−1 are attributed to the stretching vibration of C–O–Zr in this ligand.[14]

Fig. III.3 - 12 a) FTIR spectroscopy of ZrO-SiO reference coating deposited on AA2017

The coating thickness of ZrO-SiO multi-component coating is less than 3 μm as measured from cracked regions. Its thicker than ZrO single-component coating due to the introduction of GPTMS groups, which increases the flexibility of the coating and allows larger thickness without cracks.

Characterization of as-exfoliated BNNS isopropanol solution

The UV-Vis curve of BN-C in isopropanol is shown in Fig. III.3 - 13, in which the inset table shows the concentration of BNNSs in isopropanol as well as the zeta potential of the colloidal solution. By weighting measurement, BNNS exfoliated in isopropanol showed a concentration around 112 μg/mL. The absolute value of zeta potential is low, indicating the low stability of the colloidal solution.

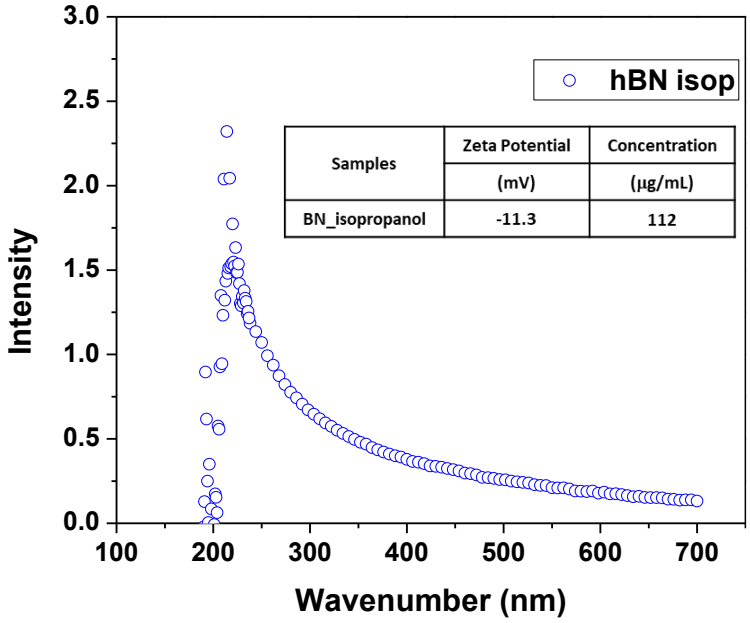

Fig. III.3 - 13 UV-Visible spectroscopy of BN-C exfoliated in isopropanol with inset table showing the parameters of the solution

Characterization of ZrO-SiO multi-component coatings

The SEM of surface morphology as well as the photo of the contact angle on ZrO-SiO_Ref and ZrO-SiO_BN, are shown in Fig. III.3 - 14. In Fig. III.3 - 14a, the scratches are unclear, while from

Fig. III.3 - 14b, the coating surface is rougher. Meanwhile, the BNNS charged coating shows a bigger contact angle than the reference coating.

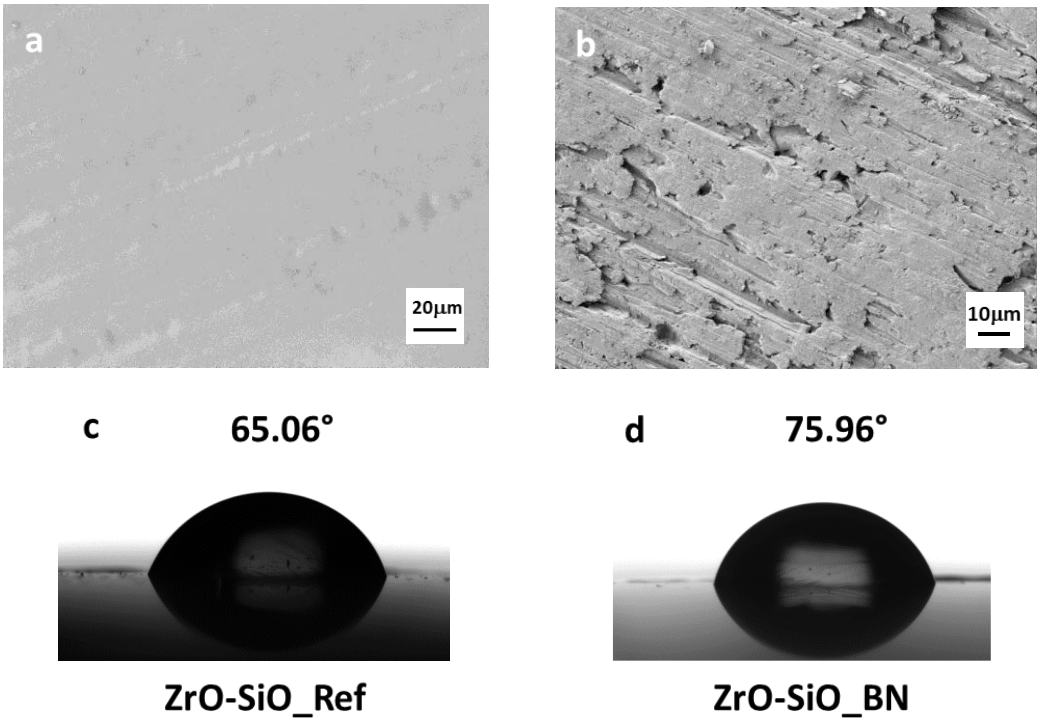

Fig. III.3 - 14 SEM Image and water contact angle of a) and c) ZrO-SiO_Ref and b) and d) ZrO-SiO_BN

III.3.3 Characterization of BNNS charged ZrO-SiO/C18 coatings on carbon steel

Characterization of ZrO-SiO/C18 organic inorganic hybrid Sol-Gel solution

The ZrO-SiO/C18 hybrid Sol-Gel solution has been synthesized to study the role of BNNS in providing a protecting behavior for active surfaces. The ODTES with -C18 alkyl group has been introduced to increase the hydrophobicity of the coating on the coating surface and within the pores.

The photo of ZrO-SiO/C18 hybrid solution is shown in Fig. III.3 - 15a. The micelle is formed due to the presence of surfactant ODTES. After a heat-treated at 55°C, this issue can be resolved, and the solution became transparent. The BNNS n-Butanol solution is shown in Fig. III.3 - 15b.

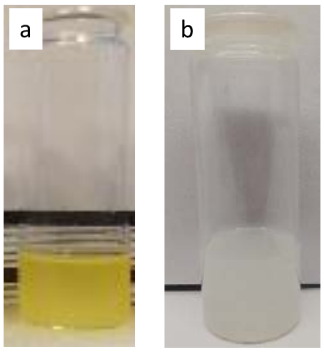

Fig. III.3 - 15 Photo of a) ZrO-SiO/C18 hybrid Sol-Gel solution and b) BNNS exfoliated n-Butanol solution

The DLS curve shows the colloidal size distribution of ZrO-SiO/C18 hybrid Sol-Gel solution after synthesis. The ZrO-SiO/C18 hybrid Sol-Gel solution is composed of coloidals of an average size of around 400 nm as principle colloidals and around 3 nm as minority ones. This means that the basic condition as well as the charge of ODTES led to a larger colloidal size in the Sol-Gel solution comparing to the ZrO-SiO Sol.

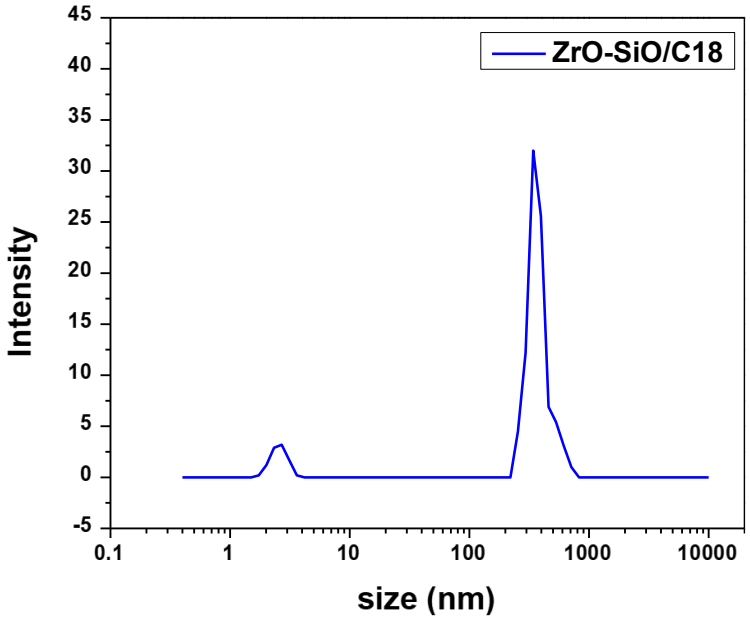

Fig. III.3 - 16 DLS of ZrO-SiO/C18 hybrid Sol-Gel solution after synthesis

The thickness of ZrO-SiO/C18 organic inorganic hybrid coating can be measured from the SEM image shown in Fig. III.3 - 17. The thickness of the reference coating is over 3 μm. The higher thickness than ZrO-SiO multi-component coating is principally due to the introduction of C18 alkyle group from ODTES which allows a higher flexibility of the coating.

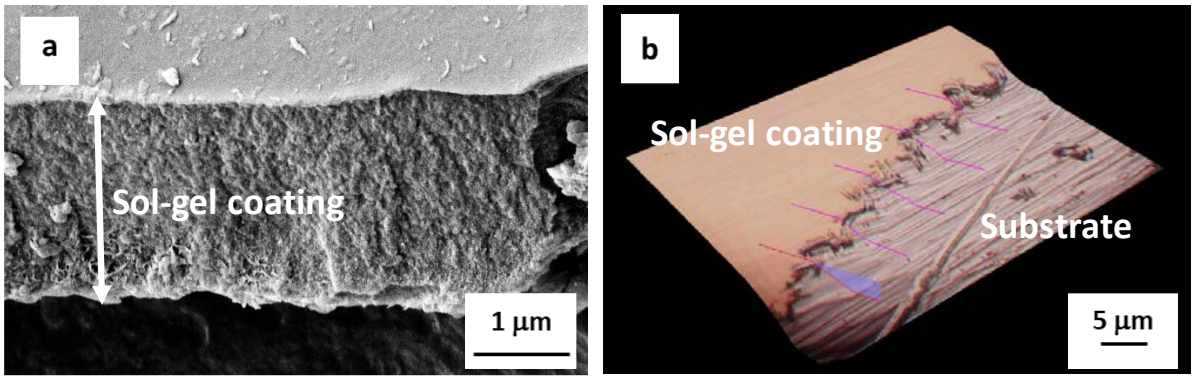

Fig. III.3 - 17 Corroded region of ZrO-SiO/C18_Ref by a) SEM and b) Confocal Optical Microscopy

Characterization of as-Exfoliated BNNS solution in n-Butanol

The UV-Vis spectra of BN-C in n-Butanol is shown in Fig. III.3 - 18, and the inset table shows the parameters of the solution. The characteristic peaks of h-BN can be observed at 210 nm, indicating the presence of BNNS. The Zeta potential test shows that the stability of BNNS in n-

Butanol is low. The concentration of BNNS in n-Butanol is between the value of BNNS in isopropanol and BNNS in water solution.

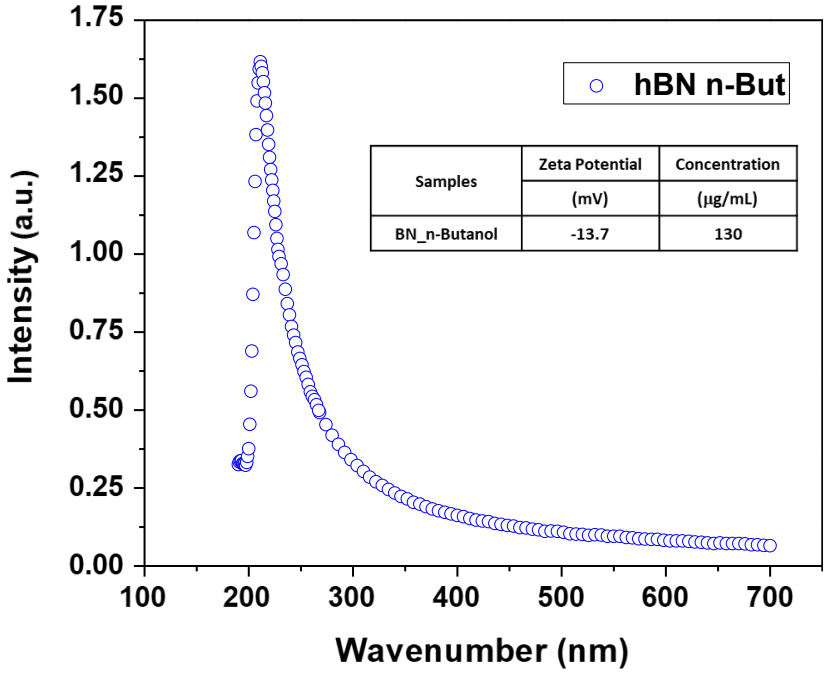

Fig. III.3 - 18 UV-Visible spectroscopy of BN-C exfoliated in n-Butanol with inset table showing the parameters of solution

The surface morphology and photos of contact angle of ZrO-SiO_Ref and ZrO-SiO_BN are shown in Fig. III.3 - 19. Both coatings showed a crack-free and homogeneous surface. The ZrO-SiO_Ref showed a contact angle of 87.27°, which is higher than the multi-component coating without ODTES. This is due to the introduction of ODTES with its apolar C-18 chain. Meanwhile, the BNNS charged coating showed a slightly increased hydrophobicity.

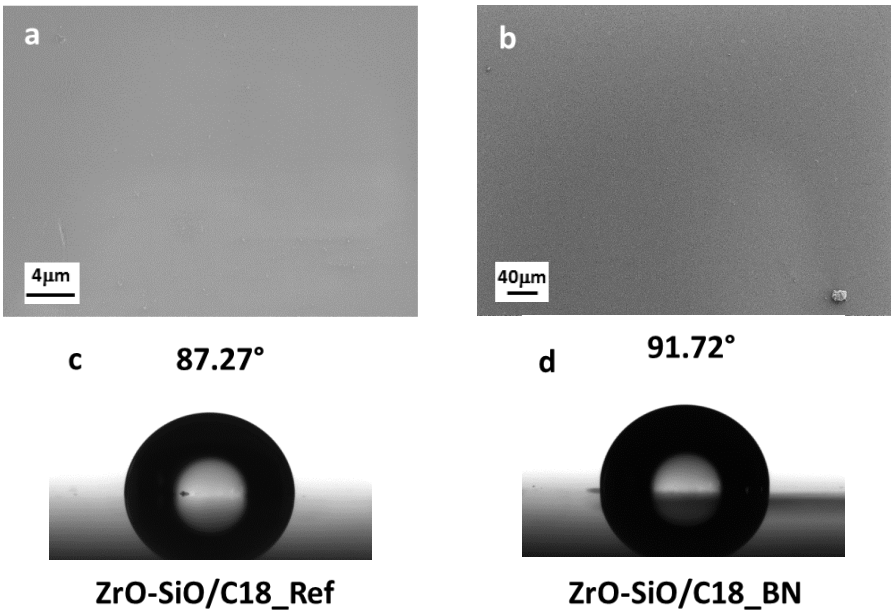

Fig. III.3 - 19 SEM Image and watercontact angle of a) and c) ZrO-SiO/C18_Ref and b) and d) ZrO-SiO/C18_BN

III.3.4 Characterization of Expanded Graphene nanosheets synthesized coatings

The expanded graphene was exfoliated into water and n-Butanol pure solutions with the same exfoliation and centrifuge parameter the BNC_Sol170. To probe the role of electrochemically expanded graphite derived nanosheets (GENS), the characterizations of both coating systems are performed.

Characterization of GENS charged ZAH coating

The GENS is firstly introduced into ZrO coating and deposited on 316L to probe its behavior in an inert system.

The TEM image of GENS and its diffusion pattern are shown in Fig. III.3 - 20. It is shown that GENS presented a-few-layered structure, while the diffraction pattern can clearly show its hexagonal crystal structure.

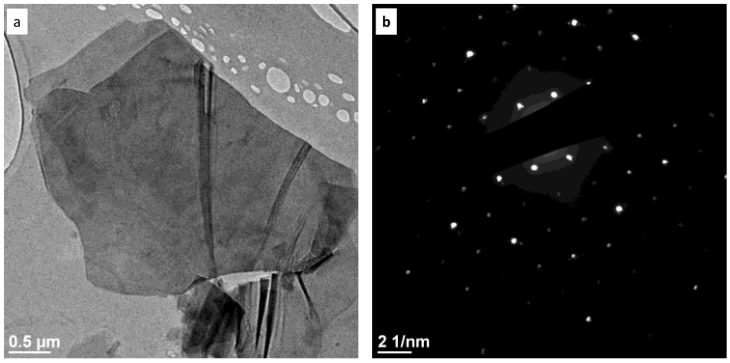

Fig. III.3 - 20 The a) TEM image of GENS exfoliated in water and b) the diffusion pattern

Fig. III.3 - 21 shows the UV-Vis of GENS exfoliated water solution. The peak at around 260 nm for GENS exfoliated from GE in water are coherent to the result reported elsewhere.[3] The zeta potential (inset table) is around -34.7 mV. However, the concentration of GENS is only 90 µg/mL, which is relatively low comparing to other 2D fillers.

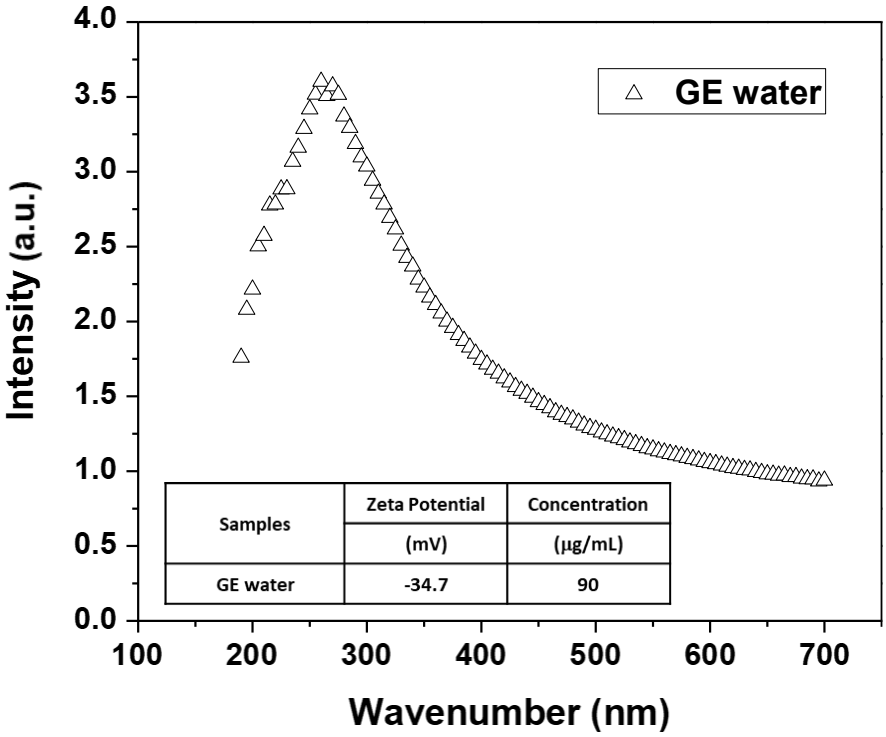

Fig. III.3 - 21 UV-Visible spectroscopy of GE exfoliated in water with inset table showing the parameters of the solution

The surface morphology and photos of the contact angle of ZrO_GE are shown in Fig. III.3 - 22. The surface showed a homogeneous and defect-free morphology while the contact angle is 93.07° indicating a hydrophobic surface.

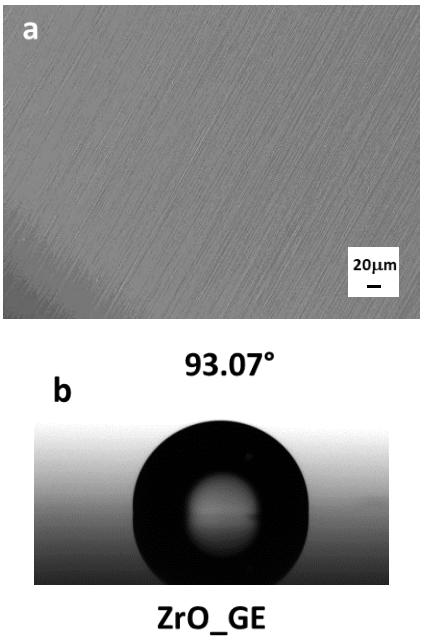

Fig. III.3 - 22 a) SEM Image and b) water contact angle of ZrO_GE

Characterization of GENS charged ZrO-SiO/C18 coating

The GENS is introduced into ZrO-SiO/C18 and deposited on carbon steel to probe its behavior in an active system.

The UV-Vis spectroscopy of GE exfoliated in n-Butanol is shown in Fig. III.3 - 23. The same characteristic peak at 260 nm of graphene oxide has been observed, proving the existence of GENS.

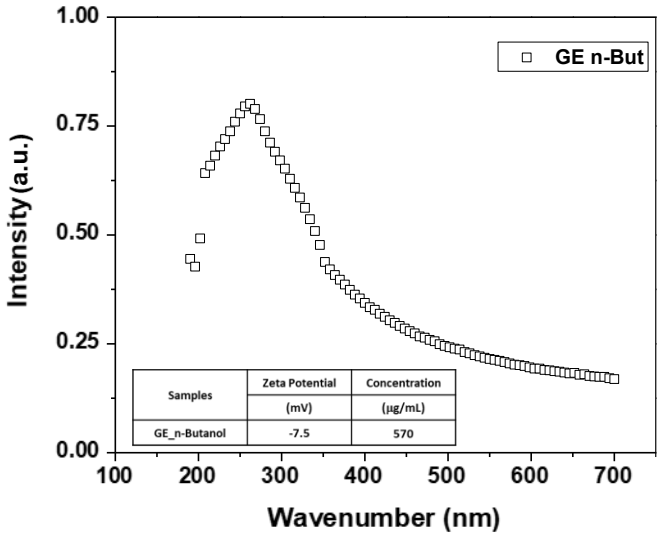

Fig. III.3 - 23 UV-Visible spectroscopy of GE exfoliated in n-Butanol with inset table showing the parameters of solution

The SEM image of surface morphology as well as the photo of the contact angle of ZrO-SiO/C18_GE, is shown in Fig. III.3 - 24. The coatings showed an inhomogeneous surface which is possibly due to the agglomeration of the high concentration GENS. It is also possibly due to the micelles of the ODTES due to the presence of ODTES. The surface showed a high contact angle around 92°, while this contact angle is slightly higher than the reference coating ZrO-SiO/C18_Ref.

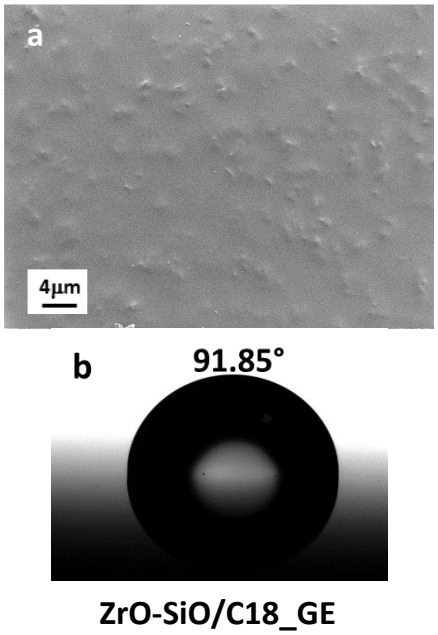

Fig. III.3 - 24 a) SEM Image and b) water contact angle of ZrO-SiO/C18_GE

The Raman spectra of ZrO_SiO/C18_Ref and ZrO_SiO/C18_GE on carbon steels are shown in Fig. III.3 - 25. The presence of GE are proved by the G-band at 1594 cm^{-1} and D-band at 1328

cm^{-1} of graphene oxide which are slightly shifted from the typical G-band at 1605 cm^{-1} and D-band at 1353 cm^{-1} of graphene oxide.[15]

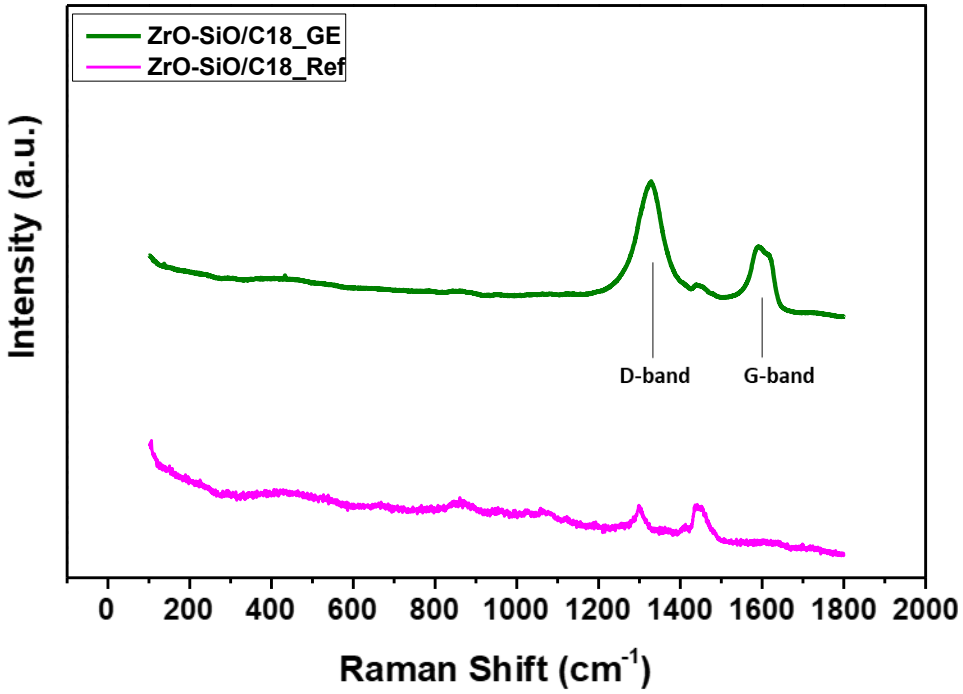

Fig. III.3 - 25 Raman shift of all ZrO-SiO/C18_Ref and ZrO-SiO/C18_GE deposited carbon steel samples

III.3.5 Characterization of Molybdenum Disulfide nanosheets synthesized coatings

Characterization of MDNS charged ZrO coating

The MoS_2 are exfoliated into water and n-Butanol pure solutions with the same exfoliation and centrifuge parameter the BNC_Sol170. Fig. III.3 - 26 shows the UV-Vis spectroscopy of

MoS_2 exfoliated in water. The distinctive shape of UV-Vis curve significate the presence of MoS_2 nanosheets.[16]

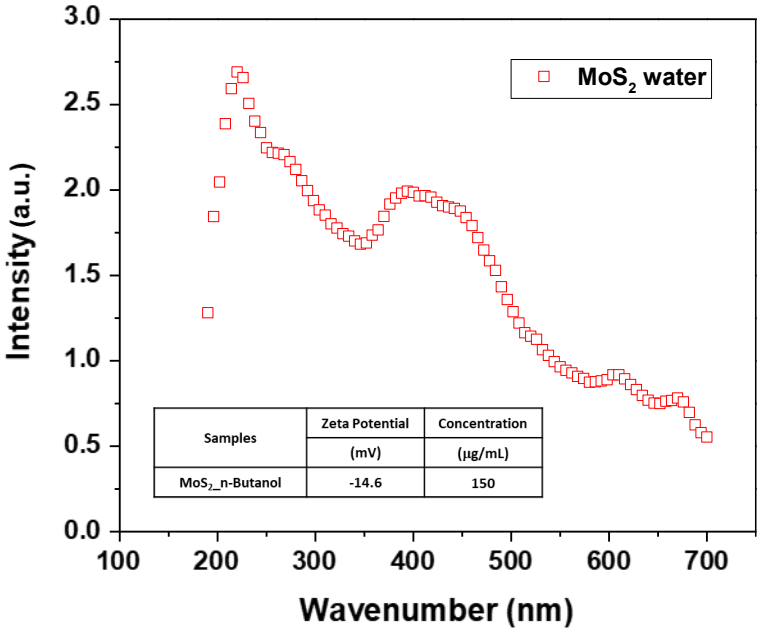

Fig. III.3 - 26 UV-Visible spectroscopy of MoS_2 exfoliated in water with inset table showing the parameters of solution

Fig. III.3 - 27 shows the SEM image and contact angle of the ZrO_MoS_2 sample. The coating is homogeneous and defect-free, while the contact angle is slightly higher than ZrO_Ref, indicating a less modification of the surface hydrophobicity by the introduction of MDNS.

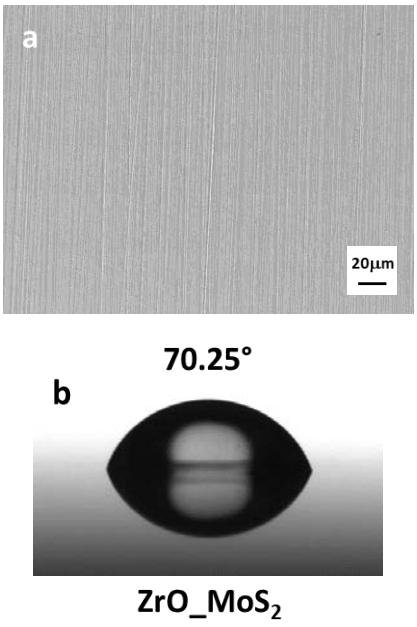

Fig. III.3 - 27 a) SEM Image and b) water contact angle of ZrO_MoS_2

Characterization of MDNS charged ZrO-SiO/C18 coating

Fig. III.3 - 28 shows the UV-Vis spectroscopy of MoS_2 exfoliated in n-Butanol, a similar shaped curve can be observed as from the MoS_2 exfoliated in water, indicating the presence of the

nanofiller. The inset table shows the zeta potential of MoS_2 exfoliated solution in n-Butanol as -12.2 mV, indicating a low stability. However, the concentration is extra high, which is around 680 μg/mL.

To sum up, MoS_2 showed a high capability of being exfoliated in pure solvent, indicating an active surface energy of the nanosheets.

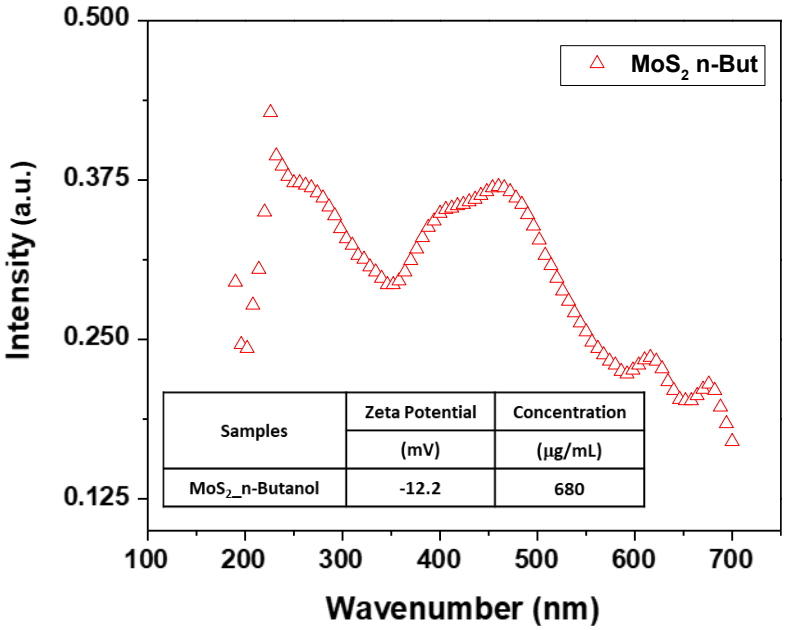

Fig. III.3 - 28 UV-Visible spectroscopy of MoS_2 exfoliated in n-Butanol with inset table showing the parameters of the solution

The SEM image of surface morphology and photo of contact angle of ZrO-SiO/C18_MoS_2 are shown in Fig. III.3 - 29. The surface is defect-free and homogeneous, while the contact angle is slightly lower than the reference sample. This is possibly due to the high surface energy of MoS_2 may give polarity to the coating surface and reduce the hydrophobicity of the coating.

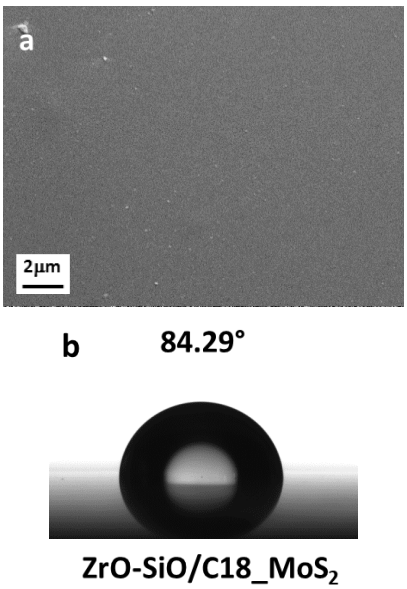

Fig. III.3 - 29 SEM Image and water contact angle of ZrO-SiO/C18_MoS_2

The Raman spectra of ZrO_SiO/C18_Ref and ZrO_SiO/C18_MoS_2 on carbon steels are shown in Fig. III.3 - 30. The presence of MoS_2 are proved by the E_{2g} (around 383 cm^{-1})and A_{1g} mode (around 408 cm^{-1}) shown in ZrO-SiO_MoS_2 curve.[17] The LA represents for the longitudinal acoustic mode and the LA influenced raman shifts (A_{1g}-LA at around 179 cm^{-1}, 2LA at around 466 cm^{-1} and A1g+LA at around 645 cm^{-1}) also fits the characteristic of MoS_2 as reported.[18]

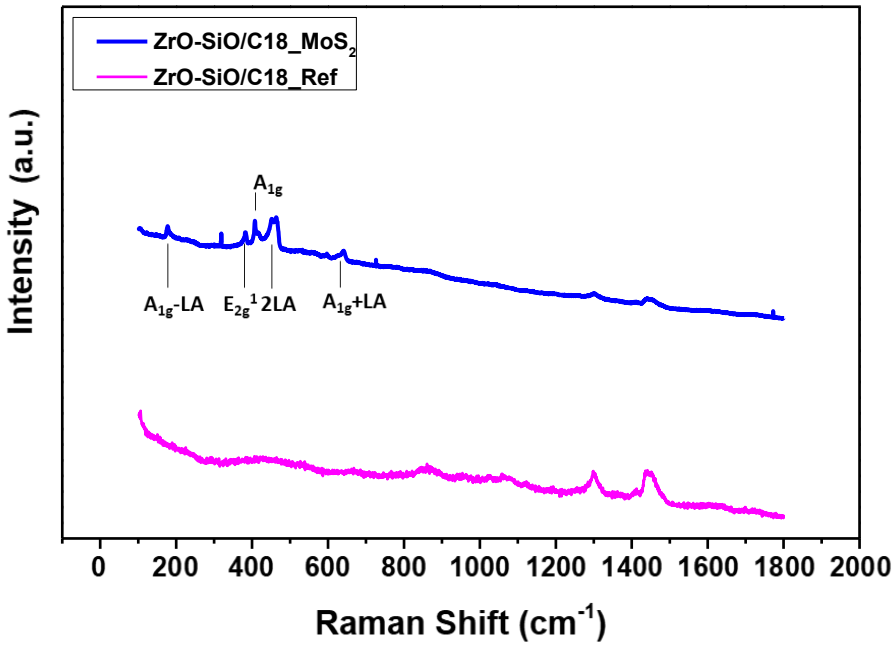

Fig. III.3 - 30 Raman shift of all ZrO-SiO/C18_Ref and ZrO-SiO/C18_MoS_2 deposited carbon steel samples

III.4 Conlusion

The three different Sol-Gel systems were successfully deposited on the corresponding substrates. The 2D materials filled coatings show defect-free and homogeneous surface. The physico-chemical and microstructure characterizations from the raw materials to the colloidal solution until the final coatings are detailed.

For Zirconium oxide single-component coating on 316L, the Sol-Gel matrix prepared shows similar morphology. Different surface hydrophobicity can be observed with the different h-BN derived BNNS and the concentration of BNNS. In order to reduce the effect of the surface tension, the electrochemical tests require a 24h immersion until the stable state.

On Aluminum alloy (AA2017), the single-component coating was firstly transferred with success. Furthermore, a ZrO-SiO multicomponent coating was synthesized to enhance the density of the Sol-Gel matrix as well as the nanocomposite coating's performance against corrosion.

For the further reinforcement of the coating barrier effect, the alkyl group (-C18) was doped in the Sol, which induces a hydrophobic surface and water repellency is the pores. This coating was deposited on carbon steel (XC90)

[1] Lin, Y.; Williams, T. V.; Xu, T.-B.; Cao, W.; Elsayed-Ali, H. E.; Connell, J. W. Aqueous Dispersions of Few-Layered and Monolayered Hexagonal Boron Nitride Nanosheets from Sonication-Assisted Hydrolysis: Critical Role of Water. J. Phys. Chem. C 2011, 115 (6), 2679–2685.
[2] Deyab, M. A.; Keera, S. T. Effect of Nano-TiO2 Particles Size on the Corrosion Resistance of Alkyd Coating. Materials Chemistry and Physics 2014, 146 (3), 406–411..
[3] Dhakate, S. R.; Chauhan, N.; Sharma, S.; Tawale, J.; Singh, S.; Sahare, P. D.; Mathur, R. B. An Approach to Produce Single and Double Layer Graphene from Re-Exfoliation of Expanded Graphite. Carbon 2011, 49 (6), 1946–1954
[4] Punckt, C.; Muckel, F.; Wolff, S.; Aksay, I. A.; Chavarin, C. A.; Bacher, G.; Mertin, W. The Effect of Degree of Reduction on the Electrical Properties of Functionalized Graphene Sheets. Appl. Phys. Lett. 2013, 102 (2), 023114.
[5] Innocenzi, P. The Sol to Gel Transition; SpringerBriefs in Materials; Springer International Publishing, 2016.
[6] Shang, J.; Xue, F.; Fan, C.; Ding, E. Preparation of Few Layers Hexagonal Boron Nitride Nanosheets via High-Pressure Homogenization. Materials Letters 2016, 181, 144–147.
[7] Coleman, J. N.; Lotya, M.; O'Neill, A.; Bergin, S. D.; King, P. J.; Khan, U.; Young, K.; Gaucher, A.; De, S.; Smith, R. J.; et al. Two-Dimensional Nanosheets Produced by Liquid Exfoliation of Layered Materials. Science 2011, 331 (6017), 568–571.
[8] Kim, J.; Kwon, S.; Cho, D.-H.; Kang, B.; Kwon, H.; Kim, Y.; Park, S. O.; Jung, G. Y.; Shin, E.; Kim, W.-G.; et al. Direct Exfoliation and Dispersion of Two-Dimensional Materials in Pure Water via Temperature Control. Nature Communications 2015, 6, 8294.
[9] Luo, X.; Zhang, Y.; Zandén, C.; Murugesan, M.; Cao, Y.; Ye, L.; Liu, J. Novel Thermal Interface Materials: Boron Nitride Nanofiber and Indium Composites for Electronics Heat Dissipation Applications. J Mater Sci: Mater Electron 2014, 25 (5), 2333–2338.
[10] Tackett, J. E. FT-IR Characterization of Metal Acetates in Aqueous Solution. Appl. Spectrosc., AS 1989, 43 (3), 483–489.
[11] Brenier, R.; Gagnaire, A. Densification and Aging of ZrO2 Films Prepared by Sol–gel. Thin Solid Films 2001, 392 (1), 142–148.
[12] Certech asbl. Cahier Technologique Sol-Gel - PDF; 2018.
[13] Le Guével, X.; Palazzesi, C.; Prosposito, P.; Della Giustina, G.; Brusatin, G. Influence of Chelating Agents on the Photopolymerization of Hybrid Ti-Based Waveguides. J. Mater. Chem. 2008, 18 (30), 3556–3562.
[14] Yu, M.; Liang, M.; Liu, J.; Li, S.; Xue, B.; Zhao, H. Effect of Chelating Agent Acetylacetone on Corrosion Protection Properties of Silane-Zirconium Sol-Gel Coatings. Appl. Surf. Sci. 2016, 363, 229–239.
[15] Johra, F. T.; Lee, J.-W.; Jung, W.-G. Facile and Safe Graphene Preparation on Solution Based Platform. Journal of Industrial and Engineering Chemistry 2014, 20 (5), 2883–2887.
[16] Ahmad, R.; Srivastava, R.; Yadav, S.; Singh, D.; Gupta, G.; Chand, S.; Sapra, S. Functionalized Molybdenum Disulfide Nanosheets for 0D–2D Hybrid Nanostructures: Photoinduced Charge Transfer and Enhanced Photoresponse. J. Phys. Chem. Lett. 2017, 8 (8), 1729–1738.
[17] Wu, J.-Y.; Lin, M.-N.; Wang, L.-D.; Zhang, T. Photoluminescence of MoS 2 Prepared by Effective Grinding-Assisted Sonication Exfoliation. Journal of Nanomaterials 2014, 2014, 1–7.
[18] Windom, B. C.; Sawyer, W. G.; Hahn, D. W. A Raman Spectroscopic Study of MoS2 and MoO3: Applications to Tribological Systems. Tribol Lett 2011, 10.

Chapter IV. Electrochemical characterization

IV.1 Introduction

The electrochemical characterizations were performed to understand the role of 2D materials on barrier effect in different coating systems. The electrochemical test performed in this work includes Open Circuit Potential (OCP) test, Potentiodynamic Polarization, electrochemical impedance spectroscopy (EIS) tests. All electrochemical tests were performed in NaCl 30g/L solution. The flow chart of the study is shown in Fig. IV.1 - 1.

For ZrO coating on 316L, the bare substrate and ZrO coated samples were firstly characterized by OCP and Polarizations in 24 hours of immersion and by EIS during 120 hours of immersion. The influence of the BNNS nanofiller is evaluated by the comparison with the bare substrate and unfilled coating. Electrochemical Equivalent Circuit (EEC) and numerical fittings are employed to establish the correlation between the electrochemical behavior and the mechanism of reactions. To understand the effect of BNNS morphology, the ZrO coating charged with BNNS exfoliated from BN-A, BN-B, and BN-C were studied. In addition, the influence of BNNS concentration on the ZrO coating's barrier effect was investigated as well. For this purpose, the BN-C derived BNNS was selected and added into the ZrO matrix with different concentrations.

Hereafter, we attempted to transfer the BNNS filled ZrO coating on aluminum alloy. However, the ZrO single component coating showed a similar behavior to the AA2017 bare substrate, indicating an insufficient barrier effect on AA2017 substrate. The study of ZrO single-component coating will thus be limited on 316L substrate for the observation of the role of 2D materials in inorganic coating and the evolution of the coating.

To study the role of 2D materials in corrosion reduction, the ZrO-SiO multi-component Sol-Gel coating was used, which allows the combination of the mechanical properties of both components. The polarization and EIS curves after one week of immersion were compared to evaluate the effect of BNNS on corrosion protection. Since corrosion and delamination were observed, an enhancement of coating matrix is required to search for a coating/BNNS couple with strong and efficient barrier effect.

Finally, the alkyl group (ODTES, -C18) was doped into the multi-component matrix on carbon steel XC90 to modify its hydrophobicity. The polarization and EIS were performed to characterize the electrochemical behavior of bare and coated carbon steel, with or without BNNS fillers.

The other 2D materials, GENS and MDNS were charged in ZrO/316L to observed their function in inorganic coating, evolution of coatings and to compare with BNNS. Then, they were charged in ZrO-SiO/C18/carbon steel system to understand their influence on the efficiency of corrosion protection.

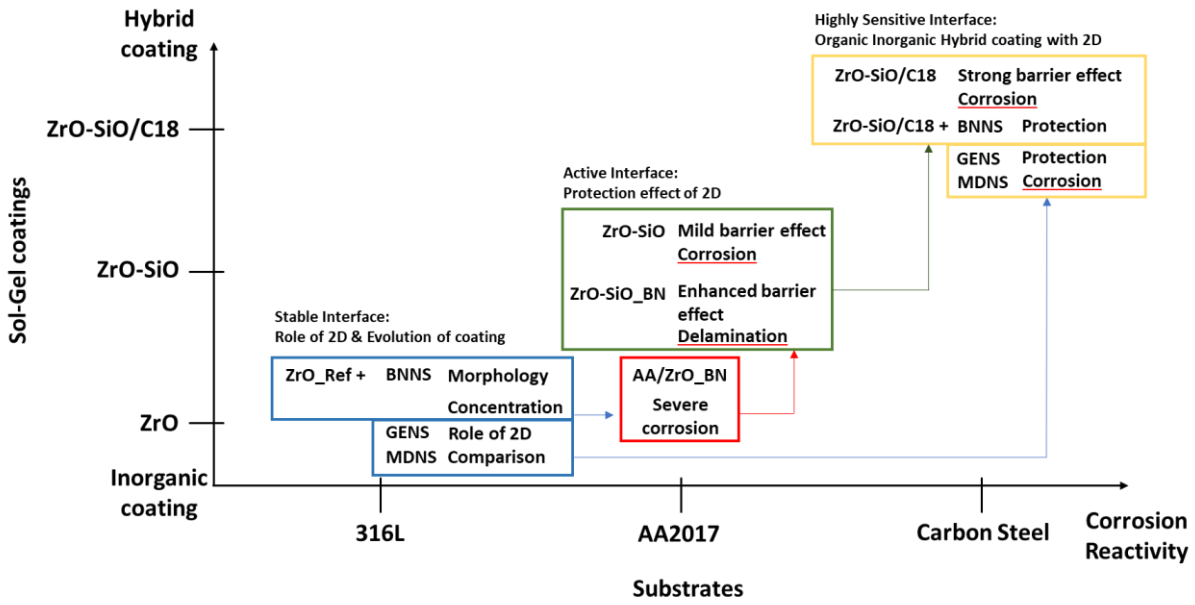

Fig. IV.1 - 1 Scheme of the research topics based on different systems

IV.2 Study of BNNS in ZrO single-component coating on 316L

The discussion starts with the study of the ZrO single-component coating in NaCl 30g/L solution by controlling parameters of BNNS fillers, size and concentration. The evolution of barrier effect of BNNS charged coating with varying parameters have been explored..

IV.2.1 Electrochemical behavior of 316L bare substrate

The electrochemical behavior of 316L has been measured to establish a reference in terms of the electrochemical behavior of the coated system.

The evolution of the open circuit potential (OCP) of bare 316L in NaCl 30 g/L for 120 hours is shown in Fig. IV.2 - 1. The OCP increases from -14 mV/SCE after 16 hours of immersion to 73 mV/SCE for 120 hours of immersion. Between 40 to 60 hours, the OCP can be considered as stabilized, expressing a stable surface reactivity.[1] After 60 hours, the OCP increases again which depicts a stable evolution of the passible film with time.

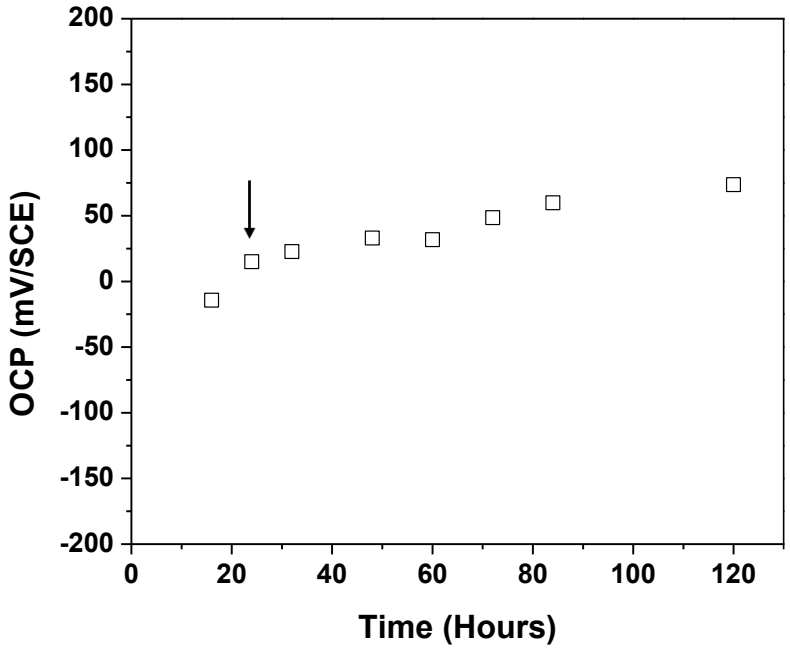

Fig. IV.2 - 1 Open Circuit Potential evolution of 316L bare substrate in NaCl 30g/L over 120 hours (Arrow indicates the OCP value at 24 hours of immersion)

Potentiodynamic polarization has been performed after 24 hours of immersion to characterize electrochemical behavior of the material. There is a specific reactivity for each potential. The polarization curves presented in Fig. IV.2 - 2 inform about these reactions. As we can see, the corrosion potential E_{corr} reaches 37 mV/SCE, which is consistent with the OCP value recorded at 24 hours of immersion, as presented in Fig. IV.2 - 1. The passive state is confirmed by the low current density from E_{corr} to 0.68 V/SCE.[2,3] After the potential of 0.68 V/SCE, the current density increases drastically due to the pitting propagation. Previously several current density transcient informed about metastable pits.[4] Fig. IV.2 - 3 shows the surface morphology after the polarizations. The bare 316L is deeply corroded since the bulk dissolution of the metal can be observed. From the zoomed image, it is observed that the pitting propagates into the bulk metal.

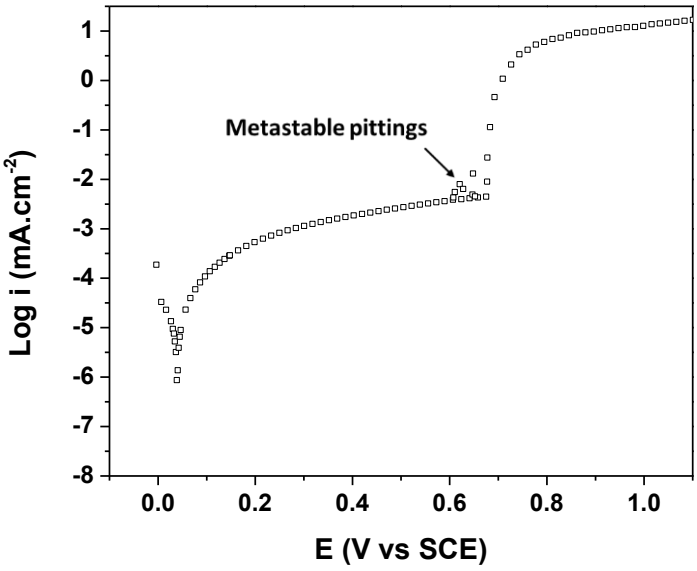

Fig. IV.2 - 2 Polarization curve of 316L bare substrate in NaCl 30g/L after 24 hours of immersion

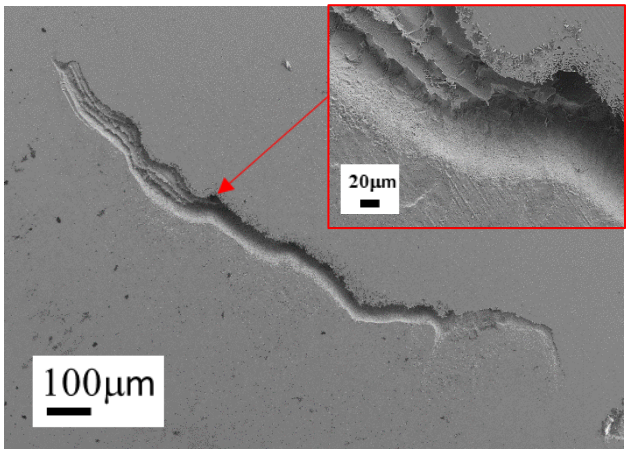

Fig. IV.2 - 3 SEM image of the morphology of 316L bare substrate after the polarization

The EIS curves of bare 316L for long-duration immersion are presented in Fig. IV.2 - 4. Nyquist curves showed a decrease in the diameter of the semicircle loop, indicating the fact that the barrier property of the passive film decreases during OCP. The Bode plot provides another representation of the same evolution, a decreasing phase angle and impedance value at the lowest frequency over time, as shown in Fig. IV.2 - 4.[5]

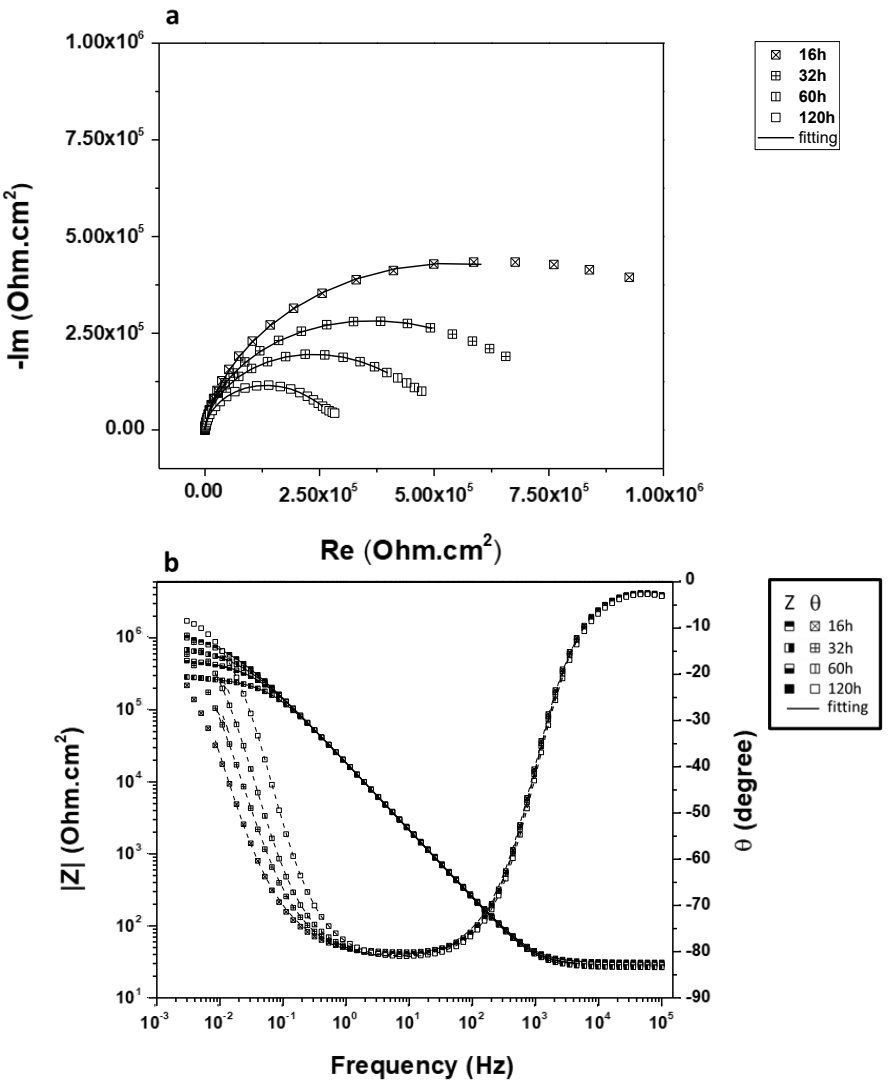

Fig. IV.2 - 4 EIS curves of 316L bare substrate over 120 hours a) Nyquist plots and Bode plots

To further exploit the EIS data, an electrochemical equivalent circuit (EEC) has been proposed in Fig. IV.2 - 5. It consists of a Randle model with a second *R*/*Q* circuit. This EEC is different than the one used classically for passive film. In this case, we consider the fact of the contamination of chloride ions and the weakening of the passive film. Boissy et al. have proposed multiple EEC for the fitting of 316L in corrosive conditions. [6] The asymmetrical behavior of the phase curve shown in Fig. IV.2 - 5 and the existence of Cl^- ions can together indicate a passive film composed of two layers: oxide and hydroxide that could be simulated by a capacitance and resistance behavior R_{film}/Q_{film}. The defects induced by the Cl^- ions stimulate the reactivity of stainless steel. This can be characterized by a material exposure, and thus simulated by a double-layer capacitance and charge transfer resistance R_{ct}/Q_{dl}. In this model, R_s represents the resistance of the electrolyte. This system is available at corrosion potential. Obviously, it should be different for pitting potential.

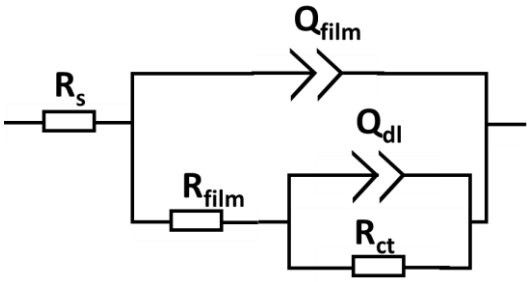

Fig. IV.2 - 5 Electrochemical Equivalent Circuit of 316L bare substrate immersed in NaCl

The fitting parameters of 316L bare substrate after 16 hours and 120 hours of immersion are shown in Table 4 - 1. It is observed that the resistance R_{film} decreases to half of the value, meaning that the barrier property of the film decreases over time which could be explain by more and more chloride in the film. The R_{ct} also decrease, indicating lower corrosion resistance over time. Thus, all three evolutions reveals that the passivation film exhibit a degradation in NaCl solution and justify to enhance the resistance of the system.[7]

Table 4 - 1 Fitting parameters of impedance curves of 316L bare substrate at 16 hours and 120 hours

Sample	R_s /ohm.cm^2	R_{film} /ohm.cm^2	α_{film}	Q_{film} /f.s^(a-1)	C_{film} /μF	R_{ct} /ohm.cm^2	α_{dl}	Q_{dl} /f.s^(a-1)
316L 16h	30.835	4.33E +05	0.93	9.67E-06	1.34	4.32E +05	0.56	3.59E -06
316L 120h	26.665	2.26E +05	0.94	9.54E-06	1.71	9.87E +04	0.50	4.75E -05

IV.2.2 Effect of ZrO single-component coating on 316L

The electrochemical behavior of zirconium acetate hydroxide derived coating without fillers (ZrO_Ref) has been compared with bare 316L and further nanocomposite coating. It constitute the reference of the electrochemical behavior of coated systems before improvement.

The electrochemical characterization follows the same protocol. First of all, the OCP is characterized and pursued with polarisation curve and impedance spectroscopy.

The OCP evolution of ZrO_Ref in NaCl 30g/L for 120 hours is shown in Fig. IV.2 - 6. In the same figure, the evolution of the bare 316L is superposed. OCP of ZrO_Ref stays stable during 120 hours between 85 ~ 95 mV/SCE, indicating the achievement of a stable state of the zirconium oxide layer after immersion. Compared with stainless steel OCP, we can observe that the bare substarte required several hours to reach a steady state. At this stage of the analysis, the coating act as a barrier that separates the substrate from the electrolyte.

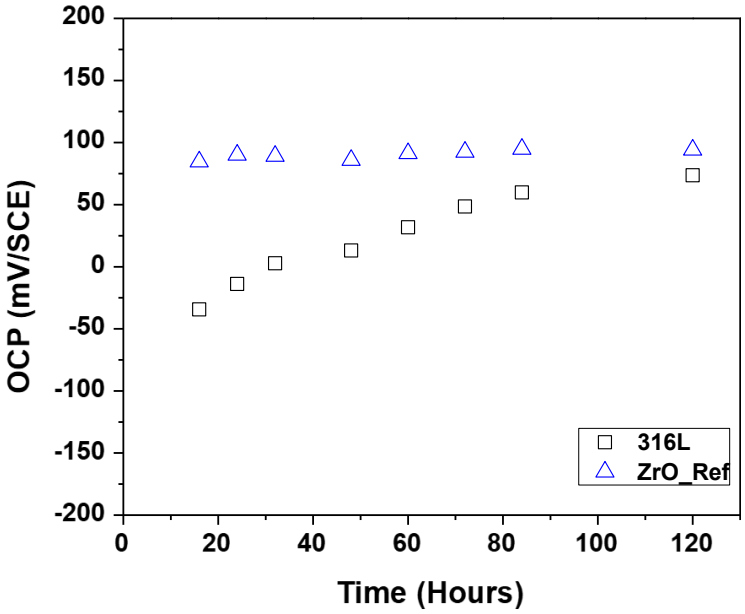

Fig. IV.2 - 6 Open Circuit Potential evolution of ZrO_Ref and 316L bare substrate in NaCl 30g/L for 120 hours

The polarization for ZrO_Ref has been performed in the same conditions as for the substrate. After 24 hours of immersion to obtain a stable electrochemical system, the polarization curves of ZrO_Ref and bare 316L substrate for comparison were plotted in Fig. IV.2 - 7. ZrO_Ref shows a nobler E_{corr}. The barrier effect provided by zirconium oxide coating is efficient since the current density is significantly lower than the one of bare 316L substrate. No pit, neither current density increasing attest that the sol-gel coating act as a barrier.

However, as shown in Fig. IV.2 - 8, after the polarization, some corrosion products can still be observed on ZrO_Ref. This phenomenon can be explained by under deposit corrosion due to the porous microstructure of the sol-gel coating that allows the penetration of the corrosive electrolyte. This phenomenon of dissolution was too slow to be recorded during polarization but can appear during the storage after electrochemical measurement.

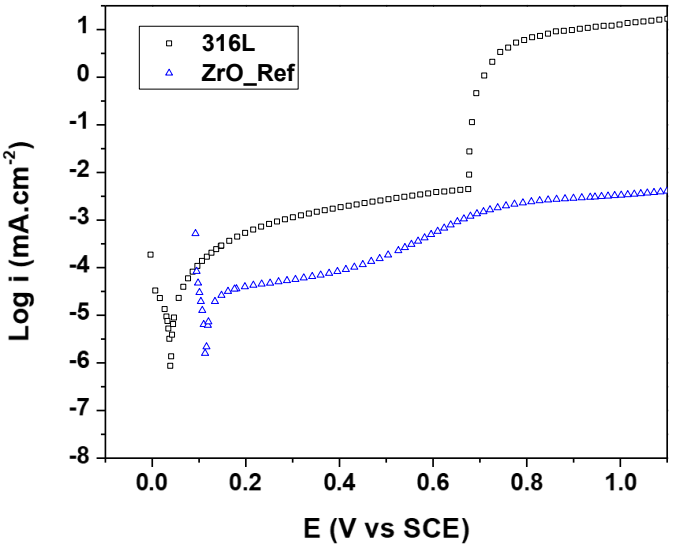

Fig. IV.2 - 7 Polarization curve of ZrO_Ref and 316L bare substrtate in NaCl 30g/L after 24 hours of immersion

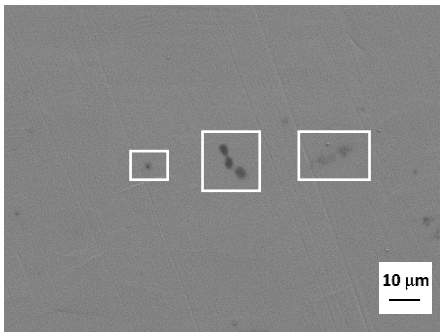

Fig. IV.2 - 8 SEM image of morphology of ZrO_Ref surface after polarization (rectangles are showing the undercoating corrosion)

The EIS curves of ZrO_Ref for long-duration immersion are presented in Fig. IV.2 - 9. The Nyquist curves of ZrO_Ref showed a similar diameter of the impedance circuit compared with 316L for 16 hours of immersion. This diameter reduces from 16h to 32h and remains stable, unlike the case of 316L substrate, where the circuit reduces severely during 120 hours.

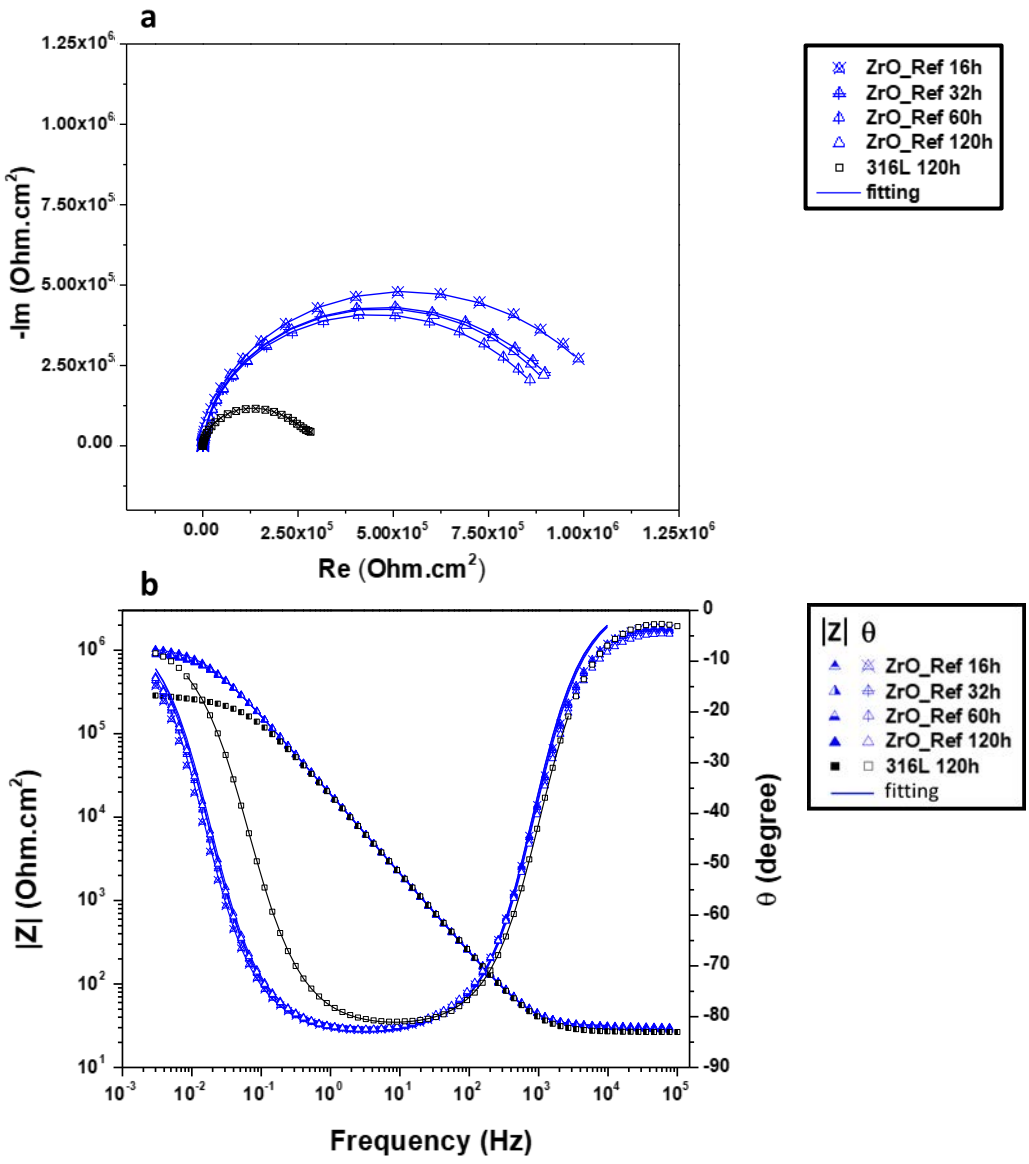

Fig. IV.2 - 9 Bode curves of ZrO_Ref over 120 hours a) Nyquist plots b) Bode plots

The EEC for EIS data fitting of ZrO_Ref is shown in Fig. IV.2 - 10.[8] Since the polarization curve showed that the coating was inert due to the glass/ceramic nature of zirconium oxide. Thus, the corrosion signal is related to the substrate reactivity. The differences between OCP and current density are due to a lower exposure rate of metal surface. The EEC is consisted of: one resistance R_s indicating solution resistance, one R_{pore}/Q_{coat} circuit at the intermediate frequency that represents the electrolyte resistance capacitance behavior related to the pores of coating and the passive film, and a low-frequency time constant R_{ct}/Q_{dl} presenting the charge transfer and double layer capacitance at the electrolyte/ metal interface undercoating. The fitting parameters are shown in Table 4 - 2.

From Table 4 - 2, both resistance R_{pore} and R_{ct} are just slightly decreased indicating a slow reaction rate. The generation of passive film may cover the pitting with this low reaction rate.[9] The α_{dl} close to 0.75 indicating a diffusion phenomena over the metal surface.

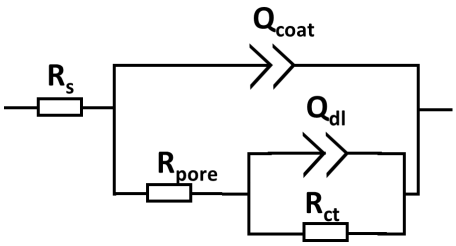

Fig. IV.2 - 10 EEC for ZrO_Ref long term duration of EIS test

Table 4 - 2 Fitting parameters of impedance curves of ZrO_Ref at 16 hours and 120 hours

Sample	R_s /ohm.cm^2	R_{pore} /ohm.cm^2	α_{coat}	Q_{coat} /f.s^(a-1)	C_{coat} /μF	R_{ct} /ohm.cm^2	α_{dl}	Q_{dl} /f.s^(a-1)
ZrO_Ref 16h	32.98	9.73E +05	0.95	9.32E -06	2.51	1.53 E +05	0.73	6.11 E -05
ZrO _Ref 120h	36.89	8.74E +05	0.95	9.22E -06	2.47	1.16 E +05	0.73	7.85 E -05

IV.2.3 Influence of BNNS charged in ZrO/316L

It is understood that the ZrO_Ref coating is protective by reducing the exposure of the metal surface. Nevertheless, the porous microstructure of the ZrO Sol-Gel matrix is the main drawback of the barrier effect offered by the coating.

To overcome this issue, a heat treatment is necessary to obtain a dense ceramic structure, as mentioned in Chapter I. However, the high-temperature heat treatment is not achievable for all systems since it can cause unexpected modifications in the substrates (like the inner stress, the change of crystallinity, and the carburizing, etc.). By introducing fillers in xerogel film, on the contrary, it is possible to bring inhibition function or change the distortion/ tortuosity of the pores in the coating to seal porosity or to delay water up-take.

Among different nanofillers, the 2D nanosheets are promising choices. The excellent impermeability in nano-metric thickness can efficiently prolong the penetration path in the coating. [10,11,12] As mentioned in previous chapters, the influence of 2D nanosheets on the

barrier effect in inorganic coatings has not been clearly explored yet. In this part, the understanding of the influence of BNNS on the barrier effect of ZrO coating is performed in the first place. Detailed elaboration parameters are already described in chapter 2. The BNNS with an average size of 4.5 µm has been exfoliated into water solution and charged in ZrO coating.

The evolution of OCP values in NaCl 30g/L for 24 hours immersion of the ZrO coating with or without charge compared to the bare 316L substrate are shown in Fig. IV.2 - 11. After 6 hours of immersion, the OCP of ZrO_BN is stabilized.

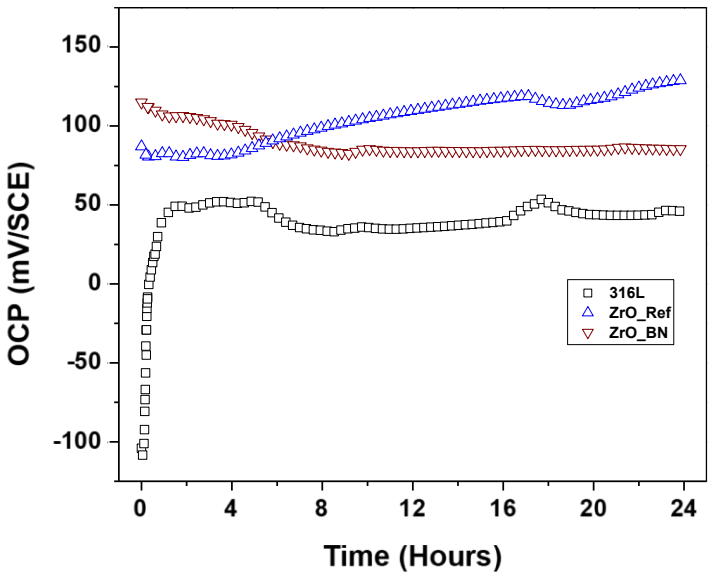

Fig. IV.2 - 11 Open Circuit Potential of ZrO_BN compared to the bare 316L substrate and ZrO_Ref for 24 hours of immersion in NaCl 30g/L solution

Fig. IV.2 - 12 shows the polarization curves of the bare 316L substrate, compared to the electrochemical behaviour of ZrO_Ref, and ZrO_BN. The BNNS charged coating exhibits higher E_{corr}, which is consistent with the observation from OCP evolution. Both lower current density and nobler E_{corr} demonstrate the improvement of the barrier effect of ZrO_BN compared with the bare 316L substrate.

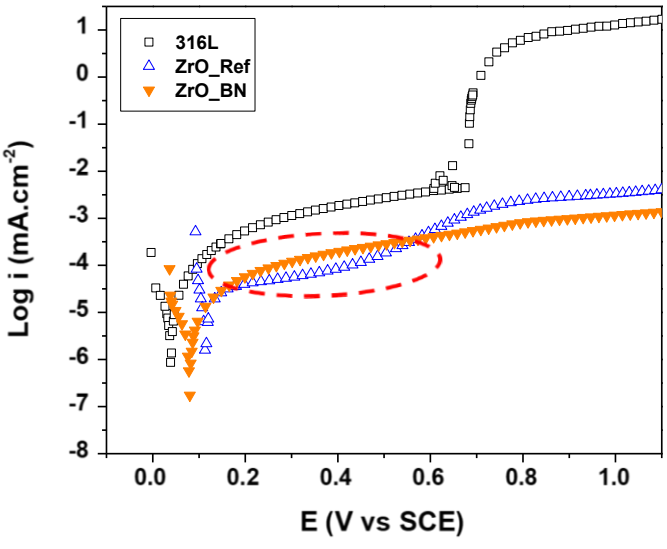

Fig. IV.2 - 12 Polarization curves in NaCl 30g/L of bared 316L substrate, ZrO_Ref and ZrO_BN (with the circuit pointing the early anodic region of both ZrO_BN and ZrO_Ref)

Moreover, the current density of ZrO_BN increases slightly from a low potential to 1.1V. The current density confirms a very low reactivity of the BN coated system which is maintained under the anodic potential range.

At the early stage of the anodic part the current density reaches by ZrO_BN is, however higher than ZrO_Ref coating. This phenomenon can be explained by that the weaker barrier effect of ZrO_Ref coating will cause a higher oxidation rate on the metal surface. Thus, the accumulation of the oxidation product within pores of the coating lowers the current density. However, once the potential reaches the value where the metastable pitting corrosion happens on the substrate, around 0.5 V vs SCE, the current density surpasses the current density of ZrO_BN. The less sensitive behavior of ZrO_BN is related to its improved barrier property.

Fig. IV.2 - 13 shows the surface morphology after the polarization. Compared with the deeply corroded bare 316L substrate, no dissolution of metal or stable pit can be observed from ZrO_BN. Nevertheless, small spots of corrosion products can be observed on the surface.

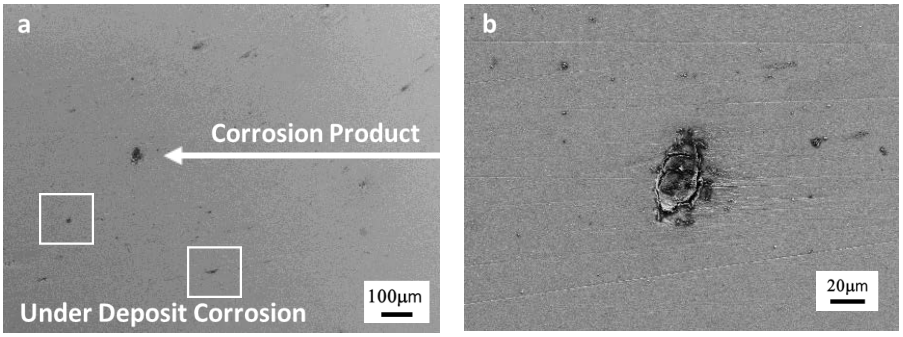

Fig. IV.2 - 13 SEM image of a) morphology of ZrO_BN after polarization and b) Zoomed corrosion product

In parallel, the EIS tests after 24 hours of immersion in 30 g/ml NaCl solution have been performed to ZrO_BN as well. The diagram of the bare 316L substrate and ZrO_Ref are superposed (see Fig. IV.2 - 14). ZrO_BN shows a clear semicircle loop with a diameter larger than both references, indicating a better corrosion resistance.

Since the BNNS charged nanocomposite coating is inert at OCP, it is appropriate to use the same EEC of the ZrO_Ref and bare 316L substrate to simulate the electrochemical behavior, as shown in Fig. IV.2 - 15. The numerical fitting results are listed in Table 4 - 3. With the addition of BNNS in the sol-gel coating, the R_{pore} of the coating increases to 2.08 x 10^6 Ohm.cm^2, which is twice of the value of ZrO_Ref (9.76 x 10^5 ohm.cm^2.). The R_{ct} increase to 3.38 x 10^6 Ohm.cm^2 that is 20 times higher than the pure sol-gel coating. The high R_{film} is generally attributed to the barrier effect of the non conductive matrix and the tortured connection pathway for the ions exchange induced by impermeable BNNS. Meanwhile, the high R_{ct} indicates low reaction rates at the metal surface. The value α_{dl} indicates diffusion phenomena in the pores.

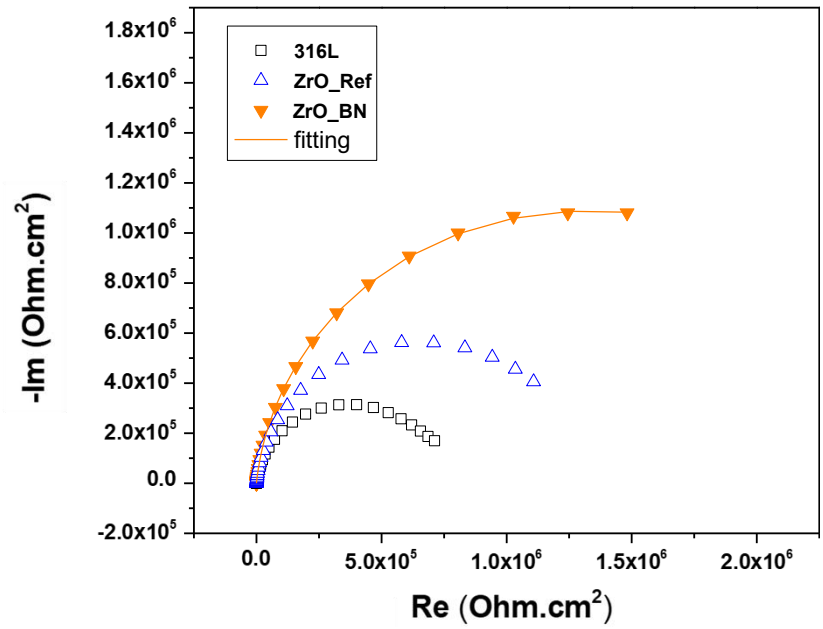

Fig. IV.2 - 14 Nyquist curve of ZrO_BN with fitting and superposed with bare 316L substrate and ZrO_Ref

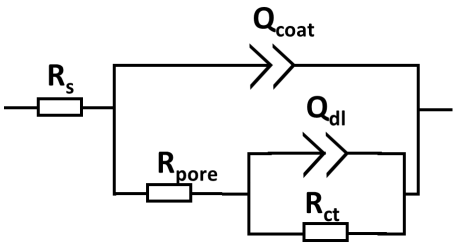

Fig. IV.2 - 15 EEC for ZrO_BN long term duration of EIS test

Table 4 - 3 Fitting parameters of ZrO_BN by BNNS with average size of 4.5 μm at 24 hours immersion in NaCl solution

Sample	R_s /ohm.cm²	R_{pore} /ohm.cm²	α_{coat}	Q_{coat} /f.s^(a-1)	C_{coat} /μF	R_{ct} /ohm.cm²	α_{dl}	Q_{dl} /f.s^(a-1)
ZrO_BN 24h	32.21	2.08E +06	0.93	1.14E -05	2.14	3.38E +06	0.53	1.81E -05

IV.2.4 Influence of morphology of BNNS on ZrO/316L

In the last part, it was understood that the BNNS improves the barrier effect of ZrO coating. However, the enhancement needs to be optimized. As an inert nanofiller, the physical properties of BNNS, especially the size of the atomic layers, may play an essential role in the improvement.[13] Thus, the three raws BN powders with different average diameters developed in chapter II were selected to perform this optimization study.

The previous ZrO_BN is of an average diameter of 4.5 μm. The other two BN powders have a larger size of 7 μm and a smaller size of 1 μm. The nanocomposite coating samples are named according to the size of the raw BN powders. For further discussion, ZrO_BNA denote to the one that has been discussed before with the intermediate size (4.5 μm) ZrO_BNB is the one with smallest BN (1 μm), ZrO_BNC is the one charged with the biggest BN (7 μm).

The evolution of Open Circuit Potential (OCP) values of BNNS charged samples in NaCl solution (3.5 *wt*%) are shown in Fig. IV.2 - 16. All coated samples show stabilized OCP after 6 hours of immersion. The OCP Values of all three samples are in the range of 80 mV, which could be considered as the same values. Among them, ZrO_BNA displays the lowest potential.

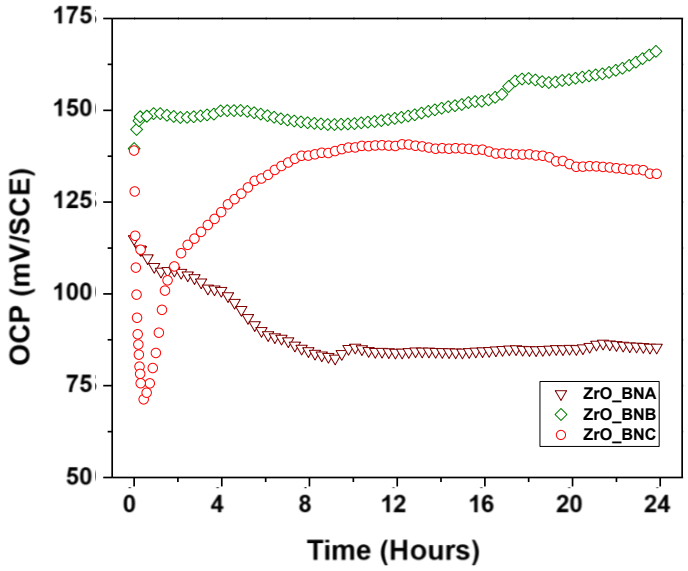

Fig. IV.2 - 16 OCP of three different BNNS charged ZrO coated samples in 24 hours of immersion in NaCl 30g/L solution

From the polarization curves of the nanocomposite coatings shown in Fig. IV.2 - 17, Different samples showed similar electrochemical behaviors. The coating limits the reactivity of the substrate significantly. Nevertheless, some differences in the behavior can be discussed.

In the case of ZrO_BNB, the nanosheet is of a smaller size than BNA, while its polarization curve is rather similar to ZrO_Ref. It seems that the smaller sized BNNS cannot influence the barrier properties. The polarization curve of ZrO_BNC shows a higher E_{corr} than ZrO_BNA and a lower current density, which is one order of magnitude lower at the beginning part of the anodic curve. The lower current densities are obtained from the biggest BNNS size that seems to promote the corrosion resistance of the coated system.

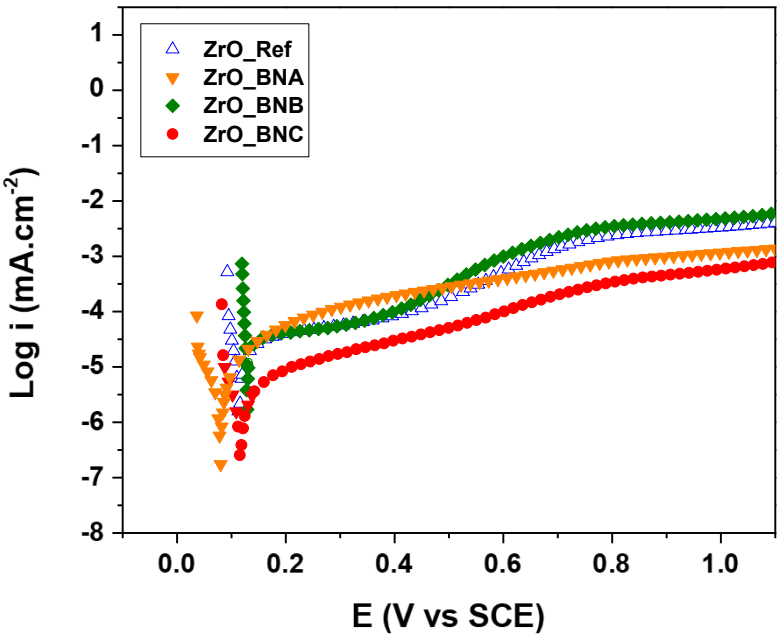

Fig. IV.2 - 17 Electrochemical dynamic polarization curves in NaCl 30g/L of all BNNS charged samples

Fig. IV.2 - 18 shows the surface morphology of both ZrO_BNB and ZrO_BNC after the polarizations. ZrO_BNC shows much less under deposit corrosion than ZrO_BNB, and ZrO_BNA (see Fig. 4.3 - 3). Both polarization curves and SEM images reveal the fact that ZrO_BNC shows the best corrosion resistance.

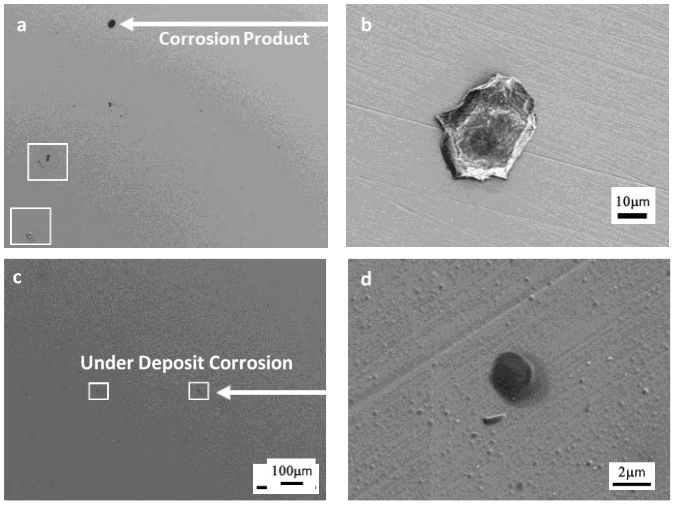

Fig. IV.2 - 18 SEM image of the surface morphology obtained with a) ZrO_BNB and b) zoom on the corrosion product of ZrO_BNB , c) ZrO_BNC and d) zoom on corrosion product of ZrO_BNC

Based on the behavior of these nanocomposite coatings, we can define the critical nanofiller size d_c as the minimum size to improve coating's barrier property. The influence of BNNS according to its different sizes can be described as:

1) Without nanofiller, the electrolyte penetrates via sol-gel coating's interparticle and intercluster pores to the substrate. The way of penetration depends on the microstructure of the Sol-Gel matrix and its affinity to the corrosive reactants, as shown in Fig. IV.2 - 19a.

2) When the BNNS average size, $d < d_c$, the nanofiller is too small to seal totally the coating's pores. Consequently, the electrochemical behavior of the coated system is mainly characterized by Sol-Gel matrix properties, as shown in Fig. IV.2 - 19b.
3) When $d \sim d_c$, the BNNS with a bigger size seals the pores inside the coating and reduce the oxidation rate, as shown in Fig. IV.2 - 19c.
4) When $d > d_c$, the penetration pathway is furtherly prolongated. The migration of the material has to take the tortuous way to reach the metal surface.[14,15] At the same time, the system's resistance is predominated by the mass transfer process, as shown in Fig. IV.2 - 19d.

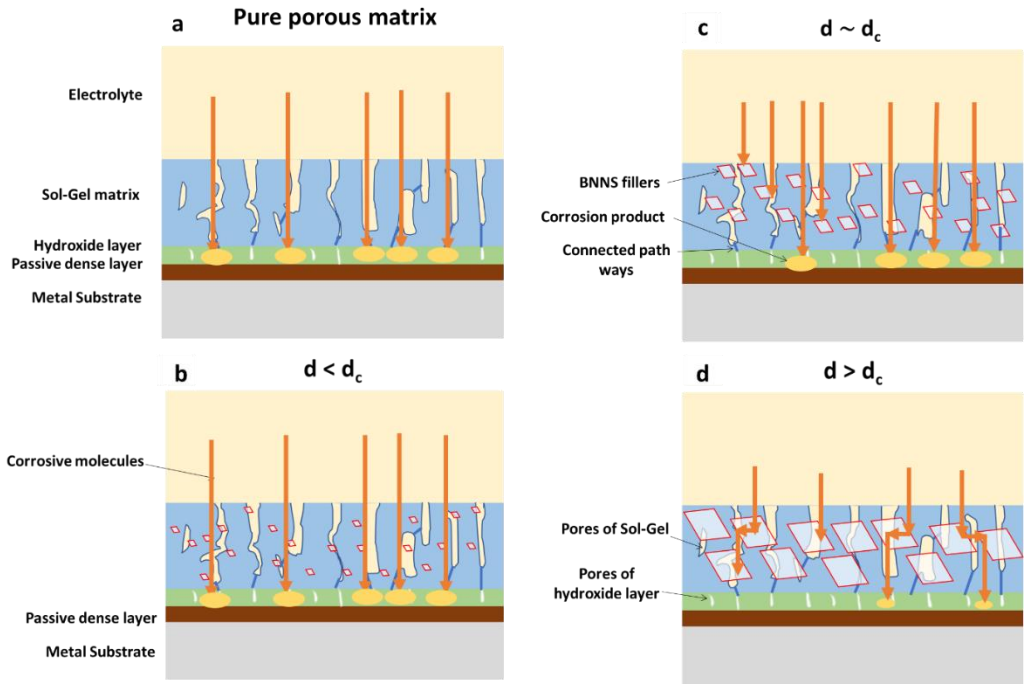

Fig. IV.2 - 19 Scheme of the 2D fillers in sol-gel coating system: a) pure porous Sol-Gel matrix without filler, b) filler with size $d < d_c$, c) filler with size $d \sim d_c$, d) filler with size $d > d_c$

The arrows indicating the penetrating corrosive reactant are mostly representing chloride ions and oxygen molecules. It is important to note that the critical dimension d_c is not an absolute value but depends closely on the mesopores of the sol-gel matrix. Meanwhile, the doping content is another vital parameter that can influence the d_c value for a coating system. It should be noted that the effect of the nanofiller is also limited by its dispersion in the Sol. For the BNNS with a much bigger size than d_c, an agglomeration may take place and limits the homogeneity of the nanocomposite. Therefore, an optimal size exists with which the coating would perform the best corrosion protection behavior.

The Nyquist plots of EIS obtained at OCP of BNNS charged coating after 24 hours of immersion in 30 g/ml NaCl solution are compared in Fig. IV.2 - 20. At high frequency, all samples behave similarly. The High-frequency behavior characterizes the capacitance properties at the electrolyte/coating interface. At low frequency, ZrO_BNC shows the biggest diameter of the semicircle loop, meaning the most promising corrosion resistance which is in good agreement with the polarization. ZrO_BNC showed slightly better EIS performance than ZrO_BNA at OCP, which is coherent to the observation from the polarization curve shown in Fig. IV.2 - 17.

Hereafter, ZrO_BNC coating was chosen for long-duration EIS analysis to study the nanocomposite coating aging in NaCl solution.

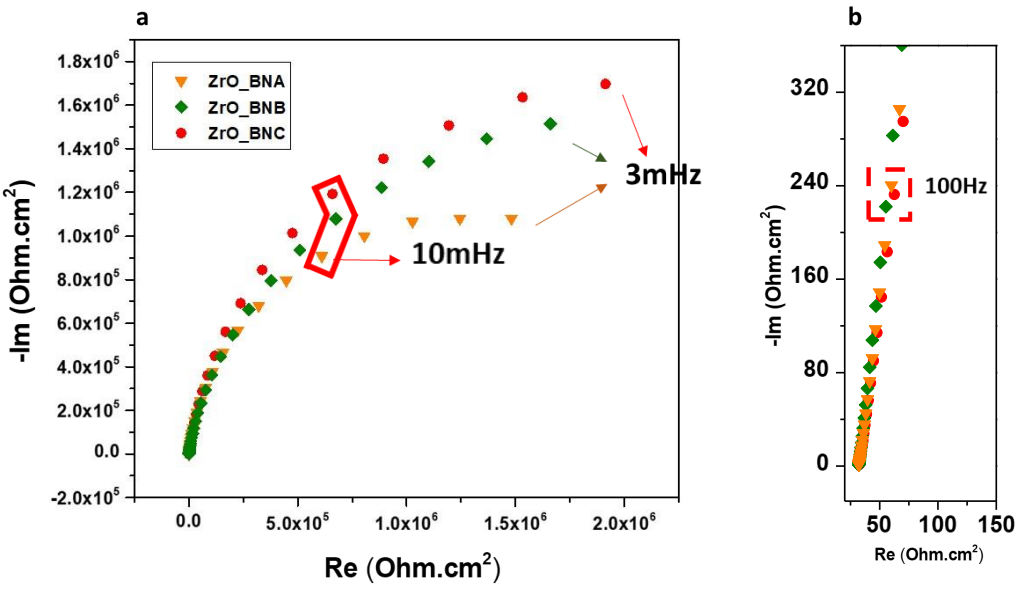

Fig. IV.2 - 20 the Nyquist curve of ZrO coated samples with three different BNNS fillers after 24 hours immersion in NaCl 30g/L at OCP with a) full range of frequency b) zoomed area at high frequency

The evolution of ZrO_BNC nanocomposite coating system was studied by longterm EIS analysis. The Nyquist and Bode plots of ZrO_BNC over immersion time is depicted in Fig. IV.2 - 21. The first observation from Nyquist curve, shown in Fig. IV.2 - 21a, reveals a constantly increasing trend of the semicircle loop over time (black arrow). This variation indicates a significant enhancement of resistance, which is unlike what happened to the 316L substrate (see Fig. 4.1 - 5) and the ZrO_Ref (see Fig. 4.1 - 12). For the laters, the semicircle loop was reduced or remained stable over immersion time.

Fig. IV.2 - 21b shows the bode curves obtained with ZrO_BNC. Two time constants can be observed, among which one stands for the resistance and capacitance of coating and film, while the other one stands for the charge transfer resistance and double layer capacitance. It can be observed that the middle frequency time constant is stable and has a maximum phase

angle of -85°, which is higher than the one of 316L at 120h. Meanwhile, the low frequency time constant shifts to a lower frequency due to an increased corrosion resistance.

To better understand the aging of ZrO_BNC, the numerical fitting of EEC was performed and discussed with the EIS measurement extended to fifty days (1200h).

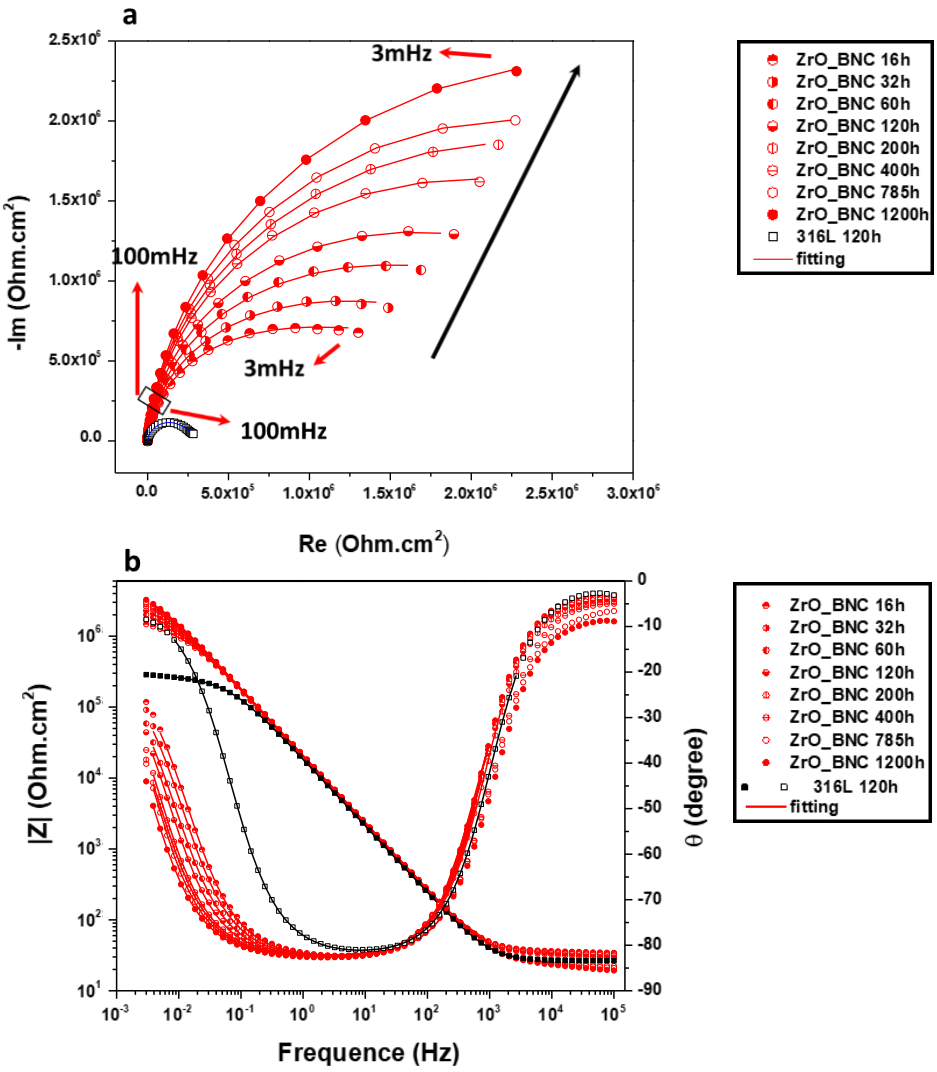

Fig. IV.2 - 21 a) Nyquist plots and b) Bode plots of ZrO_BNC long-duration tests and 316L at 120 hours as reference (Black arrow noting the evolution direction over time of the data of ZrO_BNC)

The EIS results are fitted by the numerical tool using the same EEC with two time constants as for the ZrO_Ref shown in Fig. 4.1 - 7. The fitting parameters of ZrO_BNC are shown in Annexe 1 in detail. Fig. IV.2 - 22 shows the evolution trend of R_{film} and R_{ct} for the bare 316L substrate, ZrO_Ref, and ZrO_BNC during 120h of immersion. As discussed in the reference part (IV.1.1 and IV.1.2), the overall resistance (R_{film} + R_{ct}) of 316L decreased due to the chloride ions contamination. With the deterioration in the passive film, the corrosion resistance decreases simultaneously.

Meanwhile, for pure ZrO_Ref coating, the R_{ct} value is at first higher than that of the bare substrate and then converges to the curve of 316L after 72h of immersion. This similarity can be explained by that the pure sol-gel coating cannot cause a sufficient influence on metal

surface reactivity. Since the xerogel coating is mesopores, the susceptible spots (inclusion, defects…) in the passive film can not be covered and are exposed to the electrolyte. On the other hand, the R_{film} or R_{pore} value mainly characterizes the barrier effect of the coating. The slight decrease of the R_{pore} in ZrO_Ref is due to the deterioration of the coating matrix or the adsorption of the ions through the coating. [16] The Sol-Gel coating shows, in general, good stability and inertness.

However, the evolution of ZrO_BNC is quite different compared with both the bare substrate and the ZrO_Ref. Firstly, the value of charge transfer resistance R_{ct} at the end of 120h is six times higher than the substrate and the ZrO_Ref. The higher R_{ct} value involves a lower metal surface reactivity since less metal surface under deposit is exposed to the electrolyte. In the second place, the R_{pore} of ZrO_BNC is higher than ZrO_Ref. This enhancement of the barrier property is classically explained by the "tortuous pathway" mechanism that involves a prolonged diffusion period within the coating.[17] Upon 24h, the resistance R_{pore} increases, which should be attributed to the sealing effect of the oxidation product in the already established penetration pathway.[18]

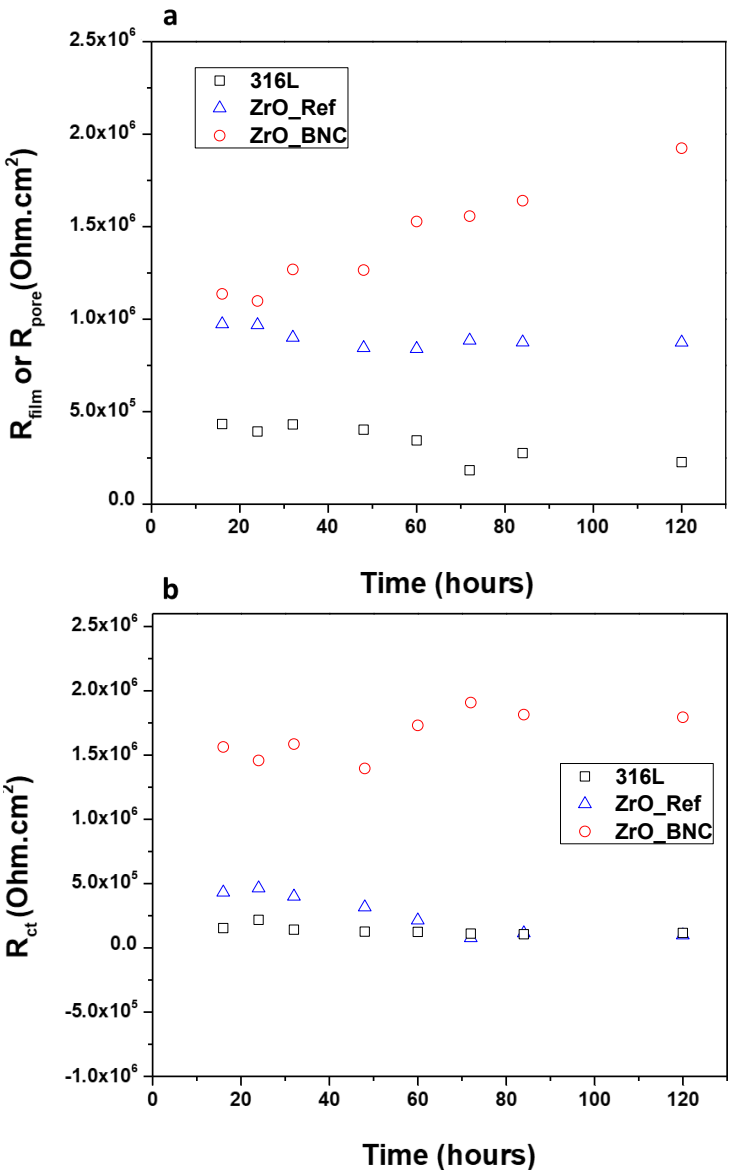

Fig. IV.2 - 22 The evolution of EIS fitting parameter value over 120 hours of the three samples a) $R_{film\ or}$ R_{pore}, b) R_{ct}

During the 1200 hours of immersion, the CPE exponent value α_{coat} stays stable over time, indicating stability of the coating and the passivation film, as shown in Fig. IV.2 - 23a. However, the CPE exponent α_{dl} of the double layer increased from 0.51 to 0.85, which reveals a transition from a diffusion to a capacitive behavior at the bottom of the pores. This transition is also associated with the accumulation of the oxidation product that seals the coating pores. Specifically, after 400h of immersion, the α_{dl} value increased from 0.51 to 0.7, indicating that the electrochemical system became a kinetic limiting process.

Besides, it can be observed that the resistance in the coating pores R_{pore} kept increasing until 1200 hours of immersion, reaching 4.73 x10^6 Ohm.cm^2 that is four times higher than the initial resistance and six times higher than the stabilized R_{pore} of ZrO_Ref. The increase of the R_{pore} is with a similar reason of the increasing trend within 120 hours. The R_{ct} slightly increased, which is almost 10 times higher than the R_{ct} of 316L substrate and ZrO_Ref, indicating as well an increased corrosion resistance over time.

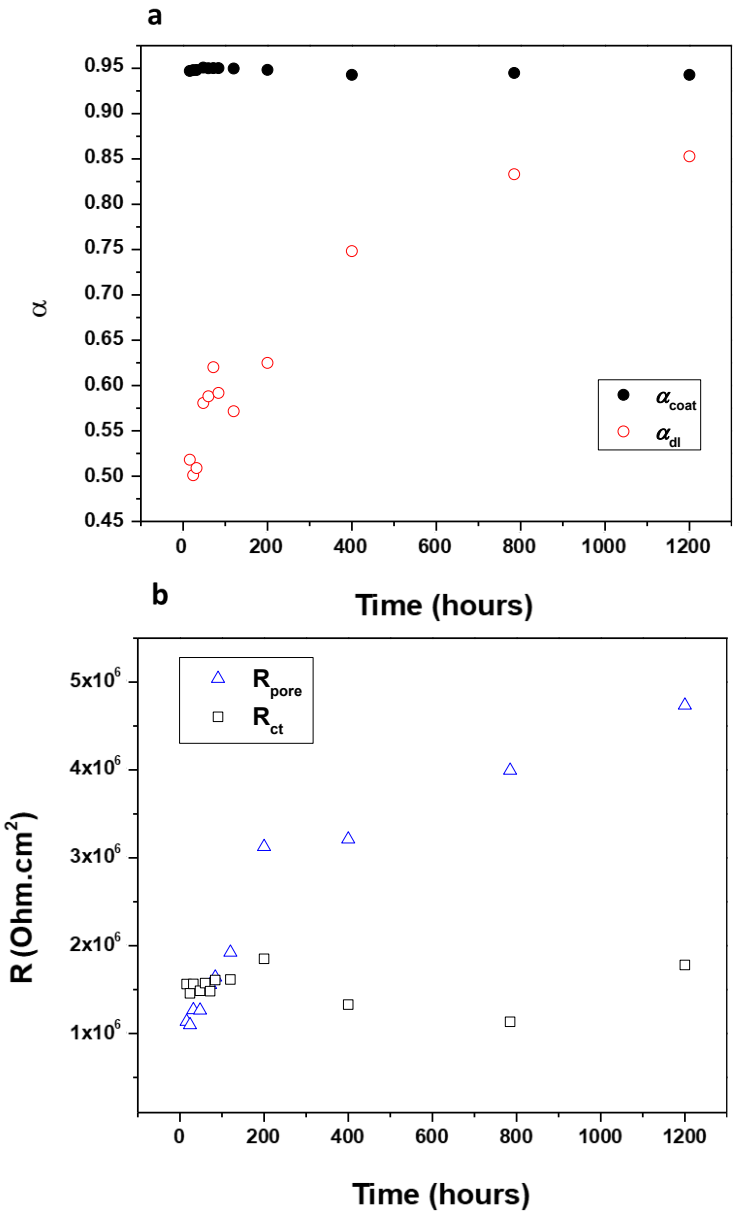

Fig. IV.2 - 23 The evolution of ZAH_BNC of a) α_{coat} and α_{dl} values and b) R_{pore} and R_{ct} values over 1200h

To sum up, the aging behavior of BNNS filler charged ZrO coating with optimized BNNS size will seal the established penetration path over time by the synergy effect of the BNNS barrier and the oxide product. The coated system behaved a robust barrier effect with a capacitive double layer and an increasing resistance (R_{pore} + R_{ct}) that is stabilized after 1200h of immersion in 3,5w% NaCl solution. This overall resistance of ZrO_BNC at 1200 hours of immersion is 6.5 x10^6 Ohm.cm^2 that is 20 times higher than the stabilized value 316L at 120 hours of immersion.

IV.2.5 Influence of concentration of BNNS on ZrO/316L

Except for BNNS's morphology, its concentration also plays a vital role in the performance of nanocomposite coating.[19] The concentration of 15 μg/mL has been reported to be a stable concentration for BNNS in aqueous solution at room temperature.[20] When the BNNS concentration becomes higher than this value, the aggregation may take place and cause unexpected defect or crack in the inorganic matrix. That is why most researchers have used aqueous solutions with various surfactants[21], appropriate ions[22], or chemically modified BNNS[23,24] to improve the homogeneity and limits these risks. Thus, it is interesting to explore the influence of high concentration BNNS (> 15 μg/mL) in zirconium-based sol-gel coating on its barrier effect.

To this end, the centrifuge time of BN-C in aqueous media is reduced to 40min, 30min, 20min, and 10min to prepare the higher concentrated colloidal solutions. The so-obtained solution concentrations are 60 μg/mL, 90 μg/mL, 130 μg/mL, and 170 μg/mL. The corresponding coatings are named ZrO_BN60, ZrO_BN90, ZrO_BN130, and ZrO_BN170, respectively. The exfoliated BNNS solutions were added to the Sol with the same preparation parameters used for ZrO_BNC then deposited on 316L substrate, see Chapter II – II.6.1. The electrochemical behavior of the samples with different concentrations will be compared.

The OCP values of the coatings are listed in Table 4 - 4. ZrO_BN130 and ZrO_BN170 samples have similar OCP values to that of the references and to that of the ZrO_BNC coatings. On the contrary, ZrO_BN60 and ZrO_BN90 display both low OCP values, which are even lower than the ZrO_Ref.

Table 4 - 4 Open Circuit Potential values of the ZrO coatings charged BNNS with different concentration

Samples	OCP (mV/SCE)
ZrO_BN170	72.5
ZrO_BN130	50.5
ZrO_BN90	-130.5
ZrO_BN60	-140.5

To further understand these behaviors, the EIS tests were performed. Fig. IV.2 - 24a plots the Nyquist curves after 24 hours of immersion in 3.5w% NaCl solution. Compared with the Nyquist plot of ZrO_Ref shown in Fig. 4.2 – 6, ZrO_BN60, and ZrO_BN90 show smaller semicircle loops. With the increase of BNNS concentration, there is a noticeable broadening

in the semicircle loop. ZrO_BN170 shows a capacitive behavior and its high frequency behavior are shown as zoomed from in Fig. IV.2 - 24b. With the continually increasing concentration of BNNS, as observed from Fig. IV.2 - 24a, the capacitive behavior increases. Finally the Faradic process is replaced by a total capacitance behavior for ZrO_BN170, which provides a substantial impermeability.

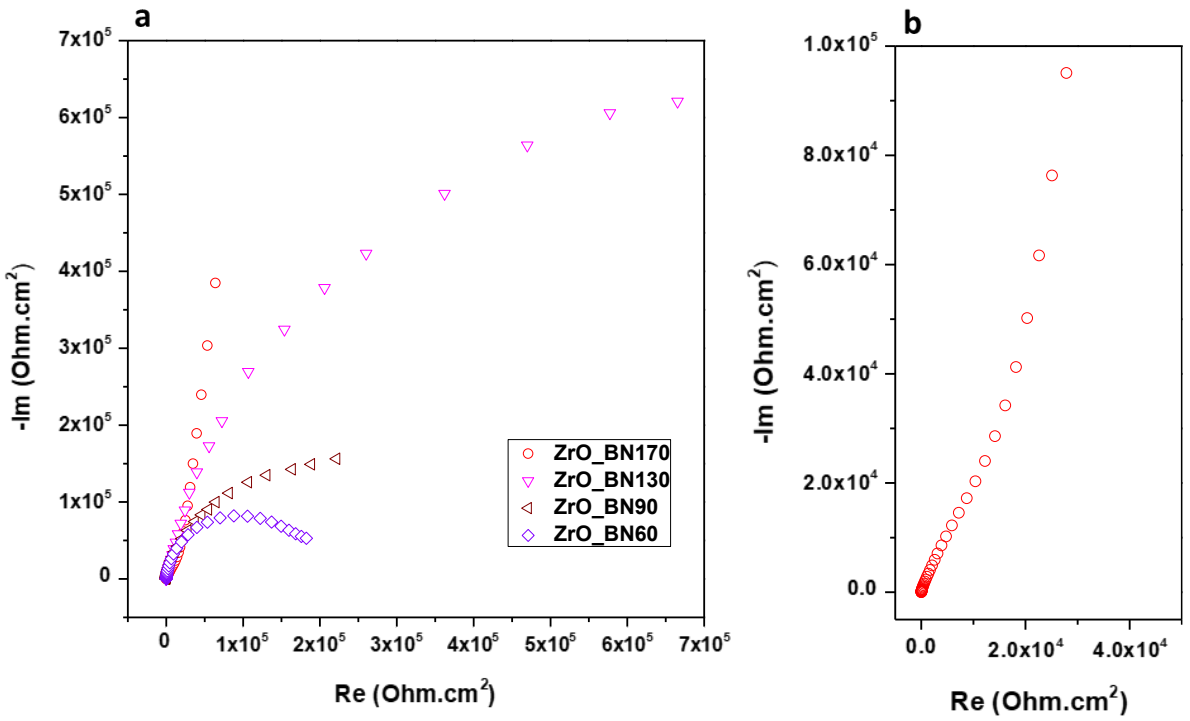

Fig. IV.2 - 24 Nyquist plots at OCP at 24 hours of immersion in NaCl solution of a) ZrO coatings charged with different BNNS b) Zoomed region at high frequency for ZrO_BN170

The Bode curves of coatings are superposed in Fig. IV.2 - 25. The corresponding EEC of all samples are shown in Fig. IV.2 - 26. We used the same EEC for ZrO_BN60, ZrO_BN90, ZrO_BN130 as for the reference samples. In Fig. IV.2 - 26b, the EEC represents for ZrO_BN170 with a CPE due to its capacitive behavior from the whole coating system. The strong capacitive behavior of ZrO_BN170, represented by Q_{sys}, blocks the detection of the signal from the coated sample, which limits the selection of the EEC. The fitting parameters of ZrO_BN60, ZrO_90 and ZrO_130 at 24 hours of immersion are given in Table 4 - 5.

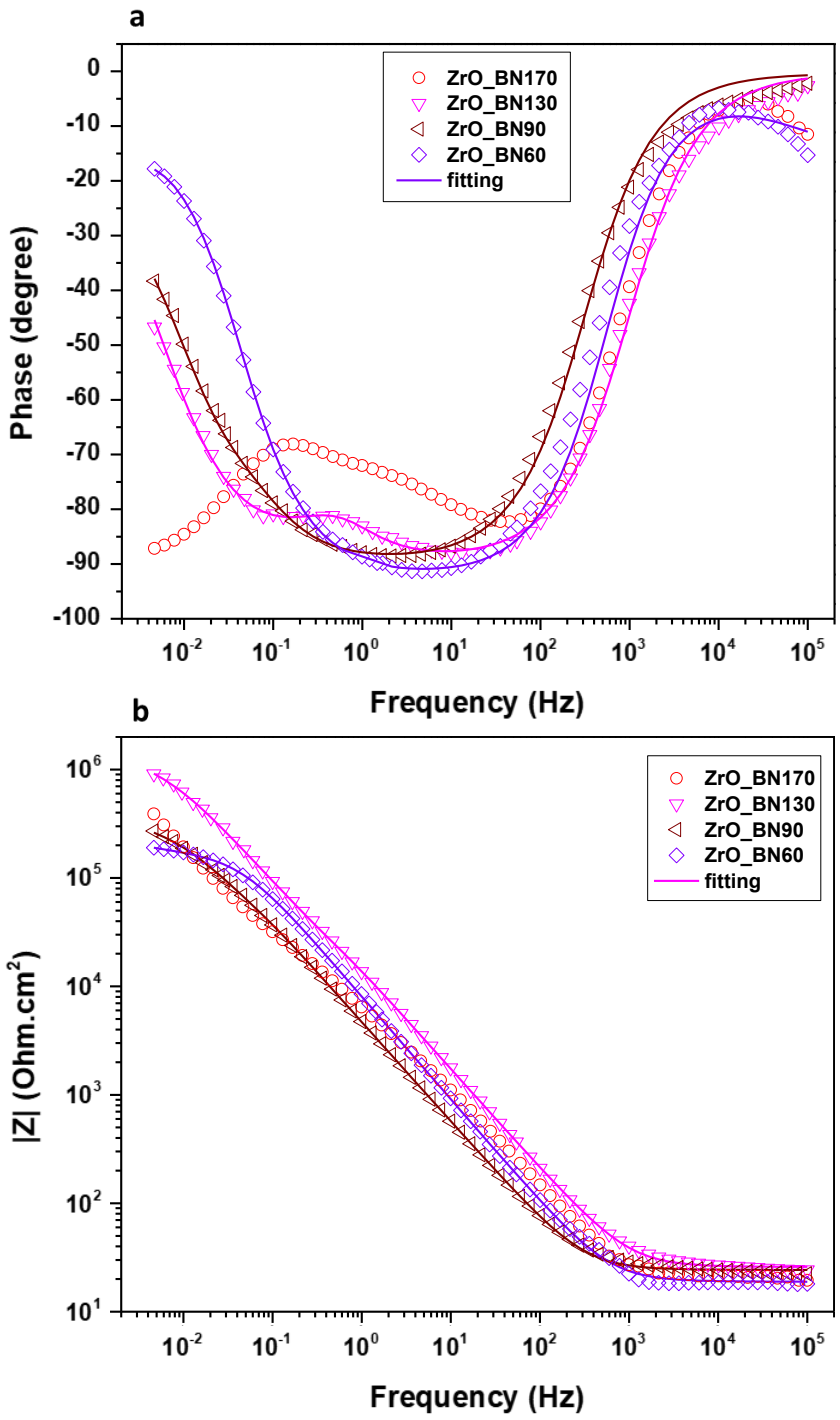

Fig. IV.2 - 25 Bode curves of ZrO coatings charged with BNNS with different concentration a) Phase curve (with red arrows indicating the lowest point of ZrO_BN170), b) Impedance curve.

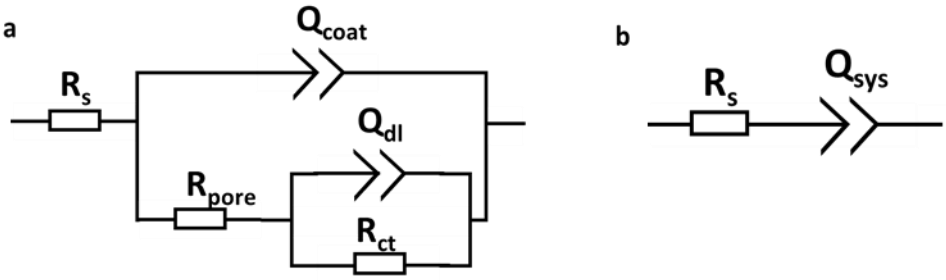

Fig. IV.2 - 26 EEC for a) ZrO_BN60, ZrO_BN90, ZrO_BN130 and b) ZrO_BN170

Fig. IV.2 - 27 plots the fitting parameters for different coatings with increasing BNNS concentration. ZrO_BNC has much higher R_{pore} and R_{ct} values than ZrO_BN60, ZrO_BN90, ZrO_BN130. ZrO_BN60 showed a low R_{pore} and R_{ct} though the concentration are much higher than the one of ZrO_BNC. It is logical that the aggregation of the BNNS reduces the nanocomposite coating's resistance in the pores since more defects will be formed. [25,26] With the concentration increase, the R_{ct} kept increase due to less corrosion, which indicates the predominant influence of BNNS has switched from defects to barrier effect. Considering ZrO_BN170, the impermeable film had been formed, no charge transfer were observable.

The capacitive behavior of the coating also evolves according to the increase of concentration. The α_{coat} stays stable for all samples, indicating a similar passive behavior of all samples. On the contrary, the α_{dl} increased with the increase of concentration of BNNS from 0.54 to 0.82 until a barrier film is observed for ZrO_BN170. This variation trend evident a transition from a kinetic limit process to a capacitive process with the increased BNNS concentration.

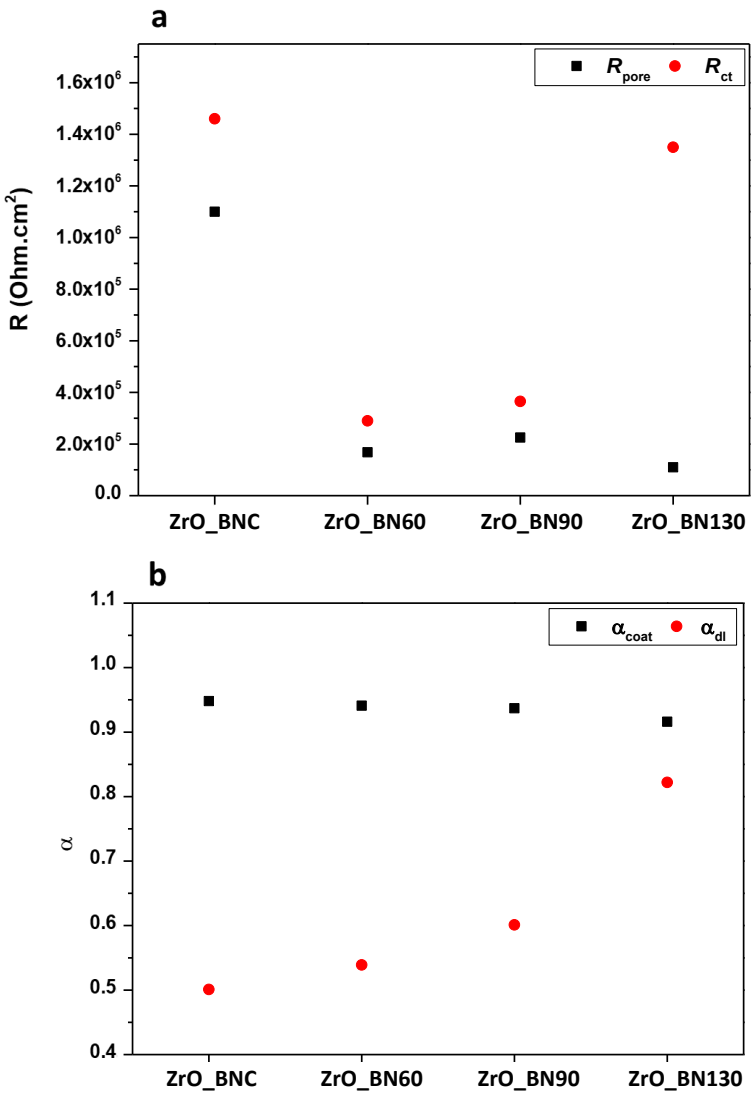

Fig. IV.2 - 27 Comparison of fitting parameters between ZrO_BNC and ZrO_BN60, ZrO_BN90, ZrO_BN130, ZrO_BN170 for a) R_{pore} and R_{ct} and b) α_{coat} and α_{dl}

Table 4 - 5 Fitting parameters of ZrO_BN60, ZrO_BN90 and ZrO_BN130 at 24 hours of immersion

Samples	R_s /Ohm.cm^2	Q_{coat} /F.s^(a-1)	α_{coat}	R_{pore} /Ohm.cm^2	C_{coat} /μF	Q_{dl} /F.s^(a -1)	α_{dl}	R_{ct} /Ohm.cm^2
ZrO_BN60	21.43	2.64 E-05	0.94	1.68 E+05	5.12	1.31 E-04	0.54	2.90 E+05
ZrO_BN90	23.83	2.68 E-05	0.94	2.25 E+05	4.72	3.28 E-05	0.61	3.65 E+05
ZrO_BN130	25.89	1.29 E-05	0.92	1.10 E+05	3.75	0.42 E-05	0.82	13.5 E+05

A hypothesis has been given to explain the electrochemical behavior of the coatings. Allowing the Sol is homogenous, the BNNSs distribution within the solid-state film was mainly manipulated by the shaping process. As observed from the SEM images shown in Fig. III.3 - 3, the BNNS are all distributed in coating in parallel. Fundamentally, dip-coating is a microscale capillary filtration process.[27] In the withdrawing direction, the substrate surface was firstly wetted by the dispersion solution. The nanofiller is driven by the capillary force along the

direction indicated by red flashes in Fig. IV.2 - 28a.[28] Çamurlu et al. noted that the agglomerated BNNS might enrich at the surface of the coating.[23] Consequently, after the drying step, a concentration gradient of BNNS inside the coating, decreasing from the outer side to the inner side, will be forged. Given the coating thickness of three-layers is 400nm, as shown in Fig. IV.2 - 28b, each dip contributed less than 150 nm in liquid-phase if we took the shrinkage into account. Since the single-dip thickness is much smaller than BNNS lateral size, these 2D materials were spread out by the capillary force and orientated in parallel with the coating surface and formed an impermeable film.

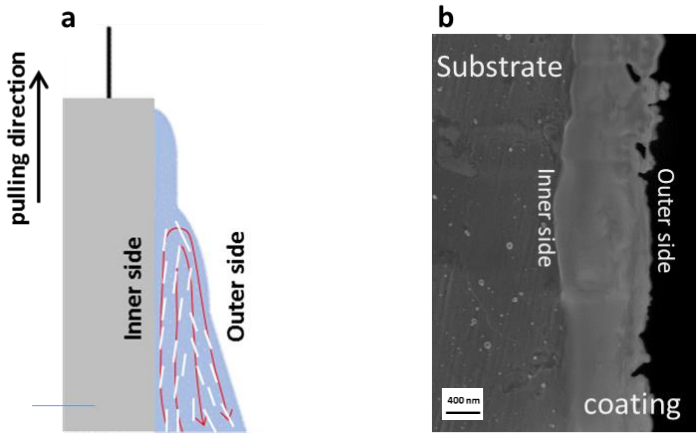

Fig. IV.2 - 28 a) Scheme of the distribution of BNNS during dip-coating b) SEM image of the cross-section of as-dipped coating

Based on the observation, it can be summarized that the influence of the BNNS concentration on the coating's barrier effect, which can be divided into three phases, see Fig. IV.2 - 27.

- I) When the BNNS concentration is low, the dispersion is well-controlled, leading to a high resistance coating system.
- II) When the concentration of BNNS increases, the effect is twofold: 1) the prolongation of the penetration pathway; 2) the aggregation inducing defects, as illustrated in Fig. IV.2 - 29a. The compromise of these two effects makes ZrO_BNC an even better candidate. Meanwhile, the electrochemical system turns more and more capacitive at low frequency.
- III) With the continually increasing BNNS, an impermeable film could be forged and allows almost no penetration to happen, as illustrated in Fig. IV.2 - 29b. The Faradic behavior is thus no more detectable by EIS.

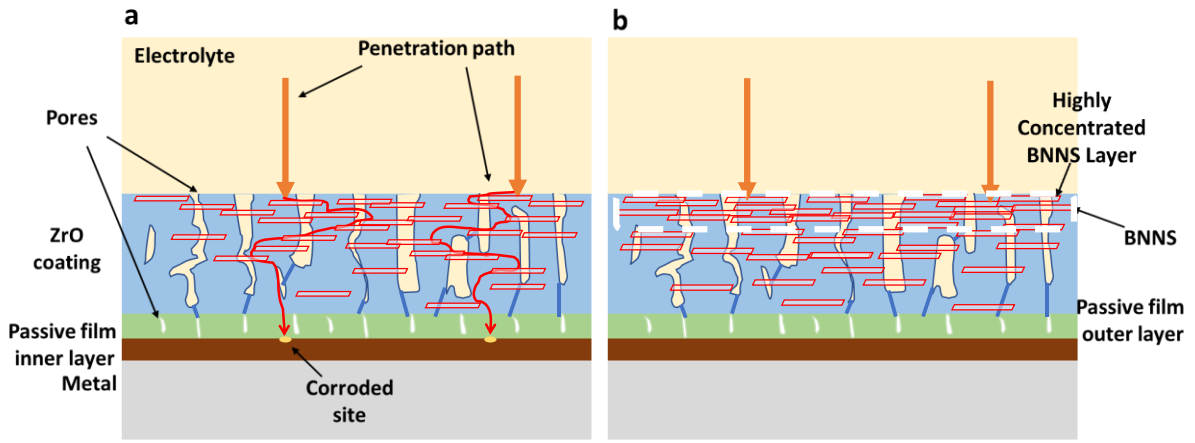

Fig. IV.2 - 29 Model of the porous structure with BNNS filler a) with increased BNNS concentration but no impermeable film b)with an impermeable film

The evolution of ZrO_BN170 immersed in NaCl 3.5wt% in longterm duration has been studied. The Nyquist curves of the ZrO_BN170 from 12 hours of immersion to 8 weeks of immersion are shown in Fig. IV.2 - 30. From Fig. IV.2 - 30a, the Nyquist curves showed a slight decrease of the capacitive due to distributions, porosity effects or fractal geometry effects (as explained in Chapter II – II.3.5) [29,30], which indicates a decrease of capacitive behavior (red arrow). To discuss the EIS behavior in detail, the analysis of Bode curves are separated into two parts before and after one week of immersion.

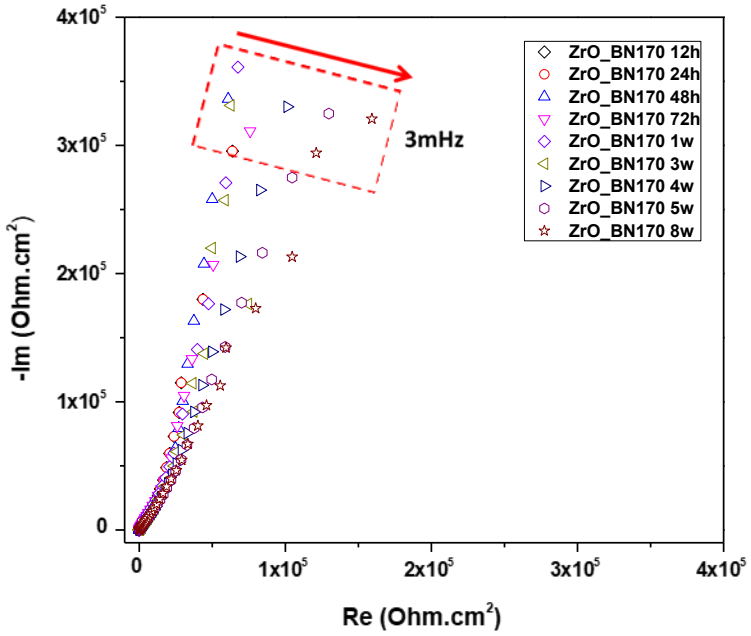

Fig. IV.2 - 30 Nyquist curve of ZrO_BN170 from 3 weeks of immersion till 8 weeks of immersion (With red arrow indicating the decreasing trend of slope of capacitive region)

The bode curves of evolution in one week are shown in Fig. IV.2 - 31. Both have shown little evolution over time, indicating the stability of the coating in one week of immersion.

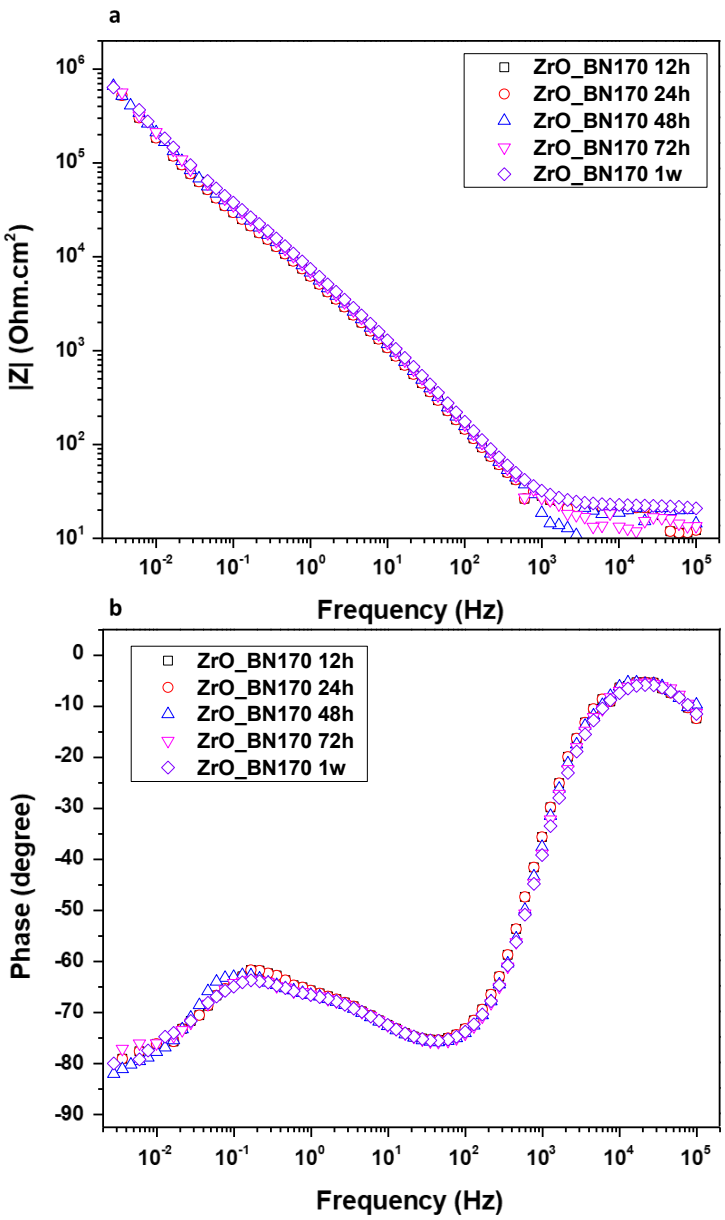

Fig. IV.2 - 31 Bode curves of ZrO_BN170 from 12 hours of immersion till 1 weeks of immersion a) Phase curves b) Impedance curves

The EIS curves and equivalent circuit for ZrO_BN170 coating starting from three weeks are shown in Fig. IV.2 - 32. At high frequency, an extra time constant at high frequencies regime ($10^5 – 10^2$ Hz) can be observed, and its influence decreased rapidly in the following five weeks and disappeared at the end of eight weeks of immersion. This phenomenon is possibly due to the double layer's evolution on the sample induced by the interaction between zirconium oxide and water. The bode phase curves shown from Fig. IV.2 - 32b. At low frequency, the phase angle increased furtherly from -75° to -67°, indicating an attenuation of the barrier effect.

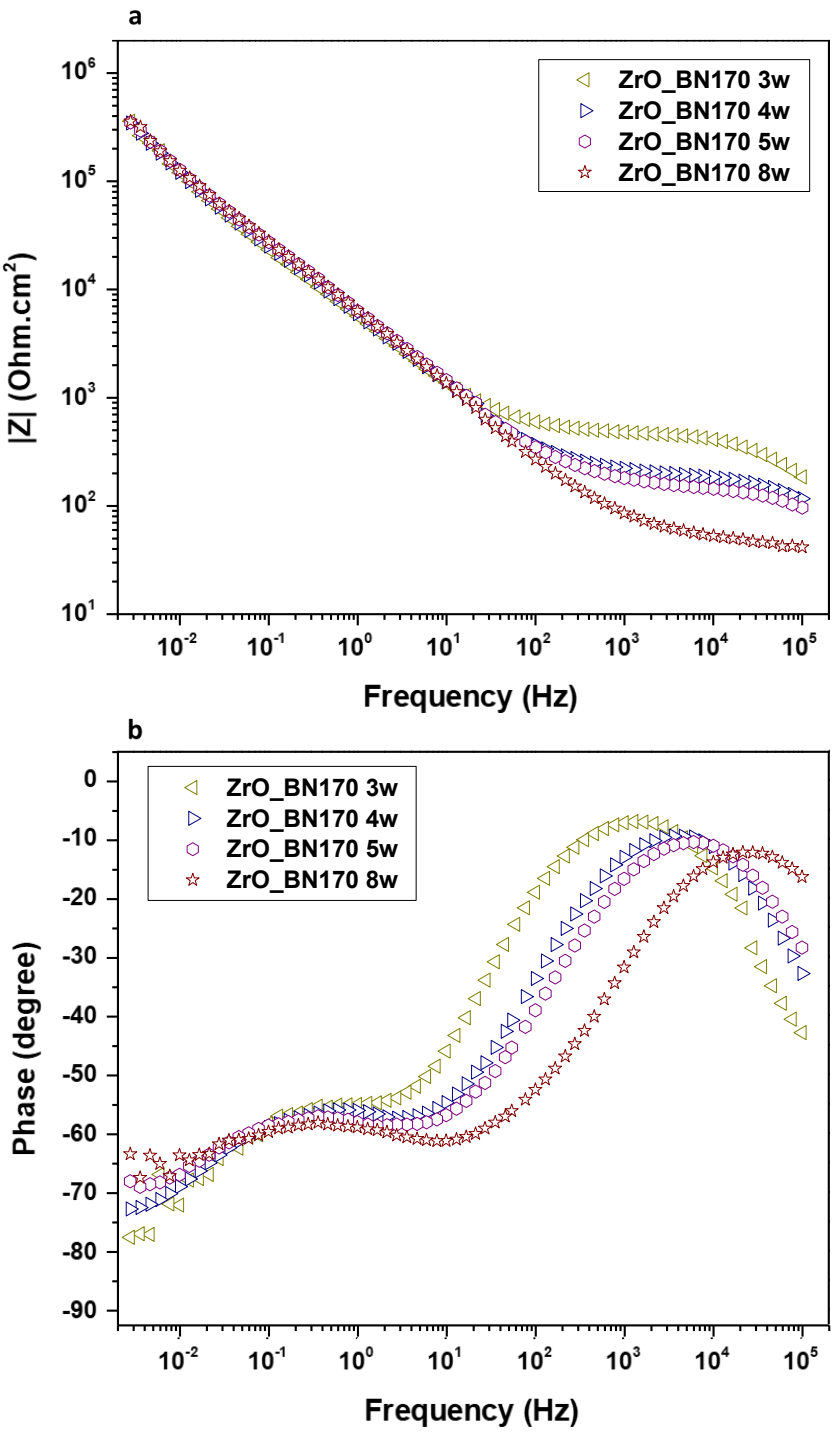

Fig. IV.2 - 32 Bode curves of ZrO_BN170 at 3, 4, 5 and 8 weeks of immersion a) Impedance curves and b) Phase curves

To sum up, the ZrO_BN170 shows excellent capacitive behavior at low frequencies regime, which characterizes a powerful barrier performer under stationary conditions. However, the degradation of this impermeability of the coating started after 3 weeks of immersion. The impermeability provided by BNNS with over critical concentration displayed still a capacitive behavior at low frequency at the end of 8 weeks of immersion. An extra time constant at high frequency is observed starting from 3 weeks of immersion while the semicircle loop of this time constant decreases rapidly in 5 weeks. This is possibly due to the interacton of ZrO coating and the water.

IV.2.6 Conclusion

The study of the influence of the morphology as well as the concentration in ZrO coatings on 316L immersed in NaCl 30g/L solution have been explored and discussed.

The morphology plays an important role in the enhancement of barrier effect by BNNS fillers in the ZrO inorganic coating, by which there is a critical size, 7 μm of average size, for an effective improvement of barrier effect.

The unfunctionalized BNNS showed two influences to the coating matrix: the barrier effect and the introduction of defects.With low concentration, when the size of the BNNS is over critical size, an enhancement of barrier effect can be acquired. When the concentration is high, the introduction of defects predominates and the coating shows decreased barrier effect. With increasing of concentration of BNNS, the influence of defects decreases and the influence of barrier effect increases. After a critical concentration, a total impermeable layer can be observed.

The coating synthesized with the study of morphology and concentration influence of BNNS showed long term stability.

IV.3 Study of BNNS in ZrO-SiO multi-component coating on AA2017

Generally, the protective coating's performance leans on its intrinsic physicochemical properties such as its surface tension, density, elemental composite, *etc*. Nevertheless, the life-time and the endurance of the coating are also associated with the coating/ substrate interface properties. In this part, we attempted to transfer the coating to a more sensitive metal and to evaluate the nanocomposite coating's performance.

Aluminum alloys have a passive film based on a dense Alumina layer, which is less stable than the passive film on 316L.[31] The galvanic couple inside the intermetallic particles distributed in the metal matrix makes it sensitive to localized corrosion, especially with the presence of chloride ions. [32] This makes Aluminum alloy behave a much higher reactivity in NaCl solution compared with 316L. By understanding the evolution of corrosion reaction as well as the regeneration of oxide film on the aluminum alloy, the barrier effect of BNNS could be probed.

IV.3.1 Electrochemical behavior of AA2017 bare substrate

The electrochemical behavior of bare AA2017 substrate has been studied firstly. The potentiodynamic polarization curve of AA substrate is shown in Fig. IV.3 - 1. The corrosion potential is located at -0.77 V *vs.* SCE. The current density steeply increased on the anodic side, indicating an active corrosion that is coherent to the literature report.[33] It is to note that no passive state is observed due to the high concentration of Cl^- ions.

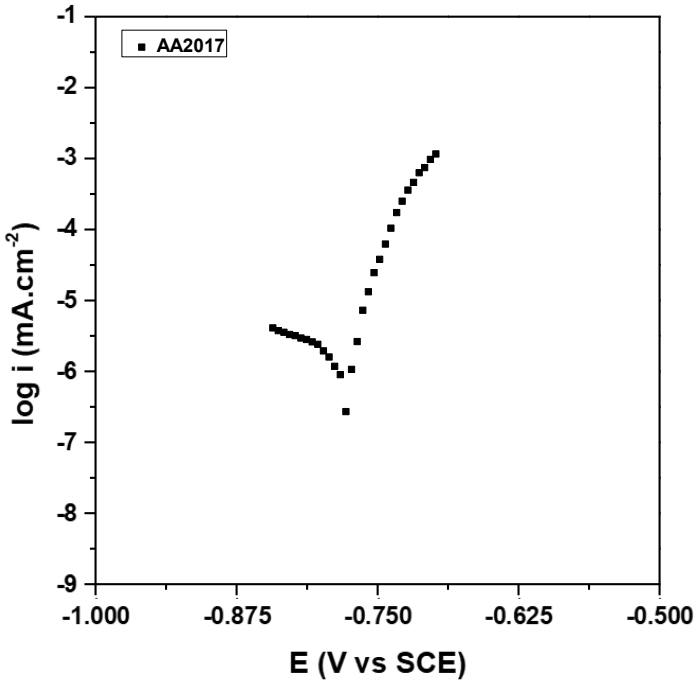

Fig. IV.3 - 1 Potentiodynamic Polarization curves of AA2017 substrate after immersed in NaCl 30g/L solution for 24 hours

The Bode curves of the AA2017 substrate after 6h or 144h of immersion in NaCl 30g/L are shown in Fig. IV.3 - 2. It is observed that AA2017 substrate shows an increasing impedance during immersion under OCP due to the growth of oxide products. The impedance value reaches 4 x 10^4 Ohm.cm^2 at 3 mHz at 144h of immersion. Two time constants can be observed, which are correlated to the oxide film property and charge transfer on the metal surface. [34]

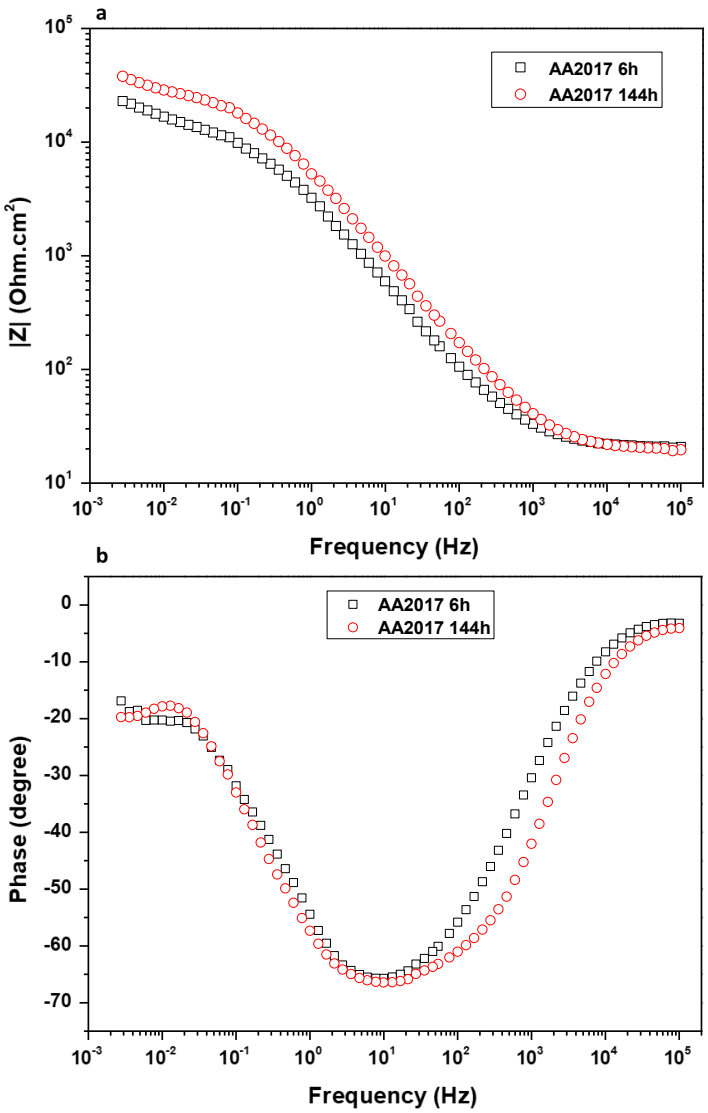

Fig. IV.3 - 2 Bode curves for AA2017 substrate during at 6 hours and 144 hours of immersion in NaCl 30g/L

IV.3.2 Effect of ZrO single-component coating on AA2017

In the first place, we attempted to transfer the ZrO_BNC coating on AA2017 substrate directly. The so-obtained sample is hereafter named AA/ZrO_BNC.

The Bode curves of both AA/ZrO_BNC and AA2017 substrate at 6h and 144h of immersion are compared in Fig. IV.3 - 1. It is observed that AA/ZrO_BNC at 6h of immersion showed a higher phase angle at the middle frequency (red arrow). This slight improvement decreases and disappears after 144 hours of immersion. The Bode curves obtained with the bare and coated AA are converged, meaning that the ZrO_BNC coating cannot bring adequate protection on AA2017.

Indeed, the porous inorganic coating enables the penetration of the corrosive molecules so that the connected aluminum surface undergoes oxidation reaction under deposit. The lateral propagation of the reaction weakens the coating/ substrate adhesion until the total coating de-adhesion.

There are two ways to overcome this issue: 1) the reinforcement of the adhesion to prevent the crack propagation at the interface after the corrosion takes place; 2) increase the coating's barrier effect that restricts the penetration from top to bottom. The first way has been widely considered in many literatures reports to the coating and substrate material coupling. Here, we essentially focus on the second way to optimize the coating's intrinsic properties. To this end, the multicomponent hybrid Sol-Gel coating is a more appropriate choice since it allows the combination of the advantage of different units in the coating.

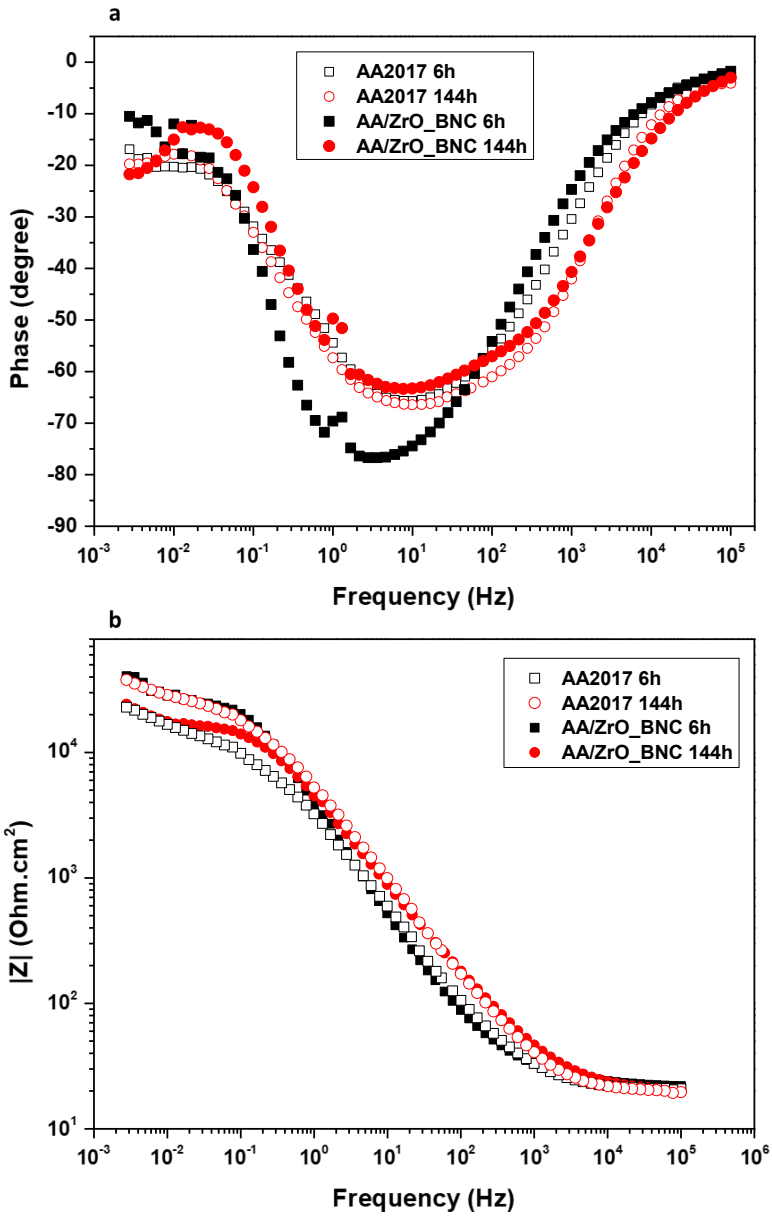

Fig. IV.3 - 3 Bode a) Phase and b) Impedance curves of comparison between AA2017 substrate and AA/ZrO_BNC at 6 hours of immersion and 144 hours of immersion in NaCl 30g/L solution

IV.3.3 Effect of ZrO-SiO multi-component coating on AA2017

The electrochemical behavior of pure ZrO-SiO multi-component coating deposited on AA2017 has been studied, named ZrO-SiO_Ref, see Chapiter II – II.3.2 and II.5.1 for the preparation parameters.

The potentiodynamic polarization curve of the AA2017 substrate and of the ZrO-SiO_Ref after 24 hours of immersion are illustrated in Fig. IV.3 - 4. The E_{corr} of ZrO-SiO_Ref lower than the substrate, indicating an earlier initial potential for the anodic reaction to come to pass. This phenomenon has also been observed by Xue et al.[35] Although the coating did not behave passive state, the current density showed two orders of magnitude lower compared to AA2017 substrate. The deposited coating reduced the exposure surface as well as blocks the penetration of corrosive molecules. It is well known that 2000 series of AA are sensitive to localized corrosion introduced by intermetallic compound,[32] at the grain boundary, and the metal crystalline. The polarization curve is a combination of these two corrosion phenomena. [36] Overall, the reference coating deposited sample showed an improved corrosion resistance with a significantly decreased reactivity of the metal surface.

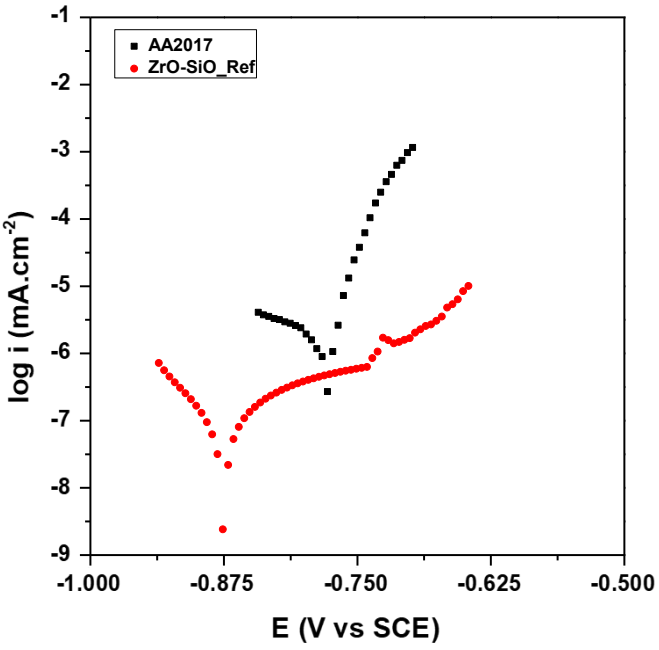

Fig. IV.3 - 4 Potentiodynamic Polarization curves of AA2017 substrate and ZrO-SiO_Ref after 24 hours of immersion in NaCl 30g/L

The bode curves of ZrO-SiO_Ref evolution after one week of immersion in NaCl 30g/L solution are shown in Fig. IV.3 - 5. From Fig. IV.3 - 5a, the evolution of the Bode curve showed a decrease trend at middle and high frequency (see red arrow). This trend is connected to the deterioration of the protective behavior provided by the coating and the oxide film on the substrate.[37]

At high frequency, f = 10^5 Hz, the phase angle initially was -70° at 6 hours of immersion and finally decreased to -40° after one week of immersion. The direction of degradation is shown with the red arrow on top right in Fig. IV.3 - 5b. The first time constant observed from high frequency is attributed to the coating's properties. Its degradation is a sign of the increase in

water penetration rate within coating.[38] At middle frequency, one time constant can be observed between the frequency of $10^1 - 10^2$ Hz. This time constant correlates to the influence of the oxide film on the AA2017 substrate.[39,40] At low frequency, the increase of phase angle indicates the increased corrosion resistance due to the generation of oxide products, see red arrow on the left in Fig. IV.3 - 5b.

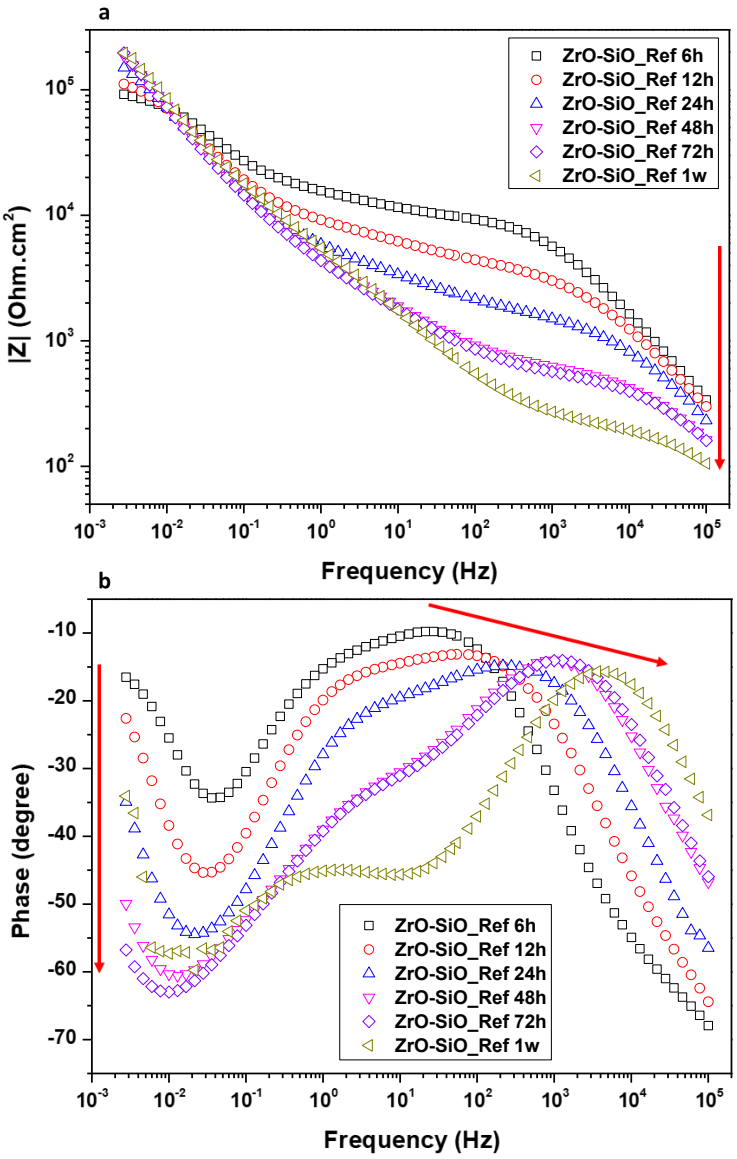

Fig. IV.3 - 5 Bode a) Impedance curves and b) Phase curves of ZrO-SiO_Ref in 1 weeks of immersion in NaCl 30g/L solution

As discussed above, the corrosion protection behavior of the coating is still low. The surface morphology of ZrO-SiO_Ref after one week of immersion has been shown in Fig. IV.3 - 6. It is observed that the under deposit corrosion cause small areas of delamination and weight loss (as shown with white arrows and zoomed region).

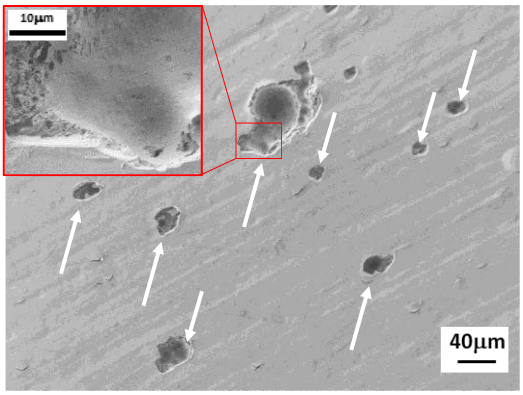

Fig. IV.3 - 6 Surface morphology of ZrO-SiO_Ref after 1 weeks of immersion (White arrows indicating the delamination, red rectangle indicating zoomed region of corroded site)

IV.3.4 Influence of BNNS charged in ZrO-SiO/AA2017

The polarization curves of the coating charged with BNNS superposed with AA2017 substrate and ZrO-SiO_Ref are shown in Fig. IV.3 - 7. ZrO-SiO_BN showed a polarization curve quite similar to that of the ZrO-SiO_Ref. The current density of ZrO-SiO_BN is two orders of magnitude lower than the AA2017 substrate, evidencing the protection effect. The lower E_{corr} showed from ZrO-SiO_BN may be explained by a lateral propagation of the under-deposit corrosion. Indeed, with the zeta potential of -11.3 mV indicating a low stability of BNNS as shown in Fig. III.3 – 12 in Chapter III, the agglomeration of BNNS is inevitable. The presence of agglomerated BNNS will decrease the adhesion property of the coating to the substrate and cause lateral propagation of corrosion until the delamination of the coating.

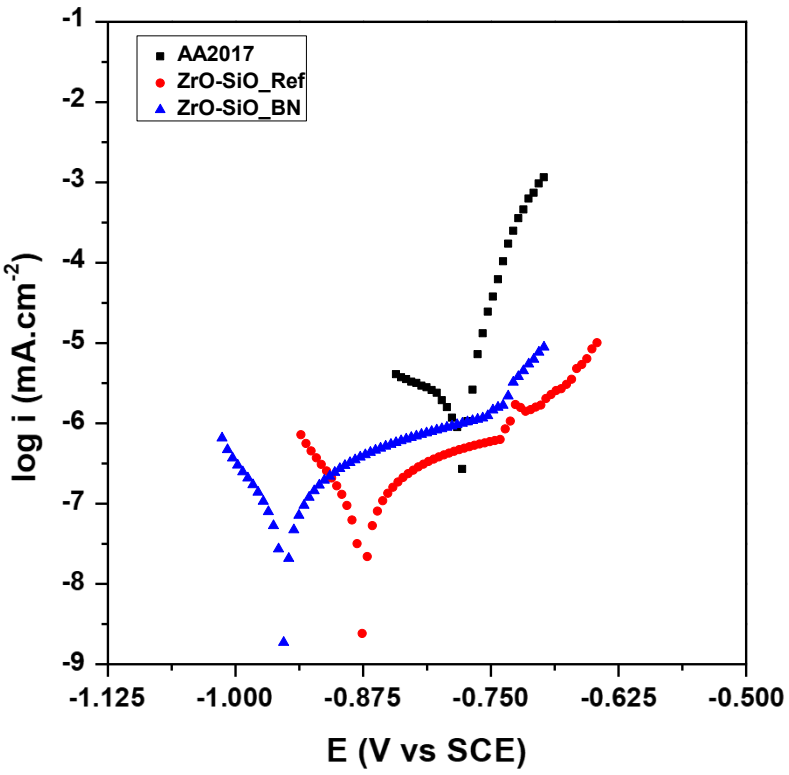

Fig. IV.3 - 7 Potentiodynamic polarization curve for ZrO-SiO_BN superposed with AA2017 substrate and ZrO-SiO_Ref

The bode curve of ZrO-SiO_BN throughout two weeks of immersion are shown in Fig. IV.3 - 8. At the frequency's regime between 10 to 10^4 Hz, a flat stage can be observed, where the coated sample displays exclusively resistive behavior.[41] A flat stage has been observed from ZrO-SiO_Ref, as shown in Fig. IV.3 - 5a. The imperfect flat stage of ZrO-SiO_Ref indicates the existence of penetration of ions, which is due to the overlap of the time constant connected to the coating and the oxide layer. The perfect flat stage of ZrO-SiO_BN represents a total resistive behavior, indicating that the electrolyte are blocked from penetrating the coating at higher frequency than the flat stage due to the sealing of pores by BNNS fillers.[42] The higher impedance value of the flat stage of ZrO-SiO_BN is due to the sealing of the pores by BNNS. Thus, the BNNS charge coating showed a better barrier effect than the reference coating due to the enhancement provided by BNNS.

Comparing to the ZrO-SiO_Ref showing an impedance degradation from 1.5 x 10^4 to 2 x 10^2 Ohm.cm^2 of the in one week, the ZrO-SiO_BN showed a slower degradation rate, from 6 x 10^4 Ohm.cm^2 to 9 x 10^2 Ohm.cm^2 in one week. This depicts that the BNNS charged coating has better stability than the coating without charge. The deterioration of the coating of ZrO-SiO_BN can also be observed from the Phase curve shown in Fig. IV.3 - 8b, from the high-frequency time constant shifted to the higher frequency, which is shown by the red arrow on top of the figure.

The time constant corresponding to the oxide layer showed an increasing capacitive behavior at middle frequency, as shown in the red rectangle in Fig. IV.3 - 8b. This indicates the regeneration of oxide film due to the corrosion. At low frequency, the phase angle also increased, meaning decreased charge transfer reaction rate thanks to the oxide film regenerated on the metal surface, as shown by the red arrow on the left side of Fig. IV.3 - 8b. This is due to the increased quantity of corrosion product which is similar to the trend observed from ZrO-SiO_Ref.

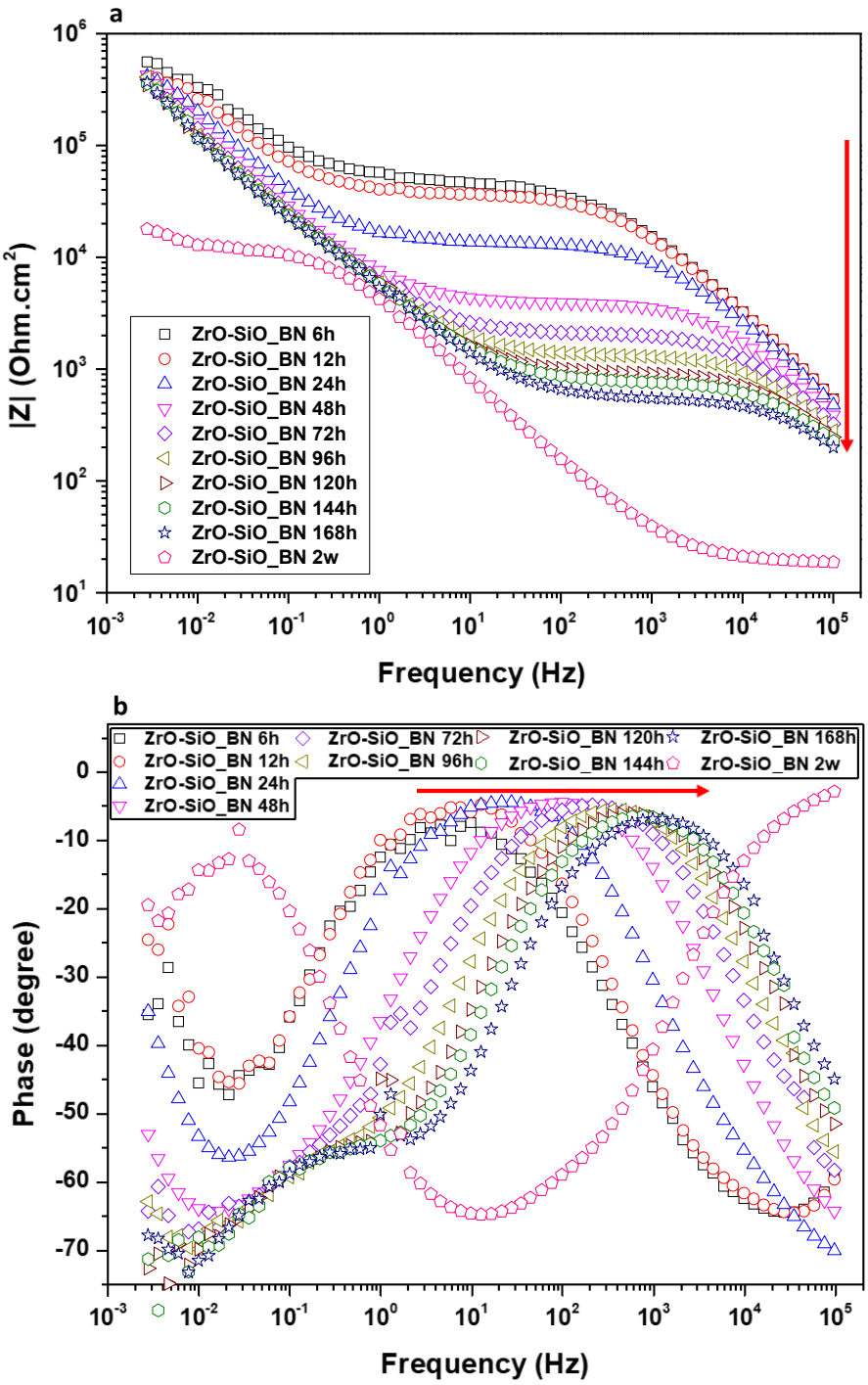

Fig. IV.3 - 8 Bode a) Impedance curves and b) Phase curves of ZrO-SiO_BN in 2 weeks of immersion in NaCl 30g/L solution

According to Bode curves, after two weeks of immersion, the ZrO-SiO_BN showed similar behavior to the bare AA2017 substrate. The surface morphology of ZrO-SiO_BN after 2 weeks of immersion displays a lot of corrosion product see Fig. IV.3 - 9.

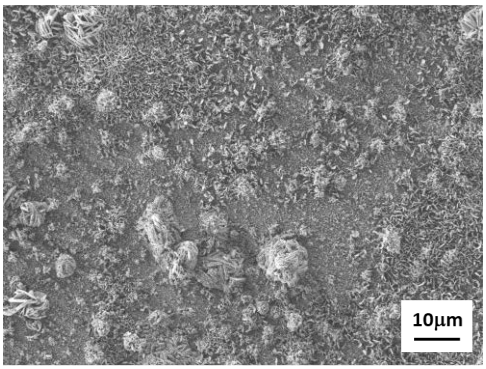

Fig. IV.3 - 9 The SEM image of surface morphology after 2 weeks of immersion in NaCl of ZrO-SiO_BN

IV.3.5 Conclusion

The AA2017 substrate, after immersed in NaCl 30g/L solution, will be severely corroded due to the corrosive environment with chloride ions. The coating without filler showed a barrier effect. However, severe corrosion phenomenon can still be observed.

The BNNS filler has been proved to be able to enhance the barrier effect by limiting the migration of ions. However, the corrosion causes delamination, indicating an insufficient corrosion protection behavior by the coating/BNNS system. The addition of BNNS may also decreases the adhesion property of the coating and accelerate the delamination.

In order to search for a coating/BNNS couple with strong and efficient barrier effect which protects the metal surface, an enhancement of coating matrix will be deposited on an even more sensitive surface to highlight the barrier effect of the BNNS enhanced coating.

IV.4 Study of BNNS fillers in Organic-Inorganic hybrid coating on carbon steel

As discussed in above part, the modification of ZrO-SiO multicomponent coating will be done by adding a hydrophobic modification to the coating with the precursor Octadecyltetraethoxysilane (ODTES). The BNNS will be charged in this coating to study the influence of barrier effect on a metal surface which is even more sensitive than AA2017.

This substrate could enable the probe of role of BNNS under a sensitive corrosion environment. The carbon steel has a much more sensitive surface to a corrosive environment. In 30g/L NaCl solution, once the substrate was reached by the electrolyte, generalized corrosion takes place.

IV.4.1 Electrochemical behavior of carbon steel bare substrate

The electrochemical behavior of bare carbon steel XC90 has been studied in NaCl 30g/L solution. The OCP value close to 24 hours of immersion shown in Table 4 - 6 is similar to the value reported by researchers. [43]

Table 4 - 6 Stabilized OCP value of carbon steel at 24 hours of immersion in NaCl 30g/L solution

Samples	OCP (mV/SCE)
Carbon steel	-729

The Polarization curve of carbon steel is shown in Fig. IV.4 - 1. The E_{corr} is lower than the value observed at OCP. From the anodic part, the current density increases steeply, which corresponds to a general corrosion phenomenon on the metal.

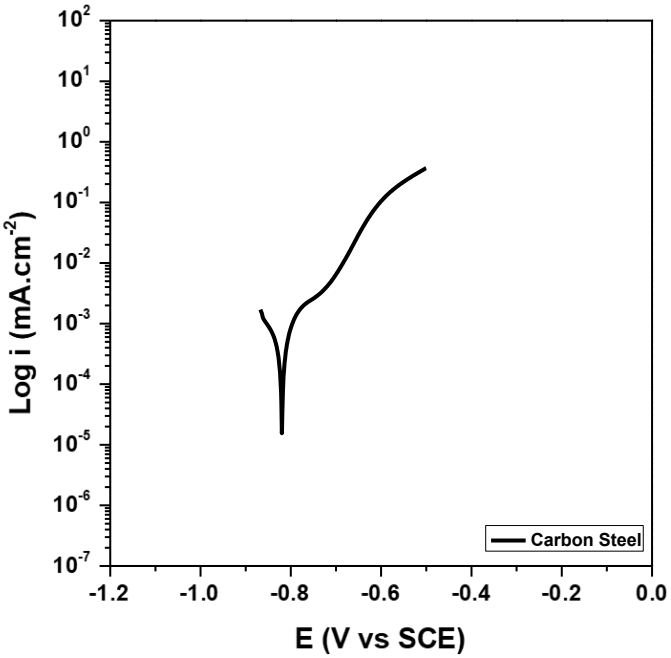

Fig. IV.4 - 1 Polarization curve of carbon steel at 24 hours of immersion

The Bode curves of EIS test in NaCl 30g/L solution at 20 hours of immersion is shown in Fig. IV.4 - 2. From both curves it is clearly observed that the sample is corroded and only one time constant exists.

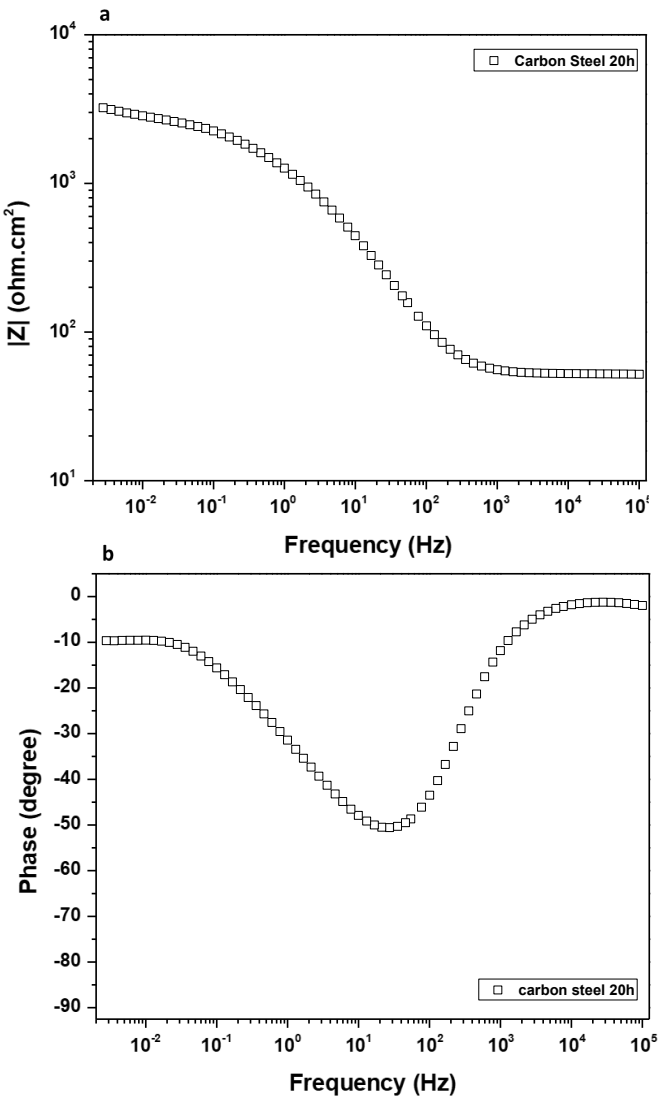

Fig. IV.4 - 2 Bode curves a) Impedance valuee b) Phase curve of carbon steel bare substrate after 20 hours of Immersion in NaCl 30g/L solution

IV.4.2 Effect of Organic-Inorganic hybrid coating on carbon steel

In the second place, the electrochemical behavior of the carbon steel deposited by ZrO-SiO/C18 coating without adding of BNNS, named as ZrO-SiO/C18_Ref, has been studied. The OCP value of CS_Ref at 24 hours of immersion in NaCl 30g/L solution has been presented in Table. 4 - 1. It is observed that the OCP of ZrO-SiO/C18_Ref is slightly higher than carbon steel substrate.

Table. 4 - 1 OCP value of ZrO-SiO/C18_Ref at 24 hours of immersion in NaCl 30g/L soultion

Samples	OCP (mV/SCE)
ZrO-SiO/C18_Ref	-533

The polarization curve of ZrO-SiO/C18_Ref superposed with carbon steel is presented in Fig. IV.4 - 3. The E_{corr} of ZrO-SiO/C18_Ref is much higher than that of the carbon steel substrate. The current density of ZrO-SiO/C18_Ref on the anodic side is over three orders of magnitude lower than carbon steel, indicating much lower corrosion rate compared to the bare substrate since the coating efficiently limits the connective metal area to the electrolyte.

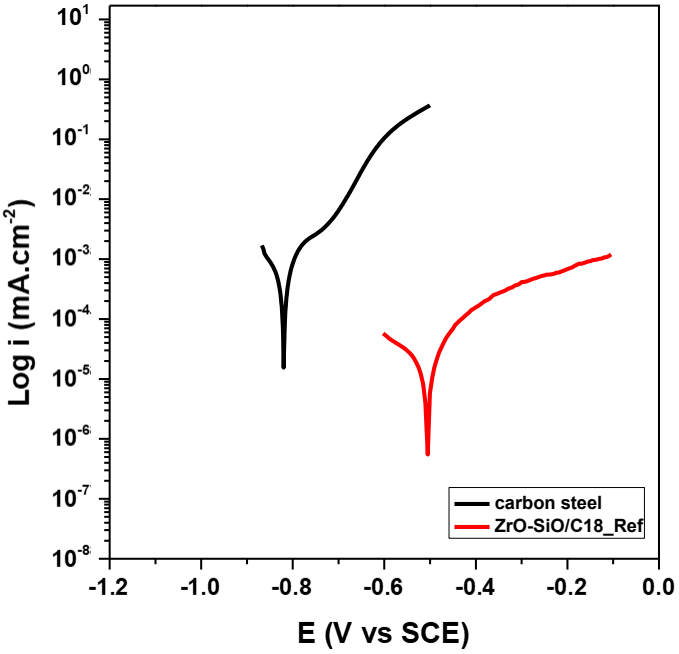

Fig. IV.4 - 3 Polarization curve of carbon steel and ZrO-SiO/C18_Ref at 24 hours of immersion

The SEM image of the surface morphology of ZrO-SiO/C18_Ref after polarization is shown in Fig. IV.4 - 4a. The coating is gravely delaminated. From Fig. IV.4 - 4b, large quantity corrosion products can be observed on the delaminated region and under deposit. It seems that the propagation of the damage continues preferentially on the coating/ substrate interface and cause the coating failure.

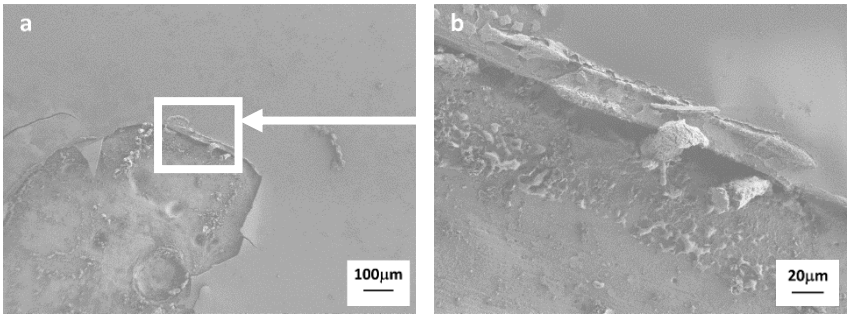

Fig. IV.4 - 4 SEM image of a) surface morphology of ZrO-SiO/C18_Ref after polarization and b) zoomed region

Nyquist curves of ZrO-SiO/C18_Ref immersion in NaCl 30g/L solution in 20 hours are presented in Fig. IV.4 - 5. The shape of Nyquist curve indicates two semicircle loops. The frequency between the two semicircle loops are always around 1Hz.[44] A rapid decrease in the diameter of the semicircle loops can be observed with time evolving. This phenomenon indicates the deterioration of the coating over time.

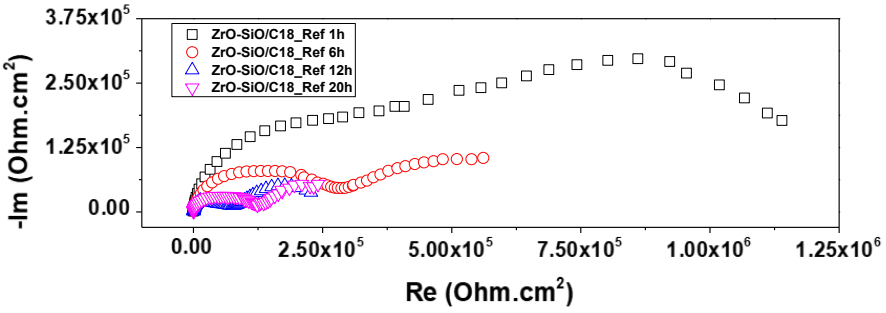

Fig. IV.4 - 5 Nyquist curve of ZrO-SiO/C18_Ref in 20 hours of immersion in NaCl 30g/L solution.

The Bode curves ZrO-SiO/C18_Ref are shown in Fig. IV.4 - 6. From Fig. IV.4 - 6a, the impedance value of coating without BNNS nanofiller at 3 mHz reduced about one order of magnitude in 20 hours.

From Fig. IV.4 - 6b, two time constants can be observed. One time constant is at high frequency (10^2 ~ 10^5 Hz) representing coating property. The shift of this time constant toward high frequency regime indicates the deterioration of barrier property of the coating. The other time constant is the one at low frequency around 10^{-1}Hz, which characterizes the charge transfer and the capacity properties of the coating/ substrate interface. This low frequency time constant stays stable over time.

To sum up, the ZrO-SiO/C18 coating without charge of fillers provide a better corrosion protection than ZrO-SiO multicomponent system coating. The ionic migration is largely blocked due to the higher hydrophobicity level of ZrO-SiO/C18, which 87.27° and 10° higher than the one of ZrO-SiO. ODTES has successfully increased the barrier property of the coating.

Nevertheless, a diffusive process was observed which means the corrosion reaction rate is rather important. The delamination of the coating can be observed after the polarization.

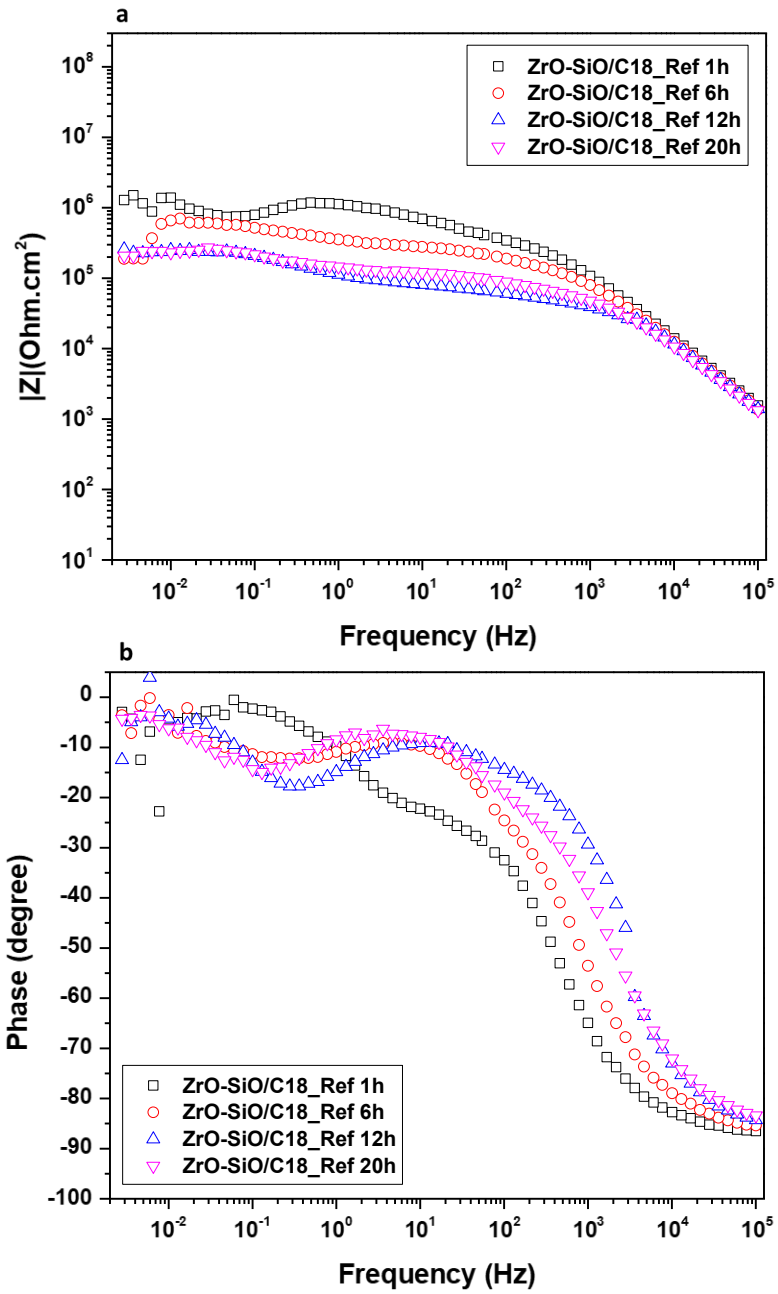

Fig. IV.4 - 6 a) Bode Impedance curves and b) Bode Phase curves of ZrO-SiO/C18_Ref with fitting in 20 hours of immersion in NaCl 30g/L solution.

IV.4.3 Influence of BNNS charged ZrO-SiO/C18/carbon steel

The BNNS charger exfoliated with a high concentration method has been charged in ZrO-SiO/C18 hybrid coating, named as ZrO-SiO/C18_BN. The electrochemical behavior has been studied and shown below to understand the property of the coating as well as the role of BNNS in protecting the carbon steel substrate.

The OCP value of ZrO-SiO/C18_BN is shown in Table. 4 - 2. The OCP value is 19 mV. This value is significantly higher compared to both the reference coating and bare substrate. The

polarization curve of ZrO-SiO/C18_BN is superposed with both reference samples in Fig. IV.4 - 7. The E_{corr} of ZrO-SiO/C18_BN is similar to the OCP value and is much higher than both reference samples, indicating a remarkably reduced surface reaction due to the presence of the coating. The current density of ZrO-SiO/C18_BN is 2.5 orders of magnitude lower than the one of ZrO-SiO/C18_Ref and 6 orders of magnitude lower than the bare substrate. The nobler E_{corr} and low current density together infers an excellent corrosion resistance of the coating system.

Table. 4 - 2 OCP value of ZrO-SiO/C18_BN at 24 hours of immersion in NaCl 30g/L solution

Samples	OCP (mV/SCE)
ZrO-SiO/C18_BN	19

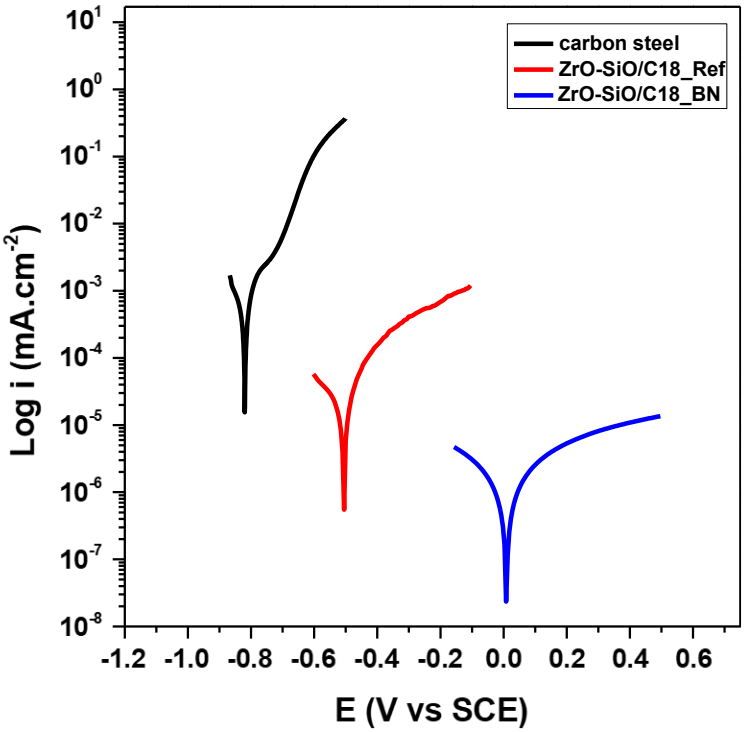

Fig. IV.4 - 7 Polarization curve of ZrO-SiO/C18_BN, ZrO-SiO/C18_Ref and carbon steel substrate at 24 hours of immersion

The SEM image of the ZrO-SiO/C18_BN after the polarization is shown in Fig. IV.4 - 8. There is neither obvious damage to the coating nor oxidation product that can be observed, proving the strong protecting behavior observed from the polarization curve up to 1.5 V vs. SCE. No delamination has been observed indicating the barrier effect of the matrix is largely enhanced by BNNS.

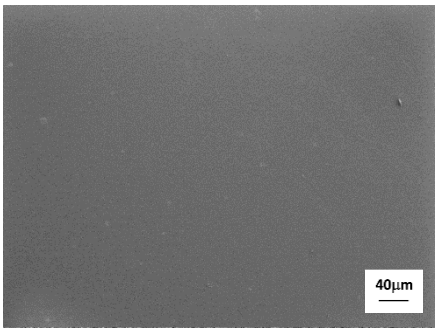

Fig. IV.4 - 8 SEM image of surface morphology of ZrO-SiO/C18_BN after polarization

Nyquist curves of ZrO-SiO/C18_BN in 20 hours of immersion in NaCl 30g/L solution are plotted for a quick observation. The asymmetric semicircle loop of ZrO-SiO/C18_BN indicating the presence of more than one time constant. The semicircle loop is of large diameter at immersion of 1 hour and decreases to 2.5 x10^6 Ohm.cm^2.

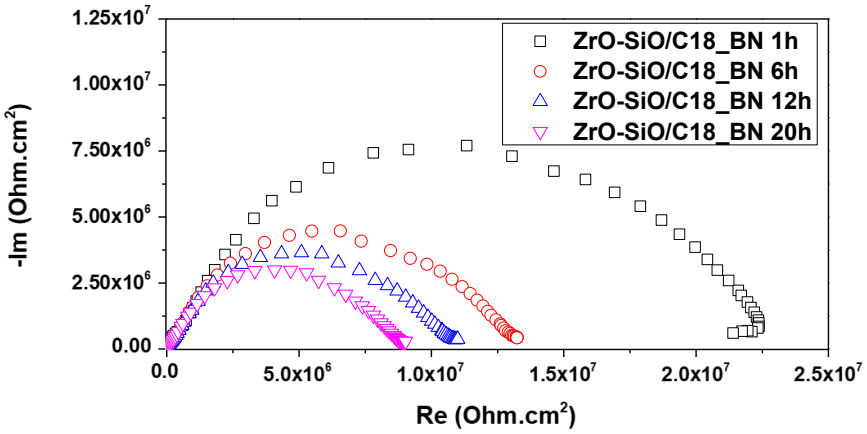

Fig. IV.4 - 9 Nyquist curves of ZrO-SiO/C18_BN during 20 hours of immersion in NaCl 30g/L solution

The Bode curves of CS_BN are shown in Fig. IV.4 - 10 with fitting results. The Bode impedance curve from Fig. IV.4 - 10a showed the protecting behavior of the ZrO-SiO/C18_BN coating varies slightly over time, and the highest impedance value reached 10^7 Ohm.cm^2 range.

From Fig. IV.4 - 10b, two clear time constants are observed. The time constant at high frequency indicates the strong and stable barrier property from the coating to the migration of ions with a phase angle close to 90° over time.[45]

The middle frequency stayed stable, together analysis with the impedance curve, the charge transfer reaction happened but is with a low density due to the high impedance value.

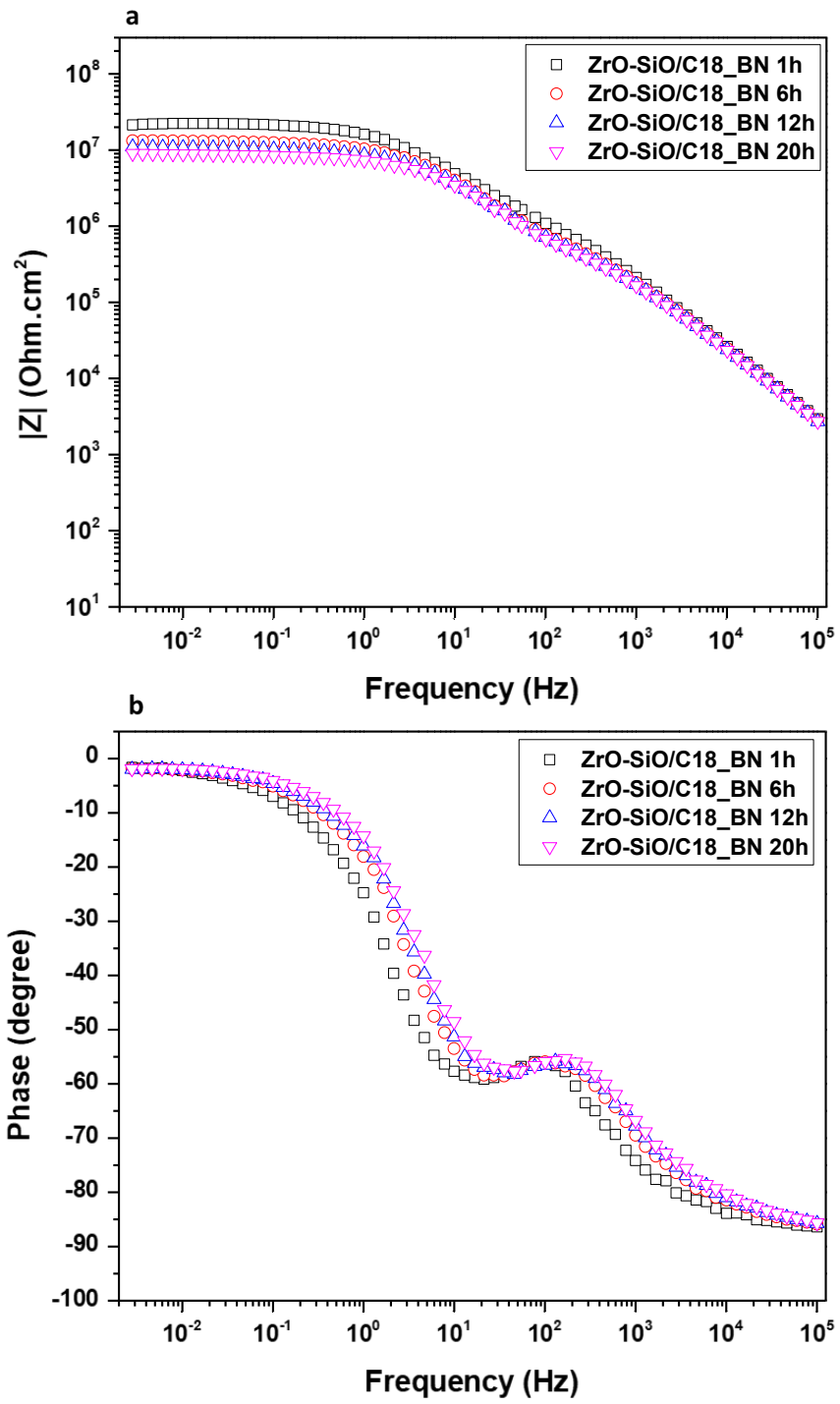

Fig. IV.4 - 10 a) Bode Impedance curves and b) Bode Phase curves, for ZrO-SiO/C18_BN during 20 hours of immersion

IV.4.4 Conclusion

The carbon steel submits active corrosion in NaCl 30g/L. The ZrO-SiO/C18 coated sample, ZrO-SiO/C18_Ref, showed a barrier property with corrosion happening under coating, meaning the adding of ODTES successfully improved the barrier property of ZrO-SiO coating. After the potentiodynamic polarization, the delamination of the coating is observed.

The ZrO-SiO/C18 coating charged with BNNS, ZrO-SiO/C18_BN, showed significant enhancement of barrier effect comparing to ZrO-SiO/C18_Ref. After potentiodynamic polarization, no modification can be observed from the coating. The charge transfer reaction happened but with a very low rate. The coating showed a stable barrier property over 20 hours of immersion, but a degradation phenomenon can be observed.

The modification of ODTES to ZrO-SiO multicomponent coating successfully put out a coating matrix to probe the enhancement of barrier property of BNNS. For futher studies, the function of other 2D materials could be explored with the two matrix that have been established by the above study. (ZrO and ZrO-SiO/C18)

IV.5 The influence of other 2D materials on Sol-Gel coatings

Having understood the role of BNNS on Sol-Gel coatings by effect of adding 2D materials, it is interesting to explore the influence of other 2D materials on Sol-Gel coatings. With these studies, not only the role of 2D materials in Sol-Gel could be verified, but also the differences between 2D materials, and the properties influencing these roles can be probed.

In this aim, the electrochemically expanded graphite derived nanosheets (GENS) and MoS_2 nanosheets (MDNS) are charged in two different Sol-Gel matrix which have been applied for the study of BNNS.

Both 2D nanofillers are firstly charged in ZrO single-component coatings deposited on 316L to observed their function in inorganic coating as well as the evolution of coated matrix in long term duration.

The nanofillers are then charged in ZrO-SiO/C18 OIH hybrid coating on carbon steel to compare their influence to the effiency of coating's barrier effect.

IV.5.1 The influence of other 2D materials on ZrO/316L

The GENS was introduced into ZrO coating to study its function in the inorganic coating's anticorrosion properties as well as the evolution of the coating. The GENS was exfoliated and centrifuged with high concentration preparation method in water (See Chapter II - II.5.1), which is the same as for the ZrO_BN170. The concentration of GENS after exfoliation is 90 μg/mL that is between the concentration of ZrO_BNC and ZrO_BN170. It should be mentioned that the graphene derived by electrochemical expansion has 9% of oxygen content (see Chapter III) due to the oxidation of carbon under high potential. The so-prepared GE is polar and can be more easily dispersed into the sol-gel matrix. This leads to a higher limit of stable concentration for GENS (90 μg/mL) than BNNS (μg/mL). The GENS charged coating was firstly deposited on 316L substrate. The sample is named ZrO_GE.

The Open Circuit Potential (OCP) evolution of ZrO_GE during five weeks of immersion has been plotted in Fig. IV.5 - 1. It is observed that the OCP was initially stable at around 65 mV vs. SCE, then stablized at 70 mV vs. SCE.

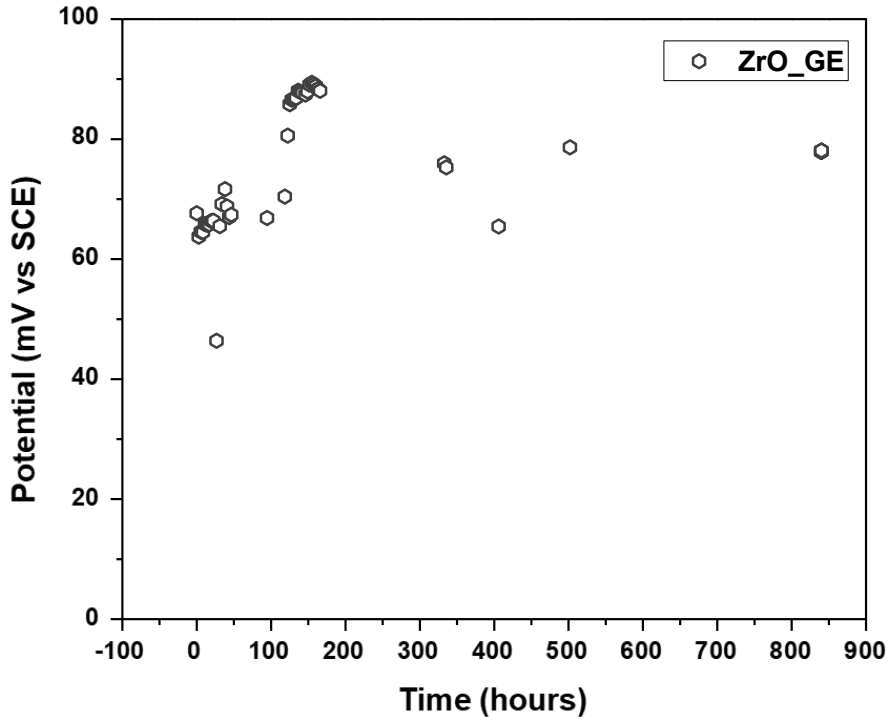

Fig. IV.5 - 1 OCP evolution of ZrO_GE during 5 weeks of immersion

The EIS Bode curves are shown in Fig. IV.5 - 2 with fittings, and the EEC for fitting is shown in Fig. IV.5 - 3. The EEC is the same as the one of ZAH_Ref, with one R_s representing solution resistance, one R_{pore}/Q_{coat} representing the resistance, and CPE for capacitance from the pores in the coating and from the passive film,the R_{ct}/Q_{dl} standing for the charge transfer resistance, and CPE for double layer capacitance.

From Fig. IV.5 - 2a, the impedance value of ZrO_GE stayed unvaried over five weeks of immersion. The impedance value reached 4 x 10^6 Ohm.cm^2 at the lowest frequency. This value is higher than the one reached by ZrO_BNC in long term duration, see IV.2.5 – Fig. IV.2 - 24.

As shown in Fig. IV.5 - 2b with the dashed line, the lowest phase angle of the middle frequency of ZrO_GE is around 87° that is 5° higher than the one observed for ZrO_BNC from Fig. IV.2 - 24. This means a stronger corrosion resistance provided by the coating enhanced passive film. Moreover, the phase angle at lowest frequency decreased from -50° to -70°. This means that the time constant at low frequency shifted to a lower frequency side. This time constant represents the charge transfer process, and this shifting indicates that the initiation of charge transfer reaction is delayed. The charge transfer is more and more discouraged with the time evolving. The shifting phenomenon of low frequency time constant was also observed from the sample ZrO_BNC during long term EIS test, which is shown in Fig. IV.2 – 24. However, the shifting of ZrO_GE is stronger than ZrO_BNC, indicating a more tortured pathway provided by GENS than by BNNS.

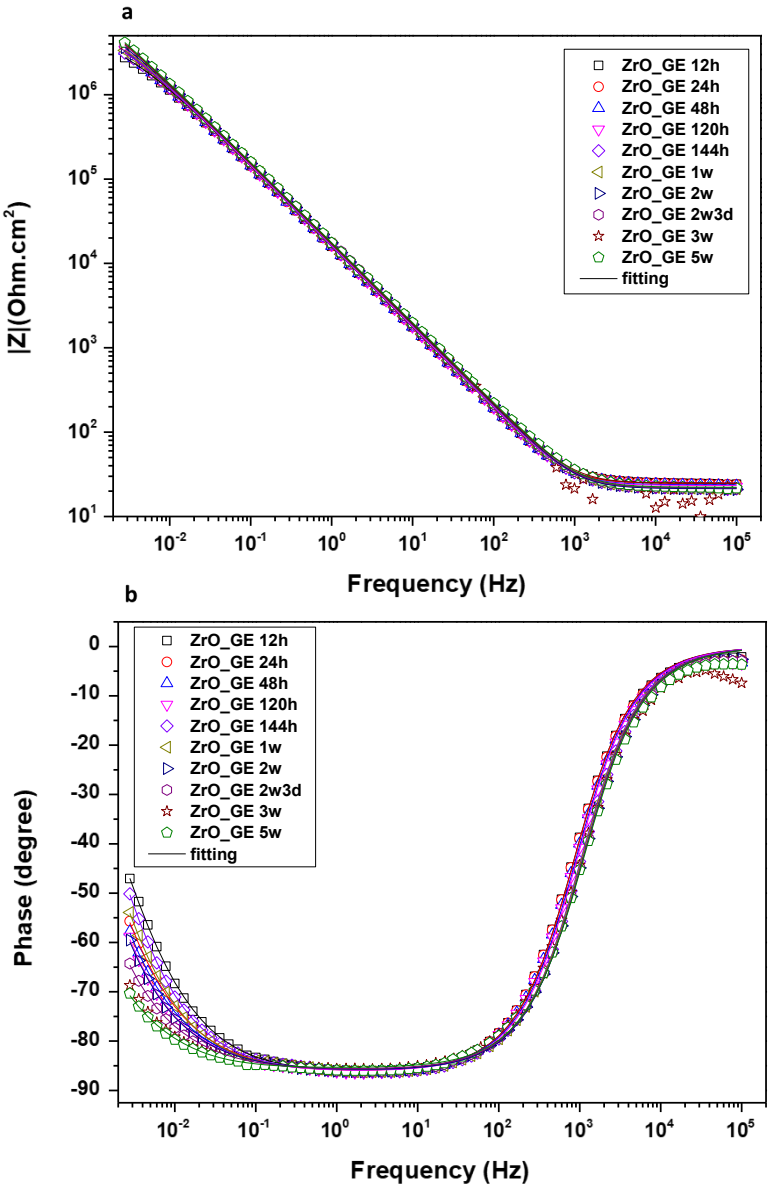

Fig. IV.5 - 2 a) Bode Impedance curves and b) Phase curves of ZrO_GE in 5 weeks of immersion in NaCl 30g/L water solution

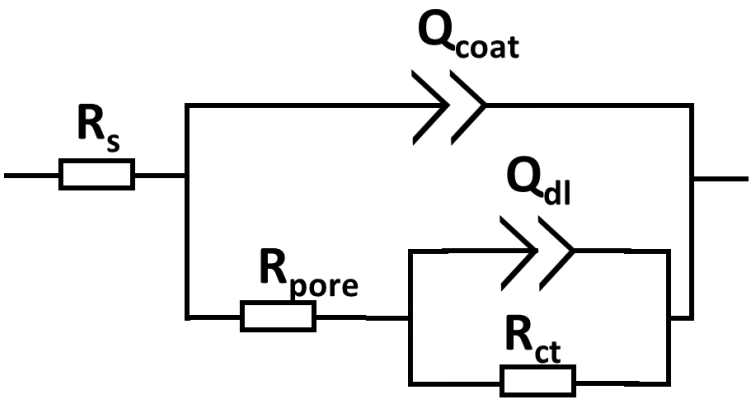

Fig. IV.5 - 3 EEC for EIS curves of ZrO_GE

The Nyquist curves of ZrO_GE as well as the surface morphology of ZrO_GE after eight weeks of immersion, are shown in Fig. IV.5 - 4. The ZrO_GE showed an increased semicircle loop during five weeks of immersion. This trend is similar to the variation of ZrO_BNC that can be explained by the synergy effect of the 2D fillers and the accumulation of the corrosion product. Moreover, the enhancement of ZrO_GE is even stronger than the one of ZrO_BNC. It seems most likely to be the result of its higher content in the inorganic matrix. The fitting parameters are shown in Appendix.

With the morphology after 8 weeks of immersion in NaCl 30/L solution shown in Fig. IV.5 - 4b, several oxide product can be observed on the surface of ZrO_GE. This oxide product stayed on the metal surface, but the whole coating was crack-free.

However, the total capacitive behavior observed from ZrO_BN170 is not presented on the sample of ZrO_GE, as shown in Fig. IV.2 – 28.

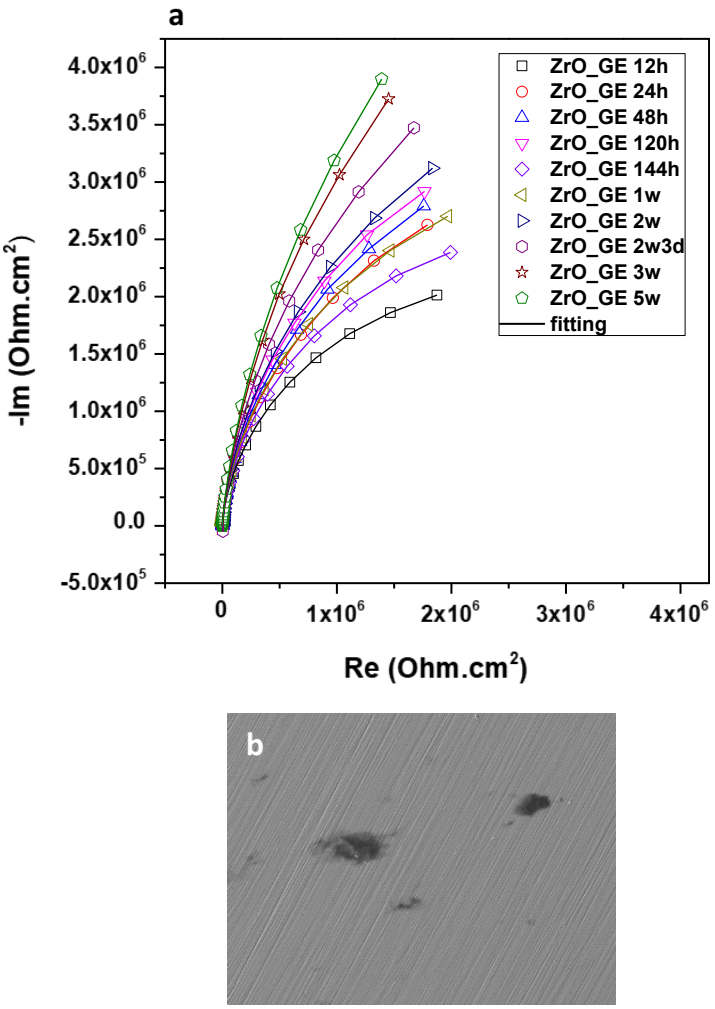

Fig. IV.5 - 4 a) Nyquist curve of ZrO_GE and b)SEM image of surface morphology of ZrO_GE after 5 weeks of immersion

The MDNS was exfoliated in water and charged in ZrO coating and deposited on 316L. The MoS_2 showed a concentration of 150 mg/mL which is similar to BNNS in ZrO_BN170 but a low stability. The defect free coating showed no observable improvement in hydrophobicity comparing to ZrO_Ref. To further understand the function of MDNS in ZrO coating, the electrochemical tests were performed.

The evolution of OCP values of ZrO_MoS_2 immersed in NaCl 30g/L in 24 hours were shown in Fig. IV.5 - 5. The OCP kept increasing over time indicating an unstable surface condition.

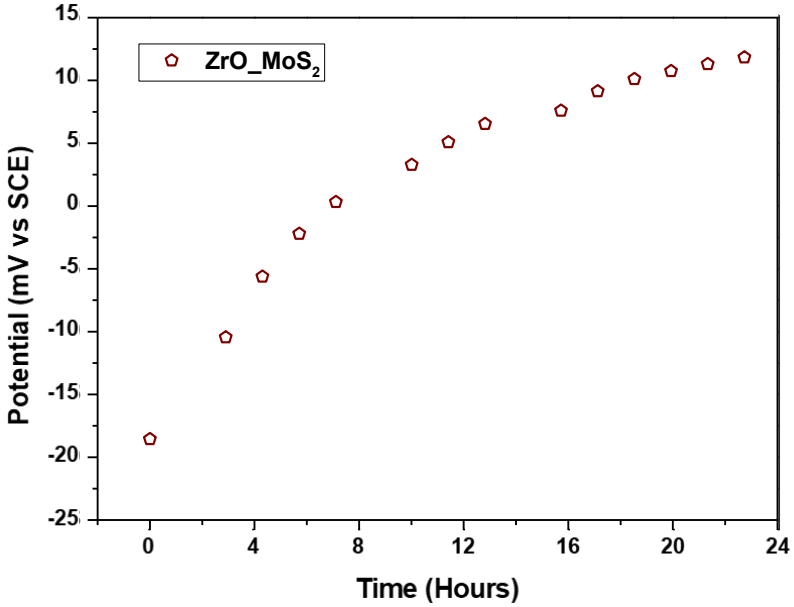

Fig. IV.5 - 5 Evolution of OCP values of ZrO_MoS_2 immersed in NaCl 30g/L in 24 hours of immersion

The polarization curve of ZrO_MoS_2 superposed with 316L substrate is shown in Fig. IV.5 - 6. The coating showed almost the same E_{corr} indicating the surface condition is similar to 316L_Sub, which is lower than ZrO_Ref. This is possibly due to a penetrable coating for corrosive molecules. The current density is one order of magnitude lower than the substrate indicating that the coating reduces the exposure surface of the coating and reduces the corrosion intensity. However, at the beginning of anodic region until 0.65 V vs. SCE, the current density of ZrO_MoS_2 is higher than the current density of ZrO_Ref. Indicating a worse corrosion resistance than ZrO_Ref. At higher frequency, the current density of ZrO_MoS_2 is similar to ZrO_Ref. ZrO_MoS_2 behaved passive state while no pitting were been observed as it has shown up over 0.68V vs. SCE for 316 substrate. The coating showed a limited barrier

effect for the bare substrate but can effectively stop the pitting at voltage lower than 1.2 V vs. SCE.

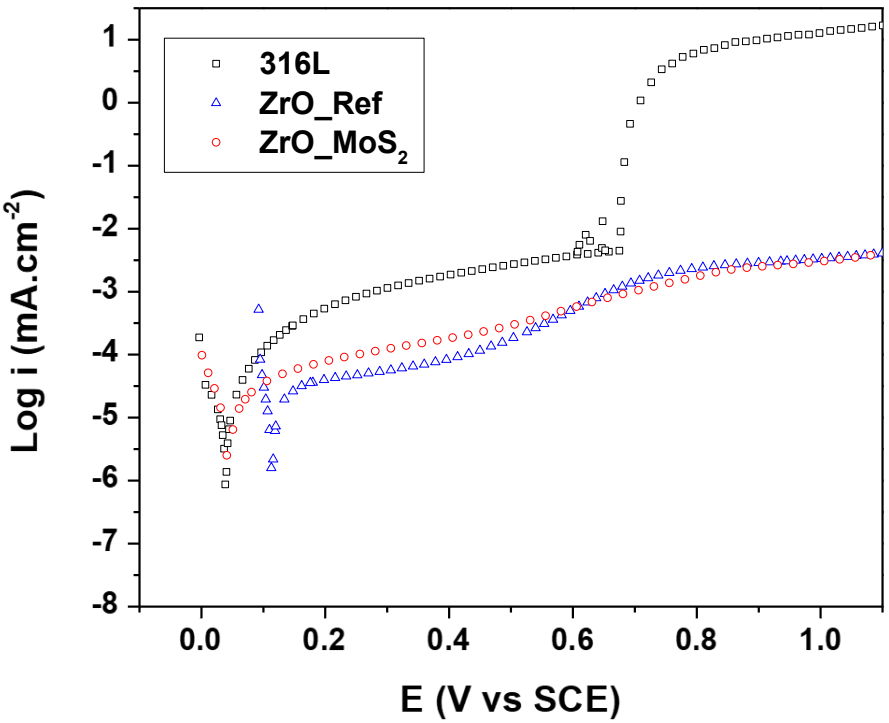

Fig. IV.5 - 6 Potentiodynamic polarization curves of ZrO_MoS_2 superposed 316L_Sub after 24 hours of immersion in NaCl solution

The Bode curves of ZrO_MoS_2 coating immersed in 72 hours are shown in Fig. IV.5 - 7. Observing from Bode Impedance curve in Fig. IV.5 - 7a, the impedance value at highest frequency is around 10^5 Ohm.cm^2 which is slightly higher than 316L substrate, indicating a limited protection behavior. The degradation of the curves is minor, indicating a stable surface condition over 72 hours of immersion.

The phase curves shown in Fig. IV.5 - 7b showed one extra time constant at frequency between 10^2 Hz to 10^3 Hz, which will be discussed in later parts. At middle and low frequency, two time constants can be observed. The time constant at middle frequency represents the passive film while the time constant at low frequency represents the charge transfer and double layer capacitance.

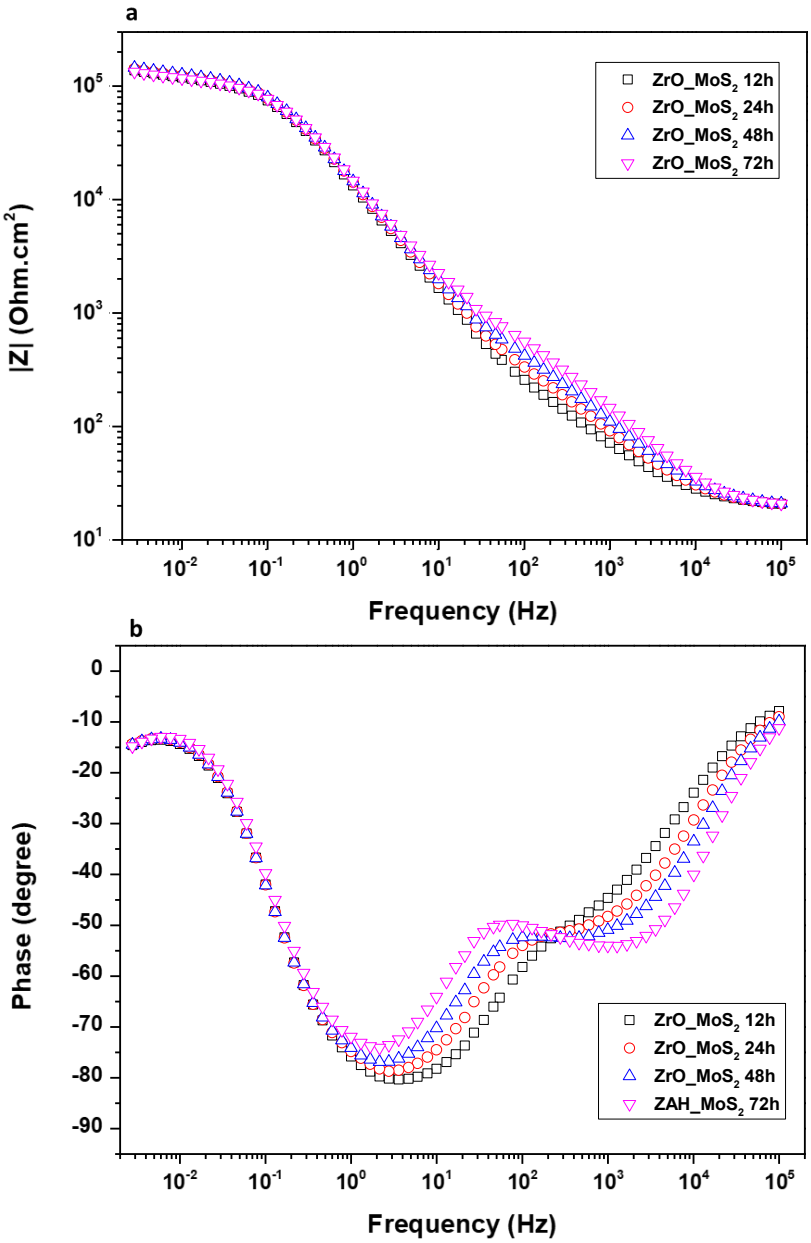

Fig. IV.5 - 7 Bode a) Impedance curves and b) Phase curves of ZrO_MoS_2 immersed in NaCl solution for 72 hours

The SEM image of ZrO_MoS_2 after 72 hours of immersion has been presented in Fig. IV.5 - 8. From Fig. IV.5 - 8 several pitting can be observed from above the coating. With zoomed areas on the particles from Fig. IV.5 - 8b to d, it is observed that the particles are of porous structure with holes inside. Though without the analysis of element, it cannot be sure whether these

particles are MoS_2 agglomerated particles, the frequent presence of these particles with holes proves that it might have connections to the extra time constant.

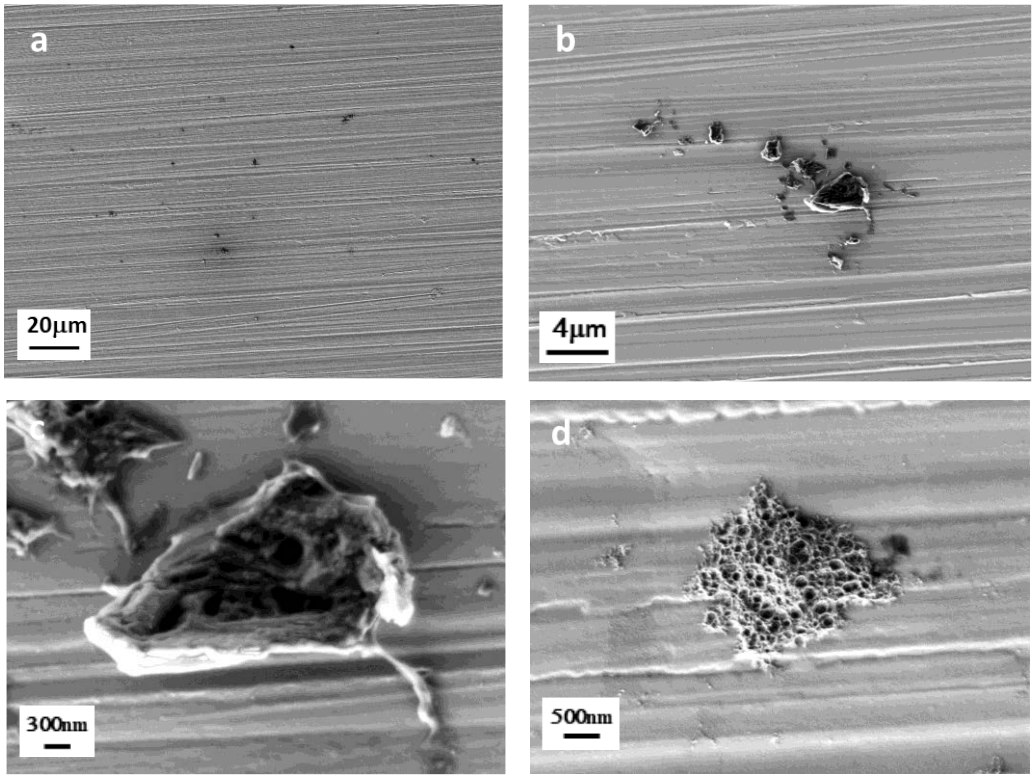

Fig. IV.5 - 8 SEM images of surface morphology of ZrO_MoS_2 after 24 hours of immersion in NaCl solutions

The Nyquist curve and the zoomed region at high frequency are presented in Fig. IV.5 - 9. The Nyquist curve showed a low semicircle loop indicating an inadequate corrosion resistance offered by the coating. At high frequency, a 45° slope can be observed at the beginning of all curves and its significance decreases over time.

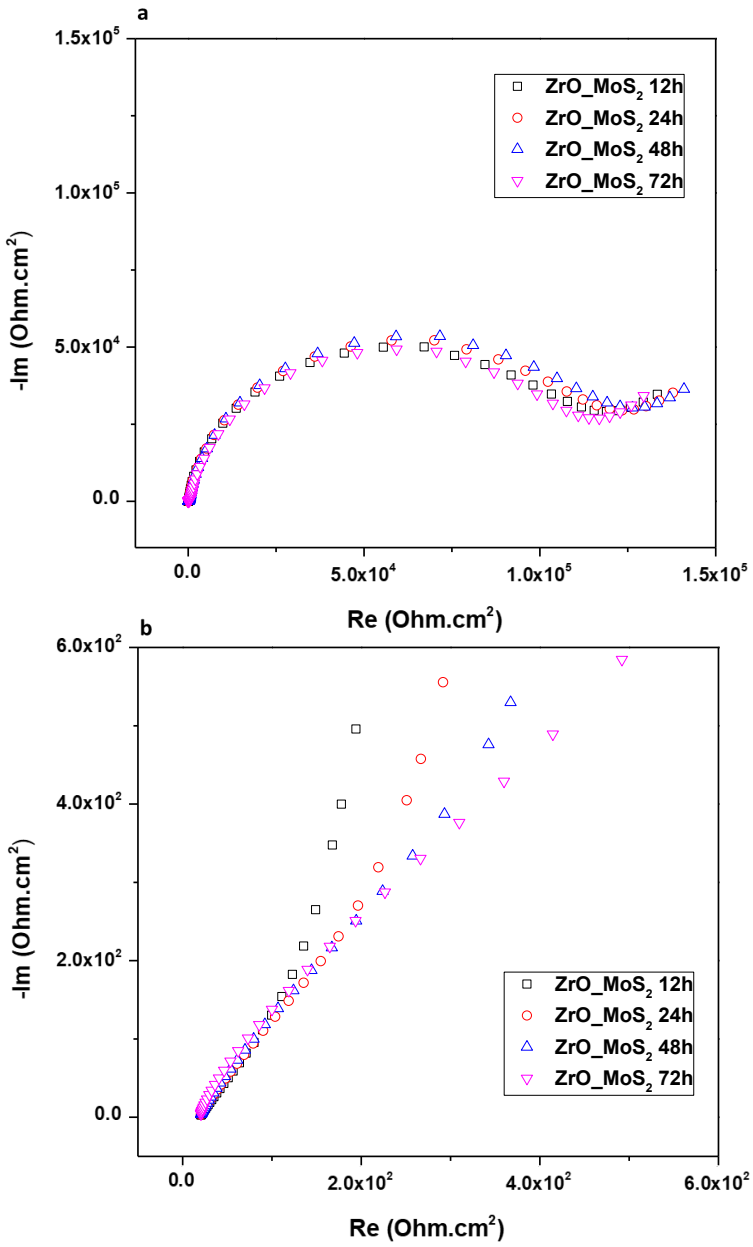

Fig. IV.5 - 9 a) Nyquist curve and b) zoomed region at high frequency of EIS tests of ZrO_MoS_2

To sum up, the ZrO_MoS_2 coating showed similar behavior to 316L_Sub observed from polarization curve. However, it showed less corrosion intensity and no pitting potential. It behaved a low function in offering tortured pathway. An extra time constant can be observed at high frequency, which could possibly be the cause for the low corrosion resistance behavior provided by ZrO_MoS_2 coating.

IV.5.2 The influence of other 2D materials on ZrO-SiO/C18/carbon steel

The GENS has been charged in ZrO-SiO/C18 coating to probe the role of GENS in a hydrophobic hybrid coating as well as to explore the role of enhancement of blocking property of isolating coatings for protection of carbon steel. GENS was exfoliated and centrifuged with the same method as for BNNS in n-Butanol. The GENS n-Butanol solution behaved an extra high concentration, 570 μg/mL but an extra low stability. The coating was named ZrO-SiO/C18_GE.

The open circuit potential of ZrO-SiO/C18_GE at 24 hours of immersion in NaCl solution is shown in Table. 4 - 3. The OCP value is 7.9 mV/SCE which is slightly nobler than the one of CS_BN.

Table. 4 - 3 OCP value of ZrO-SiO/C18_GE at 24 hours of immersion in NaCl 30g/L solution

Samples	OCP (mV/SCE)
ZrO-SiO/C18_GE	79

The polarization curve of ZrO-SiO/C18_GE superposed with reference samples after 24 hours immersed in NaCl 30g/L. The polarization curve of ZrO-SiO/C18_GE showed a much nobler E_{corr} than both reference samples, and a current density which is three times lower than ZrO-SiO/C18_Ref and more than six times lower than carbon steel substrate. Comparing to ZrO-SiO/C18_BN, the coating showed an even nobler E_{corr} and a lower current density.

The GENS has been charged in ZrO-SiO/C18 coating to probe the role of GENS in a hydrophobic hybrid coating as well as to explore the role of enhancement of blocking property of isolating coatings for protection of carbon steel. GENS was exfoliated and centrifuged with the same method as for BNNS in n-Butanol. The GENS n-Butanol solution behaved an extra high concentration, 570 μg/mL but an extra low stability. The coating was named ZrO-SiO/C18_GE.

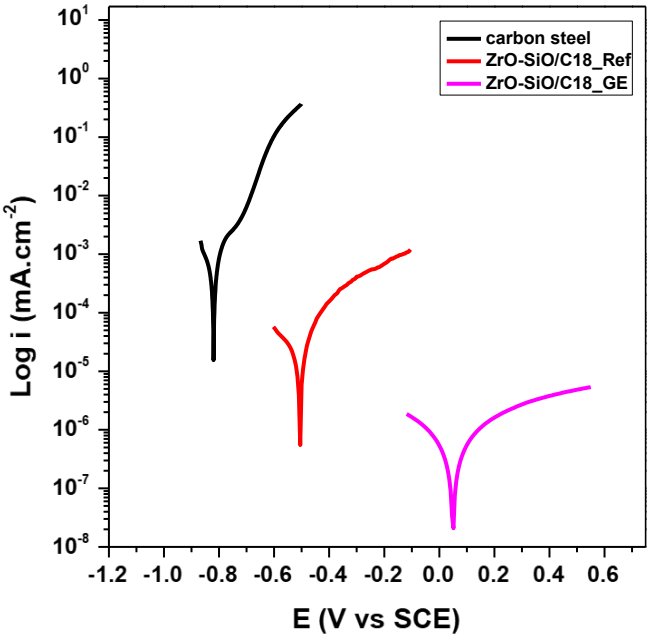

Fig. IV.5 - 10 Polarization curve of ZrO-SiO/C18_GE surperposed with reference samples after 24 hours immersed in NaCl 30g/L

The SEM image of ZrO-SiO/C18_GE surface morphology after the polarization is shown in Fig. IV.5 - 11. The surface shows no cracks or delamination or oxide product.

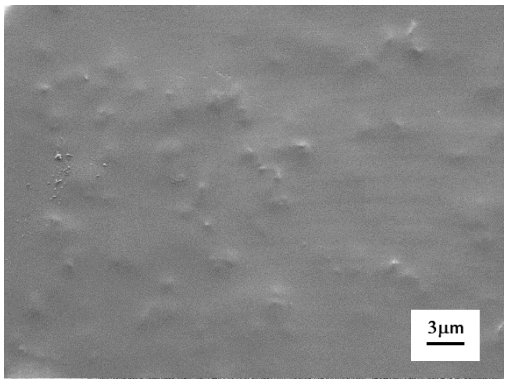

Fig. IV.5 - 11 SEM image of surface morphology of ZrO-SiO/C18_GE after the polarization

The EIS Nyquist curves were shown in Fig. IV.5 - 12. One large semicircle loop can be observed from the Nyquist curves, the semicircle loop decreased rapidly indicating the deterioration of the coating.

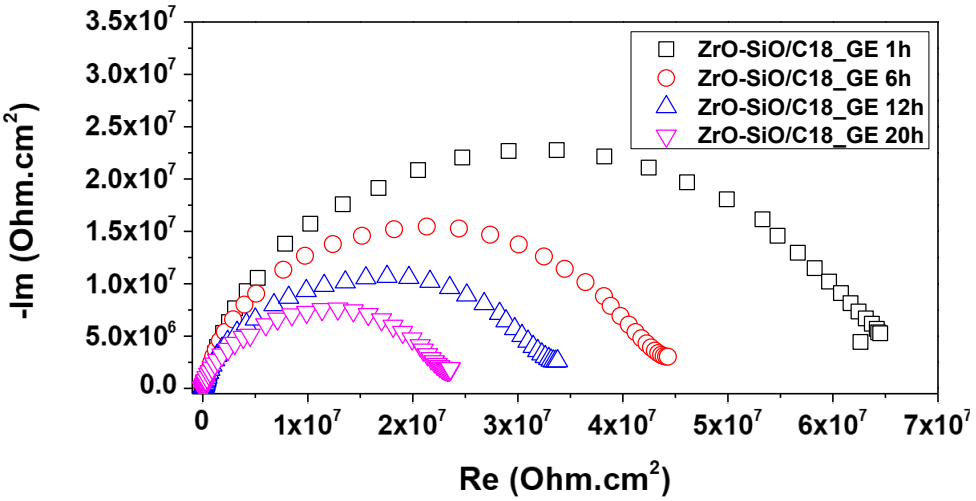

Fig. IV.5 - 12 Nyquist curves of ZrO-SiO/C18_GE immersed in NaCl 30g/L solution in 20 hours

The Bode curves are shown in Fig. IV.5 - 13. From Bode impedance curve from Fig. IV.5 - 13a, the impedance value at lowest frequency almost reached 7 x 10^7 Ohm.cm^2 and decreased to 2 x 10^7 Ohm.cm^2 after 20 hours of immersion. The corrosion happened under coating, but the corrosion rate is really low, which is similar to the case of coating ZrO-SiO/C18_BN. This protection is better than the active protection by passive film from the coatings deposited 316L. Thus, it could be a perspective that the active protection fillers can be introduced for the coating matrix.

The phase curve showed clearly two time constants which are of the same characters as ZrO-SiO/C18_BN. The time constant at high frequency indicates the coating providing the barrier effect to block the migration of ions.

At middle frequency, a time constant between 10 Hz to 10^3 Hz is observed, indicating the oxide film. It showed a larger phase angle (over -70°) than ZrO-SiO/C18_BN, which is lower than -60°. From the Phase curves, a degradation behavior is observed, which is faster than the degradation of ZrO-SiO/C18_BN.

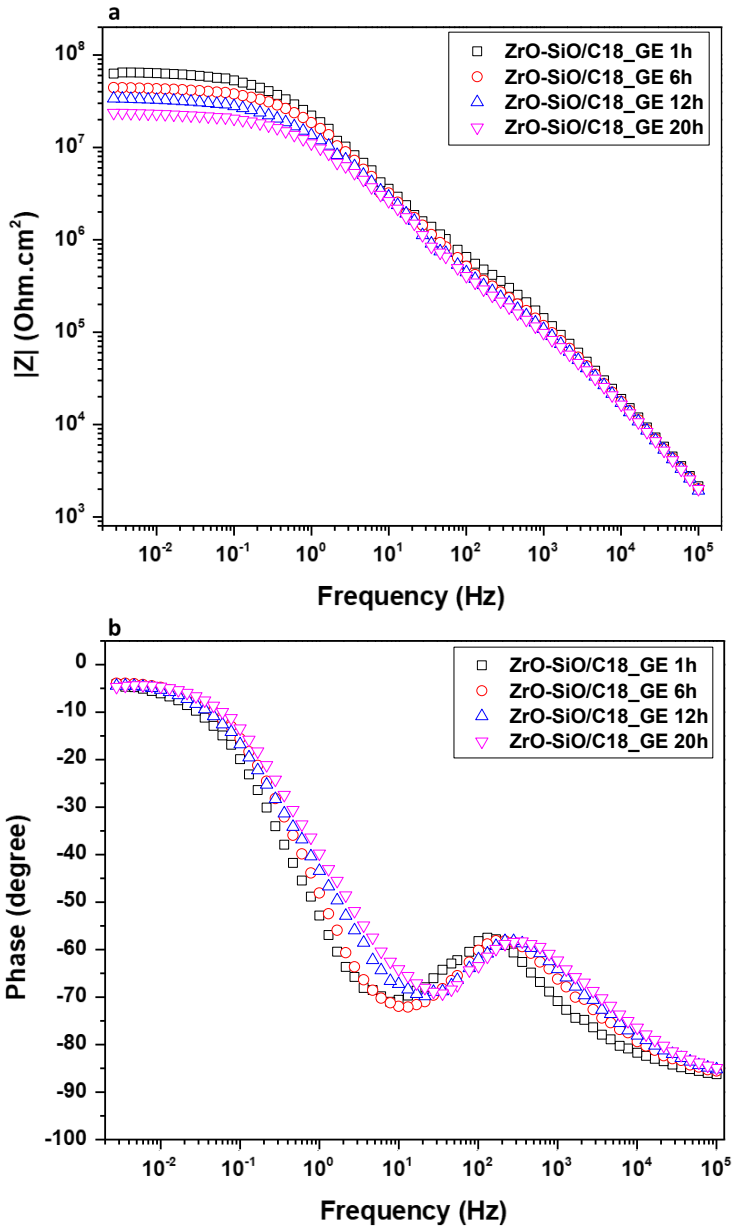

Fig. IV.5 - 13 a) Bode Impedance curves and b) Phase curves of ZrO-SiO/C18_GE immersed in NaCl 30g/L solution

To prove the roles of MDNS in hydrophobic hybrid coating and explore possible applications, the MDNS was exfoliated with the same method as to BNNS and GENS in n-Butanol. The concentration was the highest among three different 2D fillers, 680 mg/mL, but the stability was rather low. The sample was named ZrO-SiO/C18_MoS_2.

The OCP value of ZrO-SiO/C18_MoS_2 at 24 hours of immersion in NaCl 30g/L solution is shown in Table. 4 - 4. This value is slightly higher than the value of ZrO-SiO/C18_Ref and ZrO-SiO/C18_Sub.

Table. 4 - 4 OCP value of ZrO-SiO/C18_MoS_2 at 24 hours of immersion in NaCl 30g/L solution

Samples	OCP (mV/SCE)

ZrO-SiO/C18_MoS_2	-515

The potentiodynamic polarization curves of ZrO-SiO/C18_MoS_2 is shown in Fig. IV.5 - 14. The MDNS modified coating showed the same E_{corr} comparing to the ZrO-SiO/C18_Ref, indicating less barrier effect offered from the 2D material to reduce the chance of the corrosive molecules to get in touch with the metal surface. The GENS had introduced barrier effect to reduce the penetration of corrosive molecules.

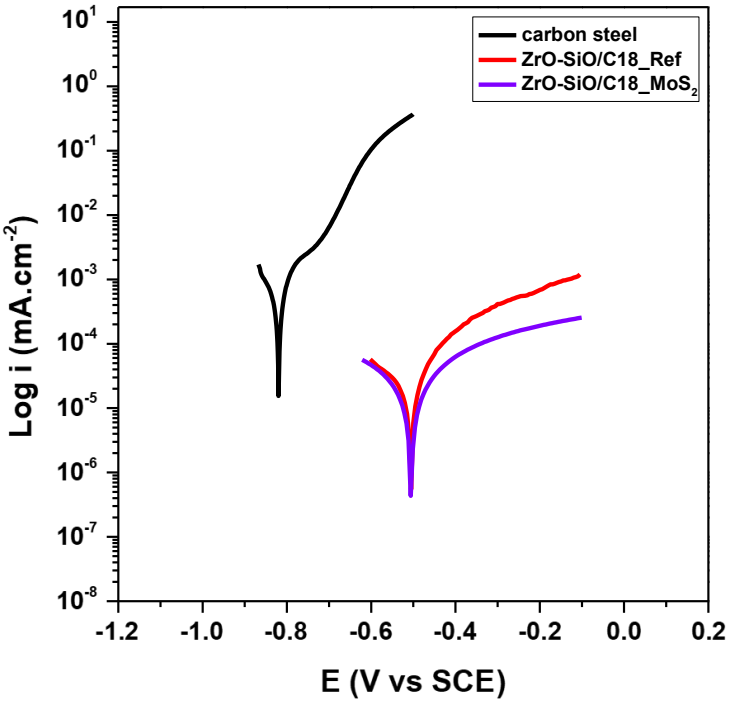

Fig. IV.5 - 14 Potentiodyanamic Polarization curve of ZrO-SiO/C18_MoS_2 after 24 hours of immersion in NaCl 30g/L solution superposed with reference samples

The SEM image of surface morphology of ZrO-SiO/C18_MoS_2 after polarization is shown in Fig. IV.5 - 15. A large area of delamination is observed while corrosion products is seen on the metal surface. This proves that the surface modification due to corrosion and the delamination of the coating could be distributed all around the metal surface.

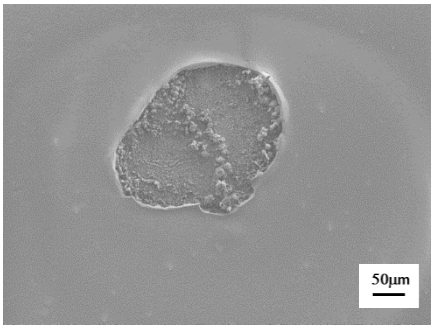

Fig. IV.5 - 15 SEM image of surface morphology of ZrO-SiO/C18_MoS_2 after polarization

Nyquist curves of ZrO-SiO/C18_MoS2 immersed in NaCl 30g/L solution in 20 hours are shown in Fig. IV.5 - 16. With a quick observation, it is understood that the semicircle loop is higher

than ZrO-SiO/C18_Ref and decreases over time. Different from ZrO-SiO/C18_Ref, no diffusion phenomenon can be observed.

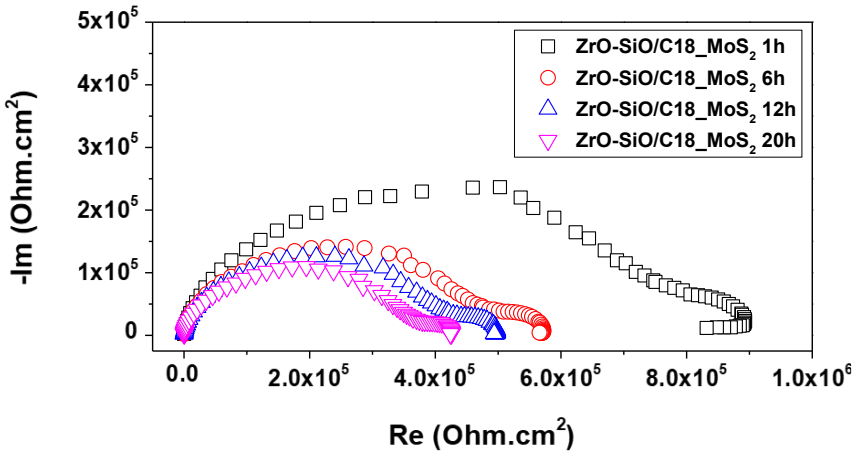

Fig. IV.5 - 16 Nyquist curves of ZrO-SiO/C18_MoS_2 immersed in NaCl 30g/L solution in 20 hours

The Bode curves are shown in Fig. IV.5 - 17. From the Bode Impedance curve from Fig. IV.5 - 17a, it is observed that the impedance value at low frequency are of the same order of magnitude comparing to ZrO-SiO/C18_Ref but without the perturbation of the signals. This indicates the surface condition is more stable comparing to the ZrO-SiO/C18_Ref. However, the improvement in corrosion resistance is limited.

From Bode phase curves shown in Fig. IV.5 - 17b, the curves are flat at middle, indicating less heavy corrosion reaction on the metal surface with low charge transfer rate. The high frequency time constant stayed stable as well as the low frequency time constant, indicating the coating are not strongly evoluted due to less corrosion phenomenon comparing to the reference sample. The ZrO-SiO/C18_MoS_2 showed a higher stability in time comparing to ZrO-SiO/C18_Ref. However, comparing to both ZrO-SiO/C18_BN and ZrO-SiO/C18_GE, ZrO-SiO/C18_MoS_2 does not introduce much protective behavior though the concentration of MoS_2 is the highest amongst all.

To sum up, the MDNS charge ZrO-SiO/C18 coating showed similar behavior to ZrO-SiO/C18_Ref with less heavy corrosion reaction on the metal surface. The ZrO-SiO/C18_MoS_2 can offer limited enhancement of blocking property of isolating coating.

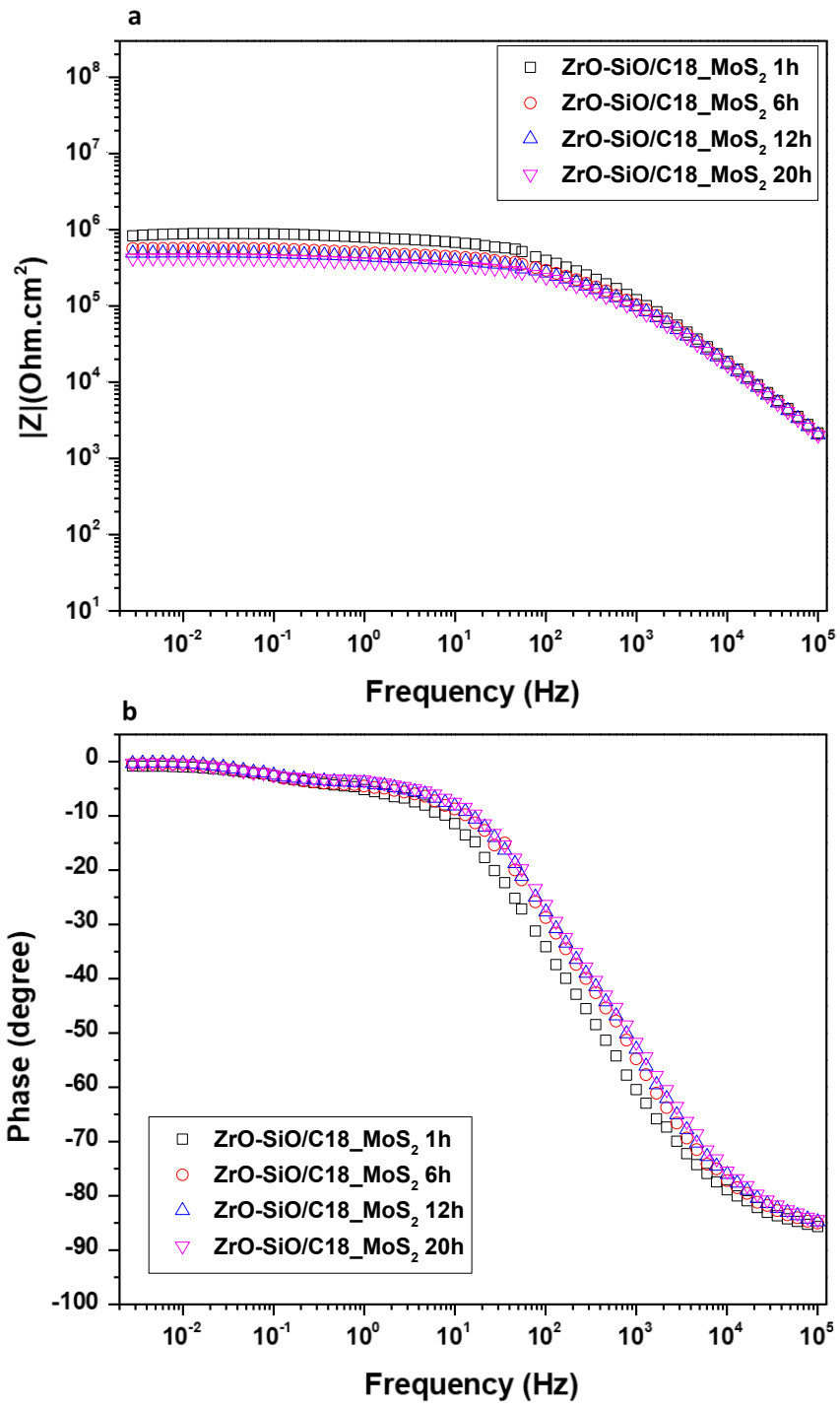

Fig. IV.5 - 17 Bode a) Impedance curves and b) Phase curves of EIS tests of ZrO-SiO/C18_MoS_2

IV.5.3 Conclusion

Both GENS charged coatings showed an improved corrosion protection behavior comparing to the reference coatings. The ZrO_GE provided tortured pathway, but no total capacitive behavior can be observed. The ZrO-SiO/C18_GE coating showed enhancement of barrier effect of the coating. The two coatings showed even higher enhancement property than the corresponding coatings charged by BNNS.

The MDNS charged ZrO coating showed inferior corrosion resistance than ZrO_Ref and similar corrosion behavior than 316L substrate. However, the impedance response of ZrO_MoS_2 is even lower than 316L_Sub with an extra time constant existing at high frequency showing extra phenomenon on introducing the corrosion reactions. The MDNS charge ZrO-SiO/C18 could not offer much enhancement of barrier effect to the coating, which showed a similar behavior comparing to ZrO-SiO/C18_Ref.

BNNS and GENS can both introduce strong barrier effect to Sol-Gel coatings, while BNNS showed distribution behavior than GENS in water solution. To achieve a stronger tortured pathway, the well distributed GENS is a good choice. For a stronger impermeability by totally blocking the ionic migration, the BNNS could be a candidate. For hybrid coatings, though GENS showed lower stability and agglomeration, its high concentration also showed a strong distribution behavior than BNNS. Both coating showed similar properties in the hybrid coating.

However, MDNS, due to its active reactivity, cannot propose good barrier properties to Sol-Gel thin coatings. Perspective could be done to explore the role of MoS_2 nanosheets in thick coatings.

IV.6 Conclusion

In this chapter, we studied the role of the 2D nanosheets in enhancing barrier effects in different coating systems.

Zirconium oxide single-component coating on 316L: Firstly, it has been proved that the morphology of BNNS plays an important role in corrosion resistance. A critical diameter exists, 7 μm in average size, for the BNNS to exhibit its barrier effect in the coating. The BNNS exfoliated from large-sized BN powder showed a prolonged penetration pathway to the coatings. The coating showed a continuous increase of barrier effect in 1200 hours of immersion because of a synergy effect between the barrier effect of BNNS and the sealing of the corroded sites by oxide product.

The concentration of BNNS in the Sol-Gel coating is another essential parameter. The suspension of BNNS in aqueous media can stay stable at a concentration lower than 15 μg/mL. Beyond this concentration value, the nanosheet agglomeration occurs spontaneously, leading to the formation of unexpected defects with a critical size that is more influential than the pores. As a consequence, the coating's corrosion resistance decreased. With the continuously increased BNNS content to 170 μg/ml, the coating exhibited a total capacitive behavior. This variation is explained by the orientation of BNNS and the formation of a highly concentrated layer driven by dip-coating capillary force.

Zirconium oxide - Silicon oxide multi-component coating on Aluminium alloy: the multi-component sol-gel coating exhibited better corrosion resistance than the ZrO coating. The BNNS charged coating enhanced the coating barrier effect. Nevertheless, the corrosion caused delamination. The addition of BNNS decreased the adhesion of coating, which in return accelerate the delamination.

Organic-inorganic hybrid coating on carbon steel (XC90): The addition of hydrophobic alkyl group (ODTES) in the ZrO-SiO Sol allows to change the surface tension and the water repellency in the pore. The coating without BNNS limited the corrosion on carbon steel. For the coating charged with BNNS, the corrosion were prohibited and delamination weren't observed.

[1] Azzi, M.; Paquette, M.; Szpunar, J. A.; Klemberg-Sapieha, J. E.; Martinu, L. Tribocorrosion Behaviour of DLC-Coated 316L Stainless Steel. Wear 2009, 267 (5), 860–866.
[2] Craig, B. D. Thermodynamics of Corrosion. In Fundamental Aspects of Corrosion Films in Corrosion Science; Craig, B. D., Ed.; Springer US: Boston, MA, 1991
[3] Goetz, R.; Landolt, D. The Influence of Chromium Content and Potential on the Surface Composition of Fe-Cr-Mo Alloys Studied by AES. Electrochimica Acta 1984, 29 (5), 667–676.
[4] Zuo, Y.; Wang, H.; Zhao, J.; Xiong, J. The Effects of Some Anions on Metastable Pitting of 316L Stainless Steel. Corrosion Science 2002, 44 (1), 13–24.
[5] Arjmand, F.; Zhang, L.; Wang, J. Effect of Temperature, Chloride and Dissolved Oxygen Concentration on the Open Circuit and Transpassive Potential Values of 316L Stainless Steel at High-Temperature Pressurized Water. Nuclear Engineering and Design 2017, 322, 215–226.
[6] Boissy, C.; Ter-Ovanessian, B.; Mary, N.; Normand, B. Correlation between Predictive and Descriptive Models to Characterize the Passive Film – Study of Pure Chromium by Electrochemical Impedance Spectroscopy. Electrochimica Acta 2015, 174, 430–437.

[7] Ferreira, E. A.; Noce, R. D.; Fugivara, C. S.; Benedetti, A. V. Evaluation of 316L Stainless Steel Corrosion Resistance in Solution Simulating the Acid Hydrolysis of Biomass. J. Electrochem. Soc. 2011, 158 (4), C95.
[8] Ćurković, L.; Ćurković, H. O.; Salopek, S.; Renjo, M. M.; Šegota, S. Enhancement of Corrosion Protection of AISI 304 Stainless Steel by Nanostructured Sol–Gel TiO2 Films. Corrosion Science 2013, 77, 176–184.
[9] Niu, J.; Barraza-Fierro, J. I.; Castaneda, H. Quantification of Protective Properties of the Coating/Corrosion Product/Steel Interface by Integration of Transmission Line Model with EIS Results. J Coat Technol Res 2015, 12 (2), 393–405.
[10] Hu, S.; Lozada-Hidalgo, M.; Wang, F. C.; Mishchenko, A.; Schedin, F.; Nair, R. R.; Hill, E. W.; Boukhvalov, D. W.; Katsnelson, M. I.; Dryfe, R. a. W.; et al. Proton Transport through One-Atom-Thick Crystals. Nature 2014, 516 (7530), 227–230.
[11] Husain, E.; Narayanan, T. N.; Taha-Tijerina, J. J.; Vinod, S.; Vajtai, R.; Ajayan, P. M. Marine Corrosion Protective Coatings of Hexagonal Boron Nitride Thin Films on Stainless Steel. ACS Appl. Mater. Interfaces 2013, 5 (10), 4129–4135.
[12] Zhao, X.; Zhang, B.; Jin, Z.; Chen, C.; Zhu, Q.; Hou, B. Epoxy Coating Modified by 2D MoS2/SDBS: Fabrication, Anticorrosion Behaviour and Inhibition Mechanism. RSC Adv. 2016, 6 (100), 97512–97522.
[13] Kim, H.; Hwang, T. Corrosion Protection Enhancement Effect by Mixed Silica Nanoparticles of Different Sizes Incorporated in a Sol–Gel Silica Film. J Sol-Gel Sci Technol 2012, 63 (3), 563–568.
[14] Nielsen, L. E. Models for the Permeability of Filled Polymer Systems. Journal of Macromolecular Science: Part A - Chemistry 1967, 1 (5), 929–942.
[15] Hussain, A. K.; Sudin, I.; Basheer, U. M.; Yusop, M. Z. M. A Review on Graphene-Based Polymer Composite Coatings for the Corrosion Protection of Metals. Corrosion Reviews 2019, 37 (4), 343–363.
[16] Hernández-Barrios, C. A.; Cuao, C. A.; Jaimes, M. A.; Coy, A. E.; Viejo, F. Effect of the Catalyst Concentration, the Immersion Time and the Aging Time on the Morphology, Composition and Corrosion Performance of TEOS-GPTMS Sol-Gel Coatings Deposited on the AZ31 Magnesium Alloy. Surface and Coatings Technology 2017, 325, 257–269.
[17] Tian, S.; Liu, Z.; Shen, L.; Pu, J.; Liu, W.; Sun, X.; Li, Z. Performance Evaluation of Mercapto Functional Hybrid Silica Sol–Gel Coating and Its Synergistic Effect with f-GNs for Corrosion Protection of Copper Surface. RSC Adv. 2018, 8 (14), 7438–7449.
[18] Liu, C.; Bi, Q.; Leyland, A.; Matthews, A. An Electrochemical Impedance Spectroscopy Study of the Corrosion Behaviour of PVD Coated Steels in 0.5 N NaCl Aqueous Solution: Part I. Establishment of Equivalent Circuits for EIS Data Modelling. Corrosion Science 2003, 45 (6), 1243–1256.
[19] Meshram, A. P.; Punith Kumar, M. K.; Srivastava, C. Enhancement in the Corrosion Resistance Behaviour of Amorphous Ni P Coatings by Incorporation of Graphene. Diamond and Related Materials 2020, 105, 107795.
[20] Kim, J.; Kwon, S.; Cho, D.-H.; Kang, B.; Kwon, H.; Kim, Y.; Park, S. O.; Jung, G. Y.; Shin, E.; Kim, W.-G.; Lee, H.; Ryu, G. H.; Choi, M.; Kim, T. H.; Oh, J.; Park, S.; Kwak, S. K.; Yoon, S. W.; Byun, D.; Lee, Z.; Lee, C. Direct Exfoliation and Dispersion of Two-Dimensional Materials in Pure Water via Temperature Control. Nature Communications 2015, 6, 8294.
[21] Zhao, W.; Zhao, W.; Huang, Z.; Liu, G.; Wu, B. Tribological Performances of Epoxy Resin Composite Coatings Using Hexagonal Boron Nitride and Cubic Boron Nitride Nanoparticles as Additives. Chemical Physics Letters 2019, 732, 136646.
[22] Liu, Z.; Li, J.; Liu, X. Novel Functionalized BN Nanosheets/Epoxy Composites with Advanced Thermal Conductivity and Mechanical Properties. ACS Appl. Mater. Interfaces 2020, 12 (5), 6503–6515.
[23] Çamurlu, H. E.; Akarsu, E.; Arslan, O.; Mathur, S. Nanocomposite Glass Coatings Containing Hexagonal Boron Nitride Nanoparticles. Ceramics International 2016, 42 (7), 8856–8862.
[24] Yang, N.; Zeng, X.; Lu, J.; Sun, R.; Wong, C.-P. Effect of Chemical Functionalization on the Thermal Conductivity of 2D Hexagonal Boron Nitride. Appl. Phys. Lett. 2018, 113 (17), 171904.
[25] Zhao, H.; Ding, J.; Yu, H. The Efficient Exfoliation and Dispersion of HBN Nanoplatelets: Advanced Application to Waterborne Anticorrosion Coatings. New J. Chem. 2018, 42 (17), 14433–14443.
[26] Ayoob, R.; Alhabill, F.; Andritsch, T.; Vaughan, A. Enhanced Dielectric Properties of Polyethylene/Hexagonal Boron Nitride Nanocomposites. J Mater Sci 2018, 53 (5), 3427–3442.
[27] Jeffrey Brinker, C.; Hurd, A. J. Fundamentals of Sol-Gel Dip-Coating. J. Phys. III France 1994, 4 (7), 1231–1242.
[28] Faustini, M.; Louis, B.; Albouy, P. A.; Kuemmel, M.; Grosso, D. Preparation of Sol-Gel Films by Dip-Coating in Extreme Conditions. J. Phys. Chem. C 2010, 114 (17), 7637–7645.
[29] Cabanel, R.; Barral, G.; Diard, J.-P.; Gorrec, B. L.; Montella, C. Determination of the Diffusion Coefficient of an Inserted Species by Impedance Spectroscopy: Application to the $H/H_xNb_2O_5$System. J Appl Electrochem 1993, 23 (2), 93–97.

[30] Diard, J.-P.; Le Gorrec, B.; Montella, C. Diffusion Impedance of Handbook of Electrochemical Impedance Spectroscopy. Bio-Logic 2017.
[31] Michel Colombié. Didier Albert.; Roger Baltus.; Matériaux métalliques propriétés, mise en forme et applications industrielles des métaux etalliages. 2è édition. DUNOD.
[32] Li, J.; Birbilis, N.; Buchheit, R. G. Electrochemical Assessment of Interfacial Characteristics of Intermetallic Phases Present in Aluminium Alloy 2024-T3. Corrosion Science 2015, 101, 155–164.
[33] Mohammadi, I.; Shahrabi, T.; Mahdavian, M.; Izadi, M. Sodium Diethyldithiocarbamate as a Novel Corrosion Inhibitor to Mitigate Corrosion of 2024-T3 Aluminum Alloy in 3.5 Wt% NaCl Solution. Journal of Molecular Liquids 2020, 307, 112965.
[34] Yasakau, K. A., Zheludkevich, M. L., Lamaka, S. V., & Ferreira, M. G. S. (2006). Mechanism of Corrosion Inhibition of AA2024 by Rare-Earth Compounds. The Journal of Physical Chemistry B, 110(11), 5515–5528.
[35] Xue, B.; Yu, M.; Liu, J.; Liu, J.; Li, S.; Xiong, L. Corrosion Protection of AA2024-T3 by Sol-Gel Film Modified with Graphene Oxide. Journal of Alloys and Compounds 2017, 725, 84–95.
[36] Urushino, K.; Sugimoto, K. Stress-Corrosion Cracking of Aged Al□Cu□Mg Alloys in NaCl Solution. Corrosion Science 1979, 19 (4), 225–236.
[37] Raps, D.; Hack, T.; Wehr, J.; Zheludkevich, M. L.; Bastos, A. C.; Ferreira, M. G. S.; Nuyken, O. Electrochemical Study of Inhibitor-Containing Organic–Inorganic Hybrid Coatings on AA2024. Corrosion Science 2009, 51 (5), 1012–1021.
[38] Loveday, D.; Peterson, P.; Rodgers, B. Evaluation of Organic Coatings with Electrochemical Impedance Spectroscopy. JCT CoatingsTech 2004, 6.
[39] Rosero-Navarro, N. C.; Pellice, S. A.; Castro, Y.; Aparicio, M.; Durán, A. Improved Corrosion Resistance of AA2024 Alloys through Hybrid Organic–Inorganic Sol–Gel Coatings Produced from Sols with Controlled Polymerisation. Surface and Coatings Technology 2009, 203 (13), 1897–1903.
[40] Boag, A.; Hughes, A. E.; Glenn, A. M.; Muster, T. H.; McCulloch, D. Corrosion of AA2024-T3 Part I: Localised Corrosion of Isolated IM Particles. Corrosion Science 2011, 53 (1), 17–26.
[41] Croes, K. J.; Vreugdenhil, A. J.; Yan, M.; Singleton, T. A.; Boraas, S.; Gelling, V. J. An Electrochemical Study of Corrosion Protection by in Situ Oxidative Polymerization in Phenylenediamine Crosslinked Sol–Gel Hybrid Coatings. Electrochimica Acta 2011, 56 (23), 7796–7804.
[42] Wittmar, A.; Wittmar, M.; Ulrich, A.; Caparrotti, H.; Veith, M. Hybrid Sol–Gel Coatings Doped with Transition Metal Ions for the Protection of AA 2024-T3. J Sol-Gel Sci Technol 2012, 61 (3), 600–612..
[43] Chaudhari, S.; Patil, P. P. Inhibition of Nickel Coated Mild Steel Corrosion by Electrosynthesized Polyaniline Coatings. Electrochimica Acta 2011, 56 (8), 3049–3059.
[44] Yuan, X.; Yue, Z. F.; Chen, X.; Wen, S. F.; Li, L.; Feng, T. EIS Study of Effective Capacitance and Water Uptake Behaviors of Silicone-Epoxy Hybrid Coatings on Mild Steel. Progress in Organic Coatings 2015, 86, 41–48.
[45] Loveday, D.; Peterson, P.; Rodgers, B. Evaluation of Organic Coatings with Electrochemical Impedance Spectroscopy. JCT CoatingsTech 2004, 6.

General Conclusion and Perspectives

Sol-Gel coatings have been considered as a promising candidate for the replacement of Chromium Conversion Coatings (CCC) for corrosion protection of metals. Neverthelss, its porosity nature (intermolecular, interparticular, intercluster pores) constitute connected corrosion pathway within the coating. Heat treatment or adding of fillers have been applied by researchers to improve the barrier effect of Sol-Gel coatings. Among them, graphene-like two-dimensional (2D) materials have got attention due to their impermeability to molecules. The 2D hexagonal Boron Nitride is interesting as a filler for corrosion protection coatings for its chemical inertness and large bandgap (5.2eV-5.9eV).

This thesis aims to study the influence of 2D materials to Sol-Gel coatings deposited on metals for corrosion protection applications. The hexagonal Boron Nitride nanosheets (BNNS) was mainly studied while electrochemically expanded graphite exfoliated nanosheets (GENS) and Molybdenum disulfide exfoliated nanosheets (MDNS) were exploited afterward. The study was performed by charging 2D nanofillers into Sol-Gel matrix on metal with different reactivities in corrosive environment. The influence of 2D materials were investigated with the help of electrochemical characterization (Open Circuit Potential, Potentiodynamic Polarization, Electrochemical Impedance Spectroscopy) in NaCl 30g/L.

The 2D materials have been proved to be able to seal the pores in the coating and enhance the barrier effect of the coating. The enhancement is due to a synergy effect provided by both Sol-Gel matrix and nanofiller. **We proposed an approach to syntheize an 2D fillers charged organic inorganic hybrid coating which shows an excellent corrosion protection to the substrate metal.**

Firstly, Zirconium oxide based (ZrO) single-component coating has been deposited on stainless steel 316L. The 316L substrate behaves inertness to general corrosion and is prone to pitting corrosion. The porous Sol-Gel inorganic coating allows the penetration of electrolyte to the stable interface of 316L which allows the role of 2D fillers during the evolution of ZrO/316L system to be observed.

By using three BN powders with three different average diameters, a critical lateral size (d_c) at 7 μm was proposed for the BN powder to provide evident barrier effect to the coating. If the average size is inferior to this onset value, the resistance reinforcement to the Sol-Gel will be minor. This study was performed with the stable suspension of BNNS in aqueous media with a concentration inferior to 15 μg/mL.

The influence of BNNS concentration superior to stable concentration has been studied. When the concentration gets higher than stable concentration, the influence of BNNS becomes twofold: 1)The formation of defects caused by aggregation of BNNS 2) The sealing effect to pores. The coating with increased concentration of BNNS (60 μg/mL) firstly showed even lower protection the coating without fillers. With the concentration kept increasing (130 μg/mL), the sealing effect predominates and the barrier effect is enhanced. After the concentration surpasses 170 μg/mL, a total capacitive behavior can be observed which can be explained by the formation of an impermeable film of BNNS.

The stable interface of 316L hinders influence of 2D materials during the corrosion process. Thus, in order to probe the barrier effect contributed to BNNS fillers, the ZrO single-component coating was directly transported to AA2017 for its higher reactivity to corrosion. Neverthelss, severe corrosion was observed, which is due to the weak barrier effect combined between ZrO porous coating and oxide film of AA2017. It was thus concluded that the ZrO/316L can be used for probing of role of 2D fillers as well as evolution of coating, but a Sol-Gel matrix with less porosity is required.

Secondly, ZrO – SiO multi-component coating deposited on AA2017 with Zirconium n-Butoxide / (3-Glycidyloxypropyl) trimethoxysilane (GPTMS) as precursor, has been synthesized. The reduction of corrosion due to the barrier effect of BNNS has been proved comparing to the coating without filler. However, delamination was observed due to corrosion. To search for a coating/BNNS couple with efficient corrosion protection to metal surface, further enhancement of the Sol-Gel matrix were required by either increasing the adhesion to slow down the delamination or by modifying the Sol-Gel matrix for a stronger barrier effect

Thirdly, to further enchance Sol-Gel matrix for a stronger barrier effect, an Organic Inorganic Hybrid (OIH) Coating is deposited on carbon steel XC90 by incorperating Octadecyltetraethoxysilane (ODTES) to ZrO – SiO multicomponent coating. Therefore, the hydrophobic alkyl group (-C18) changes the polarity of the ZrO-SiO coating to hydrophobic and increases both its flexibility and thickness. ZrO-SiO/C18 coating showed enhanced corrosion protection than ZrO-SiO coating by allowing limited corrosion to take place on the sensitive carbon steel surface. The introduction of BNNS successfully prohibited corrosion and delamination.

Finally, the study of GENS and MDNS were performed on ZrO/316L and ZrO-SiO/C18/carbon steel systems to compare with BNNS under different reactivity condition. GENS showed stronger enhancement than BNNS in both cases while MDNS showed inadequate behavior and even lowers the barrier effect of the coating. Specifically, the impermeable film was not observed by GENS nor MDNS charged in ZrO/316L, which is possibly due to the BNNS nature of inertness and low compability to Sol-Gel matrix.

The ZrO-SiO/C18 coating charged with BNNS or GENS fillers could be well applied for corrosion protection applications.

Considering all the conclusions above, future researches on the following points may allow an enhancement of the coating performance.

1. The bonding between BNNS and Sol-Gel matrix: functionalization of the BNNS could improve the bond between the BNNS and the Sol-Gel matrix. Meanwhile, by functionalization, the BNNS concentration can also be augmented.
2. The optimization of the highly concentrated BNNS film: In order to understand the mechanism of the formation of the film, BNNS with different functional groups could be applied to increase the integrity of the BNNS to the coating.
3. The optimization of influence of 2D materials other than BNNS: The optimization study of the influence of the concentration of GENS fillers to the barrier effect of ZrO and ZrO-SiO/C18 coatings in NaCl 30g/L solution.

4. <u>The identification of critical size (d_c) from exfoliated BNNS:</u> The first part study have given the existence of critical size for BN powders. To understand the influence of BNNS in detail, the d_c from exfoliated nanosheets could be explored with optimization study by specific preparation method as well as characterization with microscopies.

Table of Figures

Figures from Chapter I

Figures from Chapter II

Figures from Chapter III

Figures from Chapter IV

List of Tables

Appendix

Appendix.1 Abbreviations and Acronyms

A.1.1 Abbreviations and Acronyms of materials

Table. A - 1 Abbreviations and Acrnyms of materials

Abbreviations & Acronyms	*Full Name*
2D materials	***2-Dimensional materials***
AA	***Aluminum Alloy***
BNNS	***Hexagonal Boron Nitride Nanosheet***
BP	***Black Phosphorus***
CCC	***Chromium Conversion Coatings***
CNTS	***Carbon Nanotubes***
COFs	***Covalent Organic Frameworks***
GE	***Electrochemically Expanded Graphite***
GENS	***Electrochemically Expanded Graphite derived Nanosheet***
GO	***Graphene Oxide***
h-BN	***Hexagonal boron nitride***
LDHs	***Layered Double Hydroxides***
MDNS	***Molybdenum Disulfide Nanosheet***
MOFs	***Metal–Organic Frameworks***
MoS_2	***Molybdenum disulfide***
MXenes	***2D transition metal carbides, carbonitrides and nitrides***
IOH	***Inorganic Oragnic Hybrid***
rGO	***Reduced Graphene Oxide***
SS	***Stainless Steel***
TMDs	***Transition Metal Dichalcogenides***
YSZ	***Yttria Stabilized Zirconium***

A.1.2 Abbreviations and Acronyms of Sol-Gel Precursors

Table. A - 2 Abbreviations and Acronyms of Sol-Gel Precursors

Abbreviations & Acronyms	*Full Name*
APTES	***3-Aminopropyltriethoxysilane***
DTES	***Decyltriethoxysilane***
Epoxy	***Polyepoxides***
ETES	***Ethyltriethoxysilane***
GPTMS	***(3-Glycidyloxypropyl) trimethoxysilane***
MAPTS	***Γ-Methacryloxypropyl-trimethoxysilane***
MTES	***Methyltriethoxysilane***
MTMS	***Methyltrimethoxysilane***
ODTES	***Octadecyltriethoxysilane***
OTES	***Octyltriethoxysilane***
PDMS	***Polydimethylsiloxane***
PMMA	***Poly (methyl methacrylate)***
PTMS	***Phenyltrimethoxysilane***
PVA	***Polyvinyl Alcohol***
PVP	***Polyvinylpyrrolidone***
TEOS	***Tetraethoxysilane***
ZAH	***Zirconium Acetate Hydroxyl***
ZBO	***Zirconium n-butoxide***
ZPO	***Zirconium propoxide***
ZTB	***Zirconium tetra-butoxide***

A.1.3 Abbreviations and Acronyms of characterization tools

Table. A - 3 Abbreviations and Acronyms of characterization tools

Abbreviations & Acronyms	*Full Name*
ASE	***Auger Electron Spectroscopy***
ATR	***Attenuated Total Reflectance***
BSE	***Back Scattered Electrons***
CE	***Counter Electrode***
CVD	***Chemical Vapor Deposition***
DLS	***Dynamic Light Scattering Spectroscopy***
EC	***Electrochemical Equivalent Circuit***
EIS	***Electrochemical Impedance Spectroscopy***
FTIR	***Fourier Transformed infrared spectroscopy***
LBL	***Layer By Layer deposition***
LSV	***Linear Scanning Voltage***
OCP	***Open circuit potential***
PVD	***Physics Vapor Deposition***
Raman	***Raman Spectroscopy***
RE	***Reference Electrode***
Redox	***Reduction-Oxidation***
SCC	***Stress Corrosion Cracking***
SCE	***Saturated Calomel Electrode***
SE	***Secondary Electron***
SEM	***Scanning Electron Microscopy***
TEM	***Transmission electron Microscopy***
UV-Vis	***Ultraviolet-Visible Spectroscopy***
WCA	***Water Contact Angle***
WE	***Working Electrode***

A.1.4 Abbreviations and Acronyms for Electrochemical Equivalent Circuit

Table. A - 4 Abbreviations and Acronyms of symbols for Electrochemical Equivalent Circuit

Abbreviations & Acronyms	*Full Name*
C	*Capacity*
C_{dl}	*Double layer capacitance*
E_{corr}	*Corrosion potential*
E_{crit}	*Critical potential*
I	*Current*
i_{anode}	*Anode current density*
$i_{cathode}$	*Cathode current density*
i_{corr}	*Corrosion potential*
i_{pass}	*Current density of passive region*
M	*Restricted diffusion, Finite Length Warburg with reflective boundary condition, Finite Space Warburg*
M_{α}	*Anomalous Restricted Diffusion*
Q/CPE	*Constant Phase Element*
Q_{dl}	*Double layer capacitance related CPE*
R	*Resistance*
R_{ct}	*Charge transfer resistance*
W	*Warburg diffusion*
W_{δ}	*Bounded diffusion, Finite Length Warburg with transmissive boundary conditon*
Z	*Impedance*
α	*Parameters for CPE*
φ	*Phase angle*

Appendix.2 Characterization Tools

A.2.1 Introduction

In order to probe the properties of the materials employed in this work, different characterization tools are used.

The Spectroscopies are used to understand the properties of liquid solutions. UV-Visible Spectroscopy is used to identify the existence of 2D materials as well as measuring the concentration of exfoliated solutions. Dynamic light scattering (DLS) spectroscopy is used to characterize the colloidal size and the stability of Sol-Gel solution. Raman Spectroscopy and FT-IR Spectroscopy/Transmission mode and ATR mode are used to characterize the properties of as-desposited coatings.

The microscopies are also employed to characterize the morphology of the materials and coatings. According to the need of different size dimention to characterize, different microscopies are employed.

A.2.2 Dynamic Light Scattering Spectroscopy

The Dynamic Light Scattering Spectroscopy (DLS) was applied for the Sol-Gel solutions with the Zetasizer (Malvern, nano ZSP) to understand the colloidal size. By measuring the scattering phenomenon between the introduced laser and output laser, the particles size could be calculated. Different particle size may influence the intensity of scattered light. Since the DLS is sensitive to the particles size of the solution and is designed for nanoparticles, the Sol-Gel solution with 2D materials does not show reliable results

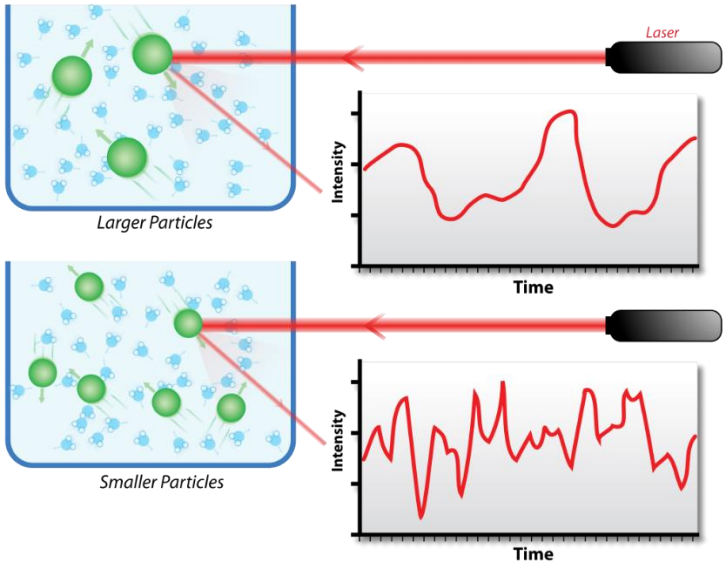

Fig. A - 1 Mechanism of DLS for particles with differernt size

A.2.3 Ultraviolet-visible Spectroscopy

Ultraviolet-Visible spectroscopy (UV-Vis) is a technique using the introduced ultraviolet light and visible light to measure the content of the target species in a liquid, gaseous or even solid under specific conditions. The species could be molecules, ions, suspending particles, etc.

Different atomic structured molecules may absorb the light with different intensity by introducing the light from ultraviolet region (100 nm – 400 nm) to visible lights region (400 nm – 750 nm) and near infrared region (750 nm – 1400 nm), different participants inside the solution (liquid, gaseous or transparent solid) absorb different intensity lights with different wave numbers. With Beer-Lambert the content of the target specie can be calculated. The Beer-Lamber law is shown in:

$$\frac{C}{l} = \alpha \cdot A \qquad \textit{Eq. A - 1}$$

In Eq.2, *C is* the concentration of charger and *A* is the intensity of the signal; *l* is the length of interaction path of light and α is the extinction coefficient. Obviously, the extinction coefficient α should be decided before the calculation. The α can be defined by measuring the angle of the slope between the concentration and Intensity from UV-Vis, as shown in Fig. A - 2. Every machine and every target specie may differ the α. Every target species will have a character wavelength for which at that wavelength the intensity of UV-Vis will be extra high. To avoid the influence of diffraction of extra high intentsity at the character wavelength. the calculation of content of the target species are perfomed with the intensity at a wavelength which has been proved to be less affected by the diffractions. With h-BN for example, the wavelength is selected at 300 nm. [1]

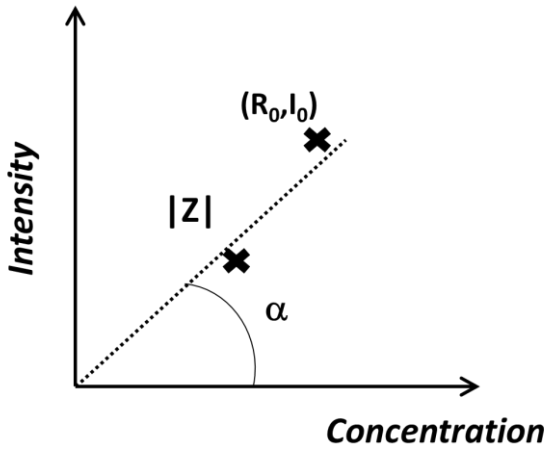

Fig. A - 2 mesurement of extinction coefficient by weighting and measuring with UV-Vis

In this work, the measurement of concentration of hexagonal Boron Nitride (h-BN) with different morphology exfoliated solution are measured by UV-Vis Spectroscopy, and for the measurement of h-BN with high concentraton method, with different solvent as well as the Graphene oxide and MoS_2 in different solvent, the concentration will be measured directly by weighting with the balance. The absorption extinction coefficient of h-BN is measured as 2924 mg/ml/mm at wavelength of 300 nm. This calculated value is coherent to the value reported from other authors, proving that this value as acceptable.[2]

A.2.4 Raman spectroscopy

As shown in Fig. A - 3, when there is a proton introduced to a materials, the electron will be scattered as shown from the scheme. The elastic scattering is called Rayleigh Scattering. The

inelastic scattering is called Stokes Raman Scattering and is of very low possibility comparing to elastic scattering. This inelastic scaterring has been applied for the identification of elements and bonds in material science and is call Raman Scattering Spectroscopy.

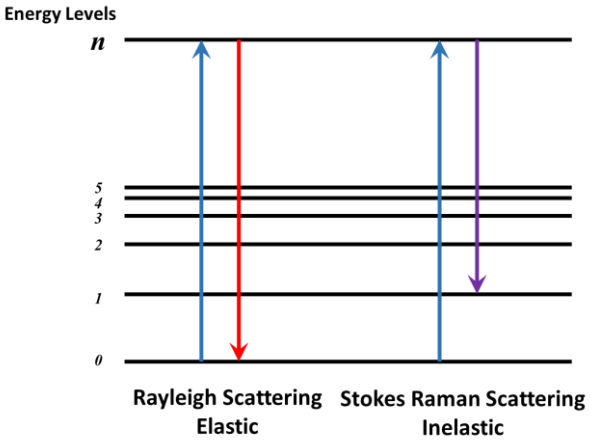

Fig. A - 3 Scheme of energy level for the explaination of Rayleigh scattering and Stokes Raman Scattering

The Raman Spectroscopy is employed confined laser to increase the chance of Raman scattering and calculate the phonon scattering from the energy loss of the detected output light. It is widely applied for the identification of the elements or molecules by detecting phonons representing the characteristic bonds.

The Raman Spectroscopy employed in this work is HORIBA, Aramis with the laser using the wavelength 514nm. Samples of ZrO-SiO/C18 coatings were directly measured in the Raman Spectroscopy after synthesis.

A.2.5 Fourier Transform Infrared Spectroscopy/ Attenuated Total Reflectance

The Fourier Transform Infrared Spectroscopy (FTIR) is following the similar principle as UV-Vis but using light at the wavelength range of Infrared. The absorption of the light will coordinate to certain bonds inside materials and is applied for the identification of bonds and existence of materials. Fourier Transform Infrared Spectroscopy/ Attenuated Total Reflectance (FTIR/ATR) is the FTIR technology applying with total reflectance phenomenon to rapidly detect the near surface region instead of bulk materials. The resolution depth is mostly under 2 microns.

For the ATR mode, as shown in Fig. A - 4., since the ATR crystal has a higher refractive index than the sample, the total reflectance phenomenon will happen. Thus, by calculating the energy lost from pre-defined light path, the identification of thin materials can be achieved. [3]

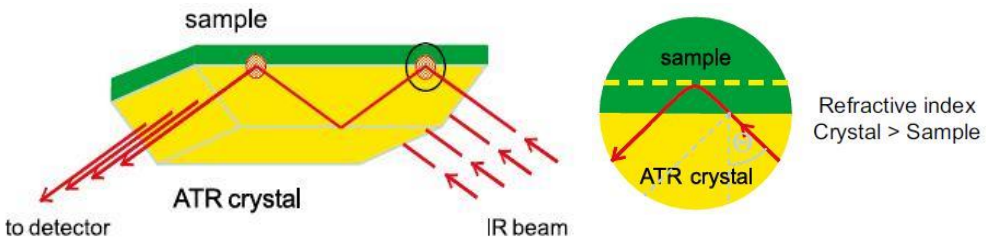

Fig. A - 4 Scheme of mechanism of FT-IR/ATR[4]

In this work, the FTIR spectra were recorded in ATR mode with a FTIR (ThermoScientific Nicolet^{TM} iN10 MX Infred Imaging Microscopy) spectrometer. Coated sampels were directly measured with the FTIR/ATR machine after the synthesis.

A.2.6 Contact angle measurement

The water contact angle (WCA) measurement are done with Kruss EasyDrop Standard located at Laboratory of iLM in *Université Lyon 1*.

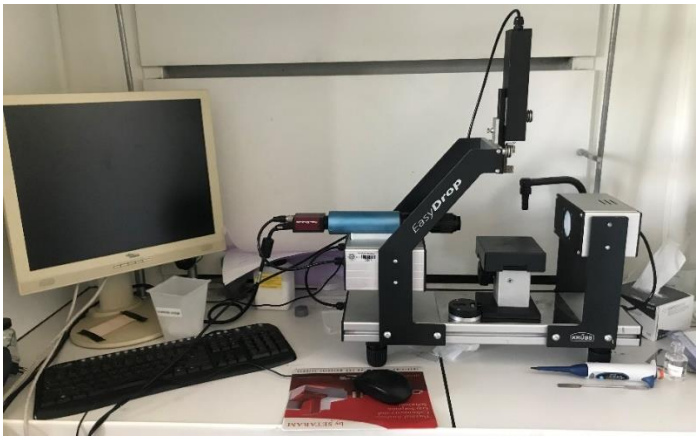

Fig. A - 5 Contact Angle measurement KRUSS EasyDrop Standard

A.2.7 Optical microscopy

To roughly identify the coatings' quality and the presence of the cracks, digital optical microscopy was employed. The digital microscopy that employed in this wotk is a Hirox Digital microscope (model KH-7700), as shown in Fig. A - 6. The image loss of sharpness is due to the low depth of field of the microscopy and the surface curvature. The Hirox system is controlled by a CT-7 controller allowing an auto 3D calibration system to correct the resolution loss. This correction compiles multiple images together and built a 3D surface morphology.

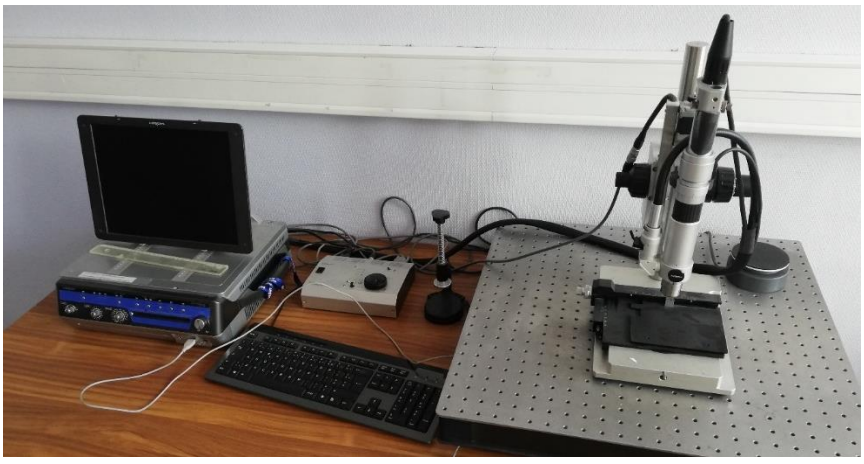

Fig. A - 6 Digital Optical Microscopy Hirox in Laboratoire de Mateis in INSA de Lyon, France

A.2.8 Scanning Electron Microscopy

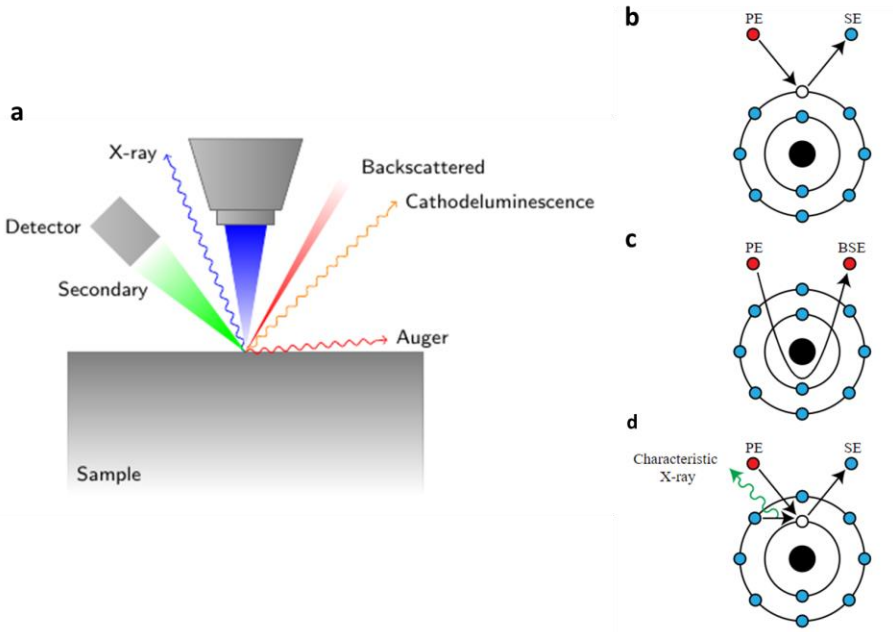

Fig. A - 7 Scheme of a) Mechanism of Scanning Electron Microscopy Mechanism of the interaction between b) PE and SE c) PE and BSE d) PE and Chacatristic other signals.

Scanning Electron Microscopy (SEM) bombards the surface of the material using accelerated electrons under high tension. The detectors collect the responding signals, such as electrons, electromagnetic waves as X-rays, etc., as shown in Fig. A - 7a. By scanning the whole sample surface and calculation with the computer software, the morphology of the target surface could be presented.

The electrons which are called Primary Electrons (PE) from the electron beam will interact with the local electrons which are orbiting around the nucleus, as shown in Fig. A - 7b-d. Different responses from the local atoms could be received.

Fig. A - 7b shows the Secondary Electrons(SE) when one electron in the orbit is baombarded out by the PE. This mode is used for detection of morphology of the surface. Fig. A - 7c shows the Back Scattered Electrons (BSE) when the PE is reflected back by elastic scattering, which is frequent in scanning heavy element. This technique is frequently used to understand the distribution of elements on a surface, by giving a map of contrast showing different colors according to atomic numbers of elements. Fig. A - 7d shows character X-ray emission which allows the detector to identify the bombarded element by calculating the identical energy level emitted of X-ray. This technique is call Energy Dispersive X-ray Spectroscopy (EDS or EDX).

The techniques mentioned above are the three most widely applied technique for SEM. Other emissions can also be observed by SEM technique, such as Auger electron and Cathodeluminescence, etc.

In this work, the ZEISS Supra55 SEM was employed for the morphology of the different samples before and after the corrosion. The higher the electron energy is, the deeper the electron can reach on the surface of the material. With the modification of voltage of the introduced electron beam, the surface morphology with different depth can be characterized. With a coating of 300 nm for example, if the voltage is chosen as 20 kV, the metal surface

under coating will be observed. If the voltage is 2kV or less, the surface morphology of the coating will be observed while the morphology under coating cannot be.

The SEM used in this work is with a ZEISS Supra55 from Clym platform from INSA de Lyon, France. The voltage used are 20 KV for deep detection and 2KV for near surface detection. The inert and stable samples were firstly cleaned with ethanol in ultrason for 15 min and rinsed with distilled water. The unstable samples were cleaned with compression air gun before the measurement.

A.2.9 Transmission Electron Microscopy

Transmission Electron Microscopy (TEM) is a technique using emitted electron to transmit the sample material and detecting the transmitted electrons. In order to transmit the material, the thickness of the materials need to be penetrable by electrons (< 100nm).

As shown in Fig. A - 8a and b, through 2 different focus path, the transmitted electron from the specimen could be focused on 2 different planes. The electronic path shown in Fig. A - 8a could give a Selected Area Electron Diffraction (SAED) pattern of the specimen as shown in Fig. A - 8d. This pattern reflects the microstructure of the specimen. Different microstructure will give out different diffraction pattern as circles, repeating dots, etc. Fig. A - 8b shows the electronic path for the TEM magnification image. The magnified image could clearly demonstrate different layers of the sample if it is thin enough, as shown in Fig. A - 8c.

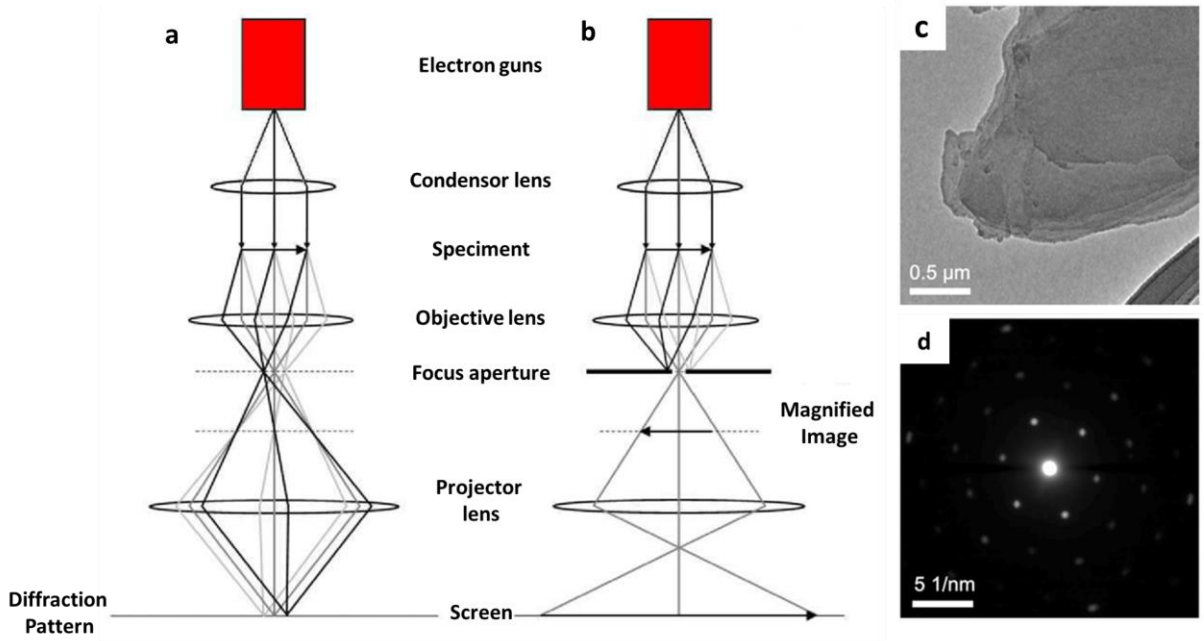

Fig. A - 8 Scheme of TEM a) Diffraction Pattern Mode and b) Magnification Image Mode ;[5] the Image of c)Magnified image and d) Diffraction Pattern [6]

The Transmission Electron Micrographs were obtained with a JOEL-2010 microscope operating at 200 kV from the Clym plateform form INSA de Lyon. The 2D materials samples were exfoliated in different solvent and the 2D materials containing solvent were dropped on to the carbon network containing copper filter and dried for a whole night before being transported for the TEM measurement.

Appendix.3 Preparation of Electrochemically expanded graphene

Electrochemically Expanded Grapheite (GE) synthesized from Graphite foil bought from Fischers, USA. The Graphite foil has been exfoliated with a potential of 20 V applied in Na_2SO_4 1 mol/L solution. The as-exfoliated GE were filtered and rinsed with water and target solvent for 3 times each. Finally, the rinsed GE have been exfoliated in water, n-Butanol with the concentration of 30 mg/mL (with undried solution directly after the synthesis of GE) for 60 hours and centrifuged for 10 min with 2000 rad/min. The powder, exfoliated water solution and exfoliated n-Butanol solution of GE are named as GE powder, GE water and GE n-But respectively. The coatings charged with GE fillers will be noted with a tail noting GE at the end.

After the exfoliation and centrifuge, the 2D materials suspension were stored and been re-exfoliated for 1 hour before added into Sol-Gel solutions.

Appendix.4 Fitting parameters of EIS tests

A.4.1 Fitting Parameters of 316L bare substrate over 120 hours of immersion

Table. A - 5 Fitting Parameters of 316L bare substrate over 120 hours of immersion

Sample	R_s /ohm.cm^2	R_{film} /ohm.cm^2	α_{film}	Q_{film} /f.s^(a-1)	C_{film} /μF	R_{ct} /ohm.cm^2	α_{dl}	Q_{dl} /f.s^(a-1)
316L 16h	30.84	4.33 E+05	0.93	9.67 E-06	1.34	4.32 E+05	0.56	3.59E-06
316L 24h	29.92	3.92 E+05	0.94	1.02 E-05	1.91	4.64 E+05	0.51	6.68E-06
316L 32h	28.99	4.30 E+05	0.94	9.79 E-06	1.83	4.05 E+05	0.55	1.09E-05
316L 48h	29.39	4.02 E+05	0.94	9.54 E-06	1.78	3.16 E+05	0.50	9.82E-06
316L 60h	28.43	3.44 E+05	0.94	9.61 E-06	1.77	2.14 E+05	0.51	1.79E-05
316L 72h	28.41	1.83 E+05	0.94	9.69 E-06	1.72	0.76 E+05	0.55	1.49E-05
316L 84h	27.91	2.75 E+05	0.94	9.59 E-06	1.74	1.15 E+05	0.54	4.39E-05
316L 120h	26.67	2.26 E+05	0.94	9.54 E-06	1.71	0.98 E+05	0.50	4.75E-05

A.4.2 Fitting Parameters of ZrO_Ref over 120 hours of immersion

Table. A - 6 Fitting Parameters of ZrO_Ref over 120 hours of immersion

Sample	R_s /ohm.cm^2	R_{pore} /ohm.cm^2	α_{coat}	Q_{coat} /f.s^(a-1)	C_{coat} /μF	R_{ct} /ohm.cm^2	α_{dl}	Q_{dl} /f.s^(a-1)
ZrO_Ref 16h	32.98	9.74 E+05	0.95	9.32 E-06	2.44	1.53 E+05	0.73	6.11 E-05
ZrO_Ref 24h	33.65	9.69 E+05	0.95	9.22 E-06	2.41	2.18 E+05	0.70	1.10 E-04
ZrO_Ref 32h	32.815	9.01 E+05	0.94	9.36 E-06	1.83	1.42 E+05	0.72	1.09 E-04
ZrO_Ref 48h	35.875	8.45 E+05	0.95	9.20 E-06	2.39	1.26 E+05	0.73	6.04 E-05
ZrO_Ref 60h	34.695	8.40 E+05	0.95	9.23 E-06	2.40	1.24 E+05	0.72	8.29 E-05
ZrO_Ref 72h	36.425	8.85 E+05	0.95	9.08 E-06	2.36	1.10 E+05	0.78	1.43 E-04
ZrO_Ref 84h	35.17	8.75 E+05	0.94	9.15 E-06	1.79	1.05 E+05	0.77	1.26 E-04
ZrO_Ref 120h	36.89	8.75 E+05	0.95	9.22 E-06	2.40	1.16 E+05	0.73	7.85 E-05

A.4.3 Fitting Parameters of ZrO_BNC over 1200 hours of immersion

Table. A - 7 Fitting Parameters of ZrO_BNC over 1200 hours of immersion

Sample	R_s /ohm.cm^2	R_{pore} /ohm.cm^2	α_{coat}	Q_{coat} /f.s^(a-1)	C_{coat} /μF	R_{ct} /ohm.cm^2	α_{dl}	Q_{dl} /f.s^(a-1)
ZrO_BNC 16h	35.6	1.14 E+06	0.947	8.76 E-06	2.12	1.56 E+06	0.518	9.33 E-06
ZrO_BNC 24h	34.4	1.10 E+06	0.948	8.73 E-06	2.17	1.46 E+06	0.501	6.56 E-06
ZrO_BNC 32h	34.8	1.26 E+06	0.948	8.67 E-06	2.17	1.56 E+06	0.508	5.69 E-06
ZrO_BNC 48h	36.0	1.26 E+06	0.950	8.62 E-06	2.28	1.48 E+06	0.580	4.83 E-06
ZrO_BNC 60h	35.9	1.52 E+06	0.950	8.63 E-06	2.31	1.57 E+06	0.588	5.34 E-06
ZrO_BNC 72h	35.5	1.55 E+06	0.950	8.68 E-06	2.32	1.48 E+06	0.620	6.06 E-06
ZrO_BNC 84h	35.2	1.64 E+06	0.950	8.67 E-06	2.33	1.60 E+06	0.591	4.98 E-06
ZrO_BNC 120h	35.3	1.92 E+06	0.949	8.66 E-06	2.28	1.61 E+06	0.571	4.72 E-06
ZrO_BNC 200h	33.6	3.12 E+06	0.948	8.55 E-06	2.25	1.85 E+06	0.624	7.65 E-06
ZrO_BNC 400h	23.7	3.21 E+06	0.942	8.84 E-06	1.98	1.32 E+06	0.748	3.61 E-05
ZrO_BNC 785h	26.2	3.99 E+06	0.944	8.51 E-06	2.03	1.13 E+06	0.833	4.12 E-05
ZrO_BNC 1200h	24.6	4.73 E+06	0.942	8.53 E-06	1.95	1.78 E+06	0.852	4.41 E-05

A.4.4 Fitting Parameters of ZrO_GE over 5 weeks of immersion

Table. A - 8 Fitting Parameters of ZrO_GE over 5 weeks of immersion

Sample	R_s /ohm. cm^2	R_{pore} /ohm.cm^2	α_{coat}	Q_{coat} /f.s^(a-1)	C_{coat} /μF	R_{ct} /ohm.cm^2	α_{dl}	Q_{dl} /f.s^(a-1)
ZrO_GE12h	24.85	2.47 E +6	0.96	1.08 E -5	3.91	2.90 E +6	0.62	3.20 E -6
ZrO_GE 24h	24.66	2.76 E +6	0.96	1.08 E -5	3.93	5.55 E +6	0.58	1.44 E -6
ZrO_GE 48h	23.79	3.12 E +6	0.96	1.08 E -5	3.95	5.88 E +6	0.60	1.46 E -6
ZrO_GE 120h	23.30	2.84 E +6	0.96	1.06 E -5	3.86	6.57 E +6	0.62	1.10 E -6
ZrO_GE 144h	22.22	2.38 E +6	0.96	1.03 E -5	3.72	4.16 E +6	0.55	1.29 E -6
ZrO_GE 168h	22.12	3.32 E +6	0.96	1.03 E -5	3.77	5.12 E +6	0.50	1.32 E -6
ZrO_GE 2w	21.36	3.08 E +6	0.96	1.01 E -5	3.68	7.71 E +6	0.54	8.11 E -7
ZrO_GE 2w3d	21.89	5.19 E +6	0.95	1.00 E -5	2.87	8.53 E +6	0.64	1.28 E -6
ZrO_GE 3w	24.75	4.77 E +6	0.95	1.01 E -5	2.89	1.16 E +7	0.57	5.38 E -7
ZrO_GE 5w	22.23	1.04 E +7	0.95	9.91 E -6	2.95	1.14 E +7	0.75	2.40 E -6

[1] Brug, G.; Vandeneeden, A.; Sluytersrehbach, M.; Sluyters, J. The Analysis of Electrode Impedances Complicated by the Presence of a Constant Phase Element. J. Electroanal. Chem. 1984, 176 (1–2), 275–295.
2 Coleman, J. N.; Lotya, M.; O'Neill, A.; Bergin, S. D.; King, P. J.; Khan, U.; Young, K.; Gaucher, A.; De, S.; Smith, R. J.; et al. Two-Dimensional Nanosheets Produced by Liquid Exfoliation of Layered Materials. Science 2011, 331 (6017), 568–571.
[3] Dhakate, S. R.; Chauhan, N.; Sharma, S.; Tawale, J.; Singh, S.; Sahare, P. D.; Mathur, R. B. An Approach to Produce Single and Double Layer Graphene from Re-Exfoliation of Expanded Graphite. Carbon 2011, 49 (6), 1946–1954. https://doi.org/10.1016/j.carbon.2010.12.068.
[4] Brucker optics. Attenuated Total Reflection (ATR) Mode - Advantages for FT-IR Spectroscopy. https://www.azom.com/article.aspx?ArticleID=5958
[5] Abbes, Omar.Etude de la diffusion réactive entre Mn et Ge à l'échelle nanométrique pour des applications en spintronique. Thesis.
[6] Rao, K. S.; Senthilnathan, J.; Liu, Y.-F.; Yoshimura, M. Role of Peroxide Ions in Formation of Graphene Nanosheets by Electrochemical Exfoliation of Graphite. Sci Rep 2015, 4 (1), 4237.

FOLIO ADMINISTRATIF

THESE DE L'UNIVERSITE DE LYON OPEREE AU SEIN DE L'INSA LYON

NOM : SHI
(avec précision du nom de jeune fille, le cas échéant)

DATE de SOUTENANCE : Février 11, 2021

Prénoms : Yu

TITRE : Study of the role of two dimensional nanosheets as fillers in Sol-Gel anticorrosion coatings deposited on metal surface

NATURE : Doctorat

Numéro d'ordre : 2021LYSEI004

Ecole doctorale : ED34

Spécialité : Matéiriaux

RESUME :

Sol-Gel coating has got attention for the replacement of hazardeous Chromate Conversion Coatings for being environmental friendly, having a mild synthesis condition as well as a controllable microstructure of the product. To overcome the shortcomings of the porous nature, fillers have been introduced to enhance the barrier effect of the coating. Two dimensional (2D) nanosheets have been studied as fillers due to their impermeability in atomic layer. To understand the role of 2D nanofillers in the enhancement of barrier effect to Sol-Gel coating, the electrochemical techniques have been performed. The role of 2D materials were probed with the interpretation of Electrochemical Impedance Spectroscopy (EIS) with 2D nanosheets charged Sol-Gel/metal systems with different reactivities to corrosion. The hexagonal Boron Nitride, electrochemically expanded Graphite and Molybdenum Disulfide derived nanosheets were exfoliated in pure solvants as fillers. For possible applications, the coated systems were immersed in NaCl 30g/L solution.

MOTS-CLÉS : Corrosion, Sol-Gel, 2D materials, EIS

Laboratoire (s) de recherche : MATEIS

Directeur de thèse: Bernard Normand Professeur des Universités de INSA-LYON

Composition du jury : Marjorie OLIVIER (Rapporteur) Professeur des Universités de Université de Mons ; Bérangère TOURY (Examinateur) Maître de Conférences HDR Université Lyon 1 ; Ingrid SERRE (Examinateur) Professeur des Universités de Université de Lille ; Marie-Pierre GIGANDET (Examinateur) Maître de conférences Université Bourgogne Franche Comté ; Stéphane BENAYOUN Professeur des Universités ; Sheng YUAN (Invité) Maître de Conférences de INSA-LYON ; Bernard NORMAND (Directeur de thèse) Professeur des Universités de INSA-LYON.